Search for strongly interacting supersymmetric particles decaying to final states with an isolated lepton with the ATLAS detector at the LHC

Jeanette Miriam Lorenz

GEBOREN IN ERLANGEN

Zusammenfassung

Diese Arbeit präsentiert zwei Suchen nach Gluinos oder Squarks, die zu Endzuständen mit mehreren Jets, einem isolierten Elektron oder Muon und mit einer hohen fehlenden Transveralenergie zerfallen. Beiden Analysen liegen Daten zugrunde, die vom ATLAS Detektor in pp-Kollisionen bei einer Schwerpunktsenergie von 8 TeV am LHC im Jahre 2012 aufgezeichnet wurden.

Die erste Analyse verwendet nur einen Teil der verfügbaren Statistik und analysiert $5,8\,\mathrm{fb}^{-1}$. Die zweite Analyse verwendet die komplette Statistik in der Höhe von $20,3\,\mathrm{fb}^{-1}$.

Die verwendeten Trigger und Methoden der Untergrundbestimmung sind in beiden Analysen gleich. Die beiden dominierenden Untergründe sind die Produktion von $t\bar{t}$ oder von $W+$Jets Ereignissen. Diese beiden Untergründe werden mit Hilfe einer teilweisen datenbasierten Methode abgeschätzt. Zur Abschätzung des kleinen QCD Untergrunds wird eine vollständig auf Daten basierende Methode eingesetzt. Die vollständige Untergrundabschätzung nach allen Selektionskriterien wird mit Hilfe eines Fits durchgeführt, welcher auf einer Likelihood-Methode basiert.

Keine der beiden Analysen findet eine positive Abweichung im Vergleich zum erwarteten Standardmodell-Untergrund. Daher berechnen beide Analysen Limits in supersymmetrischen Modellen. Die erste Analyse interpretiert das Ergebnis in einem MSUGRA/CMSSM-Modell mit Parametern $A_0 = 0$, $\tan\beta = 10$ und $\mu > 0$ und findet, dass Gluinos und Squarks mit einer Masse von weniger als 1.2 TeV ausgeschlossen sind unter der Annahme gleicher Massen für Gluinos und Squarks. Die zweite Analyse berechnet Limits in mehreren vereinfachten Modellen sowie wie auch in einem MSUGRA/CMSSM-Modell mit Parametern $A_0 = -2m_0$, $\tan\beta = 30$ and $\mu > 0$. In vereinfachten Modellen können Gluino- oder Squarkmassen unterhalb von 1.2 GeV bzw. von 750 GeV ausgeschlossen werden, sofern die $\tilde{\chi}_1^0$-Masse verschwindend gering ist. Im MSUGRA/CMSSM Modell können Gluinomassen unterhalb von 1.2 GeV für jeden Wert von m_0 ausgeschlossen werden.

Abstract

Two analyses searching for squarks and gluinos which decay into final states with multiple jets, an isolated electron or muon and a large missing transverse energy are presented. Both rely on data taken by the ATLAS detector in pp collisions at a center-of-mass energy of 8 TeV at the LHC during 2012. The first analysis uses a subset of $5.8\,\mathrm{fb}^{-1}$ of this dataset, the other analysis uses the full statistics of $20.3\,\mathrm{fb}^{-1}$.

Both analysis share the same methods regarding the triggers and the background estimation techniques. The two dominant backgrounds are $t\bar{t}$ and W+jets production. The $t\bar{t}$ and the W+jets backgrounds are estimated in a semi-data-driven method. The minor QCD multi-jet background is estimated in an entirely data-driven method. The final background estimates in the analyses are derived in a profile-log-likelihood fit.

None of the analyses sees an excess beyond Standard Model expectations. The analysis of the partial dataset derives limits in a MSUGRA/CMSSM model with parameters $A_0 = 0$, $\tan\beta = 10$ and $\mu > 0$ and excludes squarks and gluinos with masses below 1.2 TeV for equal squark and gluino masses.

The analysis of the full dataset derives limits in simplified models and in a MSUGRA/CMSSM model with parameters $A_0 = -2m_0$, $\tan\beta = 30$ and $\mu > 0$. Gluinos (squarks) with masses below 1.2 TeV (750 GeV) can be excluded for vanishing $\tilde{\chi}_1^0$ masses in simplified models. Gluino masses below 1.2 TeV can be excluded for every m_0 value in the MSUGRA/CMSSM model.

It is a capital mistake to theorize before one has data. Insensibly one begins to twist facts to suit theories, instead of theories to suit facts.
Sir A. C. Doyle in 'The Adventures of Sherlock Holmes'

To my family

Contents

Chapter 1

The search for Supersymmetry in events with an electron or a muon in the final state

The concept of Supersymmetry, proposed about 40 years ago, postulates a symmetry between fermions and bosons. Such a symmetry implies roughly a doubling of the number of elementary particles in the minimal extension of the Standard Model of Particle Physics as each particle in the Standard Model obtains a supersymmetric partner.

Supersymmetry is able to solve some of the problems present in the Standard Model and is therefore a popular extension beyond the Standard Model. Most importantly, it proposes a dark matter candidate and is able to stabilise the mass of the Higgs boson which suffers from radiative corrections.

Before the startup of the Large Hadron Collider (LHC) at CERN near Geneva, Supersymmetry was expected to be discovered soon, in fact to be "just around the corner" [1, 2]. In particular the supersymmetric partners of the gluon, the gluino, and of the quarks, the squarks, were expected to be easily accessible due to large production cross sections. The first analyses [3, 4, 5] by the ATLAS and the CMS Collaboration quickly placed stringent limits on these particles, for example excluding gluinos with masses below 600 - 900 GeV in specific models (these limits also entered the TeV range with the following years of LHC running as discussed in Chapter 2). The limits derived were however mostly placed in very special (and also simplistic) models.

The recent discovery of a scalar boson seeming to be consistent with a Standard Model Higgs boson posed further, severe constraints and thus reduced the number of possible supersymmetric models.

The tight constraints on gluinos and squarks in specific models caused a refinement in the searches for Supersymmetry in various directions. Some analyses considered the possibility that squarks of the first two generations and gluinos might be too heavy for a discovery at the LHC and focused instead on the search for potentially lighter supersymmetric particles as the stop, the supersymmetric partner of the top quark [6, 7, 8, 9], or sleptons, the supersymmetric partners of the leptons [10, 11, 12, 13]. Another direction was and is to question the simplistic models and to study more general models which are consistent with all known constraints.

The search for gluinos and squarks of the first two generations remains however interesting, in particular considering the potential high cross sections. Also, many popular supersymmetric models expect not too heavy gluinos [14].

This work presents two analyses searching for squarks and gluinos produced in pp collisions at a center-of-mass energy of 8 TeV at the LHC and recorded by the ATLAS detector in 2012. Searches for these particles are traditionally separated according to their final states. Gluinos and squarks decay into final states with many jets, undetected particles and possibly leptons. Final states without leptons have large cross sections, but searches for these final states suffer from large Standard Model QCD multi-jet backgrounds. Requiring at least one lepton in the final states reduces the QCD multi-jet background significantly, but also reduces the cross section of the process. The analyses in this work consider specifically final states with exactly one isolated lepton, electron or muon, with high transverse momentum (1-lepton analysis). Analyses targeting this final state have been performed since the start of the LHC operations. They have however evolved over the years by including novel methods and by studying a variety of supersymmetric models. This work presents the two most recent analyses.

Both of these analyses use a technique known as 'shape fit' (defined in Chapter 10) which was proposed by the author and others and first used in [15]. This technique allows the derivation of limits on supersymmetric models in a fit to data using multiple regions in a phase space. Background and signal can be particularly well separated in such a shape fit. For the analyses presented in this work, this technique implies a increased sensitivity to a broad class of different supersymmetric models. The analyses presented are thus very general. While this work particularly focuses on models with gluino and squark production and R-parity conservation (defined in Section 2.3.6), the second analysis in this work was recently shown to be also sensitive to scenarios with R-parity violation by using the methods presented in this work [16]. In addition, this analysis was also shown to be sensitive to supersymmetric models with stop or sbottom quark production in the decay of the gluino [16].

The outline of this work is as follows. Part I discusses the theoretical and experimental background. Chapter 2 gives a short overview about the Standard Model, the motivations for Supersymmetry and its theoretical concepts. This chapter also defines the models used in this work. The LHC and the ATLAS detector are discussed in Chapter 3. Part II discusses the structure of the 1-lepton analysis. Chapter 4 explains the reconstruction and identification of the particles and objects relevant for this work. Chapter 5 discusses the Standard Model backgrounds in the 1-lepton analysis and explains quantities useful in the separation of background and signal. Part III presents an analysis of a subset of the 2012 data. In particular, this part explains the methods used in 1-lepton analyses. Based on these methods and on the result of this first analysis, Part IV discusses a second analysis now considering the complete dataset recorded in 2012. This analysis was optimised for a variety of supersymmetric models as discussed in Chapter 12. No excess beyond Standard Model expectations was seen. Limits on squark and gluino masses were thus derived and are presented in Chapter 16. The work closes with a comparison to similar analyses searching for Supersymmetry.

Part I

Theory and Experiment

Chapter 2

An introduction to Supersymmetry

The Standard Model of Particle Physics, which is shortly summarised in the next section, has certain short-comings which are resolved by the concept of Supersymmetry (SUSY). A short introduction to Supersymmetry is the main aim of this chapter with a particular focus on the phenomenological implications. Various searches for Supersymmetry, described at the end of this chapter, have been performed and serve as starting point for the analyses described in this work.

2.1   The Standard Model of Particle Physics

The *Standard Model of Particle Physics* describes ordinary matter and their electromagnetic, weak and strong interactions with amazing precision (apart of neutrino masses[1]). Gravitational interactions are not described by the Standard Model. Ordinary matter is composed of fermions: Six different leptons and six different quarks along with their anti-particles can be ordered in three families. These particles are shown ordered by family and together with some of their properties in Table 2.1.

All of the fermions have spin 1/2. The forces described in the Standard Model are propagated by bosons of spin 1. The electromagnetic force, acting on any particle with electric charge, is propagated by the photon, γ. The photon is massless and the reach of the electromagnetic force is infinite. The strong force, acting on any particle with colour charge (quarks and gluons) is mediated by eight massless gluons. The weak force is mediated by two W-bosons of negative and positive electric charge, W^- and W^+, and by the neutral Z boson. The W and Z bosons are massive and the reach of the weak force is limited. They obtain their mass through the

---

[1]The Standard Model in the version presented here does not include massive neutrinos. Different proposals how to include massive neutrinos are discussed in the literature. A review can be found in [17].

Fermion	Generation			Electric charge	Colour	Weak isospin (third component)		Spin
	1	2	3			Left handed	Right handed	
Leptons	ν_e	ν_μ	ν_τ	0	-	1/2	-	1/2
	e	μ	τ	-1	-	$-1/2$	0	1/2
Quarks	u	c	t	$+2/3$	r, b, g	1/2	0	1/2
	d	s	b	$-1/3$	r, b, g	$-1/2$	0	1/2

Table 2.1: The fermions in the Standard Model. Adapted from [18].

Interaction	Couples to	Mediator	Mass [GeV]
Strong	Colour	8 gluons (g)	0
Electromagnetic	Electric charge	Photon γ	0
Weak	Weak charge	$W^\pm$, Z	$m_{W^\pm} = 80.385 \pm 0.015$ GeV [22] $m_Z = 91.1876 \pm 0.0021$ GeV[22]

Table 2.2: Interactions and their mediators in the Standard Model. Adapted from [18].

Higgs mechanism, which will be discussed in Section 2.1.5. A massive scalar of spin 0 emerges from the Higgs mechanism, the Higgs boson. A particle with a mass of 125.9 ± 0.4 GeV [19][2] so far consistent with a Standard Model Higgs boson (given the precision of the measurements) has recently been observed [20, 21] by the ATLAS and CMS Collaborations. The bosons with spin 1 are summarised in Table 2.2.

The mathematical description of the Standard Model is based on the concept of symmetries and more specifically on the principle of gauge invariance. The Standard Model can be described by two renormalisable[3] quantum field theories (QFT): $SU(2)_L \times U(1)_Y$ (L indicates that this part is only acting on left-handed particles, Y is the hypercharge) describing the electromagnetic and the weak interactions in a unified electroweak theory, and $SU(3)_C$ describing the strong interactions (C refers to colour). In the following, some of the mathematical concepts will be highlighted and some of their consequences discussed (more extensive summaries can be found in e.g. [18, 24, 25]).

2.1.1 Symmetries

Any quantum field theory is described by a Lorentz-invariant Lagrangian density $\mathcal{L}$, in the following abbreviated by Lagrangian. The dynamics of the system is derived by using the principle of least-action, $\delta S = 0$, where $S = \int d^4x \mathcal{L}$. Using the Euler-Lagrange equations, the equation of motions of the system can be obtained [26] for the fields ϕ_i, $i = 1, ..., n$:

$$\partial_\mu \left[\frac{\partial \mathcal{L}}{\partial(\partial_\mu \phi_i)} \right] = \frac{\partial \mathcal{L}}{\partial \phi_i} \qquad (2.1.1)$$

where $\mu = 1, ..., 4$ are the space-time indices. The Noether theorem states that for any generator of a (continuous) symmetry transformation under which the Lagrangian is invariant, a conserved current and so a conserved charge exists. For example, the following infinitesimal transformations under which δS shall be invariant (the following explanations and notations follow closely [26]) are considered:

$$\begin{aligned} x^\mu &\rightarrow x'^\mu = x^\mu + \epsilon^a A_a^\mu(x) \\ \phi_i(x) &\rightarrow \phi_i'(x') = \phi_i(x) + \epsilon^a F_{i,a}(\phi, \partial\phi) \end{aligned} \qquad (2.1.2)$$

where the vector $A_a^\mu(x)$ and the function $F_{i,a}(\phi, \partial\phi)$ being given and ϵ^a for $a = 1, .., n$ being infinitesimal parameters. Depending on whether or not ϵ^a depends on x, the symmetry transformations are local or global with important consequences for the theory as will be discussed

---

[2]This value is obtained in a combination of ATLAS and CMS measurements by the PDG group.

[3]*Renormalisable* quantum field theories are required so that unphysical infinite contributions to observables can be eliminated [23].

in Section 2.1.2. Following the Noether theorem due to the invariance of δS under these transformations n conserved currents exist [26]:

$$\partial_\mu j_a^\mu(\phi^{\text{cl}}) = 0 \qquad (2.1.3)$$

where ϕ^{cl} is a solution of the Euler-Lagrange equations. j_a^μ is given by

$$j_a^\mu = \frac{\partial \mathcal{L}}{\partial(\partial_\mu \phi_i)} \left[A_a^\nu(x) \partial_\nu \phi_i - F_{i,a}(\phi, \partial \phi) \right] - A_a^\mu(x) \mathcal{L} \qquad (2.1.4)$$

which simplifies to

$$j_a^\mu = -\frac{\partial \mathcal{L}}{\partial(\partial_\mu \phi_i)} F_{i,a} \qquad (2.1.5)$$

in the cases of internal symmetries that do not change coordinates (therefore $A_a^\mu(x) = 0$). Based on the conserved currents, conserved charges can be defined:

$$Q_a = \int d^3x\, j_a^0(\mathbf{x}, t) \qquad (2.1.6)$$

2.1.2 Gauge theories

The Lagrangian describing the quantum field theory is required to be invariant under local gauge transformations.

A field of spin 1/2 can be described by the following Lagrangian (leading to the Dirac equation) [24]:

$$\mathcal{L} = i\bar{\psi}\gamma^\mu \partial_\mu \psi - m\bar{\psi}\psi \qquad (2.1.7)$$

where ψ are spinor fields, $\bar{\psi} = \psi^\dagger \gamma^0$, and γ^μ are the Dirac matrices with

$$\gamma^0 = \begin{pmatrix} 1 & 0 \\ 0 & -1 \end{pmatrix}, \gamma^i = \begin{pmatrix} 0 & \sigma_i \\ -\sigma_i & 0 \end{pmatrix} \qquad (2.1.8)$$

σ_i with $i = 1, 2, 3$ are the Pauli matrices with

$$\sigma_1 = \begin{pmatrix} 0 & 1 \\ 1 & 0 \end{pmatrix}, \sigma_2 = \begin{pmatrix} 0 & -i \\ i & 0 \end{pmatrix}, \sigma_3 = \begin{pmatrix} 1 & 0 \\ 0 & -1 \end{pmatrix} \qquad (2.1.9)$$

The Lagrangian 2.1.7 is invariant under global transformations like $\psi(x) \to e^{-iq\alpha}\psi(x)$, where α does not depend on the coordinate x, but it is not invariant under local transformations with $\alpha(x)$ due to the partial derivative in Equation 2.1.7. By introducing a new field $A_\mu(x)$, the Lagrangian can however be made invariant under local transformations. While the field $\psi(x)$ transforms like

$$\psi(x) \to e^{-iq\alpha(x)}\psi(x) \qquad (2.1.10)$$

the field $A_\mu(x)$ is required to transform like

$$A_\mu(x) \to A_\mu(x) + \partial_\mu \alpha(x) \tag{2.1.11}$$

The Lagrangian can be made invariant under local transformations by adding terms including the field A_μ [24, 23]:

$$
\begin{align}
\mathcal{L} &= -\frac{1}{4}F_{\mu\nu}F^{\mu\nu} + \bar{\psi}(i\gamma^\mu D_\mu - m)\psi \tag{2.1.12} \\
F_{\mu\nu} &= \partial_\mu A_\nu - \partial_\nu A_\mu \tag{2.1.13} \\
D_\mu &= \partial_\mu + iqA_\mu \tag{2.1.14}
\end{align}
$$

It is not possible to include a mass term for A_μ in the Lagrangian, as then the Lagrangian would no longer be invariant under the transformations of the field A_μ in Equation 2.1.11. Making the Lagrangian 2.1.7 invariant under a local transformation thus requires the introduction of a massless field A_μ, which can be associated with the photon γ, so that the Lagrangian 2.1.12 describes the electromagnetic interactions in a quantum field theory (QED). Since the transformations $U(x) = e^{-iq\alpha(x)}$ of the spinor field $\psi(x)$ in Equation 2.1.10 all belong to the group of unitarity transformations in one dimension, $U(1)$, QED is a $U(1)$ gauge theory. $U(1)$ is the simplest example of a gauge theory appearing in the Standard Model. More complicated gauge theories, but all based on the same principles as discussed in this section, describe the electroweak and the strong interacting part of the Standard Model.

2.1.3 The electroweak theory

In 1933 E. Fermi proposed an explanation of the β decay of the neutron by introducing a point-like interaction between four fermions [27] with a strength proportional to G_F (the Fermi constant). Although this theory of weak interactions described low-energy phenomena correctly, it had to be modified for higher energies, where the creation and exchange of W and Z bosons cannot be ignored. Glashow, Weinberg and Salam combined the description of the electromagnetic and the weak interactions in the Glashow-Weinberg-Salam theory of electroweak interactions [28, 29] based on the symmetry group $SU(2)_L \times U(1)_Y$.

The first part, $SU(2)_L$, only acts on left-handed fermions fields with the left handed fermion fields being defined as

$$\psi_L = \frac{1}{2}(1 - \gamma_5)\psi \tag{2.1.15}$$

and the right-handed fermion fields being defined as

$$\psi_R = \frac{1}{2}(1 + \gamma_5)\psi \tag{2.1.16}$$

with $\gamma_5 = \gamma^5 = i\gamma^0\gamma^1\gamma^2\gamma^3$ and ψ being a spinor representing the original fermion. The left-handed fermions can be ordered in doublets of the weak isospin with isospin $I = 1/2$, e.g. for the leptons:

$$\psi_L = \begin{pmatrix} \nu_e \\ e^- \end{pmatrix}, = \begin{pmatrix} \nu_\mu \\ \mu^- \end{pmatrix}, = \begin{pmatrix} \nu_\tau \\ \tau^- \end{pmatrix} \tag{2.1.17}$$

8

and similarly for the quark eigenstates of the weak interaction.

These doublets can be described in a similar Lagrangian as in Equation 2.1.7, however omitting the mass term (mass terms cannot directly be included in the Lagrangian of $SU(2)_L \times U(1)_Y$, as will be discussed below):

$$\mathcal{L} = \bar{\psi}_L i\gamma^\mu \partial_\mu \psi_L \qquad (2.1.18)$$

The interactions with gauge fields can be derived by a similar procedure as before by requiring the invariance of this Lagrangian under $SU(2)_L$ transformations of the type:

$$\psi_L(x) \rightarrow e^{ig\boldsymbol{\alpha}(x)\mathbf{T}}\psi_L(x) \qquad (2.1.19)$$

where g is identified with a coupling constant, $\boldsymbol{\alpha}(x)$ is an arbitrary vector in isospin space and T_i with $i = 1, 2, 3$ (components of the vector $\mathbf{T}$) are the generators of the $SU(2)_L$ group and can be connected with the Pauli matrices by $T_i = \frac{1}{2}\sigma_i$. As the $SU(2)_L$ gauge group is non-abelian, the generators T_i do not commute:

$$[T_i, T_j] = i\epsilon_{ijk}T_k \qquad (2.1.20)$$

with ϵ_{ijk} being the Levi-Civita symbol. Requiring the invariance of the Lagrangian 2.1.18 under the $SU(2)_L$ transformation in 2.1.19 requires the extension of the Lagrangian to:

$$\mathcal{L} = \bar{\psi}_L i\gamma^\mu D_\mu \psi_L - \frac{1}{4}W_{\mu\nu}W^{\mu\nu} \qquad (2.1.21)$$

where the covariant derivative $D_\mu = \partial_\mu + ig\mathbf{W}_\mu \cdot \mathbf{T}$. is introduced. Three fields W_μ^i with $i = 1, 2, 3$ needed to be introduced similarly to the photon field in Section 2.1.2. These fields transform like

$$\mathbf{W}_\mu(x) \rightarrow \mathbf{W}_\mu(x) + \partial_\mu \boldsymbol{\alpha}(x) + g\boldsymbol{\alpha}(x) \times \mathbf{W}_\mu(x) \qquad (2.1.22)$$

Also, in order to make the theory complete, a kinetic term $-\frac{1}{4}W_{\mu\nu}W^{\mu\nu}$ for the W_μ^i fields was introduced in the Lagrangian 2.1.21 with

$$W_{\mu\nu} = \partial_\mu \mathbf{W}_\nu - \partial_\nu \mathbf{W}_\mu - g\mathbf{W}_\mu \times \mathbf{W}_\nu \qquad (2.1.23)$$

The transformations are more complicated in comparison to the transformation of the photon field in Section 2.1.2 due to the non-abelian nature of $SU(2)_L$. Due to the last term in Equation 2.1.23 self-interactions of the W_μ^i fields may occur.

The gauge group $SU(2)_L$, only describing weak interactions, is extended to $SU(2)_L \times U(1)_Y$ in order to also include electromagnetic interactions. The $U(1)_Y$ component will act in the same way on left and right-handed fermion fields. The full Lagrangian of the electroweak theory is given by

$$\mathcal{L}_{\text{electroweak}} = \bar{\psi}i\gamma^\mu D_\mu \psi - \frac{1}{4}W_{\mu\nu}W^{\mu\nu} - \frac{1}{4}B_{\mu\nu}B^{\mu\nu} \qquad (2.1.24)$$

where D_μ was modified to $D_\mu = \partial_\mu + ig\mathbf{W}_\mu \cdot \mathbf{T} + \frac{1}{2}ig'B_\mu Y$ for left-handed particles and $D_\mu = \partial_\mu + \frac{1}{2}ig'B_\mu Y$ for right-handed particles.

Y is the hypercharge defined by $Y = 2q - 2I_3$. The Lagrangian 2.1.24 also includes a kinetic term, $-\frac{1}{4}B_{\mu\nu}B^{\mu\nu}$, for the B_μ field, which is the gauge field for the $U(1)_Y$ part with

$$B_{\mu\nu} = \partial_\mu B_\nu - \partial_\nu B_\mu \tag{2.1.25}$$

The coupling strengths, g and g', are connected with the electric charge e by

$$g = \frac{e}{\sin\theta_W}, \qquad g' = \frac{e}{\cos\theta_W} \tag{2.1.26}$$

where θ_W is the Weinberg angle.

2.1.4 QCD

The strong interactions between quarks and gluons in the Standard Model are described by the gauge group $SU(3)_C$, where C refers to colour. The gauge bosons are the gluons, as shown below. Each quark exists in three colours: red, blue or green. Correspondingly, each anti-quark carries one of the three anti-colours: anti-red, anti-blue or anti-green.

A gauge invariant Lagrangian under $SU(3)_C$ is constructed according to the same principles as in Sections 2.1.2 and 2.1.3 for the quark fields $\psi_{q,k}$ (q indicating the flavour, k the colour) [23]:

$$\mathcal{L}_{\text{QCD}} = -\frac{1}{4}G_a^{\mu\nu}G_{a\mu\nu} + \sum_q \bar{\psi}_{q,j}(i\gamma_\mu D_{jk}^\mu - m_j\delta_{jk})\psi_{q,k} \tag{2.1.27}$$

$$G_a^{\mu\nu} = \partial^\mu G_a^\nu - \partial^\nu G_a^\mu - g_s f_{abc}G_b^\mu G_c^\nu$$

$$D_{jk}^\mu = \delta_{jk}\partial^\mu + ig_s\frac{(\lambda_a)_{jk}}{2}G_a^\mu \tag{2.1.28}$$

with g_s being the strong coupling constant. The generators of the group are the Gell-Mann 'λ-matrices':

$$
\lambda_1 = \begin{pmatrix} 0 & 1 & 0 \\ 1 & 0 & 0 \\ 0 & 0 & 0 \end{pmatrix}, \qquad
\lambda_2 = \begin{pmatrix} 0 & -i & 0 \\ i & 0 & 0 \\ 0 & 0 & 0 \end{pmatrix}, \qquad
\lambda_3 = \begin{pmatrix} 1 & 0 & 0 \\ 0 & -1 & 0 \\ 0 & 0 & 0 \end{pmatrix},
$$

$$
\lambda_4 = \begin{pmatrix} 0 & 0 & 1 \\ 0 & 0 & 0 \\ 1 & 0 & 0 \end{pmatrix}, \qquad
\lambda_5 = \begin{pmatrix} 0 & 0 & -i \\ 0 & 0 & 0 \\ i & 0 & 0 \end{pmatrix}, \qquad
\lambda_6 = \begin{pmatrix} 0 & 0 & 0 \\ 0 & 0 & 1 \\ 0 & 1 & 0 \end{pmatrix},
$$

$$
\lambda_7 = \begin{pmatrix} 0 & 0 & 0 \\ 0 & 0 & -i \\ 0 & i & 0 \end{pmatrix}, \qquad
\lambda_8 = \frac{1}{\sqrt{3}}\begin{pmatrix} 1 & 0 & 0 \\ 0 & 1 & 0 \\ 0 & 0 & -2 \end{pmatrix} \tag{2.1.29}
$$

Due to the non-abelian structure of $SU(3)_C$, the 'λ-matrices' do not commute, but obey the relation $[\lambda_i, \lambda_i] = 2if_{abc}\lambda_c$, where f_{abc} are the structure constants of the group. The fields G_a^μ, $a = 1,...,8$, are the gluon fields, which had to be introduced in the theory in order to make the Lagrangian $\mathcal{L}_{QCD}$ gauge invariant. The Lagrangian contains terms with triple and quartic gluon

couplings due to the non-abelian structure of the group in analogy to Section 2.1.3. Gluons carry both a colour and an anti-colour. In contrast to the W and Z bosons in the spontaneously broken $SU(2)_L \times U(1)_Y$, the gluons remain massless and $SU(3)_C$ remains unbroken. The self-interaction of the gluons results in a phenomenon called *asymptotic freedom*: gluons can be treated as approximately free particles at small distances or high energies (and therefore perturbation theory can be used), but they interact strongly at low energies or large distances. This implies, that no free gluons or quarks can exist, but quarks are confined into colour neutral combinations (*confinement*), e.g. a meson consisting of a quark with a colour and an anti-quark with the appropriate anti-colour or a baryon consisting of three quarks with three different colours. Any free gluon or quark will undergo *hadronisation*, e.g. combine with other quarks or gluons to colour-neutral mesons or baryons, where these quarks or gluons can be created out of the vacuum. Following this process of hadronisation, a shower of hadrons will emerge starting from the initial quark or gluon - this shower is called *jet*.

2.1.5   Spontaneous symmetry breaking

A mass term cannot be included in the Lagrangian in 2.1.24, because the inclusion of such a term $m\bar{\psi}\psi = m(\bar{\psi}_L\psi_R + \bar{\psi}_R\psi_L)$ would destroy the gauge invariance of $SU(2)_L \times U(1)_Y$ [23]. Masses to fermions and to gauge bosons can however be given by the Higgs mechanism [30, 31, 32] as discussed in the following for the $SU(2)_L \times U(1)_Y$ group. No detailed derivation will be given. More details can be found in the literature, e.g. [25, 33].

A complex doublet of scalar fields

$$\phi = \begin{pmatrix} \phi^+ \\ \phi^0 \end{pmatrix} \tag{2.1.30}$$

is introduced in the theory to extend the theory to include masses for fermions and bosons. The Lagrangian 2.1.24 is extended by

$$\mathcal{L}_\phi = (D_\mu\phi)^\dagger(D^\mu\phi) - V(\phi^\dagger\phi) \tag{2.1.31}$$

where

$$V(\phi^\dagger\phi) = \mu^2(\phi^\dagger\phi) + \lambda(\phi^\dagger\phi)^2 \tag{2.1.32}$$

and D_μ is the covariant derivative as defined in the last section. The format of V is limited to contain at most quartic terms in ϕ if requiring renormalisability. Furthermore, in order to avoid instabilities, the real parameter λ needs to be positive [34]. If the other real parameter $\mu^2 > 0$, the potential 2.1.32 will have only one minimum for $\langle\phi\rangle = 0$. Choosing however the parameter μ^2 to be negative, the potential will show more than one minimum and all of them are located on a circle with radius $\sqrt{-\mu^2/(2\lambda)}$. Both the $SU(2)_L$ and the $U(1)_Y$ can be spontaneously broken by choosing one specific minimum on this circle. The common choice is

$$\langle\phi\rangle_0 = \begin{pmatrix} 0 \\ v/\sqrt{2} \end{pmatrix} \tag{2.1.33}$$

with $v = \sqrt{-\mu^2/\lambda}$, the vacuum expectation value of the Higgs field. The doublet ϕ can be evaluated around this minimum by

$$\phi = e^{\frac{-i\boldsymbol{\xi}\cdot\boldsymbol{\sigma}}{2v}} \begin{pmatrix} 0 \\ (v+\eta)/\sqrt{2} \end{pmatrix} \qquad (2.1.34)$$

where η is a real field, $\boldsymbol{\xi}$ is a vector of three real fields and $\boldsymbol{\sigma}$ is a vector containing the three Pauli matrices. Inserting ϕ into the Lagrangian in 2.1.24 extended by the one in 2.1.31, $\mathcal{L}_{\text{full}} = \mathcal{L}_{\text{electroweak}} + \mathcal{L}_{\phi}$, a mass term for the field η appears, whereas the three fields ξ_i, $i = 1, 2, 3$, remain massless (the ξ_i fields are three massless Goldstone bosons). However, by applying a gauge transformation on ϕ the appearance of the fields $\boldsymbol{\xi}$ can be removed in the Lagrangian $\mathcal{L}_{\text{full}}$. The Lagrangian $\mathcal{L}_{\phi}$ takes the form:

$$\mathcal{L}_{\phi} = \left(\frac{1}{2}(\partial_\mu\eta)(\partial^\mu\eta) + \mu^2\eta^2 \right) + \frac{1}{2}\frac{g^2v^2}{4}\left(|W_\mu^+|^2 + |W_\mu^-|^2 \right) + \frac{1}{2}\frac{v^2}{4}|g'B_\mu - gW_\mu^3|^2 \qquad (2.1.35)$$

where two massive $W^\pm$ bosons appeared:

$$W_\mu^\pm = \frac{W_\mu^1 \mp iW_\mu^2}{\sqrt{2}} \qquad (2.1.36)$$

The two fields B_μ and W_μ^3 can be transformed into the observable massive and neutral Z boson field, Z_μ, and the massless γ field, A_μ:

$$\begin{aligned} Z_\mu &= \cos\theta_W W_\mu^3 - \sin\theta_W B_\mu \\ A_\mu &= \sin\theta_W W_\mu^3 + \cos\theta_W B_\mu \end{aligned} \qquad (2.1.37)$$

The massless photon field γ is a consequence of the fact that $\mathcal{L}_{\text{full}}$ is still invariant under a $U(1)$ transformation with electromagnetic charge $q = I_3 + 1/2Y$. Thus, $SU(2)_L \times U(1)_Y$ is broken to $U(1)_{em}$. Also, a new boson, the massive η field, appeared - the Higgs boson.

The value of v depends on the Fermi constant G_F, $v = 2M_W/g = (\sqrt{2}G_F)^{-1/2}$, and is therefore known: $v = 246$ GeV.

The Lagrangian $\mathcal{L}_{\text{full}}$ is extended by terms of the form $\mathcal{L}_{\text{HF}} = g_f(\bar\psi_R\phi^\dagger\psi_L + \bar\psi_L\phi\psi_R)$ with the coupling strength $g_f = \frac{\sqrt{2}m_f}{v}$ in order to introduce a coupling between fermions and the Higgs field. Due to this coupling , the fermions obtain masses.

Whereas both the electroweak part and the strong part of the Standard Model could be measured to high precision in many collider experiments (for example at the electron-positron collider LEP, at the proton-antiproton collider Tevatron and finally also at the proton-proton collider LHC), a particle consistent with a Standard Model Higgs boson has only been observed recently.

On July 4th, 2012, both the ATLAS and CMS Collaborations announced the discovery of a new boson with a mass around 125 GeV consistent with a Standard Model Higgs boson within the experimental uncertainties [20, 21]. These two measurements were only based on a subset of the available data of both experiments (around 5 fb^{-1} of proton-proton collisions at 7 TeV and between 5 and 6 fb^{-1} at 8 TeV for each of the experiments). Both the ATLAS and CMS collaborations have updated their searches to all data available since then.
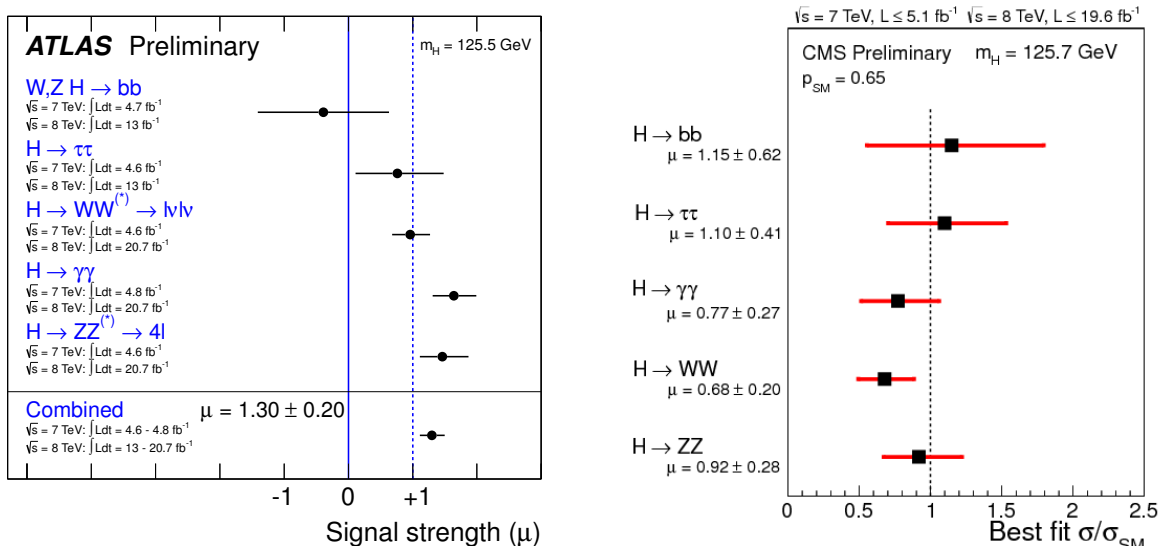
Figure 2.1: The couplings of the scalar boson recently found to other particles have been measured by the ATLAS (left, [38]) and the CMS (right, [39]) Collaborations. Within the uncertainties, the coupling strengths are as requested by a Standard Model Higgs boson.

At a mass of 125 GeV the decay of the Higgs boson into two photons is the most relevant for ATLAS and CMS, because the precise mass resolution allows for a separation of the signal from the background [22]. The decay of the Higgs boson into two Z bosons which further decay into four leptons is also important due to high branching ratios and a clean signature. The decay of the Higgs boson to two W bosons, both decaying further into a lepton and a neutrino, provides additional sensitivity.

The ATLAS Collaboration measures the mass of the newly found boson in the two channels with the best mass resolution [35]. In the channel with the boson decaying to two photons a mass of $m = 126.8 \pm 0.2(\text{stat}) \pm 0.7(\text{sys})$ GeV is obtained. In the case of the boson decaying via two Z bosons to four leptons, a mass of $m = 124.3^{+0.6}_{-0.5}(\text{stat})^{+0.5}_{-0.3}(\text{sys})$ GeV is found. Both measurements are combined to $m = 125.5 \pm 0.2(\text{stat})^{+0.5}_{-0.6}(\text{sys})$ GeV [35]. Similar values have been obtained by the CMS Collaboration for the mass of the observed boson: $125.8 \pm 0.4(\text{stat}) \pm 0.4(\text{syst})$ GeV [36].

The spin of the new particle has been found to be consistent with 0 by both collaborations [37, 36]. The couplings of the boson to other particles are summarised in Figure 2.1. Given the uncertainties of the measurements, the coupling strengths are compatible with a Standard Model Higgs boson.

Many theories beyond the Standard Model require a modified Higgs sector with respect to the Standard Model. Supersymmetry for example requires five Higgs bosons. Two of them are expected to show similar properties as a Standard Model Higgs boson. The details regarding Higgs bosons in supersymmetric theories will be discussed in Section 2.3.4. The recent observation thus provides constraints on physics models beyond the Standard Model, as discussed for the case of Supersymmetry in Section 2.5.1.

2.2 Motivations for Supersymmetry

Although the Standard Model describes fermionic matter and the phenomena related to electromagnetic, weak and strong interactions to high precision at so far accessible energies, it is not

Figure 2.2: Radiative corrections to the Higgs boson mass can be obtained by scalar boson loops (left) or fermion loops (right). Adapted from [49].

expected to be a complete theory. Many questions remain unanswered in the Standard Model as for example the origin of the three fermion generations observed or the origin of the values of the 19 free parameters needed in the description of the Standard Model. Furthermore at the Planck scale ($M_P = 10^{19}$ GeV) the strength of the gravitational force gets comparable to forces described in the Standard Model, so that a theory of quantum gravity is required. Many attempts have been made to construct unified theories of the Standard Model and gravity, as for example superstring theories, but these could not be tested experimentally yet.

Some of the problems arising in the Standard Model can elegantly be solved by Supersymmetry, which connects fermionic and bosonic states by a new symmetry (a more extended list can be found in [40] for example):

- **Dark matter:** In 1930, F. Zwicky postulated the existence of Dark Matter (i.e. non-luminous matter) [41] following the observation that galaxies in the Coma cluster are too fast to be held together by the gravitational forces of visible matter. For a star outside the hub and the disk of a spiral galaxy, a velocity proportional to $1/\sqrt{r}$ can be expected due to gravitational forces by the luminous matter in the hub and the disk. However, these distant stars possess a velocity being independent of the radius, implying that the mass in spiral galaxies must be mainly distributed (80-90%) in the halo and thus giving a lower bound on the dark matter density of[4] $\Omega_{DM} \gtrsim 0.1$ [42]. The existence of dark matter was fortified by many further observations such as the survey of galaxies and galaxy clusters, with the conclusion that dark matter is required to hold the clusters together, the analysis of redshifts of supernovae and the fluctuations in the cosmic microwave background investigated by COBE [43, 44], WMAP [45, 46] and Planck [47]. A recent review of the observations is given in [48]. The observations by Planck concluded that the fraction of Dark Matter in the universe amounts to 26.8% and of ordinary matter to 4.9%, while the rest has the form of Dark Energy and amounts to 68.3% [47].

  Different candidates were proposed for cold particle dark matter (see for a summary [22]), among those axions, heavy neutrinos, primordial black holes and WIMPs (weakly interacting massive particles) [22] with masses between 10 GeV and 1 TeV. In general, a candidate for Dark Matter needs to be stable on cosmological time scales and to be only very weakly interacting with electromagnetic radiation (otherwise it would be luminous). The candidate also needs to provide the correct relic density.

  The lightest supersymmetric particle to be discussed below offers an interesting candidate for Dark Matter fulfilling these requirements.

- **Hierarchy or fine-tuning problem:** The hierarchy problem is related to the large difference in magnitude between the weak scale (defined by the vacuum expectation value for the Higgs field ϕ and so on the order of 100 GeV) and the Planck scale, at which a quantum theory for gravity gets necessary.

---

[4]$\Omega_{DM} \equiv \rho_{DM}/\rho_{crit}$ with ρ_{crit} the critical mass density of the universe.
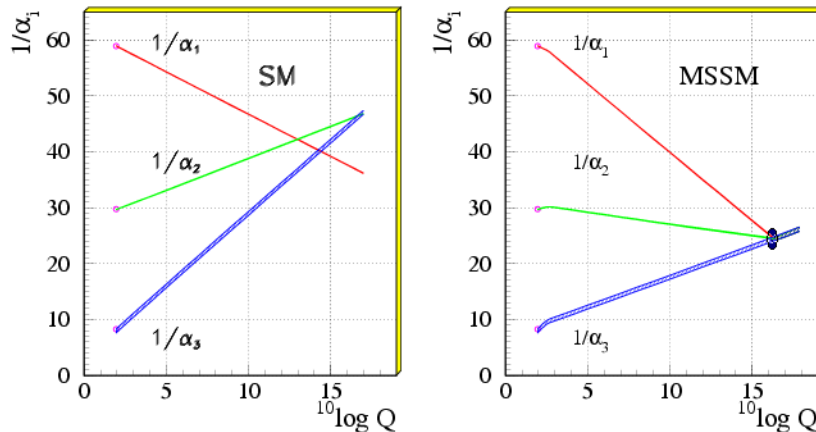
Figure 2.3: The inverse gauge couplings evolved to higher $\log Q^2$ do not meet in the Standard Model. In supersymmetric GUTs the inverse couplings are modified and meet at $Q^2 \sim (10^{16} \text{ GeV})^2$ [22, 51].

The bare mass of the Higgs boson is modified by loop corrections (where either a fermion or a boson runs in the loop) as displayed in Figure 2.2. A fermion loops modifies the Higgs mass by [49]:

$$\Delta m_H^2 = -\frac{|\lambda_f|^2}{8\pi^2}\Lambda_{UV}^2 + ... \tag{2.2.38}$$

where λ_f gives the coupling strength of the fermion to the Higgs boson and Λ_{UV} is the cut-off scale used in the regularisation of the loop integral. A scalar boson loop gives the following correction to the Higgs mass [49]:

$$\Delta m_H^2 = \frac{\lambda_S}{16\pi^2}\Lambda_{UV}^2 + ... \tag{2.2.39}$$

The order of magnitude of the correction to the Higgs boson mass depends in both cases on the choice of the value of Λ_{UV}. Taking Λ_{UV} as the scale of new physics, Λ_{UV} can be as high as the Planck scale ($\sim 10^{19}$ GeV). In this case, the correction to the square of the bare Higgs mass is on the order of $\sim 10^{30}$ and more. Manual fine-tuning, i.e. the introduction of a term balancing such a large contribution, is necessary in order to keep the Higgs boson mass at the electroweak scale. The corrections of fermion and scalar boson loops to the Higgs boson mass however have different signs. In particular, the corrections would neatly cancel if two scalar bosons with $\lambda_S = |\lambda_f|^2$ would compensate the contribution of one fermion (as can be seen by comparison of Equations 2.2.38 and 2.2.39)[5]. This is the case in supersymmetric theories, as will be shown below.

- **Unification of gauge couplings:** The inverse gauge couplings evolve linearly in $\log Q^2$ in the Standard Model and do not meet. However, in supersymmetric GUT theories, the inverse couplings are modified by the inclusion of supersymmetric particles so that the inverse couplings meet at $Q^2 \sim (10^{16} \text{ GeV})^2$ as visualised in Figure 2.3.

- **Connection to gravity:** Making Supersymmetry a local theory necessitates the introduction of a graviton with spin 2 (which also has a supersymmetric partner, the gravitino). The graviton is massless and mediates the gravitation interactions.

---

[5]The terms omitted in Equations 2.2.38 and 2.2.39 have at most a logarithmic dependency on Λ_{UV}. They will also cancel if the scalar bosons and the fermion have the same masses (see for example [50]). If this is not the case, the required fine-tuning to stabilise the Higgs boson mass will be small due to a at most logarithmic dependency on Λ_{UV} if the masses of the scalar bosons partnering the fermion are not too large.

- **Higgs mass:** The minimal supersymmetric extension of the Standard Model (MSSM, explained below) poses tight constraints on the mass of the lightest Higgs boson similar to a Standard Model Higgs boson. It may not be heavier than approximately 135 GeV [40]. The recently observed boson is therefore compatible with supersymmetric theories (but not with all).

2.3 Supersymmetry

Supersymmetry (SUSY) is a symmetry relating bosonic and fermionic states. The fermionic operator Q with spin 1/2 transforms a fermion into a boson and vice-versa, where the spin is changed by $\Delta S = 1/2$:

$$
\begin{aligned}
Q|\text{fermion}\rangle &= |\text{boson}\rangle \\
Q|\text{boson}\rangle &= |\text{fermion}\rangle
\end{aligned}
\tag{2.3.40}
$$

Supersymmetry is an extension of the space-time symmetry reflected in the Poincaré group. Historically, SUSY emerged from attempts to combine internal and external symmetries[6]. However, in 1967, Coleman and Mandula showed in the famous no-go-theorem that this is not possible [52]. They however assumed that the new symmetry were to be generated by a bosonic charge of integer spin [33]. Relaxing this assumption and also considering fermionic charges of spin 1/2, Golfand and Likhtman were able to find an extension of the Poincaré group in 1971 [53]. In the following years, supersymmetric theories in two and in four dimensions were studied [54, 55, 56]. In 1973, Wess and Zumino proposed a four-dimensional supersymmetric theory, which was also interesting in phenomenological considerations [57, 58, 59]. Further interest was raised, as Iliopoulos, Ferrara and Zumino showed that in supersymmetric theories many divergences disappear that are present in other field theories [60, 61].

2.3.1 Algebra

The supersymmetric algebra is constructed by extending the Poincaré algebra with the spinorial charge Q as follows [33, 34, 50][7]:

$$
\begin{aligned}
\left[P^\mu, Q\right] &= \left[P^\mu, \bar{Q}\right] = 0 & (2.3.41) \\
\{Q, \bar{Q}\} &= 2\sigma_\mu P^\mu & (2.3.42) \\
\{Q, Q\} &= \{\bar{Q}, \bar{Q}\} = 0 & (2.3.43) \\
\left[M^{\mu\nu}, Q\right] &= -\sigma^{\mu\nu} Q & (2.3.44) \\
\left[M^{\mu\nu}, \bar{Q}\right] &= -\bar{\sigma}^{\mu\nu} \bar{Q} & (2.3.45)
\end{aligned}
$$

where P^μ are the generators of translations and $M^{\mu\nu}$ the generators of Lorentz transformations. The vectors $\sigma^\mu = (1, \sigma^i)$ and $\bar{\sigma}^\mu = (1, -\sigma^i)$ with $i = 1, 2, 3$ contain the Pauli-matrices and $\sigma^{\mu\nu} = \frac{i}{4}\left(\sigma^\mu \bar{\sigma}^\nu - \sigma^\nu \bar{\sigma}^\mu\right)$ and $\bar{\sigma}^{\mu\nu} = \frac{i}{4}\left(\bar{\sigma}^\mu \sigma^\nu - \bar{\sigma}^\nu \sigma^\mu\right)$.

---

[6] The following summary was extracted from [33].

[7] Indexes referring to Weyl spinors, representing a left or right-handed particle with spin 1/2, have been suppressed.

The charges (and generators of the supersymmetric transformations) Q and $\bar{Q}$ are charges in the sense of the Noether theorem and can be constructed from the SUSY transformations [34, 49].

The supersymmetric algebra has important consequences for the theory. Equation 2.3.42 connects Supersymmetry to space-time translations (in fact the supersymmetric charge can be considered as 'square-root' of P^{μ} [33]). Equation 2.3.41 indicates that supersymmetric transformations are global, so independent of the position in space-time [49]. This equation also shows that $-P^2$ commutes with the operators Q and $\bar{Q}$. Particles related by Q or $\bar{Q}$ (these particles are called *superpartner*) must therefore have the same mass [34, 49]. It can also be shown that Q and $\bar{Q}$ commute with the generators of gauge transformation [49]. This implies that superpartners will have the same electric charge, colour degrees of freedom and the same weak isospin.

2.3.2 Supermultiplets

Superpartners are ordered in a *supermultiplet*. All particles in a supermultiplet have the same properties apart from the spin. In principle, as stated above, the superpartners should also have the same mass, but as supersymmetric particles (sparticles) have not been seen yet, the sparticles need to be heavier than their Standard Model partners. Supersymmetry is not an exact symmetry therefore, but the symmetry needs to be broken (softly, as discussed in Section 2.3.5).

Each supermultiplet can be shown to contain the same number of fermionic and of bosonic degrees of freedom [49],

$$n_F = n_B \tag{2.3.46}$$

The simplest supermultiplets that can be constructed are [33]:

- The *chiral supermultiplet* containing one complex scalar field (sfermion) and its partner a two-component Weyl fermion with spin 1/2. An additional complex field F needs to be included in this supermultiplet, which balances fermionic and bosonic degrees of freedoms off-shell in loops. On-shell, the field F can be eliminated by its equations of motions: $F = F^* = 0$.

- The *vector (or gauge) supermultiplet* containing a massless Weyl fermion, the gaugino λ^a, of spin 1/2 and a massless gauge boson of spin 1, A_a^{μ} (a is an index of the gauge group). Similarly as in the case of the chiral supermultiplet, an auxiliar real scalar field D^a needs to be added to balance the fermionic and bosonic degrees of freedom off-shell. Again, this field can be eliminated on-shell by its equations of motion.

The supermultiplets, including the spin 2 supermultiplet containing the graviton and the gravitino, are summarised in Table 2.3.

2.3.3 Supersymmetric Lagrangian

The simplest supersymmetric model (the Wess-Zumino model) without interactions between scalars and fermions in the chiral supermultiplet is described in the action [33, 49, 63]

Spin	Name	Helicities	States	Particles	Degrees of freedom
1/2	chiral supermultiplet	−1/2 or 1/2	1 + 1	1 spin 1/2 complex chiral fermion	2
		0	1 + 1	1 complex scalar	2
1	gauge supermultiplet	−1	1	one spin 1 gauge boson	2
		1	1		
		−1/2	1	one spin 1/2 Majorana gaugino	2
		1/2	1		
2	$N = 1$ supergravity multiplet	−2	1	one spin 2 graviton	2
		2	1		
		−3/2	1	one spin 3/2 Majorana gravitino	2
		3/2	1		

Table 2.3: The simplest supermultiplets for spin 1/2, 1 and 2. Adapted from [62].

$$S = -\int d^4x (\mathcal{L}_{\text{scalar}} + \mathcal{L}_{\text{fermion}}) \tag{2.3.47}$$
$$\mathcal{L}_{\text{scalar}} = \partial^\mu \phi \partial_\mu \phi^*$$
$$\mathcal{L}_{\text{fermion}} = i\psi^\dagger \bar{\sigma}^\mu \partial_\mu \psi$$

As discussed above, an auxiliary filed F is included in the chiral supermultiplet in order to balance the number of fermionic and bosonic degrees of freedom off-shell. The Lagrangian for this field, which needs to be added to the Lagrangian in 2.3.47, is given by $\mathcal{L}_{\text{aux}} = F^*F$. This provides the equations of motion for the field F with $F = F^* = 0$ which are required to remove the field on-shell.

The simple model in Equation 2.3.47 is extended by interactions between fermions and scalars. The full Lagrangian, containing interactions, is given by [33, 49, 64]:

$$\mathcal{L} = \partial^\mu \phi \partial_\mu \phi^* + i\psi^\dagger \bar{\sigma}^\mu \partial_\mu \psi + \frac{1}{2} m^{ij} \psi_i \psi_j + \frac{1}{2} m^*_{ij} \psi^{\dagger i} \psi^{\dagger j} + V + \frac{1}{2} y^{ijk} \phi_i \psi_j \psi_k + \frac{1}{2} y^*_{ijk} \phi^{*i} \psi^{\dagger j} \psi^{\dagger k} \tag{2.3.48}$$

with the potential $V = F_i F^{*i}$ for the auxiliary field F. The first two terms are the kinetic terms for the scalar and the fermion field from the Wess-Zumino model without interactions. Two mass terms for the fermion fields follow. The last two terms add the interactions between scalars and fermions with y^{ijk} and y^*_{ijk} giving the Yukawa couplings.

Both the potential V and the interaction terms can be derived from the *superpotential W*, which is given by [33]:

$$W = \frac{1}{2} m^{ij} \phi_i \phi_j + \frac{1}{6} y^{ijk} \phi_i \phi_j \phi_k \tag{2.3.49}$$

At most cubic terms in ϕ may appear in the superpotential W in order to keep the Lagrangian in 2.3.48 renormalisable [33]. The field F is given by the first derivative in ϕ of W:

$$F_i = -\frac{\partial W(\phi)}{\partial \phi^i} = -W^*_i$$
$$F^{*i} = -\frac{\partial W(\phi)}{\partial \phi_i} = -W^i \tag{2.3.50}$$

18

Particle	Spartner	Spin of spartner
Quark q	Squarks $\tilde{q}$	0
$\rightarrow$ Top t	Stop $\tilde{t}$	
$\rightarrow$ Bottom b	sbottom $\tilde{b}$	
...		
Leptons l	Sleptons $\tilde{l}$	0
$\rightarrow$ muon μ	Smuon $\tilde{\mu}$	
$\rightarrow$ Electron e	Selectron $\tilde{e}$	
$\rightarrow$ Neutrino ν	Sneutrino $\tilde{\nu}$	
...		
Gauge bosons	Gauginos	1/2
$\rightarrow$ Photon γ	Photino $\tilde{\gamma}$	
$\rightarrow$ Boson Z	Zino $\tilde{Z}$	
$\rightarrow$ Boson B	Bino $\tilde{B}$	
$\rightarrow$ Boson W	Wino $\tilde{W}$	
$\rightarrow$ Gluon g	Gluino $\tilde{g}$	
...		
Higgs bosons $H_i^{\pm,0}$	Higgsinos $\tilde{H}_i^{\pm,0}$	1/2

Table 2.4: Particles in the MSSM. Adapted from [33]

The model described in the Lagrangian 2.3.48 does not include interactions between the chiral and the gauge supermultiplets, which are however observed in nature. Without being explicit here (details can be found in e.g. [49]), it is noted that interactions between gauginos arise when extending the model to include also interactions between chiral and gauge supermultiplets. Also, the potential V needs to be extended by terms for the auxiliary field D to $V = F_i F^{*i} + \frac{1}{2} \sum_a D^a D_a$ where the last term includes interactions between gauge fields [33].

2.3.4 The Minimal Supersymmetric Standard Model

The Minimal Supersymmetric Standard Model (MSSM) is the smallest possible extension (in the sense of additional particles) of the Standard Model to include supersymmetric particles. In its construction, all Standard Model particles are sorted into supermultiplets - fermions into chiral supermultiplets and bosons with spin 1 in the gauge supermultiplet. Since the particles within one supermultiplet have the same quantum numbers apart from the spin, no supersymmetric candidate (*spartner*) can be found within the Standard Model for any particle in the Standard Model. Therefore, all spartners will be new particles, so far undiscovered. Spartners differ in spin by 1/2 from their Standard Model partner. Left and right-handed fermions need to be in different supermultiplets, as otherwise left and right-handed particles would be connected and thus act in the same way under weak interactions, which is in contrast to the observations. However, spartners of fermions cannot carry properties as 'left' or 'right', but the spartners of left-and right-handed partners may still show very different properties [33]. Spartners of left-and right-handed particles will mix.

The particles of the MSSM are summarised in Table 2.4. Spartners of fermions obtain the name of the fermion with 's' as prefix. Spartners of gauge bosons receive an 'ino' as suffix on the name of the gauge boson. In both cases, supersymmetric particles are indicated by ' ˜ '.

An extended Higgs sector with two doublets for the Higgs fields is necessary in the construction of supersymmetric models in order to give mass to 'up' and to 'down' type fermions. This is related to the superpotential, which may not contain complex conjugates of superfields. Therefore two separate Higgs supermultiplets with opposite hypercharge quantum numbers need to be

used [33]. The two Higgs doublets have the form

$$H_u = \begin{pmatrix} H_u^0 \\ H_u^- \end{pmatrix}, \qquad H_d = \begin{pmatrix} H_d^+ \\ H_d^0 \end{pmatrix} \tag{2.3.51}$$

where the components of the doublets are complex fields. In total, the two Higgs doublets carry eight degrees of freedom, but three of them are given to the W and Z bosons during electroweak symmetry breaking. The remaining five degrees of freedom are realised in five Higgs bosons:

- two neutral CP even Higgs bosons: h^0, H^0 - these bosons can be similar to the Higgs boson in the Standard Model,

- one neutral CP odd Higgs boson A^0,

- two charged Higgs bosons: $H^\pm$.

The spartners of the Higgs bosons, the higgsinos, will mix with the photino, the zino or the winos to neutralinos $\tilde{\chi}_i^0$ with $i = 1, 2, 3, 4$ or charginos, $\tilde{\chi}_j^\pm$ with $j = 1, 2$.

Interactions in the MSSM are determined by the following superpotential [33]

$$W_{\text{MSSM}} = Y_u Q U^C H_u + Y_d Q D^C H_d + Y_e L E^C H_d + \mu H_u H_d \tag{2.3.52}$$

where Y_u, Y_d, Y_e are 3×3 matrices containing the Yukawa couplings, Q and L are superfields containing left-handed quarks and leptons and U^C, D^C, E^C are the charge conjugates of the right-handed quarks and leptons (these superfields correspond to the chiral supermultiplets). The superpotential also contains the term $\mu H_u H_d$ (called μ-term) with the higgsino mass parameter μ. This term is allowed by the symmetries in the MSSM and thus needs to be included in the superpotential [33]. Its precise origin is however unknown and the size of the μ parameter is not determined. Supersymmetric models useful for the phenomenology require the μ parameter to be in the order of the electroweak scale [65]. The μ-term could be related with the soft breaking in Supersymmetry. It can be eliminated if considering an extended superpotential [33] compared to Equation 2.3.52:

$$W_{\text{NMMSM}} = \frac{1}{6} k S^3 + \frac{1}{2} \mu_S S^2 + \lambda S H_u H_d + W_{\text{MSSM}} \tag{2.3.53}$$

In this superpotential, which extends the MSSM to the Non-Minimal Supersymmetric Standard Model (NMSSM), a further singlet chiral supermultiplet S has been added. The term $\lambda S H_u H_d$ can give an effective μ-term, if the scalar part of S has a non-zero vacuum expectation value. Implications of this extended superpotential are that the Higgs boson may be heavier in the NMSSM than in the MSSM. The spartner of the S can mix with the neutralinos $\tilde{\chi}^0$.

2.3.5 Soft breaking

As discussed above, Supersymmetry is a broken symmetry, as no supersymmetric particles have been seen yet and exact Supersymmetry would require the same mass for supersymmetric partners. The breaking of Supersymmetry needs to be *soft* which means that the terms responsible for breaking may not reintroduce quadratic divergences in the theory. Therefore, the general form of the Lagrangian responsible for soft breaking is [33, 49]:

$$\mathcal{L} \supset \mathcal{L}_{soft} = -\frac{1}{2}(M_a \lambda^a \lambda^a + c.c.) - m_{ij}^2 \phi_j^* \phi_i - (\frac{1}{2} b_{ij} \phi_i \phi_j + \frac{1}{6} a_{ijk} \phi_i \phi_j \phi_k + c.c.) \tag{2.3.54}$$

which contains mass terms for scalars and gauginos. In the MSSM, $\mathcal{L}_{soft}$ has a more specific form [49]:

$$
\begin{aligned}
-\mathcal{L}_{soft} \;=\; & \frac{1}{2}(M_3\tilde{g}\tilde{g} + M_2\tilde{W}\tilde{W} + M_1\tilde{B}\tilde{B} + c.c.) + \\
& \tilde{Q}^\dagger m_Q^2 \tilde{Q} + \bar{\tilde{U}}^\dagger m_{\bar{U}}^2 \bar{\tilde{U}} + \bar{\tilde{D}}^\dagger m_{\bar{D}}^2 \bar{\tilde{D}} + \tilde{L}^\dagger m_L^2 \tilde{L} + \bar{\tilde{E}}^\dagger m_{\bar{E}}^2 \bar{\tilde{E}} + \\
& (\bar{\tilde{U}}^\dagger a_U \tilde{Q} H_u - \bar{\tilde{D}}^\dagger a_D \tilde{Q} H_d - \bar{\tilde{E}}^\dagger a_E \tilde{L} H_d + c.c.) + \\
& m_{H_u}^2 H_u^* H_u + m_{H_d}^2 H_d^* H_d + (b H_u H_d + c.c.)
\end{aligned}
\tag{2.3.55}
$$

Nearly all new parameters (apart from the parameter μ in superpotential) of the MSSM with respect to the parameters of the Standard Model come from the soft breaking. The new 109 parameters arise from[8] [33]:

- the gaugino masses M_1, M_2, M_3: 6 parameters,

- the squark and slepton masses $m_Q, m_L, m_{\bar{U}}, m_{\bar{D}}, m_{\bar{E}}$: hermitian 3×3 matrices, 45 parameters,

- the trilinear couplings a_U, a_D, a_E: complex 3×3 matrices, 54 parameters,

- quadratic couplings of the Higgs boson: 4 parameters.

The precise breaking mechanism is unknown. The breaking is often assumed to happen in a *hidden* sector, from which it is mediated to the visible sector containing all the MSSM particles [22]. The hidden sector would contain all particles not in the MSSM. The breaking is mediated from the hidden to the visible sector by messenger fields in a messenger sector. Two common approaches exists (apart from other more exotic approaches [22]):

- **Gravity mediated:** Gravity is mediating the SUSY breaking. In this case, the gravitino has a mass in the order of the electroweak scale and its couplings are roughly gravitational in strength [22]. In this case the gravitino is often not important for the phenomenology of Supersymmetry and so usually not considered [22].

- **Gauge mediated:** The SUSY breaking is mediated by gauge forces, so by the virtual exchange of messenger fields. The messenger sector contains particles with $SU(2) \times U(1) \times SU(3)$ quantum numbers [22].

In this work, only the gravity mediated models are considered.

2.3.6 R-parity conservation

Lepton and baryon number violating terms could be added to the superpotential W [49]:

$$
W_{\mathrm{RPV}} = \lambda_{ijk} L_i L_j E_k^C + \lambda'_{ijk} L_i Q_j D_k^C + \lambda''_{ijk} U_i^C D_j^C D_k^C + \mu'_i L_i H_u
\tag{2.3.56}
$$

The parameters λ_{ijk}, λ'_{ijk} and λ''_{ijk} are arbitrary and dimensionless, whereas the parameters μ'_i have dimension mass. As no proton decay has been observed so far (limits on the life time exceed $10^{29} - 10^{30}$ years [22]), constraints on the parameters λ can be derived: $|\lambda'\lambda''| < O(10^{-9})$

---

[8]Their number can be reduced to 105 parameters by using symmetry considerations and by refining the fields.

[33]. In order to forbid baryon and lepton number violating terms, *R-parity* conservation is postulated [49]:

$$R = (-1)^{3(B-L)+2S} = \begin{cases} +1 & \text{for Standard Model particles} \\ -1 & \text{for SUSY particles} \end{cases} \quad (2.3.57)$$

where B is the baryon number, L the lepton number and S the spin.

The R-parity is a multiplicative quantum number and needs to be conserved at any interaction vertex. It has therefore important consequences:

- Supersymmetric particles can only be produced in pairs.

- Heavy supersymmetric particles decay into lighter supersymmetric particles.

- The lightest supersymmetric particle (LSP) is stable.

Due to cosmological constraints [66], the LSP also needs to be electrically and colour neutral and thus may only interact weakly. Otherwise, heavy nuclei containing supersymmetric particles should have been observed already [64]. Therefore, the gluino cannot be the LSP.

The LSP is a promising candidate for dark matter. Various candidates for the LSP were studied in the past. The sneutrino as LSP is ruled out due to direct searches by LEP and cosmological searches. The gravitino as LSP is an attractive option and realised in particular in gauge mediated models. The third option is the lightest neutralino, $\tilde{\chi}_1^0$, as candidate for the LSP.

This work only considers supersymmetric models with R-parity conservation and the lightest neutralino as LSP.

2.3.7 The constrained MSSM (CMSSM)

Many attempts have been made to reduce the large number of parameters due to soft SUSY breaking to a smaller set of parameters, which allows to test the resulting models experimentally. One of the common simplifications is realised in the *constrained MSSM* (CMSSM) (also sometimes called MSUGRA[9]). In the MSUGRA/CMSSM model the universality of some parameters at the GUT scale or at the supergravity scale is assumed, so that only five parameters remain in addition to the Standard Model parameters [22, 33]:

- M_1, M_2 and M_3 are assumed to be equal at high scales. This results in a common parameter $m_{1/2} = M_1 = M_2 = M_3$ for gaugino masses

- The scalar masses of squarks and sleptons are assumed to have the same value m_0 (universal scalar mass) at high scales:

  $m_Q^2 = m_{\tilde{U}}^2 = m_{\tilde{D}}^2 = m_{\tilde{L}}^2 = m_{\tilde{E}}^2 = m_0^2$ and $m_{H_u}^2 = m_{H_d}^2 = m_0^2$

- The trilinear couplings and the Yukawa couplings are connected by the universal coefficients A_0: $a_U = A_0 y_u$, $a_d = A_0 y_d$, $a_e = A_0 y_e$

The two additional parameters are the angle between the Higgs vacuum expectation values: $\tan\beta = \frac{\langle H_u^0 \rangle}{\langle H_d^0 \rangle}$ and the sign of μ in the superpotential. The MSUGRA/CMSSM model, despite being considered in many experimental searches and also in this work, is usually considered to be too simplistic to be realised in nature [22].

---

[9]Historically, the MSUGRA and the cMSSM models were different. They have however been unified in recent years [22], although some authors emphasise their differences [67]. In this work, the models are not distinguished.

2.3.8 The phenomenological MSSM

Attempts have been made to define more realistic supersymmetric models for experimental tests. One direction, extensively studied recently (e.g. by T. Rizzo et al. in [68, 69]), is the phenomenological MSSM (pMSSM) [70], which reduces the 105 parameters of the MSSM to 19 real parameters as follows [22]:

- three gaugino masses M_1, M_2 and M_3,

- two Higgs sector parameters m_A and $\tan\beta$,

- the Higgsino mass parameter μ,

- five squark and slepton squared-mass parameters (corresponding to $m_Q, m_L, m_{\bar{U}}, m_{\bar{D}}, m_{\bar{E}}$) for the first two generations (which are assumed to be degenerate),

- five squark and slepton squared-mass parameters for the third generation,

- three third-generation parameters for the trilinear couplings (A_t, A_b and A_τ)[10].

This reduction is obtained by imposing the following requirements on the MSSM [68]:

- All parameters arising from the soft breaking are real, therefore no new sources of CP violation.

- Minimal flavour violation at the electroweak scale, so that the flavour physics is controlled by the CKM matrix.

- The masses of the first two generation sfermions are degenerate.

- The Yukawa couplings of the first two generations are negligible.

The pMSSM does not make assumptions about the breaking mechanism in Supersymmetry.

2.3.9 Simplified models

In contrast to the previous two concepts, *simplified models* [71] do not aim to give complete supersymmetric models. Instead, they focus on a particular decay chain of some sparticle. Only the sparticles in this specific decay chain are allowed. Other sparticles are assumed to be very massive and thus decouple. This is technically achieved by setting their masses to 4.5 TeV, well beyond the current limits of supersymmetric particles. These models thus contain only a small number of sparticles in addition to the Standard Model particles and the decays of these have a determined branching ratio (in most simplified models set to 100%).

Limits in more general supersymmetric models can be deduced from simplified models. A more general supersymmetric model is split into multiple simplified models for each decay chain appearing. Based on limits on the cross sections in each of the simplified models, limits in the more general supersymmetric model can be derived by adding the effective cross sections (branching ratio times the limit on the cross section in the simplified model) for each of the simplified models, corrected by the experimental efficiencies [71].

---

[10]The couplings to the first two generations are neglected as their impact is taken to be negligible [22].
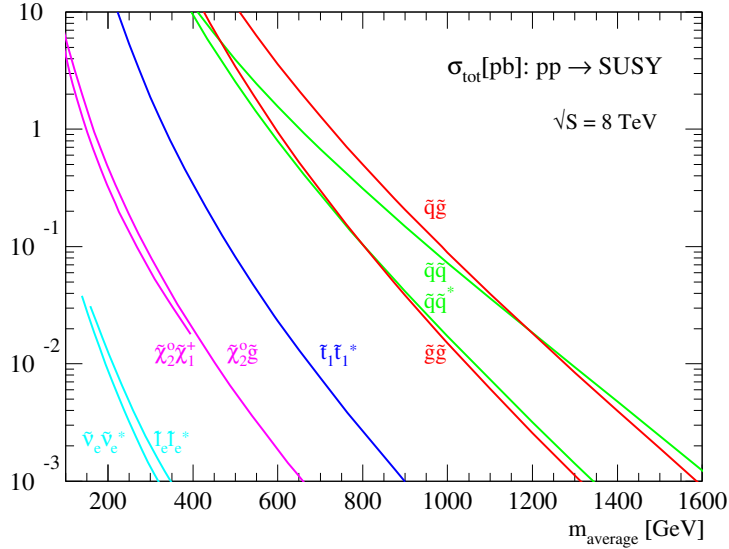
Figure 2.4: Cross sections for a center-of-mass energy of 8 TeV in pp collisions for the production of different supersymmetric particles [73]. While the cross sections for the production of squarks and gluinos are always the highest in comparison to other sparticles with the same mass, the cross sections of heavy gluinos and squarks can be significantly lower than the cross sections of lighter supersymmetric particles. The cross sections were calculated by the tool Prospino 2 [72, 73].

2.4 Phenomenology of Supersymmetry produced in strong production

In pp collisions, the cross section for the production of squarks and gluinos is expected to be rather large due to QCD couplings compared to supersymmetric particles only produced in electroweak production. In many supersymmetric models, squarks and gluinos are however the heaviest particles. In such a case, their cross sections would be relatively small. The cross sections for different sparticles is given in Figure 2.4 as calculated by the developers of the cross section calculation tool Prospino 2 [72, 73].

2.4.1 Production of squarks and gluinos

Gluinos can be produced either by quark-quark scattering or annihilation ($q_i\bar{q}_i \rightarrow \tilde{g}\tilde{g}$) or by gluon-gluon scattering or annihilation ($gg \rightarrow \tilde{g}\tilde{g}$). The Feynman diagrams at lowest order resulting in gluino pair production are presented in Figure 2.5. This figure also shows the diagrams for the pair production of squarks and the production of a gluino-squark pairs. The processes resulting in squark pair production are [62]:

$$
\begin{aligned}
q_i q_j &\rightarrow \tilde{q}_i \tilde{q}_j \\
q_i \bar{q}_j &\rightarrow \tilde{q}_i \bar{\tilde{q}}_j \qquad (i \neq j) \\
q_i \bar{q}_i &\rightarrow \tilde{q}_j \bar{\tilde{q}}_j \\
gg &\rightarrow \tilde{q}_i \bar{\tilde{q}}_i
\end{aligned}
\qquad (2.4.58)
$$

Pairs of gluinos and squarks are produced in $qg \rightarrow \tilde{q}\tilde{g}$ processes.

24
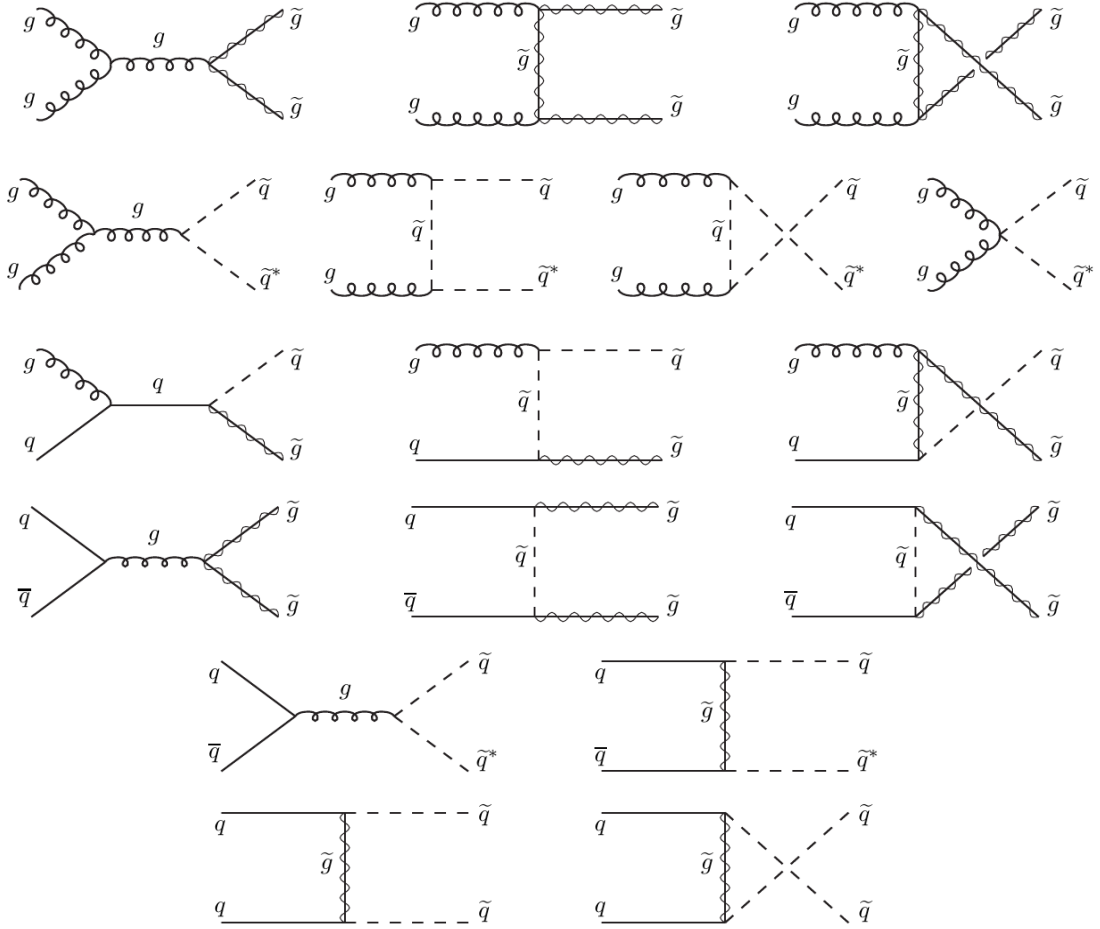
Figure 2.5: The production of gluinos or squarks by gluino scattering or annihilation is shown in the first and second row. The third row shows diagrams for the production of squark-gluino pairs by gluon-quark scattering. The last three rows show the production of gluinos and squarks by quark scattering or annihilation [49].

2.4.2 Decay of squarks and gluinos

The decay of the gluino always occurs via an intermediate squark. If the mass of the gluino is larger than the mass of the squark, a two-body decay will occur with $\tilde{g} \to q\tilde{q}$. This decay is expected to dominate due to QCD couplings. If this two-body decay is kinematically not allowed on-shell, the three-body decays with an off-shell squark $\tilde{g} \to qq\tilde{\chi}_i^\pm$ or $\tilde{g} \to qq\tilde{\chi}_i^0$ appear.

The decay of a squark into a quark and a gluino, $\tilde{q} \to q\tilde{g}$, is preferred if kinematically allowed $(m_{\tilde{q}} > m_{\tilde{g}})$. Otherwise, two-body decays of squarks to charginos $(\tilde{q} \to q\tilde{\chi}_i^\pm)$ or neutralinos $(\tilde{q} \to q\tilde{\chi}_i^0)$ are preferred. The possible decays of gluinos and squarks are summarised in Table 2.5.

Neutralinos and charginos occasionally appear in the decay of gluinos and squarks. They will further decay via the following options [49] (only the dominant decays shown):

$$
\begin{aligned}
\tilde{\chi}_i^0 &\to Z\tilde{\chi}_j^0, \quad W\tilde{\chi}_j^\pm, \quad h^0\tilde{\chi}_j^0, \quad l\tilde{l}, \quad \nu\tilde{\nu} \\
\tilde{\chi}_i^\pm &\to W\tilde{\chi}_j^0, \quad Z\tilde{\chi}_1^\pm, \quad h^0\tilde{\chi}_0^\pm, \quad l\tilde{\nu}, \quad \nu\tilde{l}
\end{aligned}
\tag{2.4.59}
$$

In summary, the decay of gluinos and squarks into lighter sparticles will result in a cascade decay, in which the lighter sparticles decay in even lighter sparticles until finally the lightest

$m_{\tilde{q}} < m_{\tilde{g}}$	$m_{\tilde{g}} < m_{\tilde{q}}$
$\tilde{g} \to \bar{q}\tilde{q}_{L,R}$	$\tilde{q}_{L,R} \to q\tilde{g}$
	$\phantom{\tilde{q}_{L,R}} \to q\tilde{\chi}_l^0,\ l = 1,...,4$
	$\tilde{q}_L \to q'\tilde{\chi}_k^\pm,\ k = 1,2$
$\tilde{q}_{L,R} \to q\tilde{\chi}_l^0,\ l = 1,...,4$	$\tilde{g} \to q\bar{q}\tilde{\chi}_l^0,\ l = 1,...,4$
	$\phantom{\tilde{g}} \to q\bar{q}'\tilde{\chi}_k^\pm,\ k = 1,2$
$\tilde{q}_L \to q'\tilde{\chi}_k^\pm,\ k = 1,2$	$\tilde{g} \to \bar{t}\tilde{t}_1 + t\bar{\tilde{t}}_1$ if $m_{\tilde{g}} > m_{\tilde{t}_1} + m_t$
$\tilde{q} \to q\bar{b}\tilde{b}_1 + qb\bar{\tilde{b}}_1$ if $m_{\tilde{q}} > m_b + m_{\tilde{b}_1}$	$\tilde{g} \to \bar{b}\tilde{b}_1 + b\bar{\tilde{b}}_1$ if $m_{\tilde{g}} > m_{\tilde{b}_1} + m_b$

Table 2.5: Depending on the relative mass of the squark and the gluino, their decays are summarised. This table was slightly adapted from [62].

supersymmetric particle is reached (in this work the lightest neutralino, $\tilde{\chi}_1^0$). Some examples of cascade decays will be presented in the next section. In general, the cascades can be complex and long. This work focuses on particular cascade decays of gluinos and squarks, which results in final states containing many jets (originating from quark and gluon production in the cascade decay) and at least one isolated lepton. The lepton can be produced by a W or Z boson decay, where the W or Z bosons in turn have been produced in the decay of a chargino or a neutralino, or it can be produced in the decay of sleptons or sneutrinos.

2.4.3 Models used in this work

Two different classes of models are considered in this work: MSUGRA/CMSSM models and simplified models.

MSUGRA/CMSSM models

Two different MSUGRA/CMSSM models are used in this work. In both cases the parameters $\tan\beta$, A_0 and the sign of μ were fixed. This leaves only the universal scalar mass m_0 and the universal gaugino mass $m_{1/2}$ as free parameters. For selected values in m_0 and $m_{1/2}$ about 10000 events each have been generated[11]. The ($m_0,m_{1/2}$) values chosen build two-dimensional grids (which are shown in Figure 2.6). Only the strong production of gluinos and squarks and the associated electroweak production (a gluino or squark in association with a gaugino) was simulated. The grids are defined as follows:

- **MSUGRA/CMSSM grid:** This grid was defined with $\tan\beta = 10$, $A_0 = 0$ and $\mu > 0$. No assumption about the mass of the lightest neutral CP even Higgs boson, h^0, has been made. Therefore, it is not necessarily compatible with the recently discovered boson with a mass of $\sim$ 125 GeV[12].

- **'Higgs aware' MSUGRA/CMSSM grid:** This grid with parameters $\tan\beta = 30$, $A_0 = -2m_0$ and $\mu > 0$ is compatible with a Higgs boson of $\sim$ 126 GeV (within errors) over a large part of the grid.

Figure 2.7 shows the decay spectra for two selected points with the parameters $(m_0, m_{1/2}) = (3000, 400)$ GeV in both grids. In this work, mainly the right part in these two plots is interesting,

---

[11]With `SOFTSUSY` [74] and `HERWIG++` [75]

[12]This is due to historical reasons, as the grid was defined before the discovery of this boson.
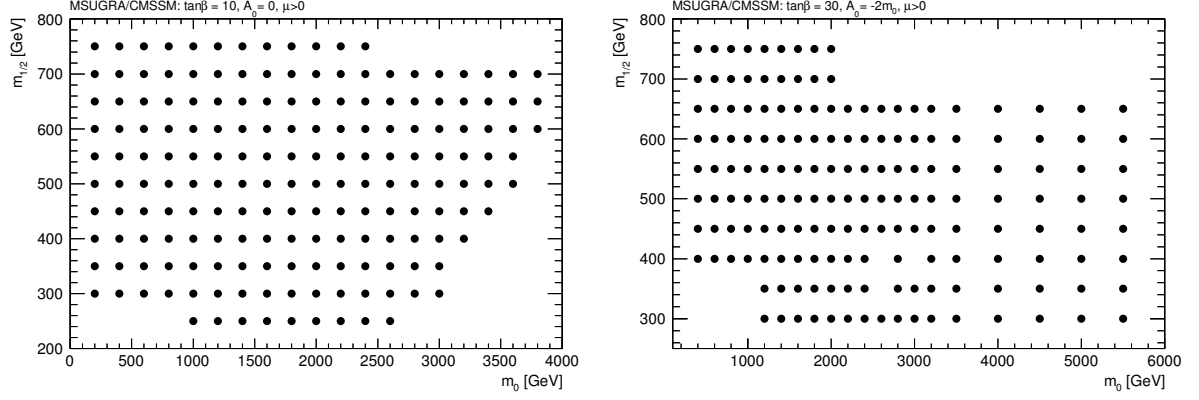
Figure 2.6: The points in the ('Higgs aware') MSUGRA/CMSSM grids are shown in the (right) left plot.
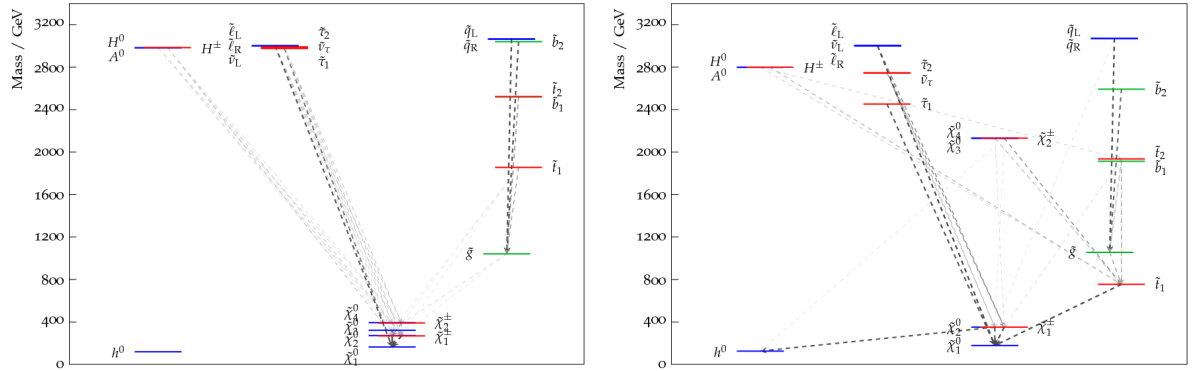
Figure 2.7: Two decay spectra for the point with parameters $(m_0, m_{1/2}) = (3000, 400)$ GeV are shown for the MSUGRA/CMSSM grid (left) and the 'Higgs aware' MSUGRA/CMSSM grid (right). Favoured decays are indicated by darker lines than suppressed decays. These spectra were created by using the tool PySLHA [76].

which show the decays of the squarks and the gluinos. In both cases, the first two-generation squarks are heavier than the gluino. However, in the 'Higgs aware' MSUGRA/CMSSM grid, the lightest stop is lighter than the gluino. This implies that the gluino dominantly decays via a stop into the $\tilde{\chi}_1^0$ in contrast to the other MSUGRA/CMSSM grid, where the decay is through charginos and neutralinos.

Simplified models

This work considers two different types of simplified models differing in the number of intermediate sparticles between the initial squark or gluino and the final $\tilde{\chi}_1^0$. All grids used are displayed in Appendix A.

In the *simplified models with one step*, the gluino or the squark decays via only one intermediate particles into the $\tilde{\chi}_1^0$. In all simplified models with one step considered in this work the intermediate particle is the lightest chargino, $\tilde{\chi}_1^\pm$. The $\tilde{\chi}_1^\pm$ decays further into a W boson and the $\tilde{\chi}_1^0$. The decay of the W-boson can result in a final state with a lepton. Different simplified models with one step are analysed. Their definitions use the mass difference between the $\tilde{\chi}_1^\pm$ and the $\tilde{\chi}_1^0$ relative to the mass difference between the gluino or squark and the $\tilde{\chi}_1^0$: $x = \frac{m_{\tilde{\chi}_1^\pm} - m_{\tilde{\chi}_1^0}}{m_{\tilde{g}/\tilde{q}} - m_{\tilde{\chi}_1^0}}$.

- **Pair-production of gluinos** with decay of each gluino via a $\tilde{\chi}_1^\pm$ to a $\tilde{\chi}_1^0$:
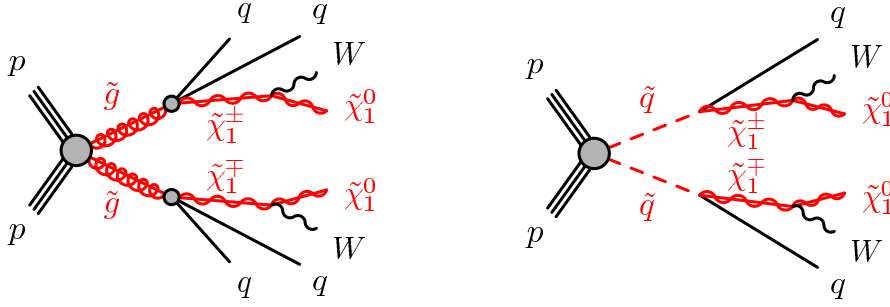
Figure 2.8: Diagrams for the simplified models with one step used in this work. The diagram with initial gluino pair production is shown left, the one with initial squark pair production right.

The first grid is defined with fixed $x = 1/2$ so that both the $\tilde{\chi}_1^0$ and gluino masses are free parameters. In the second grid, the mass of the $\tilde{\chi}_1^0$ is fixed to 60 GeV and x is varied (as well as the gluino mass). A diagram for this simplified model is shown in Figure 2.8. As each of the initial gluinos decays by emitting two quarks, which undergo hadronisation into two jets, the final states of this simplified model contain at least four jets. Considering only final states with a lepton (from the decay of one of the W-bosons), two further jets are expected from the decay of the other W-boson. In total, for this group of simplified models, signatures with at least six jets (more can be created by initial state radiation) and one lepton can be expected. As will be discussed later, the $\tilde{\chi}_1^0$ escapes detection experimentally, as only interacting weakly. It thus results in *missing energy* in the transverse plane of the colliding particles, $E_{\mathrm{T}}^{\mathrm{miss}}$, in the event (the missing transverse energy is defined in Section 4.4). The analyses presented in this work will therefore require final states with many jets, a lepton and $E_{\mathrm{T}}^{\mathrm{miss}}$ in order to look for the decays described by these simplified models.

- **Pair-production of squarks** with decay of each squark via a $\tilde{\chi}_1^\pm$ to a $\tilde{\chi}_1^0$:

  Each of the initial squarks decays into the $\tilde{\chi}_1^\pm$ by emission of one quark, resulting in a jet. A diagram for these simplified models is shown in Figure 2.8. The final states with one lepton will contain at least four jets, two of them from a hadronic W boson decay. Again, missing transverse energy will appear due to the two $\tilde{\chi}_1^0$ in the final state. Similarly to the gluino case, two grids are defined, one with free squark and $\tilde{\chi}_1^0$ masses but fixed $x = 1/2$, the other with free squark mass and variable x. The mass of $\tilde{\chi}_1^0$ is set to 60 GeV in the latter case.

In the *simplified models with two steps* the initial gluinos or squarks decay via two intermediate particles into the $\tilde{\chi}_1^0$. Two different classes of simplified models with two steps are used:

- **Involving W and Z bosons:**

  The diagrams are shown in Figure 2.9. Each gluino (squark) decays by emitting two (one) quarks to a $\tilde{\chi}_1^\pm$. The $\tilde{\chi}_1^\pm$ further decays to a W boson and the second-lightest neutralino $\tilde{\chi}_2^0$. The $\tilde{\chi}_2^0$ decays to a Z boson and the $\tilde{\chi}_1^0$. Due to the production of W and Z bosons and their subsequent decays, zero to six leptons are expected in the final state. The grid is defined such that the mass difference between the $\tilde{\chi}_1^\pm$ and the $\tilde{\chi}_1^0$ is half the mass difference between the gluino (squark) and the $\tilde{\chi}_1^0$. The mass difference between the $\tilde{\chi}_2^0$ and the $\tilde{\chi}_1^0$ is a quarter relative to the full mass difference between gluino (squark) and $\tilde{\chi}_1^0$.

- **Decay via sleptons and sneutrinos:**

  This type of simplified model contains different decay options for the gluino or squark. Each of the initial gluinos or squarks decays to either a $\tilde{\chi}_1^\pm$ or a $\tilde{\chi}_2^0$ with equal probability.

28
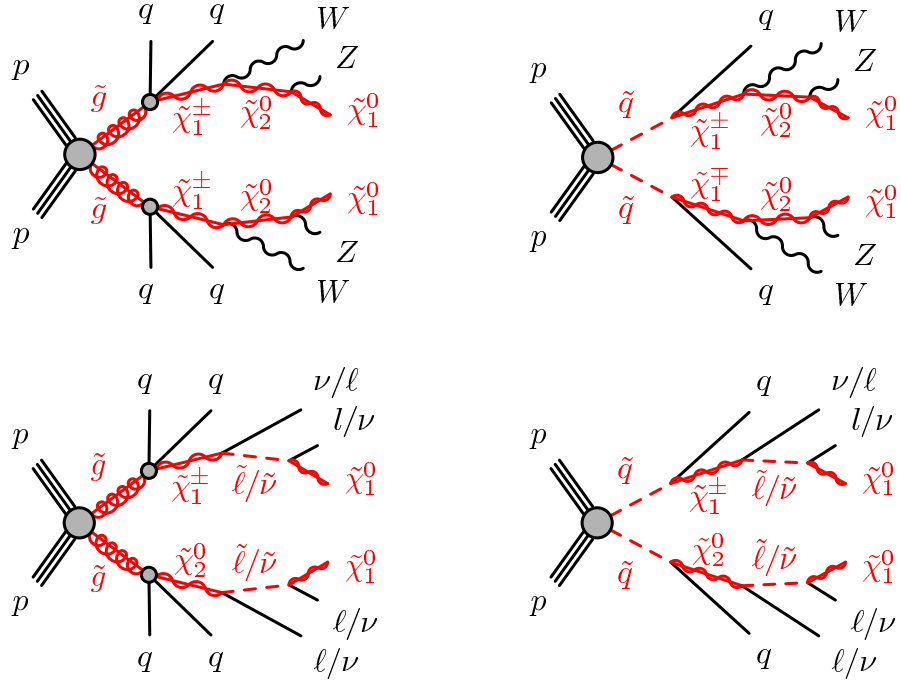
Figure 2.9: Diagrams for simplified models with two steps. The top row shows the diagrams for the simplified models with the decay involving W and Z bosons. The bottom row shows the diagrams with the decay via sleptons and sneutrinos. The diagrams with initial gluino pair production are shown left and the ones with initial squark pair production right.

The $\tilde{\chi}_1^\pm$ further decays into a slepton and a neutrino or into a lepton and a sneutrino, with equal probability. The slepton (sneutrino) further decays to a lepton (neutrino) and the $\tilde{\chi}_1^0$. The $\tilde{\chi}_2^0$ decays into a pair of slepton and lepton or of sneutrino and neutrino with equal probability with further decays of the slepton or sneutrino. In summary, five different final states appear in this model, all containing jets and between zero and four charged leptons. A diagram is shown in Figure 2.9.

For each grid point in the simplified models between 20000 and 60000 simulated events are available[13].

2.5 Constraints on Supersymmetry

Both theoretical considerations and experimental searches have constrained the supersymmetric parameter space considerably in the last years. Some of these constraints are discussed in the following.

2.5.1 The observation of a boson compatible with a Standard Model Higgs boson

The masses of the five Higgs bosons in the MSSM at tree level are given by [49]:

---

[13]Generated by `MadGraph` [77] and `PYTHIA` [78]

$$m_{h^0, H^0} = \frac{1}{2}(m_{A^0}^2 + m_Z^2 \mp \sqrt{(m_{A^0}^2 + m_Z^2) - 4m_{A^0}^2 m_Z^2 \cos^2 2\beta}) \qquad (2.5.60)$$

$$m_{A^0}^2 = \frac{2b}{\sin(2\beta)} \qquad (2.5.61)$$

$$m_{H^\pm}^2 = m_{A^0}^2 + m_W^2 \qquad (2.5.62)$$

The mass of the lighter CP even and neutral Higgs boson h^0 is bounded from above by the mass of the Z-boson:

$$m_{h^0} < |\cos(2\beta)| m_Z \qquad (2.5.63)$$

This implies that the lightest neutral Higgs boson should be lighter than the Z boson. Including radiative corrections, however, the mass of the lightest Higgs boson can be modified considerably [22] (the following equation is an approximation also considering the one-loop level):

$$m_{h^0}^2 \lesssim m_Z^2 \cos^2(2\beta) + \frac{3g^2 m_t^4}{8\pi^2 m_W^2}\left[\ln(M_S^2/m_t^2) + \frac{X_t^2}{M_S^2}\left(1 - \frac{X_t}{12 M_S^2}\right)\right] \qquad (2.5.64)$$

$$M_S^2 = \frac{1}{2}(M_{\tilde{t}_1}^2 + M_{\tilde{t}_2}^2)$$

$$X_t = A_t - \mu \cot\beta$$

with M_S^2 giving the average of the squared masses of both stop quarks and X_t being the top-squark mixing factor.

For $m_{\tilde{t}_1, \tilde{t}_2} \lesssim 1$ TeV the mass of the lightest Higgs boson cannot exceed ~ 130 GeV. Both h^0 and H^0 can have similar properties as a Standard Model Higgs boson. The recently discovered boson is often assumed to be the lighter one, h^0. Using Equation 2.5.64, constraints on other sparticles and on supersymmetric models in general can be derived (for example see [79, 80, 81, 82, 83, 84, 85]), but are model dependent. In particular, Equation 2.5.64 allows to infer constraints for the values of $\tan\beta$ and the stop sector. A mass of 125 GeV corresponds to almost the maximal value that Equation 2.5.64 can take. Such a value can be achieved by different means, i.e. by maximising the $\tan\beta$ value, by a large mixing of the two stops $\tilde{t}_1$ and $\tilde{t}_2$, or by large stop masses [83]. The precise implications on the sparticle spectrum depend on the specific model. However, a Higgs boson with a mass of 125 GeV already rules out the MSUGRA/CMSSM grid presented in the last section, as the analysis in [79] shows, and favours the parameters of $\tan\beta = 30$ and $A_0 = -2m_0$ chosen for the 'Higgs aware' MSUGRA/CMSSM grid. In fact, a Standard Model-like Higgs boson at the measured mass poses the tightest constraints on supersymmetric models so far [14]. This is also connected to the hierarchy problem discussed earlier, which requires not too heavy supersymmetric partners to avoid a significant fine-tuning[14]. As consequence the stop quarks are expected to be relatively light (considerably lighter than the squarks of the first two generations) with masses of $O(1)$ TeV. The squarks of the first two generations may however be very heavy and possibly beyond the reach of the LHC with masses of $O(10)$ TeV. The gluino is also required to be relatively light ($\sim 1-5$ TeV) in most models consistent with the measured mass of the Higgs boson candidate and with acceptable low

---

[14]Fine-tuning was not defined precisely in Section 2.2. Different attempts exist in the literature (see for a discussion [14]). The amount of fine-tuning thought to be acceptable is highly dependent on this definition. Also, it is not known which level of fine-tuning should be acceptable. Thus, the request for little fine-tuning is more a tendency than a precise requirement.

Model	Assumption	$m_{\tilde{q}}$[GeV]	$m_{\tilde{g}}$[GeV]
MSUGRA/CMSSM	$m_{\tilde{q}} \approx m_{\tilde{g}}$	1400	1400
	all $m_{\tilde{q}}$	-	800
	all $m_{\tilde{g}}$	1300	-
Simplified model $\tilde{g}\tilde{g}$	$m_{\tilde{\chi}_1^0} = 0$	-	900
	$m_{\tilde{\chi}_1^0} > 300$ GeV	-	no limit
Simplified model $\tilde{q}\tilde{q}$	$m_{\tilde{\chi}_1^0} = 0$	750	-
	$m_{\tilde{\chi}_1^0} > 250$ GeV	no limit	-
Simplified model $\tilde{g}\tilde{q}, \tilde{g}\bar{\tilde{q}}$	$m_{\tilde{\chi}_1^0} = 0, m_{\tilde{q}} \approx m_{\tilde{g}}$	1500	1500
	$m_{\tilde{\chi}_1^0} = 0$, all $m_{\tilde{g}}$	1400	-
	$m_{\tilde{\chi}_1^0} = 0$, all $m_{\tilde{q}}$	-	900

Table 2.6: The limits on squark and gluino masses as measured in direct searches at the ATLAS and CMS experiments in ~ 5 fb^{-1} pp collisions at 7 TeV (status: March 2012). The limits are given in simplified models and in a MSUGRA/CMSSM grid. This table is adapted with respect to [22].

fine-tuning [14, 86], but heavier than the stop quarks. Consequently, the favoured decay of the gluino proceeds through stop and sbottom quarks with a similar topology as shown in Figure 2.7 right plot. The second analysis presented in this work is sensitive to signatures involving the stop quark production in the decay of a gluino.

2.5.2 Direct searches for Supersymmetry at the LHC

As the search for gluinos and squarks is the scope of this work, only results of searches for gluinos and first and second generation squarks are reviewed in this section (limits for other supersymmetric particles are for example summarised in [22] and also given in the appendix). Only results by the ATLAS and CMS experiments until March 2012 are presented (~ 5 fb^{-1} in pp collisions at 7 TeV). The results at 8 TeV will be derived in the analyses in the main body of this work. At the end of this work, these results will also be compared to results by other analyses obtained from collisions at 8 TeV.

Before the LHC era, squarks and gluinos have been searched for at the LEP electron-positron collider with a maximal center-of-mass energy of $\sqrt{s} = 209$ GeV. Profiting from the clean experimental environment in electron-positron collisions, the limits obtained by LEP are still competitive for gauginos and sleptons, but not for gluinos or squarks. The D0 and CDF experiments have also searched for squarks and gluinos in $p\bar{p}$ collisions with $\sqrt{s} = 1.96$ TeV and in total $10 - 11$ fb^{-1}, but also their limits [22, 87, 88] are superseded by the limits obtained by the LHC experiments.

The limits on the squark and gluino masses as obtained by the LHC experiments are summarised in Table 2.6. These limits have been derived in simplified models and in the MSUGRA/CMSSM grid with parameters $\tan\beta = 10$, $A_0 = 0$ and $\mu > 0$. In this MSUGRA/CMSSM grid, the limits by three ATLAS analyses (two analyses only considering hadronic final states [89, 90] and a third analysis considering final states with an isolated lepton [15]) are shown in Figure 2.10 for 5 fb^{-1} of pp collisions at 7 TeV. These analyses exclude gluino masses below 800 GeV for all squark masses and below 1.4 TeV for equal gluino and squark masses. Squark masses below 1.3 TeV can be excluded for all gluino masses[15].

---

[15]The preliminary limits in this plot have been superseded by the limits in the papers [91, 92, 93] which were published in summer 2012. To that time, the analysis of the 8 TeV data had already started. Therefore, the limits presented in this plot were taken as reference for the results with the first 5.8 fb^{-1} of 8 TeV data. These limits
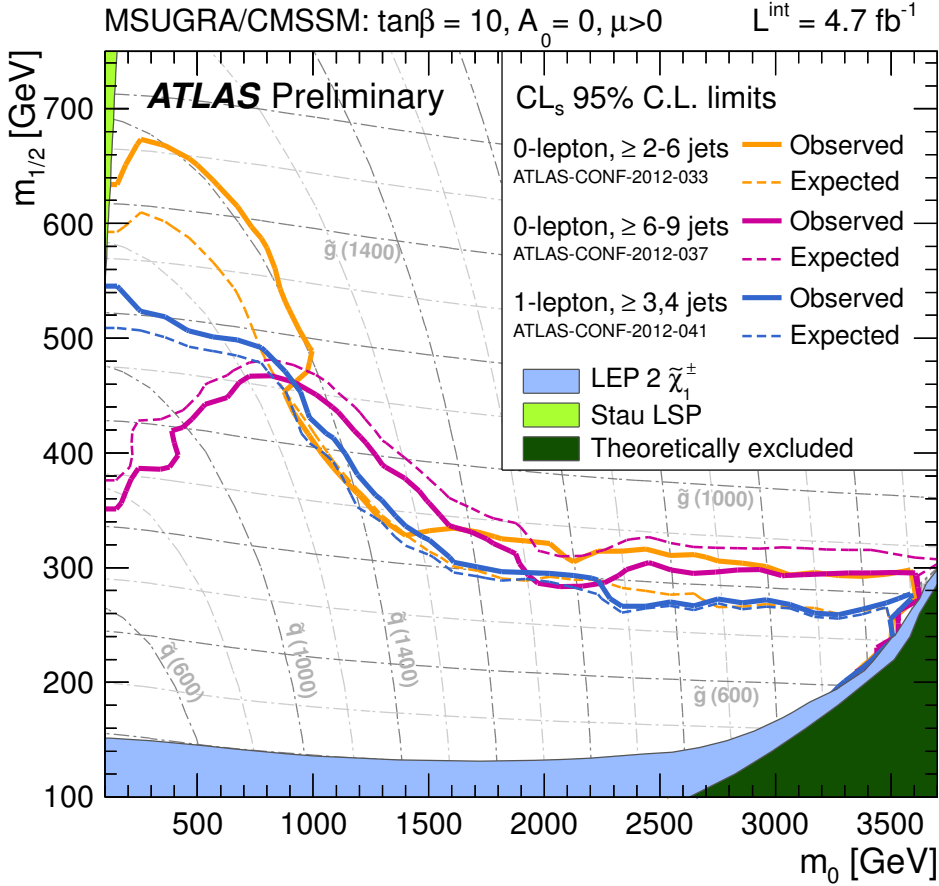
Figure 2.10: Limits in the MSUGRA/CMSSM grid [22, 15] as obtained in 5 fb^{-1} of pp collisions at 7 TeV taken by the ATLAS experiment. The yellow solid (dashed) curve gives the observed (expected) limit for an analysis requiring between at least two and six jets [89]. The magenta curves present the observed (solid) and expected (dashed) limits for an analysis requiring between at least six and nine jets [90]. Both of these analyses veto events with electrons or muons. The third analysis [15] requires an isolated electron or muon and at least three or four jets. The observed limit (solid) and expected limit (dashed) for this analysis is shown in blue. The author has calculated the limit for the analysis requiring an isolated electron or muon and at least three or four jets.

2.5.3 Further constraints

Further constraints on supersymmetric models arise from the precision measurements of rare processes in the Standard Model whose branching ratios could be modified (either enhanced or reduced) by additional processes involving sparticles.

Severe constraints on some supersymmetric models can be derived from the recent measurement [94, 95] of the branching ratio of the process $B_s \rightarrow \mu^+ \mu^-$ by the LHCb and CMS collaborations, consistent with Standard Model predictions. As flavour-changing neutral currents are forbidden at tree level in the SM and can only proceed through higher orders, this process is highly suppressed in the SM with a branching ratio of $\mathcal{B}(B_s \rightarrow \mu^+ \mu^-) = (3.57 \pm 0.30) \cdot 10^{-9}$ (see [95] and references therein). The LHCb collaboration measured [94] a branching ratio of $\mathcal{B}(B_s \rightarrow \mu^+ \mu^-) = (2.9^{+1.1}_{-1.0}) \cdot 10^{-9}$, the CMS collaboration [95] a branching ratio of $\mathcal{B}(B_s \rightarrow \mu^+ \mu^-) = (3.0^{+1.0}_{-0.9}) \cdot 10^{-9}$. Both are consistent with SM expectations and thus constrain the contributions by physics beyond the Standard Model. Constraints on the MSUGRA/CMSSM

---

are also used in the following chapters of this work as reference.

models were analysed in e.g. [96], showing that some models can be excluded depending on their $\tan\beta$ parameter. Most MSUGRA/CMSSM models are unaffected however, if they have $\tan\beta \lesssim 40$, because in these cases the supersymmetric contributions to the branching ratio are small.

Further constraints on Supersymmetry arise from investigations of the rare decay $B \to X_s\gamma$ [97], however they are also highly model dependent (e.g. [98]).

Many experiments also directly search for WIMP Dark Matter candidates colliding elastically with nuclei in detectors (see [22, 99] for recent reviews). Although some experiments reported excesses (DAMA/LIBRA [100], CoGent [101], Cresst [102], CDMS II [103]), no conclusive Dark Matter signal has been seen yet [99]. The currently tightest limits on spin-independent interactions of Dark Matter are obtained by the XENON100 experiment [104], starting to constrain supersymmetric Dark Matter Candidates. Further constraints on Dark Matter candidates are obtained in indirect searches for the annihilation of two WIMP particles [22]. The results of direct and indirect searches for Dark Matter are to be complemented with the collider searches for a supersymmetric Dark Matter candidate, although no severe constraint on Supersymmetry can be obtained yet.

Chapter 3

LHC, ATLAS and simulation

The discovery of the Higgs boson was one of the major aims for which the Large Hadron Collider (LHC) [105] was built at CERN near Geneva. Now that a scalar particle so far consistent with a Standard Model Higgs boson has been discovered by the two multi-purpose detectors ATLAS [106] and CMS [107], its detailed properties are studied. With a design center-of-mass energy of 14 TeV, the LHC is also hoped to give access to physics beyond the Standard Model, as for example Supersymmetry.

After a long phase of design and construction, the LHC started operation on September 10th 2008. This was immediately followed by a severe incident related to the superconducting interconnects between two of the magnets which caused severe damage to the machine. After repair and safety works, the machine started operation again end of March 2010 at a center-of-mass energy of 7 TeV. A lower than design energy was chosen for the first three years of operation in order to avoid similar incidents as in 2008. Running at the design energy is foreseen after 2014 and requires the upgrade of all interconnects between the magnets. After two years running at 7 TeV, a third year (2012) with a center-of-mass energy of 8 TeV followed. Most data was collected in the third year, and this data is also the fundament for the work presented here.

This chapter gives a short overview about the LHC and its preaccelerators and introduces the ATLAS detector.

3.1   The Large Hadron Collider

The LHC is a hadron-hadron collider with proton-proton, lead-lead and proton-lead collisions[1]. It reuses the tunnel but also parts of the injection infrastructure of the electron-positron collider LEP, which was in operation between 1989 and 2000. The possibility of reusing the existing infrastructure was a strong motivation to build the LHC at CERN due to cost-saving reasons. The ring built for LEP has a length of 26.7 km and lies between 45 and 170 metres under the surface. It is located between the French Jura and the Léman Lake with an inclination of 1.4 % towards the lake. Being constructed for an electron-positron collider the LEP ring consists of eight straight sections and eight arcs. The straight sections were necessary to minimise losses due to synchrotron radiation occurring at electron-positron colliders. For a hadron-hadron collider as the LHC, the current design of the straight sections is less useful. Due to limited space in the LEP tunnels, it was not possible to build two separate rings for the LHC, which are needed for counter-rotating beams. Therefore, the LHC uses the so-called twin-born magnet design in which two beam lines can be placed very closely to each other by sharing the same cold mass

---

[1]The following information is extracted from [105].

	2010	2011	2012	Nominal
Center-of-mass energy [TeV]	7	7	8	14
Bunch spacing [ns]	150	50	50	25
Number of bunches	368	1380	1380	2808
Maximal bunch intensity (protons/bunch)	$1.2 \cdot 10^{11}$	$1.45 \cdot 10^{11}$	$1.7 \cdot 10^{11}$	$1.15 \cdot 10^{11}$
Peak luminosity $[cm^{-2}s^{-1}]$	$2.1 \cdot 10^{32}$	$3.7 \cdot 10^{33}$	$7.7 \cdot 10^{33}$	$1.0 \cdot 10^{34}$

Table 3.1: The design parameters of the LHC (right) are compared with the values as realised in the years 2010 - 2012. This table is taken from [108] in a shortened and modified version.

and cryostat. A mixture of different magnet types (among those dipole, quadrupole, sextupole, octupole and decapole magnets) is required to focus the beams and to bend them in order to keep them on the ring tracks. The superconducting magnets are operated at temperatures of 1.9 Kelvin. The dipole magnets can provide a magnet field up to 8.3 Tesla.

Some design parameters are compared with the average values realised in the three years of operation in Table 3.1. Although the LHC stayed below the design values regarding the center-of-mass energy and also the number of bunches in the beam, it nearly reached the design luminosity of $1.0 \cdot 10^{34} \frac{1}{cm^2 s}$ (the luminosity is defined in Section 3.2.9), in part because the maximal bunch intensity was higher than designed.

Figure 3.1 shows a sketch of the LHC collider ring including the preaccelators. The acceleration chain [109] starts with a bottle of hydrogen. The hydrogen is ionised and the resulting protons are injected into the LINAC 2, which has an Alvarez drift tube design. The protons are accelerated to 50 MeV and injected into the PS Booster, which consists of superimposed synchrotron rings and accelerates to 1.4 GeV. This step allows to inject more protons into the following Proton Synchrotron. After the protons have been accelerated to 25 GeV, they are passed on to the Super Proton Synchrotron (SPS) with a circumference of 7 km. In this ring, their energy is increased to 450 GeV. Two transfer tunnels of 2.5 km length each connect the SPS with the LHC and allow the injection of two counter-rotating beams into the LHC. In the case of heavy-ions collisions, the preaccelator chain is modified and starts with LINAC 3.

The LHC delivers particle beams to seven different experiments which are all placed in four of the eight interaction points (in the straight sections of the LHC ring). Among those experiments are two general purpose experiments:

- ATLAS (**A T**oroidal **L**HC **A**pparatu**S**) [106],

- CMS (**C**ompact **M**uon **S**olenoid) [107],

and five specialised experiments:

- LHCb (**L**arge **H**adron **C**ollider **b**eauty, specialised for *B*-physics) [111],

- ALICE (**A L**arge **I**on **C**ollider **E**xperiment, studying the properties of the quark-gluon plasma) [112],

- LHCf (**L**arge **H**adron **C**ollider **f**orward, uses particles emitted forward by LHC collisions to simulate cosmic rays) [113],

- TOTEM (**TOT**al elastic **A**nd diffractive cross section **M**easurement, specialised for studying forward physics) [114],

- MoEDAL (**Mo**nopole and **E**xotics **D**etector **A**t the **L**HC, searching for magnetic monopoles) [115].

CERN's accelerator complex
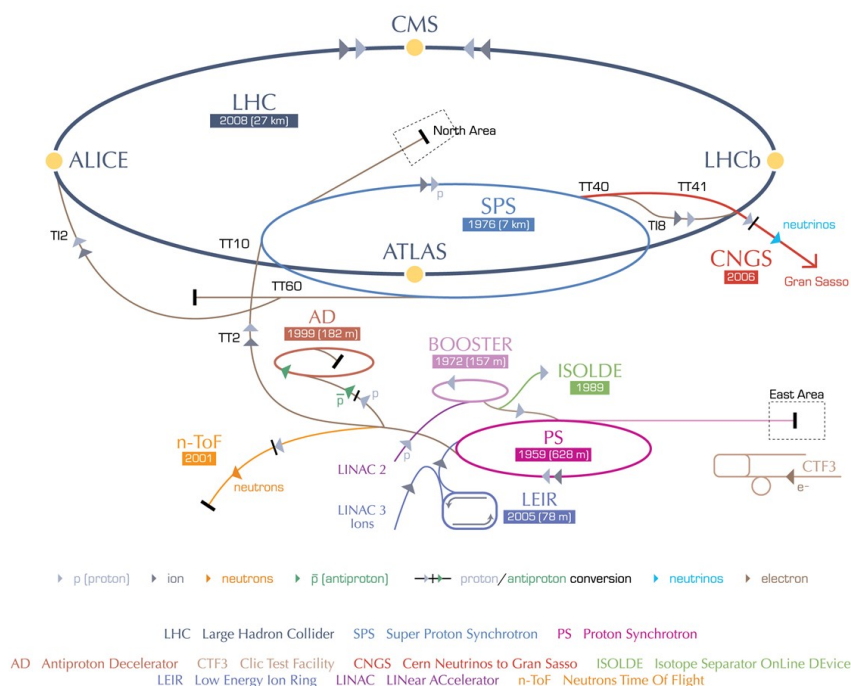
Figure 3.1: A sketch of the LHC injection chain [110].

3.2 ATLAS

The design of the ATLAS detector is driven by the LHC design parameters on the one hand and by the physics processes of interest (as for example precision measurements of the Standard Model, Higgs physics and theories beyond the Standard Model) on the other hand[2]. Proton-proton collisions with 10^{11} protons per bunch 40 million times per second or heavy-ion collisions with design luminosities of $10^{27} \frac{1}{cm^2 s}$ imply dealing with high interaction rates, radiation, particles multiplicities and particle energies [106]. Precision measurements in space as well as in momentum of various particles require a high granularity allowing for the separation of the particles and for a good track reconstruction. Equally, a wide coverage is needed to study particles emitted in most directions. The identification of primary and secondary particles is important for many processes, but in particular needed in the identification of jets originating from b-quarks. The following sections aim to shortly introduce the detector components designed to fulfil these constraints.

3.2.1 Coordinate system

The right-handed coordinate system with which the detector is described has its origin in the interaction point of the two beams. The z-axis points in the beam direction, the x-axis to the centre of the LHC ring and the y-axis upwards. The azimuthal angle ϕ is measured around the beam axis if looking in the beam direction. The polar angle θ is measured away from the beam axis. The angle θ is more conveniently described by the pseudorapidity $\eta = -\ln\left(\tan\frac{\theta}{2}\right)$.

---

[2]The information in the following sections is extracted from [106].
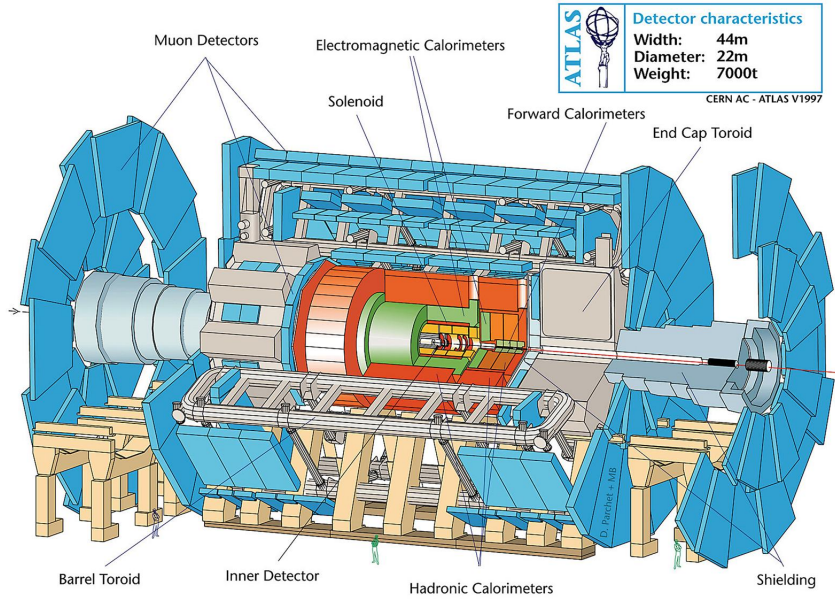
Figure 3.2: A sketch of the ATLAS detector [106].

It is replaced by the rapidity $y = \frac{1}{2}\ln\left(\frac{E+p_z}{E-p_z}\right)$ for massive particles. Many quantities are only measured in the transverse plane, which is the $x - y$ plane. The distance ΔR between objects is defined by $\Delta R = \sqrt{\Delta\eta^2 + \Delta\phi^2}$.

3.2.2 General layout and magnet system

Being a multi-purpose detector, subdetectors of the ATLAS detector are ordered in an onion-like structure around the beam line (a sketch of the ATLAS detector is shown in Figure 3.2). More precisely, a set of subdetectors are ordered in cylinders around the beam line (barrel). This is complemented by two groups of subdetectors ordered in disks orthogonal to the beam on both sides of the cylindrical detectors to detect very forward or backward particles (end-caps). The inner detector responsible for tracking is closest to the beam line. It is surrounded by a superconducting solenoid magnet which provides a magnetic field of 2 Tesla for tracking in the inner detector [106]. The magnet is kept very thin to reduce the amount of material in front of the calorimeters surrounding the solenoid and the inner detector. The calorimeters consist of two parts: the electromagnetic calorimeter is responsible for the detection of photons and electrons, the hadronic calorimeter is responsible for the detection of jets. Outside of the calorimeters the muon system follows. Three superconducting toroids with an eight-fold azimuthal symmetry [106] provide the magnetic field for tracking inside the muon system.

3.2.3 Inner detector

The Inner Detector is composed of three different detector types. Two of them are precision tracking detectors, the third is a transition radiation tracker. The layout is illustrated in Figure 3.3. The precision tracking detectors are responsible for a precise momentum and vertex measurement and extend up to $|\eta| < 2.5$. Among those, the pixel detector (made of silicon) is closest to the beam line. Three layers are ordered in cylinders around the beam line and in disks orthogonal to the beam at large $|\eta|$ in the end-caps. Most of the pixels have the same size with $(R - \phi) \times z = 50 \times 400 \ \mu m^2$ [106]. The precision obtained is 10 μm in $(R - \phi)$ and 115 μm in

38
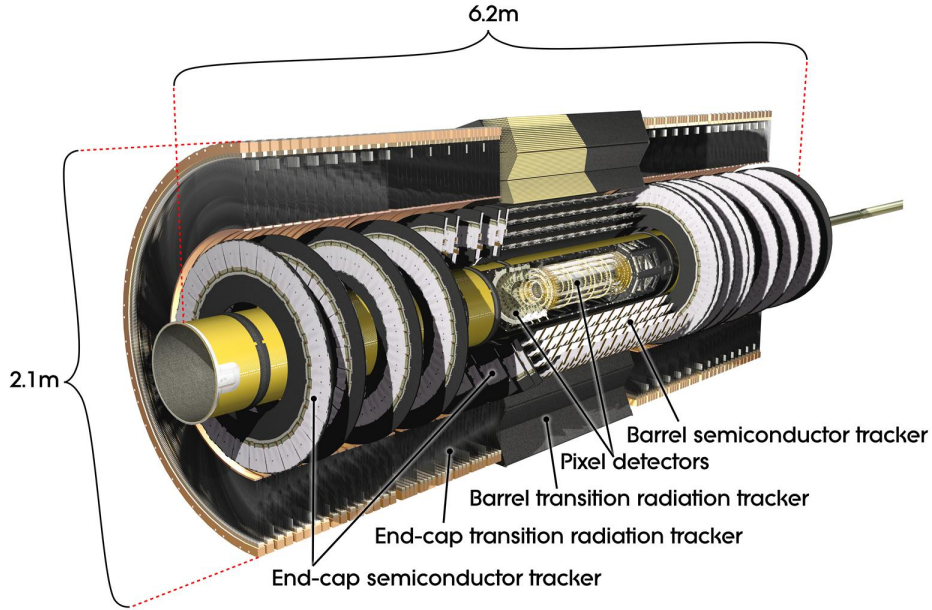
Figure 3.3: Sketch of the ATLAS inner detector showing the pixel detector in the middle closest to the beam line, surrounded by the SCT and the TRT [106].

z (barrel) or in R (end-cap) [106]. For the detection of the secondary vertices the layer of the inner detector closest to the beam line (the b-layer) is essential.

The pixel layers are surrounded by four layers of the silicon microstrip tracker (SCT) in the barrel. Silicon microstrip trackers are also placed behind the pixel layers in the end-caps. The SCT provides a precision of 17 μm in $(R-\phi)$ and of 580 μm in z (barrel) or in R (end-cap) [106].

The two precision tracking detectors are complemented by a transition radiation tracker (TRT) composed of 4 mm diameter straw tubes (filled with a xenon gas mixture). The TRT, surrounding the pixel detectors and the SCT, extends up to $|\eta| = 2$ and provides only $R - \phi$ information. As a large number of hits ($\sim$ 36) is expected for a track, the TRT gives an important contribution to the momentum measurement. It is also used in the electron identification. Its precision is 130 μm in $(R - \phi)$ [106].

3.2.4 Calorimeters

Different calorimeters surround the Inner Detector and provide a coverage up to $|\eta| = 4.9$. Different technologies depending on $|\eta|$ are used. A finer granularity is used for smaller $|\eta|$ values corresponding to the dimensions of the Inner Detector. A coarser granularity is used at larger $|\eta|$ values which is sufficient for jet or missing transverse energy measurements. The calorimeters need to be thick enough to completely contain electromagnetic or hadronic showers and to limit the punch-through to the muon system.

The electromagnetic calorimeter (ECal), which is closest to the Inner Detector, is essential in the electron and photon detection. It is a lead-liquid argon (LAr) calorimeter with electrodes (kapton) and absorbers (plates of lead) resembling an accordion in shape [106]. This design avoids azimuthal cracks which would result in inefficiencies [106]. The thickness of the electromagnetic calorimeter corresponds to more than 22 radiation lengths (X_0) in the barrel and more than 24 X_0 in the end-caps [106]. The barrel electromagnetic calorimeter extends up to $|\eta| = 1.475$ and consists of two identical half-barrels with a gap at $z = 0$. The end-cap calorimeters consist of
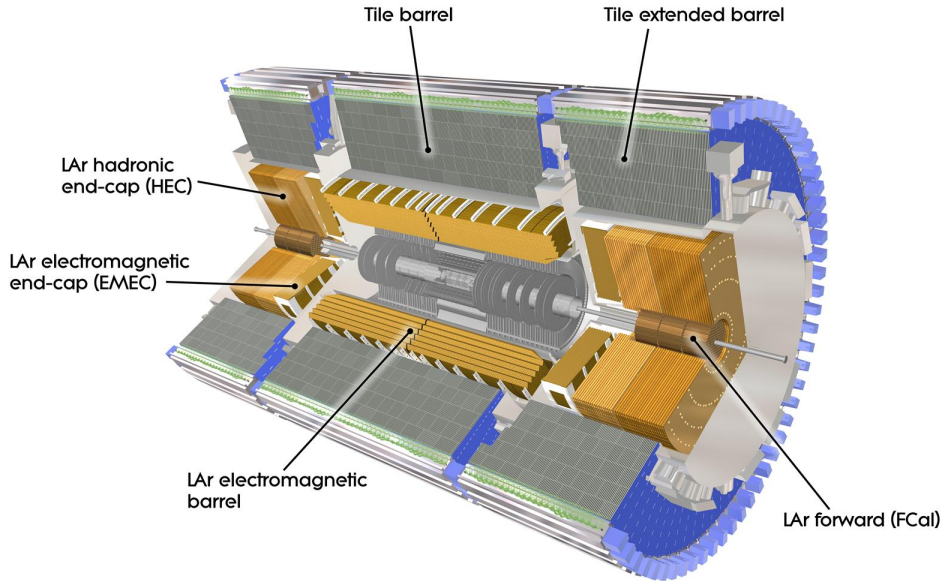
Figure 3.4: The ATLAS calorimeters in the barrel are shown schematically with the electromagnetic calorimeter closer to the beam line and enclosed by the hadronic calorimeter [106].

two coaxial wheels with $1.375 < |\eta| < 2.5$ and $2.5 < |\eta| < 3.2$. The electromagnetic calorimeter is complemented by a presampler, an active argon layer, in front of it. The presampler allows to measure the energy losses of electrons and photons before the calorimeter.

The hadronic calorimeter is placed outside of the electromagnetic calorimeter. It has a thickness of 9.7 interaction lengths (λ) in the barrel and 10 λ in the end-cap [106]. The hadronic calorimeter consists of three parts:

- The tile calorimeter is a sampling calorimeter with steel as absorber and scintillating tiles as active medium [106]. It is placed directly outside the envelope of the electromagnetic calorimeter as it extends up to $|\eta| = 1$ (barrel) and $0.8 < |\eta| < 1.7$ (extended barrel). It consists of three layers with 1.5 (1.5), 4.1 (2.6) and 1.8 (3.3) interaction lengths in the barrel (end-cap).

- The LAr hadronic end-cap calorimeter is a sampling calorimeter with copper plates as absorber and liquid argon as active medium. It consists of four layers in two independent wheels per end-cap and covers $1.5 < |\eta| < 3.2$. It has some overlap with the tile calorimeter and also with the LAr forward calorimeter.

- The LAr forward calorimeter covers the very forward region with $3.1 < |\eta| < 4.9$. As the thickness of the calorimeter is limited, it uses a high-density design [106] with a depth of 10 interaction lengths. It consists of three modules using copper (optimised for electromagnetic measurements) and tungsten (for hadronic measurements) with liquid argon as active medium.

3.2.5 Muon system

The muon system consists of four different muon chamber types used either for the precision measurement of the muon track or for triggering as described below. The muon chambers are embedded in a toroidal magnetic field created by a barrel magnet for $|\eta| < 1.4$ and by two
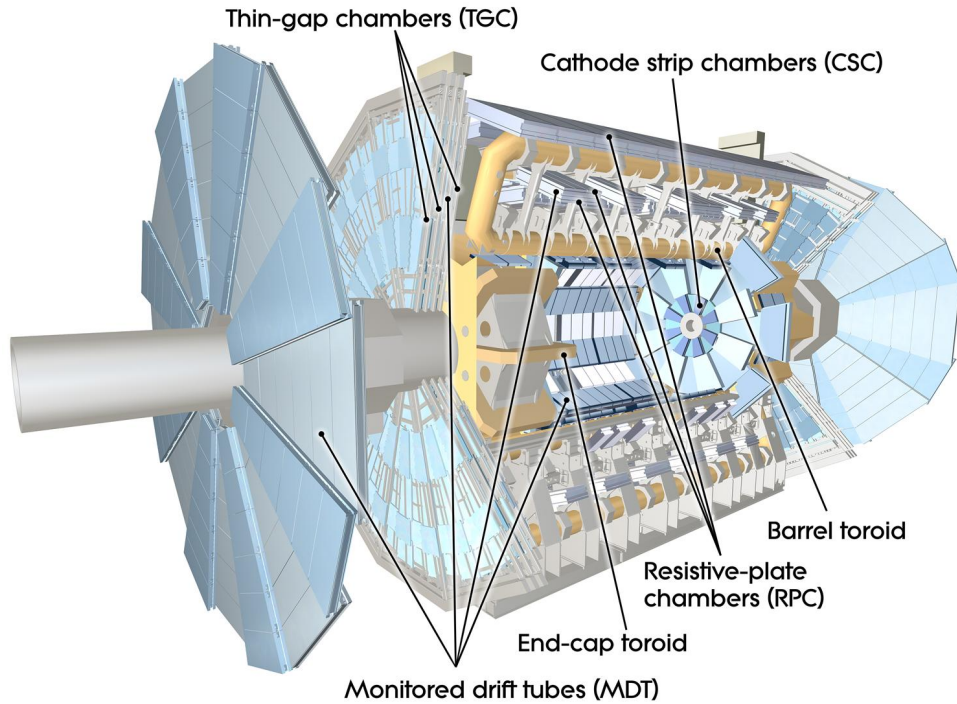
Figure 3.5: The ATLAS muon system, including the four different types of muon chambers. The magnet system surrounding the muon detectors is shown in yellow [106].

end-cap magnets for $1.6 < |\eta| < 2.7$ (all magnet components provide the magnetic field for the transition region for $1.4 < |\eta| < 1.6$). The magnetic field is mostly orthogonal to the muon tracks. The chambers are installed in three layers around the beam axis in the barrel or in three planes in the end-caps. Monitored Drift Tubes (MDTs) mainly provide the precision measurement of muon tracks [106]. At larger $|\eta|$ ($2 < |\eta| < 2.7$) Cathode Strip Chambers (CSCs, multiwire proportional chambers with cathodes segmented into strips) are used in the first layer instead of MDTs, because they provide higher granularities and are able to deal with higher particle fluxes [106]. The alignment of muon chambers versus each other is important to ensure a precise momentum measurement for which multiple chambers are required. Therefore, the relative position of the chambers but also internal deformations are monitored by alignment sensors. Two further chamber types are used within $|\eta| < 2.4$ for the trigger system: Resistive Plate Chambers (RPCs) in the barrel and Thin Gap Chambers (TGCs) in the end-caps. They provide identification of bunch-crossings and information for the muon triggers as momentum and track information [106]. In addition, they provide the measurement of a second coordinate orthogonal to the measurements by the MDTs.

3.2.6 Forward detectors

The luminosity delivered to ATLAS is determined by the two forward detectors LUCID and ALFA. LUCID (LUminosity measurement using Cherenkov Integration Detector) measures inelastic pp scattering in forward direction and is thus able to record the luminosity while data-taking [106]. It is placed $\pm 17\ m$ from the interaction line. ALFA (Absolute Luminosity For ATLAS), $\pm 240\ m$ from the interaction point, determines the luminosity by using elastic scattering at small angles. For this Roman Pots are used with scintillating fibre trackers placed inside [106]. The Roman Pots can be moved as close as $1\ mm$ to the beam. The third forward detector, the Zero-Degree Calorimeter (ZDC) is placed at $\pm 140\ m$ from the interaction point.
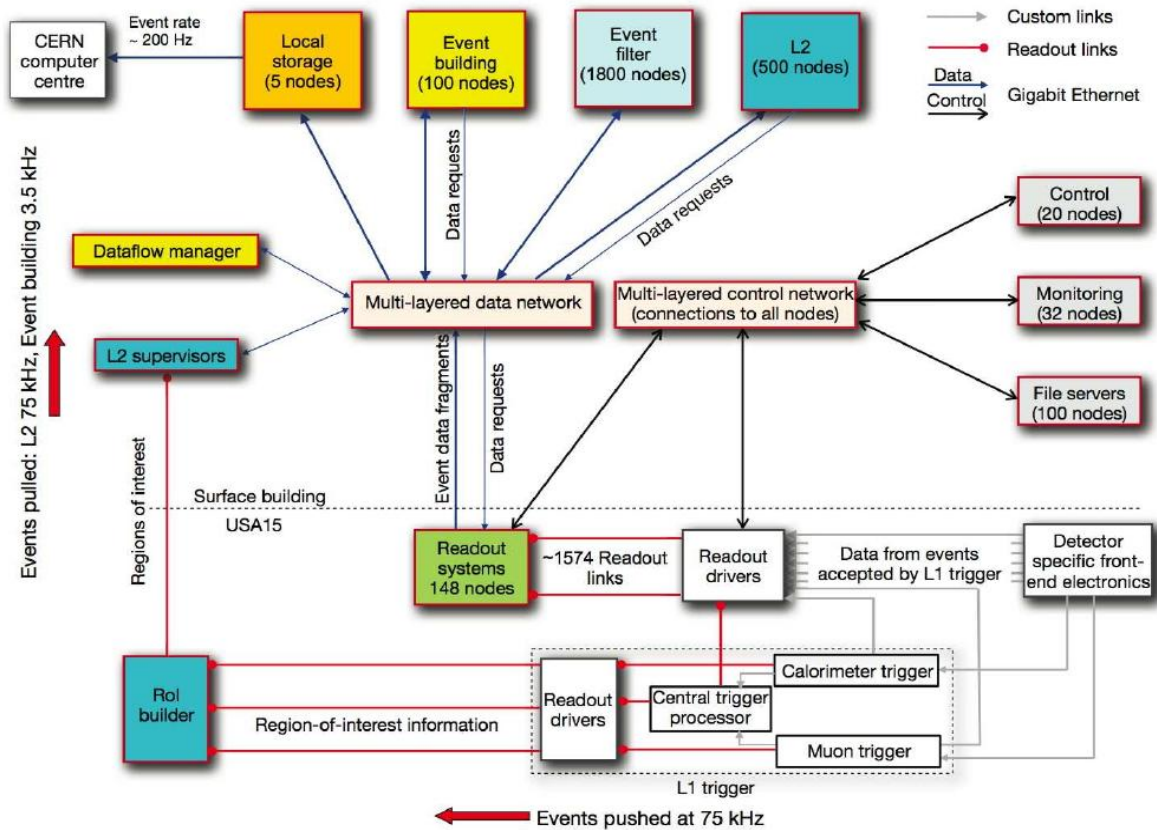
Figure 3.6: A sketch of the Trigger and Data Acquisition System (TDAQ) [106].

It measures the rate of neutral particles in very forward directions ($|\eta| \geq 8.2$) and so provides information about the centrality in heavy-ion collisions [106].

3.2.7 Trigger and Data Acquisition System

Often, the interesting phenomena are only produced with a very small cross section and are therefore hidden under copious QCD processes. An important challenge is therefore to select interesting events already during the data-taking process, as only interesting processes can be recorded due to disk space and processing time restrictions. The selection is performed by the ATLAS trigger system, which consists of three levels. The first level (Level 1, L1) is hardware based and has only access to reduced information of the event and the detector. The calorimeter with reduced granularity is used to select events containing electrons, photons, taus, jets and missing transverse energy. Muons are selected by using the muon trigger chambers. The decision of Level 1 is based on the particle type recorded and its properties, which need to satisfy pre-defined threshold values. A rate reduction to 75 kHz in less than 2.5 μs is required [106]. Signals recorded by Level 1 define 'Regions-of-Interest' (RoI) in η and ϕ. Level 2 (L2) uses the full detector information (both in precision and granularity etc.) in the RoIs to further reduce the rate to 3.5 kHz [106]. As this level is software-based, the processing time may be a bit longer with 40 ms [106]. Events passing Level 2 are passed on to the Event Filter (EF) which is also software-based. Algorithms close to the offline reconstruction and identification algorithms of objects can be run due to looser time constraints. A further rate reduction to approximately 400 Hz (for the data-taking in 2012) needs to be achieved. Figure 3.6 details the Trigger and Data Acquisition System (TDAQ) which receives and buffers the data from the detector parallel

to Level 1. It transmits any data requested to Level 2 and later to the Event Filter. Events accepted by the Event Filter are moved to permanent storage.

Further details regarding the electron and muon triggers will be given in Chapter 9.

3.2.8 Event Data Model and Grid

The byte stream of raw data recorded by the ATLAS detector can amount up to one Petabyte per year. A direct analysis or a distribution of the raw data to the analysers is therefore not possible. Derived data formats are defined in the *Event Data Model* [116]:

- The *Event Summary Data* (ESD) is directly processed from raw data and contains the full reconstruction output as tracks including their hits, energy clusters in the calorimeters etc. This format is further processed to other formats and not used for the analysis itself. ESDs are only kept for few weeks and afterwards deleted. Smaller ESDs (dESD) which only contain a subset of the original ESD are however kept for e.g. detailed analysis of reconstruction algorithms.

- The *Analysis Object Data* (AOD) format is derived from ESDs and contain a summary of the reconstructed event. Their size is smaller with respect to the ESDs.

Both of these data formats are only accessible by using the *Athena Software framework* [117] based on GAUDI [118], in which the whole ATLAS software (in particular the trigger algorithms and the reconstruction of objects) is written.

This work is based on the analysis of D3PDs (DPD: Derived Physics Data), which contains only a subset of the information in the AODs and only a subset of the original object and detector information according to the needs of the specific analysis. D3PDs have a n-tuple structure and can thus be analysed by using the ROOT framework [119]. D3PDs for SUSY analyses are centrally produced by the ATLAS collaboration. These n-tuples are further reduced in size for the specific analyses presented in work [120].

The D3PDs were analysed by using the Grid infrastructure described in the ATLAS operation model [121, 122, 123, 124]. This model includes the world-wide distribution of the recorded data. The raw data as recorded by the detector is transferred to the computing and server farm at CERN, the Tier-0, where the raw data is moved to permanent storage and further distributed to 10 computing centres spread over the world, the Tier-1 sites. A fast reconstruction and calibration is already run at Tier-0 within 48 h from data-taking. A full reconstruction (including possible adjustments obtained in the initial fast reconstruction) is afterwards run at the Tier-1 sites. This includes the ESD and AOD creation. The AODs are further distributed to 40 Tier-2 sites. Data in D3PD formats are produced from AODs and are distributed over different Grid sites (belonging to Tier-1, Tier-2 or local sites, the Tier-3 sites). Due to the world-wide distribution of data, any analysis job will be sent to the site hosting the data instead of copying the data to the site from which the analysis job was started. This allows a fast and efficient processing of the large data sample recorded.

3.2.9 Luminosities

The data sample collected by the ATLAS detector is quantified by the integrated luminosity L related to the number of events N recorded and their cross section σ:

$$L = \int \mathcal{L} dt = \int \frac{N}{\sigma} dt \qquad (3.2.1)$$

where $\mathcal{L}$ is the instantaneous luminosity being measured at a specific time. A precise knowledge of the luminosity is necessary to scale background expectations obtained from Monte Carlo samples correctly (and thus to compare to the number of recorded events).

The instantaneous luminosity delivered by the LHC is given by [105]:

$$\mathcal{L} = \frac{n_b f_r n_1 n_2}{2\pi \Sigma_x \Sigma_y} \tag{3.2.2}$$

where n_b is the number of bunches in the ring, f_r is the revolution frequency and n_1 and n_2 are the number of particles in the two colliding bunches. The horizontal and vertical profiles of the colliding beams are given by Σ_x and Σ_y, respectively. Due to the imprecise knowledge of some of these quantities in general, the instantaneous luminosity cannot be calculated directly from this equation. Instead, the following relations are used [125]:

$$\mathcal{L} = \frac{\mu n_b f_r}{\sigma_{\text{inel}}} = \frac{\mu_{\text{vis}} n_b f_r}{\sigma_{\text{vis}}} \tag{3.2.3}$$

with μ the average number of inelastic interactions, σ_{inel} the cross section of inelastic pp collisions, $\mu_{\text{vis}} = \epsilon \mu$ the observed interaction rate per crossing related to μ by the efficiency ϵ to record the collision by the detector and the method. The visible cross section $\sigma_{\text{vis}} = \epsilon \sigma_{\text{inel}}$ is also related to σ_{inel} by the efficiency ϵ. The currently recorded luminosity can thus be inferred from μ_{vis} if σ_{vis} is known. The observed interaction rate is thus measured by different detectors during the collisions, including the LUCID detector described earlier (the detailed algorithm are described in [125]). This measurement occurs both online during data-taking as well as offline after data-taking by using inner detector information in triggered events. The visible cross section σ_{vis} is obtained from van-der-Meer scans [126], in which both beams are separated by a known distance, in special collisions with lower interaction rates. The luminosity can be determined precisely by using Equation 3.2.2 in these special collisions [125].

Uncertainties on the measurement of the luminosity arise from both the measurements of σ_{vis} and μ_{vis} and can be evaluated by comparing the different algorithms and methods. These differ in their acceptances, sensitivities to pile-up, instrumental effects and to backgrounds. Furthermore, the van-der-Meer scans could only be taken rarely (in special runs in April and November 2012 for the 2012 data-taking), although the general run conditions are constantly changing. Thus, the main uncertainties are related to the determination of σ_{vis} in the van-Der-Meer scans. In total, the uncertainties accumulate to $\pm 2.8\%$ for the 2012 data-taking.

Figure 3.7 shows the number of colliding bunches, the peak interaction rates and the instantaneous luminosities for Run 1 consisting of the data-taking of pp collisions at 7 TeV in 2010 and 2011 and at 8 TeV in 2012. The peak values of all three quantities increased continuously in this period. This was reflected in increasing rates of trigger chains and thus the need to constantly tighten the trigger menu[3] in order to stay within the acceptable trigger output rates. Implications of this will be discussed in Chapter 9.

In total, the ATLAS detector recorded 45 pb^{-1} of pp collisions at a center-of-mass energy of 7 TeV in 2010, 5.08 fb^{-1} in 2011 and 21.3 fb^{-1} of pp collisions at 8 TeV in 2012, while the LHC delivered 48.1 pb^{-1}, 5.46 fb^{-1} and 22.8 fb^{-1}, respectively. The collected statistics was thus the largest in 2012 and the statistics of 2010 is negligible in comparison. This is illustrated in Figure 3.8.

---

[3]A trigger menu comprises all triggers used during data-taking.
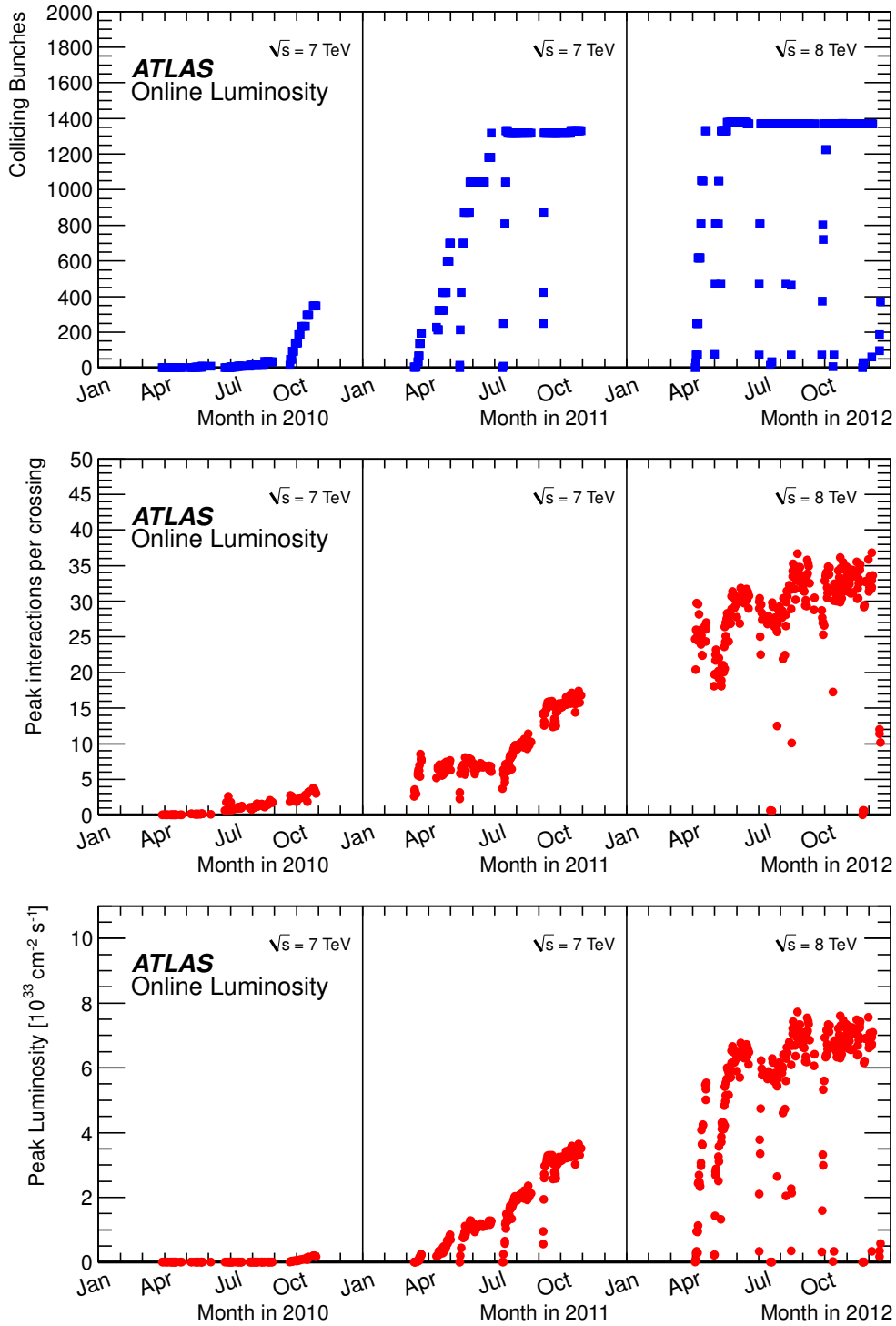
Figure 3.7: The evolution of the number of bunches (top row), of pileup (middle row) and of the instantaneous luminosities (bottom row) are given for the collisions in 2010, 2011 and 2012 in dependence of time. A steady increase of the peak values of all three quantities can be seen [127, 128, 129].
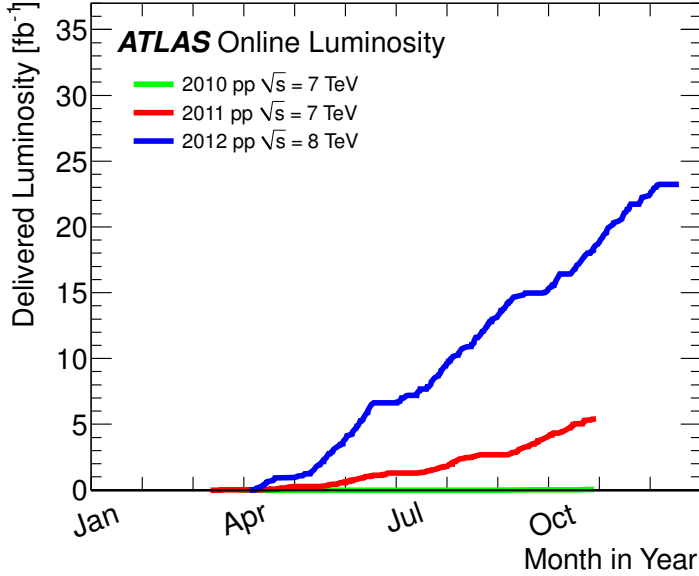
Figure 3.8: The integrated luminosity as collected in the 2010, 2011 and 2012 data-taking shown versus time [130].

The analyses discussed in this work consider final states with many different particles which are reconstructed by using all detector components. Only data taken at periods in which all of the relevant detector components were working well is thus considered in this work. For the data-taking in 2012, this accumulates to a statistics of 20.3 fb^{-1}. This work covers two different analyses: the first analysis uses 5.8 fb^{-1} of data taken in 2012 (5.8 fb^{-1} analysis), the second analysis considers the full statistics (20.3 fb^{-1} analysis). Previous analyses focusing on the final state discussed in this work have considered the data taken in 2010 [3] and 2011 [131, 132, 133].

3.3 Monte Carlo simulation

Monte Carlo event generators are used to model particle collisions. Events generated by them are passed on to GEANT4 [134] which simulates the passage of particles through matter and thus simulates the ATLAS detector response to the generated particles. The simulated hits and energy deposits are further processed like data following the reconstruction methods described in Chapter 4. The Monte Carlo samples obtained thus reflect the data and are used for the simulation of background and signal processes. Monte Carlo samples are both necessary for the estimation of backgrounds and for the optimisation of signal regions in this work. An overview about Monte Carlo generators is given in [135] with the theory described in [136] and summarised in [22, 137]. This section draws its information from these resources.

3.3.1 Simulation

The typical collision process is difficult to simulate due to different reasons. A large number of particles is involved in the typical collision process so that a precise calculation of all contributions in all orders of perturbation theory is impossible. The calculation at a fixed order is also demanding due to divergences of the matrix elements involved and the required integrations of large phase-spaces [136]. Some parts of the collision, in particular the hadronisation process,
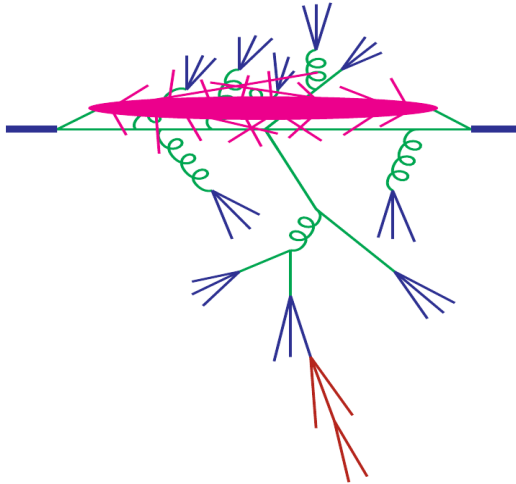
Figure 3.9: A collision event can be divided in different components due to the factorisation theorem depending on the momentum transferred (as described in the text). The middle green line indicates the hard scattering process, the outgoing green gluon and quark lines the parton shower. The hadronisation is indicated by the blue lines and the further decay of unstable hadrons by the red lines. The hard scattering is accompanied by the underlying event indicated in magenta colour. The plot is taken from [137].

cannot be calculated by using perturbative methods and thus rely on models of the confinement of quarks and gluons.

Given the difficulties, the simulation of a collision event is separated into multiple steps depending on the momentum transfer involved. Perturbation theory can be used for processes with larger momentum transfer, but not for processes with low momentum transfer. A separation is possible due to the factorisation theorem (see [138] and references therein) and is illustrated in Figure 3.9. The different categories are described in the following.

The cross section of the *hard process*, that is the hard scattering or annihilation of two particles, can be calculated by methods of the perturbative QCD (pQCD), but only to a certain order in α_s. The cross section of the collision of particles a and b resulting in n is given by [136]:

$$\sigma = \sum_{a,b} \int_0^1 dx_a dx_b \int d\phi_n f_a^{h_1}(x_a, \mu_F) f_b^{h_2}(x_b, \mu_F) \frac{1}{2x_a x_b s} |\mathcal{M}_{ab\to n}|(\phi_n; \mu_F, \mu_R) \tag{3.3.4}$$

where ϕ_n indicates the phase space, h_1 and h_2 the parent hadrons to which a and b belong, x_a and x_b is the momentum transfer of these two particles in the collision, μ_F and μ_R are the factorisation and renormalisation scales, respectively. The computation of the matrix element $\mathcal{M}_{ab\to n}$ is performed by various tools [136]. It is performed at leading order (LO) by most generators and corrected to NLO by *K-factors*. Some Monte Carlo generators also perform a calculation of the cross sections at next-to-leading order (NLO). The parton distribution functions (PDFs) $f_a^{h_1}(x_a, \mu_F)$ and $f_b^{h_2}(x_b, \mu_F)$ give the probability to find a parton a or b with a momentum fraction x if probing the initial hadron at a scale μ_F [136]. PDFs also include non-perturbative effects and are therefore not directly calculable. Instead, they are evaluated in global fits to deep inelastic scattering experiments, Drell-Yan events and collision data of various collider experiments. The PDFs are documented in the LHAPDF library [139].

The hard process is calculated at fixed order and needs to be corrected to higher orders by effects of gluon radiation in the following *parton shower*. Radiated gluons can emit further gluons as they carry colour charge. Quarks or gluons radiate further gluons until an energy

scale of 1 GeV [136], for which the pQCD is not longer applicable and confinement effects get important. The description of the parton shower is valid for low momentum transfers or collinear radiations, but is not accurate for high-energetic emissions or emissions at large angles.

The parton shower and the hard process are combined in the *matching* process for which different methods exists [136].

The parton showers result in coloured objects which are transformed into colour-singlet hadrons in the following *hadronisation* step. This process, which is non-perturbative, is described by QCD-inspired phenomenological models [136]. The two common models are the Lund string model [140, 141] and the cluster model [142] (and references in [136]).

The Lund model considers an increasing linear potential between quark and anti-quark [136]. The string or colour-flux tube thought to connect the quark q and anti-quark $\bar{q}$ breaks into another quark-anti-quark pair $q'\bar{q}'$ if a certain energy is reached. The pairs $q\bar{q}'$ and $q'\bar{q}$ are colour-singlets and move apart. These pairs may break again if they have a sufficient invariant mass or form a ordinary hadron otherwise [136].

The cluster model is based on the preconfinement property of QCD [143], stating that, regardless of the original hard process and at energy scales Q_0 much smaller than those of the hard process, partons in the shower are clustered in colour-singlets with an universal invariant mass only depending on Q_0 and the QCD scale λ [136]. Technically, the algorithm starts from the splitting of gluons in quark-anti-quark pairs followed by a clustering of close (anti-)quarks with appropriate colour. If the cluster energy is above the cut-off value Q_0, the cluster splits in further clusters until the transverse momenta of all clusters are below the cut-off value. The clusters form the final mesons.

Additionally to the hard process, further interactions may occur in an event (*underlying event*), due to colour exchanges between further remnants of the colliding protons (*multi parton interactions*) and due to initial or final state radiation [136].

3.3.2 Monte Carlo generators

This work uses Monte Carlo simulations from *general-purpose* generators and from more specialised generators. The general-purpose generators used include:

- `HERWIG`: This generator [144] (Hadron Emission Reactions With Interfering Gluons) includes initial and final state radiation in the parton shower and uses the cluster model for the hadronisation. The underlying event can be simulated by the external tool `Jimmy` [145] which considers multi-scattering [135].

- `PYTHIA`: The `PYTHIA` generator [78] was originally written in `Fortran` (the version 6.4 is currently in use) and was rewritten in `C++` recently (`PYTHIA 8`). The Lund model is used for hadronisation.

- `SHERPA`: This generator is written in `C++`. Its modular structure facilitates its maintenance. The strength of this generator lies in the perturbative regime [136].

In addition to the general-purpose generators, different tree-level generators are used which need to be complemented by a general-purpose generator for the simulation of the parton shower, the hadronisation and the underlying event[4]:

- `AcerMC` [146]

---

[4]The following information is taken from [135]

48

This generator is specialised for the simulation of Standard Model processes in LHC pp collisions and provides an efficient event generation.

- `AlpGEN` [147]

  This generator is particularly designed for events with large jet multiplicities. The masses of b and t-quarks are included.

- `MadGraph` [77]

  This matrix element generator can generate $2 \rightarrow n$ processes and decays. The user specifies the initial and final state particles and `MadGraph` generates all Feynman diagrams and provides code for the evaluation of the matrix element. Identical sub-diagrams are re-used in the calculation.

- `MC@NLO` [148]

  This generator includes NLO corrections. The parton shower and hadronisation needs to be simulated by `HERWIG`.

Part II

The structure of the 1-lepton analysis

Chapter 4

Object definitions

This chapter describes the reconstruction and identification of detector quantities resulting in electron, muon and jet candidates, in the following referred to as *objects*. Also the reconstruction and calculation of the missing transverse energy is described.

In addition, this chapter outlines which requirements need to be satisfied by the objects to be used in the analyses presented here and indicates related systematic uncertainties.

4.1 Electrons

The electron reconstruction and identification procedure uses information of the inner detector and the electromagnetic calorimeter. After reconstructing electron candidates from hits in the inner detector and energy deposits in the electromagnetic calorimeter, the quality of the candidates can be determined during the identification step.

Reconstruction: The electron reconstruction [149, 150] for central electrons ($|\eta| < 2.47$) starts with the identification of electromagnetic seed clusters in the electromagnetic calorimeter. For this a sliding window algorithm [151] is used with a window size of 3×5 in units of $\eta \times \phi = 0.025 \times 0.025$ which corresponds to the granularity in the second layer of the electromagnetic calorimeter [149].

Around the seed cluster, a region of interest is defined with a radius of $\Delta R = 0.3$, in which tracks are searched for by a modified pattern recognition algorithm [152] based on the Kalman filter [153]. This algorithm and the following fitting of the tracks consider losses due to bremsstrahlung [154].

The tracks found are extrapolated to the middle layer of the electromagnetic calorimeter. An extrapolated track is loosely matched to the seed cluster if close enough in η and ϕ (see [149, 150] for the detailed requirements). Any matched track is re-fitted with the Gaussian Sum Filter method [155], a variant of the Kalman filter accounting for non-linear losses due to bremsstrahlung.

The track-cluster matching algorithm is repeated with the refitted track, but imposing tighter matching criteria in η and ϕ. An electron candidate is defined if at least one track matches the cluster. The best matching track is chosen to evaluate the kinematics of the electron; tracks with at least one pixel detector hit are preferred in the procedure. The electron cluster is rebuilt in the following by using 3×7 (barrel) or 5×5 (end-cap) longitudinal towers of cells. The

energy of the resulting electron is the sum of the energy within the cluster, the energy deposit in front and behind the electromagnetic calorimeter and the energy deposited around the cluster in the electromagnetic calorimeter. The η and ϕ coordinates of the electron are taken from the associated track.

Identification: The identification sequences intend to select most efficiently isolated electrons while rejecting background electrons from mismeasured hadronic jets, heavy flavour hadron decays, photon conversions or Dalitz decays. This is achieved by considering longitudinal and transverse shower shapes, the track quality, the quality of the track cluster matching etc. The precise criteria are detailed in [150] and are shown in Table B.2 in Appendix B.

Three levels with increasing purity and background rejection define `loose++`, `medium++` and `tight++` electrons as detailed in Table B.1 in Appendix B. The analyses presented in this work use `medium++` and `tight++` electrons. The difference between both quality levels is in particular the rejection of electrons consistent with a photon conversion in the `tight++` criteria.

Electrons in this work: Different electron objects are used within the analyses presented in this work. Preselected electrons of `medium++` quality are required to be within $|\eta^{\text{clus}}| < 2.47$ (where η is measured for the cluster, not for the track) and have $p_T > 10$ GeV. This type of electrons is used in calculation of the missing transverse energy as explained below. Only isolated electrons are of interest for the analyses, in particular, any electron should be isolated from any jet by requiring the $\Delta R(e, \text{jet}) > 0.4$. Electrons falling into this category are called loose electrons in the following. Some electrons originating from heavy flavour hadron decays or from photon conversions satisfy the loose electron requirements. Such electrons can be suppressed by only accepting `tight++` electrons and adding a further isolation requirement by demanding that the p_T sum of all tracks with $p_T > 1$ GeV in a cone around the electron of $\Delta R = 0.2$ (p_T^{cone20}) divided by the p_T of the electron falls below 0.1, $p_T^{\text{cone20}}/p_T < 0.1$. Electrons belonging to this category are referred to as signal electrons in the following. They will be used in the definition of the signal regions below.

Events with electrons of `medium++` quality and with $p_T > 10$ GeV falling into the transition region between the calorimeters of barrel and end-cap, $1.37 < |\eta| < 1.52$, are vetoed.

Table 4.1 summarises the different categories of electrons used within this work.

Electron related systematic uncertainties: Systematic uncertainties arise from the electron reconstruction and identification. Their sizes are determined in a Tag & Probe method based on the selection of $Z \to ee$ or $J/\psi \to ee$ events. For electrons with $p_T > 20$ GeV only the results based on $Z \to ee$ events are relevant. The uncertainties on the identification efficiency correspond to 6 % and 2 % for electrons with $p_T < 25$ GeV and $p_T > 25$ GeV, respectively [150]. The uncertainties on the reconstruction efficiency are smaller than 1.5% [150].

The energy scale in the electromagnetic calorimeter needs to be calibrated due to [149] the limited knowledge about the material in front of it, the uncertainties on the energy measurement by the presampler, the differences found in the calibration for $Z \to ee$ or $J/\psi \to ee$ events, cross-talk between different cells in different layers in the calorimeter resulting in different energy scales etc. The analyses presented in this work thus consider uncertainties on the energy scale and resolution with size of $O(2\%)$.

Cut	Value/description
Preselected Electron	
Algorithm	Electron algorithm
Acceptance	$p_{\mathrm{T}} > 10$ GeV, $|\eta^{\mathrm{clust}}| < 2.47$
Quality	`medium++`
Overlap	$0.2 < \Delta R(e, \mathrm{jet}) < 0.4$
Loose Electron	
Preselected electron +	
Geometrical isolation	$\Delta R(e, \mathrm{jet}) > 0.4$
Signal Electron	
Loose electron +	
Quality	`tight++`
Isolation	$p_{\mathrm{T}}^{\mathrm{cone20}}/p_{\mathrm{T}} < 0.10$
Acceptance	$p_{\mathrm{T}} > 25$ GeV
Crack Electron	
Quality	`medium++`
Acceptance	$p_{\mathrm{T}} > 10$ GeV, $1.37 < |\eta| < 1.52$
Isolation	Not applied.

Table 4.1: The different categories of electrons utilised in the analyses.

4.2 Muons

Muon reconstruction and identification: The muon reconstruction uses information from the muon spectrometers and the inner detector mainly. Four different types are reconstructed [156] of which two are used in this work and described in the following.

For `combined` muons, the tracks are reconstructed independently in the muon spectrometer and in the inner detector. A combined track is formed by a statistical combination of both tracks. Two different approaches exist for this. This work generally uses muons of the `staco` type [157]. For this type, inner detector and muon spectrometers track segments are combined. The other possibility, however not used for the muons considered in this work, is the creation of a fully refitted track based on inner detector and muon spectrometer information (a description can be found in [158]).

`Segment-tagged` muons, also used in this work, use inner detector tracks extrapolated to the muon spectrometer. A muon is found if the track can be associated to at least one track segment in muon chambers. This method is useful for muons with low transverse momentum, but also in order to recover losses due to regions in the muon spectrometer where no muon chambers were installed. This is the case at $\eta \approx 0$, where service material for the inner detector and the calorimeters is installed and for $1.1 < \eta < 1.3$, where not all muon chambers foreseen had been installed during Run 1, causing a muon track to traverse only one layer of muon chambers.

Muons in this work: Different types of muons are used within this work and detailed in Table 4.2.

Preselected muons are created by the `staco` algorithm and either a combined or at least a segment-tagged muon. The muon is required to be within $|\eta| < 2.4$, corresponding to the acceptance of the triggers used, and to have $p_{\mathrm{T}} > 10$ GeV. The quality of the muon may be

Cut	Value/description
Preselected muon	
Algorithm	`staco`, `combined` or `segment-tagged` muon
Acceptance	$p_{\mathrm{T}} > 10$ GeV, $|\eta| < 2.4$
Quality	`loose`
Inner detector	Number of pixel hits + number of crossed dead pixel sensors > 1
	Number of SCT hits+number of crossed dead SCT sensors ≥ 6
	Pixel holes + SCT holes < 3
	≥ 1 b-layer hit when it can be expected
track quality	If $|\eta| < 1.9$: $n_{\mathrm{TRT}} > 5$ and $n_{\mathrm{TRT}}^{outliers} < 0.9 n_{\mathrm{TRT}}$
	If $|\eta| \geq 1.9$ and $n_{\mathrm{TRT}} > 5$: $n_{\mathrm{TRT}}^{outliers} < 0.9 n_{\mathrm{TRT}}$
Bad muon	
Preselected muon +	
Charge	$\frac{\sigma(q/p)}{|q/p|} > 0.2$
Loose muon	
Preselected muon +	
Acceptance	$\Delta R(\mu, \mathrm{jet}) > 0.4$
Cosmic muon	
Loose muon +	
Impact parameters	$|z_\mu - z_{PV}| > 5$ mm, $d_0 > 2$ mm
Signal muon	
Loose muon +	
Acceptance	$p_{\mathrm{T}} > 25$ GeV
Track isolation (excluding muon track)	$\sum p_{\mathrm{T}}$ in ΔR cone of $0.2 < 1.8$ GeV

Table 4.2: Different muon categories used in this work. In this table, n_{TRT} is the total number of TRT hits, including outliers.

loose. Different quality criteria are imposed on the hits recorded by the inner detector. There must be at least one hit in the pixel detector or at least one dead pixel sensor crossed by the track. Similarly the number of hits in the SCT together with the number of dead SCT sensors crossed by the track need to exceed or equal six hits. Less than three holes (so sensors or pixels crossed by the track but not showing a signal) may be present in the pixel and SCT detectors. Also, if expected, at least one hit in the b-layer is required. Further quality criteria are required for the reconstructed track, demanding for the regions with $|\eta| < 1.9$ that more than five hits have been counted in the TRT and in addition $n_{\mathrm{TRT}}^{\mathrm{outliers}} < 0.9 n_{\mathrm{TRT}}$. The last condition is also required for regions with $|\eta| \geq 1.9$ if more then five TRT hits have been associated to the track. Preselected muons are in particular used within the calculation of the missing transverse energy below.

Events with badly reconstructed muons are rejected by requiring the events to not contain any muons with $\frac{\sigma(q/p)}{|q/p|} > 0.2$ (where q is the charge of the muon) in addition to the preselection criteria. Similarly, events with cosmic muons are rejected, cosmic muons being identified by

cuts on the longitudinal and transverse impact parameters.

The analyses presented in this work veto an event if a second muon is present, if this muon falls into the category of a loose muon. This is defined based on the preselected muon category and by requiring in addition the muon to be isolated from any jet in a cone of $\Delta R(\mu, \text{jet}) = 0.4$ around the muon.

A signal muon, used in the definition of the signal regions, is defined by requiring the loose muon to pass a tighter p_T cut, $p_\text{T} > 25$ GeV, and by imposing an additional isolation criterion related to the tracks around the reconstructed muon: $\sum p_\text{T}$ of all tracks with $p_\text{T} > 1$ GeV in a cone of $\Delta R = 0.2$ around the muon needs to be smaller than 1.8 GeV.

Muon related systematic uncertainties Similarly to electrons, different systematic uncertainties are used within this work related to the muon reconstruction or the muon momentum scale or the resolution of the inner detector or the muon spectrometer. Muon reconstruction efficiencies and the corresponding uncertainties have been evaluated on $Z \to \mu\mu$ events [159, 160, 156]. The uncertainties are within $O(1\%)$, with the largest uncertainties for high energetic muons with $p_\text{T} > 1$ TeV due to the difficulty to account for energy losses in the extrapolation to high energies. Momentum corrections (and thus uncertainties on the momentum scale and resolution) are mainly evaluated from the dimuon mass resolution in $Z \to \mu\mu$ events [161, 156]. The momentum resolution is influenced by the material passed by the muons, the alignment between the inner detector and the muon spectrometer and by the the spatial resolution of the single hits recorded. These uncertainties are mostly negligible for this work.

4.3 Jets

Jets used in this work are reconstructed by using the anti-k_t algorithm [162] with a distance parameter of 0.4 and with topological clusters as input. The lowest energetic jets possible to reconstruct have $p_\text{T} > 7$ GeV [163]. A calibration procedure is executed afterwards.

Topological clusters: Cells in the hadronic calorimeter with an energy deposit exceeding 4σ (where σ indicates a noise threshold) seed the cluster building [163]. Iteratively, any cells with an energy deposit exceeding 2σ around the seed cell are added. Finally, all neighbouring cells next to the cluster are added, regardless of the energy deposit in them. This algorithm successfully suppresses noise. The created clusters can be split into smaller clusters by a re-iteration around the maxima within the created topological cluster in order to improve the splitting between showers and close-by particles [163]. The cells contributing to a cluster define its energy, its coordinates are calculated from energy-weighted averages of the η and ϕ coordinates of the cells.

A calibration of the topological cluster and of the jets created afterwards is necessary [163] due to the non-compensation behaviour of the calorimeter for hadrons, due to inactive detector regions, leakage of particles to regions outside the calorimeter, particles belonging to a jet but not assigned to it as well as further inefficiencies in the jet reconstruction as for example the noise cuts applied. The first step in this calibration corrects the energy of the topological clusters. In this work jets calibrated with the local cluster weigthing (LCW) approach are used, in which clusters are identified as being of electromagnetic or hadronic origin based on the properties of the recorded showers. A correction is then applied depending on the origin, being derived by comparison to simulated charged and neutral pion events [163, 164].

Jet finding: The constructed topological clusters form the input to the jet finding algorithm, being based on a sequential combination of objects. Following [162] the distance between two objects i and j is defined here as:

$$d_{ij} = \min\left(p_{\mathrm{T}i}^{2k}, p_{\mathrm{T}j}^{2k}\right)\frac{(\Delta R)_{ij}^2}{R^2} \qquad (4.3.1)$$

where R is a distance parameter, set to 0.4 within this work, and $(\Delta R)_{ij}^2 = (y_i - y_j)^2 + (\phi_i - \phi_j)^2$ is the distance between both objects (calculated with the rapidity y). The parameter k can take different values. The distance between an object i and the beam is given by

$$d_{iB} = p_{\mathrm{T}i}^{2k} \qquad (4.3.2)$$

The minimal value in a list of all d_{ij} and d_{iB} is determined. Both objects i and j are merged in the case that the minimal value is a d_{ij}. Otherwise, if d_{iB} is minimal, the object i is considered as jet and removed from the list. The values of k define different jet finding algorithms: $k = 1$ results in the k_t algorithm [165, 166], $k = 0$ in the Cambridge-Aachen algorithm [167, 168] and $k = -1$ in the anti-k_t algorithm [162] used in this work. This last algorithm has various advantages [162], as soft objects with $\Delta R < R$ are merged into one hard jet, so that the jet boundaries are not affected by soft radiation. If two hard objects are within R, these are merged. Two hard objects within a distance of $R < \Delta R < 2R$ are not combined, instead the energy of these two objects is shared among them according to their relative transverse momentum.

Calibration: In addition to the calibration of the topological clusters, further calibration steps are executed as described in [163, 164, 169].

In-time pile-up from additional collisions in the same event and *out-of-time* pile-up from additional collisions initiated by previous or following events, can modify the reconstructed jets in their energy but also in their reconstructed direction, because the pile-up causes additional energy deposits in the calorimeters. This additional energy deposits are subtracted in the calibration procedure by application of the jet area method [170] in which a medium energy density ρ caused by the pile-up is calculated and multiplied by the area A covered by the jet. The product $\rho \cdot A$ is subtracted from the transverse momentum of the jet [169] and thus a corrected transverse momentum obtained.

The energy of the jets needs to be corrected to the *jet energy scale* (JES) due the reason mentioned above. This correction is based on a comparison with truth jets in simulated Monte Carlo samples [163]. Using in-situ techniques, differences between Monte Carlo simulation and data are corrected for in a further calibration step. These corrections are determined in Z+jets, γ+jets events and in systems with a hard p_{T} jet recoiling against a system of low p_{T} jets [164].

Uncertainties on the jet energy scale can be broken down into multiple categories including the detector description, the physics modelling, uncertainties due to the methods used or due to limited statistics. They also depend on the flavour composition of the jets, in particular, if a jet originates from a heavy-flavour decay. Close-by objects or jets and pile-up can show an effect as well.

This work uses all the uncertainties on the jet energy scale in a statistical combined form considering their correlations. These uncertainties can be significant, as detailed in section 10.3.4. Further systematic uncertainties arise from the jet energy resolution [171] (JER), $\frac{\sigma(p_{\mathrm{T}})}{p_{\mathrm{T}}}$, which can also be significant.

Pile-up: In-time and out-of-time pile-up creates additional energy deposits in the calorimeters, which influences the jet reconstruction but also the reconstruction of the missing transverse energy below. Pile-up modifies therefore the jet energy scale and the jet mass, as well as the direction of hard jets. These effects are accounted for in the jet calibration. In addition, pile-up can create additional jets in the event, not originating from the primary interaction. Systematic uncertainties are assigned due to the presence of pile-up as the amount of pile-up is higher in data than in the Monte Carlo simulations used. The Monte Carlo simulation is thus reweighted (by using the variable μ defined in Section 3.2.9) to reflect the situation in data. The uncertainties are obtained by varying the constant reweighting factor by 10 %.

b-Jets: The tagging of jets originating from the decay of hadrons containing b-quarks (b-jets) gives an effective way to identify $t\bar{t}$ events as explained in Section 8.1. The rejection of events containing b-jets is useful in the selection of W+jets events.

Different tagging algorithms have been exploited since the beginning of data-taking, culminating in an optimised algorithm, called `MV1`, based on a neural network to be also used in this work. Any b-tagging algorithm first needs to reject backgrounds such as K_s, Λ decays, photon conversions etc. which could mimic the properties of a B-hadron decay by creating a secondary vertex in the event (apart from the primary vertex). The secondary vertex in decays of B-hadrons is due to the long life-time of the b-quarks. The background rejection is based on transverse and longitudinal impact parameters and properties of the created vertex including properties of the tracks contributing to it [172].

The neural network of `MV1` algorithm uses the b-tagging output weights (so the probabilities that a jet found is a b-jet) of the taggers `JetFitter+IP3D`, `IP3D` and `SV1` [173].

The tagger `IP3D` belongs to the algorithms using impact parameters to tag b-jets [172]. Normalised distributions of signed transverse and longitudinal impact parameter significances (so $\frac{d_0}{\sigma_{d_0}}$ and $\frac{z_0}{\sigma_{z_0}}$ with d_0 and z_0 being the transverse and the longitudinal impact parameters, respectively) are compared to Monte Carlo simulations in a likelihood ratio technique to identify b-jets against light jets (so jets created in the hadronisation process of lighter quarks) [172].

The `SV1` tagger is an algorithm based on the properties of secondary vertices [172]. Due to the relatively high mass of the b-quark the properties of the secondary vertex, point of the decay of the B-hadron, and its distance to the primary vertex are distinguishable from decays of hadrons containing c quarks or lighter quarks. The secondary vertex is reconstructed by an algorithm starting from vertices consisting of pairs of two tracks belonging to the considered jet and with sufficient distance to the primary vertex. Vertices consistent with decays of other long-lived particles or with material interactions are discarded. The two-track-vertices are then combined into the secondary vertex. The `SV1` tagger uses the invariant mass of all tracks belonging to the secondary vertex and the ratio of the sum of the energies of the tracks belonging to the vertex and to the jet as well as the number of two-track vertices in a likelihood-ratio technique. The distance ΔR between the jet and the connecting line between primary and secondary vertex is equally used [172].

The `JetFitter` tagger uses the Kalman filter to identify a line connecting primary and secondary vertices and their position, also separating vertices from B or D-hadron decays [172]. Similar variables as for the `SV1` tagger and the flight length significance between the vertices are used to separate between b, c- and light jets. The `JetFitter` tagger is combined with `IP3D` tagger in a neural network [172].

The efficiency to tag b-jets, but also c-jets or light jets was evaluated in [173, 174, 175, 176]. The tagging efficiency on b-jets is measured in $t\bar{t}$ events with decay to final states containing a

Cut	Value/description		
Jet Type	no	b-jet	(overlap removal)
	Preselected jet		
Algorithm	Anti-k_t, $R = 0.4$, topological clusters		
Acceptance	$p_\mathrm{T} > 20$ GeV		
	$|\eta| < 2.5$		No limit on $|\eta|$
Overlap	$\Delta R(\mathrm{jet}, e) > 0.2$		
Quality	reject events with `very loose` bad jets		
	Signal jet		
	Preselected jet +		
Acceptance	$p_\mathrm{T} > 30$ or 40 GeV		–
	$|\eta| < 2.5$		–
Other	–	`MV1`>0.980	–

Table 4.3: Summary of the jet and b-jet selection criteria.

single lepton or two leptons [174]. The efficiency to mistakenly tag a c-jet as b-jet is evaluated in D^{*+} mesons [176]. Mistag rates for light jets are measured in inclusive jet samples [176].

The tagging efficiencies in data and Monte Carlo samples are different. Therefore, this work uses scale factors to correct the Monte Carlo simulation for the differences, which have been evaluated in the studies named above. Uncertainties on the scale factors were also derived. The systematic uncertainty on the b-tagging efficiency is the largest b-tagging related uncertainty for the analyses presented here with an average value of 15%. The uncertainties on the efficiencies on the tagging of c-jets is smaller and on the tagging of light jets almost negligible.

Jets in this work: The analyses in this work use jets reconstructed with the anti-k_t algorithm and a distance parameter of 0.4. Their reconstruction is based on topological cluster calibrated according to the LCW calibration and with their energy corrected to the jet energy scale. Only jets with a minimal transverse momentum of $p_\mathrm{T} > 20$ GeV are considered. Generally, jets need to be within $|\eta| \leq 2.5$. Since both the jet and the electron reconstruction are based on energy deposits in the calorimeters, an electron will also always be reconstructed as jet. An overlap removal between jets and electrons is thus executed, involving all jets within $|\eta| = 4.9$, in which jets closer than $\Delta R = 0.2$ to an electron are dismissed. Events containing `very loose` bad jets are rejected. Those jets do not originate from the hard scattering process, but can arise from calorimeter noise, cosmic muons in time with collisions, the beam halo (due to interactions in the tertiary collimators in the beam-line outside the ATLAS detector) and from beam-gas events (where a proton from the beam collided with gas around the beam pipe) [163]. Further sources are non-collision backgrounds causing sporadic noise bursts in the hadronic end-cap calorimeter or coherent noise in the electromagnetic calorimeters [163]. Different variables related to the deposited energy fractions in different parts of the calorimeters, to the time assigned to the jet, to its charge and its quality are used in the definition of `very loose` bad jets (these variables are described in detail in [163]).

Signal jets used in the definition of the selection cuts of the analyses described here correspond to the preselected jets with tighter criteria on the transverse momentum. The analysis in the first part of the work uses signal jets with $p_\mathrm{T} > 40$ GeV, the analysis in the second part $p_\mathrm{T} > 30$ GeV. Based on the signal jet selection, b-jets are defined by requiring the `MV1` tagger resulting in a value of at least 0.980, corresponding to a b-tagging efficiency of 60% and a purity of 95%.

4.4 Missing Transverse Energy

Some particles as neutrinos or the LSP cannot be recorded by the ATLAS detector as they are only weakly interacting. This can result in a significant energy imbalance in the transverse plane of the detector, resulting in missing transverse energy (E_T^{miss}). Due to momentum conservation, the p_T sum of all recorded and missed particles must add to zero:

$$\sum \vec{p}_T^{\,\text{reconstructed particle}} + \vec{p}_T^{\,\text{miss}} = 0$$
$$\vec{p}_T^{\,\text{miss}} = -\sum \vec{p}_T^{\,\text{reconstructed particle}} \tag{4.4.3}$$

where one combined momentum vector has been used for the missed particles in the transverse plane. Neglecting masses, the missing transverse energy is defined as:

$$E_T^{miss} := |\vec{p}_T^{\,\text{miss}}| = |-\sum \vec{p}_T^{\,\text{reconstructed particle}}| \tag{4.4.4}$$

Weakly interacting particles give rise to *true* E_T^{miss}. *Fake* E_T^{miss} can arise from mis-measured jets, pile-up or noise in the calorimeters and from dead or noisy read-out channels. Any particles missed due to dead detector regions, the limited coverage of the detectors or inactive regions between the subdetectors can equally fake a missing transverse energy.

Reconstruction Different reconstruction algorithm were used for the reconstruction of the E_T^{miss}. Only the algorithm important for the offline reconstruction will be discussed here, but a more detailed discussion about E_T^{miss} algorithms as employed by the triggers is given in the description of the triggers used in this work in Chapter 9.

As all visible particles need to be included in the calculation, all detector components are relevant. The E_T^{miss} reconstruction [177, 169] takes fully calibrated physics objects as input in the following order: electrons, photons, taus, jets, muons. A de-composition of the objects into constituent topological clusters is required to not double-count topological clusters contributing to different objects. Energy losses in the calorimeter for combined muons are subtracted, also to avoid double-counting. In addition, a soft term is added to the calculation, adding all soft energetic energy deposits as topological clusters and tracks not assigned to any reconstructed physics object. A certain minimal energy threshold is required in order to not include noise in the calculation. An overlap between topological clusters and tracks is removed.

Components of the E_T^{miss} along x and y directions are calculated separately:

$$E_{x(y)} = E_{x(y)}^{miss,e} + E_{x(y)}^{miss,\gamma} + E_{x(y)}^{miss,\tau} + E_{x(y)}^{miss,jets} + E_{x(y)}^{miss,\text{Soft Term}} + E_{x(y)}^{miss,\mu} \tag{4.4.5}$$

where each term is the negative sum of the reconstructed objects. The missing transverse energy is the absolute value:

$$E_T^{miss} = \sqrt{(E_x^{miss})^2 + (E_y^{miss})^2} \tag{4.4.6}$$

The missing transverse energy can be very sensitive to pile-up, as all the remaining energy deposits in the calorimeter are included in the soft term. Various methods exist to correct the E_T^{miss} calculation for contributions by pile-up. No correction is used for the E_T^{miss} definition used in this work, because the E_T^{miss} has not been seen to be very pile-up sensitive in the context of SUSY analyses, due to the only small contribution of the soft term to the full E_T^{miss} [177].

E_T^{miss} **related systematics** Systematic uncertainties on the E_T^{miss} arise from all uncertainties on the contributing objects, which need to be propagated, and from uncertainties on the soft term [178, 177]. The latter arises mainly from pile-up and the modelling in Monte Carlo simulations. They are evaluated in $Z \to ll$ events without additional jets by a comparison between data and Monte Carlo simulation [177]. The scale of the soft term is taken from the data to Monte Carlo ratio, the resolution evaluated on the $E_{x(y)}^{\mathrm{miss}}$ terms.

Analysis specific E_T^{miss} calculation The E_T^{miss} calculation for this work was adapted to the objects as used within the analyses and defined in the previous sections. In particular, the objects included fulfil the following requirements:

- jets: based on LCW topological clusters with jet energy scale calibration for jets with $p_T > 20$ GeV and without jet energy scale calibration for $10 < p_T < 20$ GeV,

- preselected electrons,

- preselected muons,

- the contributions of the soft terms are included with the LCW calibration,

- taus are not directly included in the calculation, but they are included in the jet component,

- photons are included if they have a minimum transverse momentum of 10 GeV.

Chapter 5

The 1-lepton analysis

5.1 Motivation of the 1-lepton channel

The strong production of gluinos and squarks and their following decays result in final states with multiple jets and missing transverse energy, $E_{\mathrm{T}}^{\mathrm{miss}}$, due to LSPs escaping the detector. The final states may or may not contain leptons. Final states without any leptons have the highest cross sections due to QCD couplings, but are largely dominated by QCD multi-jet background production. Requiring at least one isolated lepton in the final state helps suppressing this background. In addition, the requirement of an isolated lepton allows the use of lepton specific kinematic variables. In particular, the transverse mass

$$m_{\mathrm{T}} \;=\; \sqrt{2 \;\cdot\; E_{\mathrm{T}}^{\mathrm{miss}} \cdot p_{\mathrm{T}}(\mathrm{lepton}) \cdot \; (1 - \cos \Delta\phi(\vec{E}_{\mathrm{T}}^{\mathrm{miss}}, \vec{p}_{\mathrm{T}}(\mathrm{lepton})))} \qquad (5.1.1)$$

allows to suppress the $W+$jets background effectively, as discussed below. The lepton requirement is also beneficial for triggering the interesting events, because triggers with lepton requirements can be used. These triggers can apply weaker criteria on quantities of other objects as for example the jet momenta or $E_{\mathrm{T}}^{\mathrm{miss}}$. This allows the analyses here to use less stringent cuts on these variables, which is beneficial for the background estimation as shown in Section 8.1. However, the trigger requires a minimal cut of 25 GeV on the lepton transverse momentum. Supersymmetric signals with small mass differences between the gluino/squark and the LSP may result in less energetic leptons. Dedicated analyses (requiring a 'soft' lepton) have been designed for such situations [131, 179]. This work will focus on final states with a 'hard' lepton, so with $p_{\mathrm{T}}(\mathrm{lepton}) > 25$ GeV. A comparison and a combination of the analyses presented in this work and analyses requiring at least one soft lepton will be presented in Section 16.2.

Furthermore, a veto on any further lepton is imposed. Dedicated analyses exist for final states with two and more leptons [131, 180]. Separating final states with one or two (and more) leptons simplifies the background estimation techniques as will be shown in Section 8.2.

The selected lepton is required to be an electron or a muon (thus the name 'lepton' always refers to electrons and muons in the following). Analyses considering final states with taus are discussed elsewhere [181].

5.2   Standard Model backgrounds in the 1-lepton channel

Final states containing a lepton, multiple jets and $E_\mathrm{T}^\mathrm{miss}$ can also be realised by Standard Model processes. Neutrinos or mis-measured jets can result in $E_\mathrm{T}^\mathrm{miss}$. Multiple jets are produced by initial or final state radiation or in $t\bar{t}$ pair decays. Other Standard Model backgrounds, as the Z+jets background, have two isolated leptons in the final state, but the second lepton could be missed. Possible reasons for this are that the second lepton is outside the geometrical acceptance, that it does not pass the kinematic requirements or the quality requirements as defined in Chapter 4.

$t\bar{t}$ **background:**   The decay of $t\bar{t}$ events is the dominant background in the 1-lepton analysis as it results in similar final states as the supersymmetric signal. A diagram of a possible decay is shown in Figure 5.1. Both top and anti-top quark decay to a W-boson and a b-jet. Final states with an isolated lepton are obtained if one of the W bosons decays to a lepton and a neutrino and the other to quarks. In this case, the final state will contain at least four jets (not including jets from initial or final-state radiation), an isolated lepton and $E_\mathrm{T}^\mathrm{miss}$ from the decay of one W boson. Also $t\bar{t}$ events with decays to final states with two leptons (each of the W-bosons decays to a lepton and a neutrino) can contribute to the background, if one lepton is not identified.
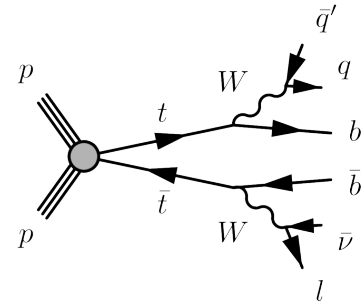
Figure 5.1:   Diagram for an example $t\bar{t}$ decay.

W+**jets background:**   The decay of a W-boson produced in association with jets may result in final states with one isolated lepton and a neutrino. The signature is therefore similar to the signal. This background is the second most important background to the analyses in this work.

QCD background: QCD multi-jet events are strongly suppressed by the requirement of an isolated lepton and also by the large $E_\mathrm{T}^\mathrm{miss}$ criterion in the signal regions. Nevertheless, QCD multi-jet background events can enter the signal regions if one of the jets has been misidentified as lepton or - more often - if one lepton was created in the decay of a heavy quark, most often a b-quark.

Smaller backgrounds: Smaller backgrounds in the signal regions are:

- Z+jets production with decay to two leptons, where one has not been identified or selected.

- Single top production with a similar topology as $t\bar{t}$ events decaying into final states with one lepton, but with smaller cross sections.

- $t\bar{t}$ + vector boson production also with a similar topology as $t\bar{t}$ events but with smaller cross sections.

- Diboson production, where the bosons may be either a W or Z-boson. The cross section of this process is also low and its topology is close to the W+jets or Z+jets backgrounds.

The magnitudes of the background processes with respect to the signal are illustrated in Sections 7.2.1 and 10.3.4 for the $5.8\,\mathrm{fb}^{-1}$ analysis and in Section 15 for the $20.3\,\mathrm{fb}^{-1}$ analysis.

5.3 Discriminating variables

Different variables are used in this work to discriminate background from signal:

- **Jet multiplicity, N_{jet}:**

  As discussed in Section 2.4.3, the final states considered in this work contain between four (for initial squark pair production) and six jets (for initial gluino pair production) plus additional jets from initial or final state radiation. The signal may thus be separated from some backgrounds (as for example the W+jets, but not the $t\bar{t}$ background) by requiring multiple jets.

- **Missing transverse energy, E_T^{miss}:**

  A signal event is expected to show a larger missing transverse energy, E_T^{miss}, than background events due to the LSPs escaping the detector. The QCD multi-jet background is also expected to show lower E_T^{miss} values and can be suppressed by a cut on this variable.

- **Transverse mass, m_T:**

  The transverse mass, m_T, was first used in the search for W-bosons [182, 183]. If the E_T^{miss} in the event was to come only from the neutrino in the W decay, the m_T distribution would show a clear end-point at the W mass for the W+jets background, but in SUSY events this distribution is smeared out due to the existence of the LSPs. As will be shown in Section 12, some SUSY models tend to show high m_T values, considerably larger than the background, which is helpful in suppressing the background further.

- **Inclusive effective mass, m_{eff}^{incl}:**

  Considering the topology of a signal event, the inclusive effective mass, $m_{eff}^{incl} = \sum p_T^{jet} + p_T^{lepton} + E_T^{miss}$, collects the transverse momenta or energies of all particles showing up in the final state of a supersymmetric decay chain. All jets in the event with a transverse momentum exceeding a certain threshold (40 GeV for the $5.8\,\text{fb}^{-1}$ analysis and 30 GeV for the $20.3\,\text{fb}^{-1}$ analysis) are included in this sum. This variable is thus connected to the mass scale of the initially pair-produced particles.

- **Truncated effective mass, m_{eff}^{excl}:**

  The truncated effective mass, $m_{eff}^{excl} = \sum_{n\ jets} p_T^{jet} + p_T^{lepton} + E_T^{miss}$, differs from the inclusive effective mass by only considering the n jets with highest p_T in the event which are also used in the definition of the signal regions, see Section 7.2.2 and Chapter 12. As discriminating variable, the ratio $E_T^{miss}/m_{eff}^{excl}$ is used. This variable indicates fluctuations in E_T^{miss} as function of the activity in the calorimeter [131]. A cut on this variable is thus useful to reject events with mis-measured jets. It was also used in previous analyses due to the observation that the signal tends to show higher $E_T^{miss}/m_{eff}^{excl}$ values [3, 184].

The cut values in these variables are given for the $5.8\,\text{fb}^{-1}$ analysis in Chapter 7 and for the $20.3\,\text{fb}^{-1}$ analysis in Chapter 12.

Part III

The 5.8 fb^{-1} analysis

Chapter 6

Overview

This part presents the analysis of the first $5.8\,\mathrm{fb}^{-1}$ of the 2012 data, taken between April 5th and June 18th 2012. The results of this analysis were made public in [185].

A typical analysis searching for supersymmetric particles with (semi-)data-driven background estimation techniques uses control, validation and signal regions as explained in the following. A signal region (SR) is defined by all criteria applied to enhance the signal fraction while rejecting background events. The signal regions of this analysis are described in Chapter 7. They use the discriminating variables defined in Chapter 5. Among these variables are the inclusive effective mass ($m_{\mathrm{eff}}^{\mathrm{incl}}$) and the missing transverse energy ($E_{\mathrm{T}}^{\mathrm{miss}}$) which are particularly useful in suppressing the background and in enhancing the signal as demonstrated in Chapter 7. The location of the signal regions at higher values of $m_{\mathrm{eff}}^{\mathrm{incl}}$ and $E_{\mathrm{T}}^{\mathrm{miss}}$ and with respect to the control and validation regions is indicated in Figure 6.1.

The dominant backgrounds in the signal regions are $t\bar{t}$ and W+jets production which are estimated by a semi-data-driven method. The method uses control regions (CRs) with relaxed selection criteria (on $m_{\mathrm{eff}}^{\mathrm{incl}}$ and $E_{\mathrm{T}}^{\mathrm{miss}}$ in this analysis) in comparison to the signal regions as schematically shown in Figure 6.1. The background to be estimated is enhanced in the control regions while no signal is present. The Monte Carlo prediction for the background, in this case for the $t\bar{t}$ and W+jets backgrounds, is scaled to the recorded data in the defined control regions. The background estimates in the signal regions are obtained by extrapolating from the control to the signal regions based on Monte Carlo information. This extrapolation is cross-checked in validation regions (VRs) which use selection criteria between those of the control and signal regions (for example at lower values of $E_{\mathrm{T}}^{\mathrm{miss}}$). The validation regions are chosen such that the signal contamination is small in them, while the properties of the backgrounds should be similar in the validation and signal regions.

This background estimation method is detailed in Section 8.1 which also defines the control and validation regions used. The Monte Carlo samples used are described in Section 7.1. The normalisation of the Monte Carlo samples to data is performed via a simultaneous fit in the control regions by using a profile-log-likelihood method. This procedure is detailed in Chapter 10.

The QCD multi-jet background is a very small background in the signal regions but cannot be estimated by using Monte Carlo simulation due to the difficulty to simulate this background accurately enough and in sufficient statistics for the phase space interesting for this analysis. Instead, the background is estimated by using a entirely data-driven matrix method, as explained in Section 8.2.

As the QCD multi-jet background estimation uses control regions with relaxed isolation criteria for the selected lepton, dedicated triggers needed to be defined and were implemented for this
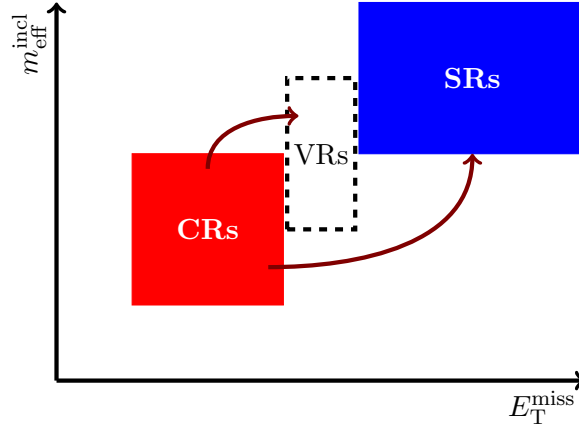
Figure 6.1: Schematic sketch of the control (CRs, in red), validation (VRs, in black dashed) and signal regions (SRs, in blue) in the $E_\mathrm{T}^\mathrm{miss}$-$m_\mathrm{eff}^\mathrm{incl}$ plane. Control regions are used in the (semi-)data-driven background estimation techniques. The background estimates in the signal regions are obtained by extrapolation from the control regions. The extrapolation is indicated by dark red arrows. The extrapolation is cross-checked in validation regions located between the control and signal regions.

analysis. Proposals for such triggers are presented in Section 9 along with performance of the finally implemented triggers. The section concludes with an overview about the triggers used in this analysis.

The final results of this analysis in terms of yields in the signal regions and of an interpretation in the MSUGRA/CMSSM model are calculated by using the tool *HistFitter* [186] as described in Section 10.2. This tool allows the simultaneous fitting of different regions to obtain limits on the presence of new physics. In this analysis, the signal regions are divided into four subregions along the $m_\mathrm{eff}^\mathrm{incl}$ distribution to enhance the sensitivity to the studied models. This procedure is further explained in Section 10.4.4.

The final results are detailed in Sections 10.3.4 and 10.4.4.

Chapter 7

Selection criteria and signal regions

This chapter presents the definition of the signal regions for the $5.8\,\text{fb}^{-1}$ analysis. The signal regions were first proposed in context of the 7 TeV analysis in [15, 131] which used two different sets of signal regions, one set requiring three jets, the other one at least four jets. The latter set of signal regions was shown to provide sensitivity to the area in the MSUGRA/CMSSM grid with large m_0 values and to provide access to a larger part of the grid than the other set of signal regions. Therefore, it was chosen as basis for the $5.8\,\text{fb}^{-1}$ analysis, which aimed to analyse the first 8 TeV data quickly. A thorough re-optimisation of the signal regions was postponed to a later time and is presented in Chapter 12.

This chapter first gives an overview about the Monte Carlo samples used in the $5.8\,\text{fb}^{-1}$ analysis, as the definition of the signal regions below will be motivated by background distributions taken from Monte Carlo.

7.1 Monte Carlo samples

Monte Carlo samples are essential in the background estimation methods detailed in Chapter 8. The Monte Carlo generators used in this analysis along with the cross section for each process are detailed in Table 7.1. This table also shows at which order the cross sections were calculated.

The $t\bar{t}$ background is simulated by using the `MC@NLO` generator. The `AlpGEN` generator is used for the W+jets and Z+jets backgrounds. For the `MC@NLO` and `AlpGEN` samples, the parton showers and fragmentation processes are simulated with `HERWIG` with `JIMMY` [145] for the underlying event. The `AcerMC` and the `MC@NLO` generators are used in the simulation of the single t events. Diboson events are generated by the `HERWIG` generator. The PDFs `CTEQ6L1` [187] or `CT10` [188] are used for `AlpGEN` and `HERWIG` or `MC@NLO` samples. For every Monte Carlo sample the ATLAS underlying event tune `AUET2` [189] is used.

The theoretical cross section for the W+jets or Z+jets samples are calculated with `DYNNLO` [190] and the PDF set `MSTW2008NNLO` [191], for the diboson samples with `MCFM` [192] and the PDF set `MSTW2008NLO` and for $t\bar{t}$ with `HATHOR` [193] and the PDF set `MSTW2008NNLO`.

Physics process	Generator	Cross section (nb)	Calculation	
$t\bar{t}$	MC@NLO 4.06 [148]	0.238	NLO+NLL	[193]
$W(\to \ell\nu)$ + jets	ALPGEN 2.14 [147]	12.19	NNLO	[194]
$Z/\gamma^*(\to \ell\ell)$ + jets	ALPGEN 2.14 [147]	1.15	NNLO	[194]
Single-top (t-chan)	AcerMC [146]	0.0095	NLO	[195]
Single-top (s-chan)	MC@NLO 4.06 [148]	0.0006	NLO	[196]
Single-top (Wt-chan)	MC@NLO 4.06 [148]	0.0224	NLO	[197]
WW	HERWIG 6.5.20 [144]	0.0547	NLO	[192]
WZ ($66 < M_Z < 116$ GeV)	HERWIG 6.5.20 [144]	0.0333	NLO	[192]
ZZ ($M_Z > 60$ GeV)	HERWIG 6.5.20 [144]	0.0112	NLO	[192]

Table 7.1: The Monte Carlo samples with their generators and cross sections as used in this analysis [185].

7.2 The selection cuts

7.2.1 Preselection cuts

In order to reject non-collision backgrounds, poorly reconstructed jets or data taken during phases where not all detector components were available, a set of preselection cuts was applied:

- Only data being certified as good for physics analyses was considered. When any component of the detector was not available for a certain data-taking period or had other technical problems, the data concerned is rejected.

- Only events passing an electron+E_T^{miss} or muon+jet+E_T^{miss} trigger are accepted. The trigger requirements are discussed in Chapter 9. Due to the triggers, only events with $E_T^{miss} > 100$ GeV and $p_T > 80$ GeV for the jet with the highest transverse momentum are accepted. The triggers are not efficient for events not fulfilling these conditions.

- Any event is required to have a primary vertex consistent with the beamspot envelope and with five tracks associated.

- Events containing jets due to detector noise, cosmic rays or in general originating from non-collision background are rejected.

- Events with cosmic muons are rejected.

7.2.2 Definition of the signal regions

The definition of the signal regions uses the discriminating variables defined in Chapter 5.

Lepton criteria: The one lepton selection requires either a tight electron or a tight muon as defined in Sections 4.1 and 4.2 with $p_T > 25$ GeV. As different isolation and trigger criteria are used for electrons and muons, this analysis separates those events into an *electron* and a *muon channel*. Events with a second loose electron or muon with $p_T > 10$ GeV are vetoed.

Criterion on the jet multiplicity, N_{jet}: The decay of pair-produced squarks and gluinos results in at least four to six jets (as discussed in the Section 2.4.3). Therefore, any accepted event is required to contain at least four jets with $p_T > 80$ GeV each. The signal regions presented

	Signal regions
N_{lep}	1 (electron or muon)
p_{T}^{ℓ} (GeV)	> 25
$p_{\mathrm{T}}^{\ell_2}$ (GeV)	< 10
N_{jet}	≥ 4
$p_{\mathrm{T}}^{\mathrm{jet}}$ (GeV)	$> 80, 80, 80, 80$
$E_{\mathrm{T}}^{\mathrm{miss}}$ (GeV)	> 250
m_{T} (GeV)	> 100
$E_{\mathrm{T}}^{\mathrm{miss}}/m_{\mathrm{eff}}^{\mathrm{excl}}$	> 0.2
$m_{\mathrm{eff}}^{\mathrm{inc}}$ (GeV)	> 800

Table 7.2: The definition of the two signal regions for the $5.8\,\mathrm{fb}^{-1}$ analysis [185]. The same selection criteria are applied for both signal regions, except of the lepton criteria: One signal region selects events with a tight electron, the other signal region events with a tight muon. The $5.8\,\mathrm{fb}^{-1}$ analysis is thus divided into an electron and a muon channel.
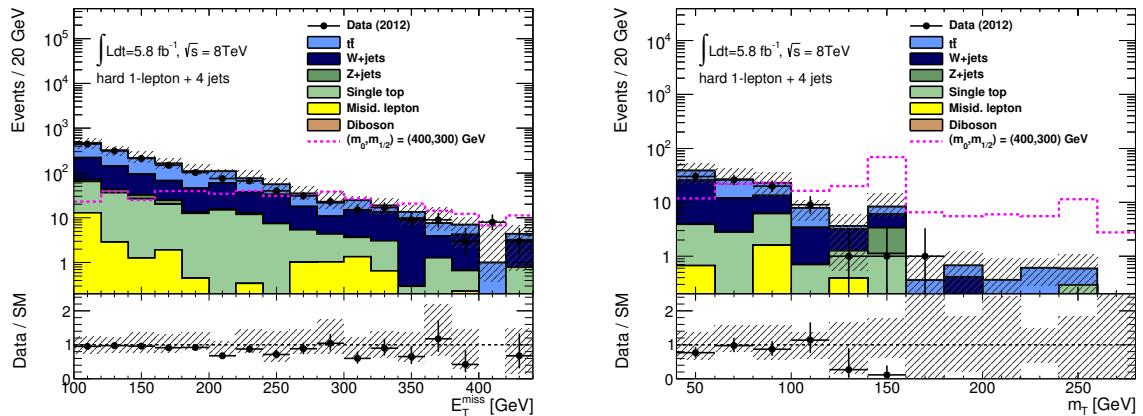
Figure 7.1: The $E_{\mathrm{T}}^{\mathrm{miss}}$ distribution (left plot) is shown after requiring the event to contain four jets with $p_{\mathrm{T}} > 80$ GeV and one electron or muon and $E_{\mathrm{T}}^{\mathrm{miss}} > 100$ GeV. A cut on $E_{\mathrm{T}}^{\mathrm{miss}} > 250$ GeV is used. The right plot shows the m_{T} distribution after this cut. A cut on $m_{\mathrm{T}} > 100$ GeV is very effective in suppressing the Standard Model background. A MSUGRA/CMSSM signal point with coordinates $(m_0, m_{1/2}) = (400, 300)$ GeV is overlaid. The events in the electron and muon channels were combined for these plots.

here were originally optimised for large m_0 values in the MSUGRA/CMSSM grid [15, 131], where longer decay chains and gluino pair production dominate. The signal regions were shown to have less sensitivity at lower m_0 values in the MSUGRA/CMSSM grid [198] where squark pair production dominates. The reason for this is that signal regions requiring four jets might be too tight for squark pair production if some of the jets in the cascade decay of the squarks are too low energetic or missed by other reasons.

Criterion on the missing transverse energy, $E_{\mathrm{T}}^{\mathrm{miss}}$: The $E_{\mathrm{T}}^{\mathrm{miss}}$ distribution in events containing an isolated electron or muon after the jet requirements is shown in Figure 7.1. A cut of $E_{\mathrm{T}}^{\mathrm{miss}} > 250$ GeV is placed.

Criterion on the transverse mass, m_{T}: The m_{T} distribution is shown in Figure 7.1 in events with an isolated electron or muon after the cut on $E_{\mathrm{T}}^{\mathrm{miss}}$. A cut of $m_{\mathrm{T}} > 100$ GeV is placed in order to reject W+jets background.
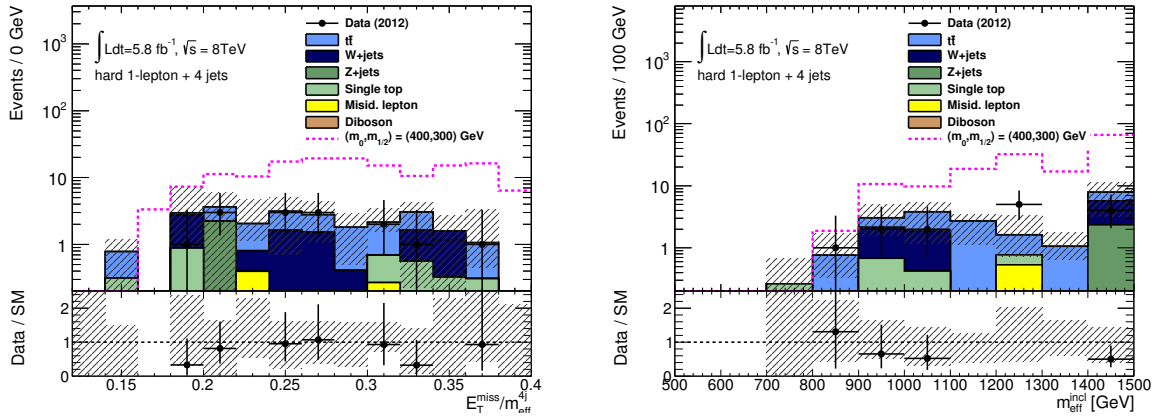
Figure 7.2: The $E_T^{miss}/m_{eff}^{excl}$ distribution is shown after the cut on m_T (left plot) in events containing either an electron or a muon. A cut of $E_T^{miss}/m_{eff}^{excl} > 0.2$ is applied to increase the signal fraction. The m_{eff}^{incl} distribution is shown after this cut (right plot). Cutting on $m_{eff}^{incl} > 800$ GeV defines the signal regions. A MSUGRA/CMSSM signal point with coordinates $(m_0, m_{1/2}) = (400, 300)$ GeV is overlaid. The events in the electron and muon channels were combined for these plots.

Criterion	$t\bar{t}$	W+jets	Single top	Diboson	Z+jets	QCD multi-jet	Signal
On N_{jet}	880.6	546.5	193.5	0.6	27.0	22.6	501.4
On E_T^{miss}	72.8	72.2	22.5	0.3	2.2	3.1	247.4
On m_T	10.8	8.1	3.2	0.1	2.2	0.3	167.4
On $E_T^{miss}/m_{eff}^{excl}$	10.2	6.2	2.0	0.1	2.2	0.4	156.7
Signal regions (SRs)	10.3	6.2	1.7	0.1	2.2	0.4	156.7
SRs + $m_{eff}^{incl} > 1000$ GeV	8.8	4.7	0.9	0.0	2.2	0.4	144.1

Table 7.3: The event yield after different selection criteria for the backgrounds and an example signal point with coordinates $(m_0, m_{1/2}) = (400, 300)$ GeV. Apart from the selection criteria used in the definition of the signal regions, also the yields in one subset of the signal regions is reported. This region is defined by a tighter criterion on m_{eff}^{incl}. The numbers in this table are given without dividing the specific regions into an electron or a muon channel.

Criterion on the ratio of the missing transverse energy and the truncated effective mass, $E_T^{miss}/m_{eff}^{excl}$: A cut on $E_T^{miss}/m_{eff}^{excl} > 0.2$ with the truncated effective mass $m_{eff}^{excl} = \sum_{4\ jets} p_T^{jet} + p_T^{lepton} + E_T^{miss}$ (considering the four jets with highest p_T in the event) is placed. This cut rejects only little background, as visualised in Figure 7.2. A re-optimisation of this cut will be presented in Section 12.

Criterion on the inclusive effective mass, m_{eff}^{incl}: The final cut defining the signal regions (SRs) is placed on $m_{eff}^{incl} > 800$ GeV. Due to the previous cuts on the transverse momenta of jets and on E_T^{miss} any event will show at least $m_{eff}^{incl} \gtrsim 600$ GeV. Figure 7.2 suggests even higher cuts in m_{eff}^{incl} in order to enhance the signal versus the background. Therefore, the cut on $m_{eff}^{incl} > 800$ GeV is to be considered as minimal cut on this variable and will be tightened in the further course of this analysis (see Section 10.1).

The event yield for the different background processes and for a MSUGRA/CMSSM model with parameters $(m_0, m_{1/2}) = (400, 300)$ GeV is summarised in Table 7.3. In the signal regions, the $t\bar{t}$ background is largest and the W+jets background the next important component. Other backgrounds are small. The signal to background ratio is 7 for the particular signal chosen. This ratio can be increased by applying tighter criteria on m_{eff}^{incl}.

Chapter 8

Background estimation techniques

Most background estimation techniques are based on information from Monte Carlo simulation. Smaller backgrounds such as single top and diboson production are entirely taken from Monte Carlo simulation. The background estimation techniques for the $t\bar{t}$, W+jets, Z+jets and QCD multi-jet backgrounds are semi-data-driven or entirely data-driven and are described in the following.

8.1 $t\bar{t}$ and W+jets background

This background estimation is semi-data-driven as it uses shape information from simulation (in the extrapolation from the control to the signal regions) but the normalisation from data.

Four control regions being dominated by $t\bar{t}$ or W+jets events are defined close to the signal regions in the electron and muon channels. Their criteria are detailed in Table 8.1. The requirement on the jet multiplicity (N_{jet}), the transverse momenta of the jets ($p_{\text{T}}^{\text{jet}}$) and the transverse mass (m_{T}) are identical in the signal and control regions. In contrast, the cut on inclusive effective mass, $m_{\text{eff}}^{\text{incl}} > 500$ GeV, is lower in the control regions in comparison to the signal regions. Additionally, an upper cut on $m_{\text{eff}}^{\text{incl}} < 1300$ GeV is introduced. Requiring lower values in $m_{\text{eff}}^{\text{incl}}$ in the control regions than in the signal regions helps to increase the background to be estimated. The control regions are fully orthogonal to the signal regions by requiring $100 < E_{\text{T}}^{\text{miss}} < 180$ GeV. The lower cut at $E_{\text{T}}^{\text{miss}} = 100$ GeV is due to the trigger requirements as explained in Chapter 9. The upper cut reduces the signal contribution in the control regions significantly. Two control regions enriched in $t\bar{t}$ events can be defined in the electron and in the muon channel, respectively, by requiring that at the least one jet among the four jets with the highest p_{T} has been b-tagged (Top control regions, TR). Correspondingly, two control regions dominated by W+jets events can be defined by requiring that none of the leading four jets has been b-tagged (W+jets control regions, WR). The $m_{\text{eff}}^{\text{incl}}$ distribution in these control regions is shown in Figure 8.1.

To obtain the $t\bar{t}$ and W+jets background estimates ($N_{\text{pred}_j}^{\text{SR}_k}$ with j indicating the background) in the signal region k (SR$_k$), the $t\bar{t}$ and W+jets Monte Carlo prediction (MC^j) is normalised to data simultaneously in all control regions i (CR$_i$). Other background yields in the control regions as for example the QCD multi-jet background are subtracted from the data before the normalisation. Technically this is done by using the profile log-likelihood method described in Chapter 10. This normalisation factor is then applied to the Monte Carlo prediction in the

	W+jets control region	Top control region
N_lep	1	1
$p_T^{\ell_1}$ (GeV)	> 25	> 25
$p_T^{\ell_2}$ (GeV)	< 10	< 10
N_jet	≥ 4	≥ 4
p_T^jet (GeV)	$> 80, 80, 80, 80$	$> 80, 80, 80, 80$
$N_{b-\text{tag}}$	0	≥ 1
E_T^miss (GeV)	$\in[100, 180]$	$\in[100, 180]$
m_T (GeV)	>100	>100
m_eff^inc (GeV)	$\in[500,1300]$	$\in[500,1300]$

Table 8.1: Definitions of the W+jets and $t\bar{t}$ control regions [185]. The criteria on E_T^miss and on m_eff are relaxed with respect to the signal regions defined in Table 7.2 and the presence of b-jets is required for the Top control region, whereas events without a b-tagged jet among the leading three jets are selected for the W-jets control region. Each of these control regions is defined in the electron and in the muon channel separately.

signal region:

$$N_{\text{pred}_j}^{\text{SR}_k} = \frac{(N_\text{data}^{\text{CR}_i} - N_\text{other\ backgrounds}^{\text{CR}_i})}{N_\text{prediction}(\text{MC}^j, \text{CR}_i)} \times N_\text{prediction}(\text{MC}^j, \text{SR}_k) \qquad (8.1.1)$$

Equation 8.1.1 can be reformulated to:

$$N_{\text{pred}_j}^{\text{SR}_k} = (N_\text{data}^{\text{CR}_i} - N_\text{other\ backgrounds}^{\text{CR}_i}) \times C_{\text{CR}_i \to \text{SR}_k}^{j} \qquad (8.1.2)$$

where $C_{\text{CR}_i \to \text{SR}_k}^{j} = \frac{N_\text{prediction}(\text{MC}^j, \text{SR}_k)}{N_\text{prediction}(\text{MC}^j, \text{CR}_i)}$ gives the transfer factor between control region i and signal region k for background j, which is entirely Monte Carlo based. In the case of Equation 8.1.2, the background in the signal regions is estimated by measuring the data yield in the control regions and by extrapolating it to the signal regions using transfer factors based on Monte Carlo. In contrast to the mathematically identical Equation 8.1.1, common systematic uncertainties on the Monte Carlo simulation in control and signal regions may cancel in the transfer factor $C_{\text{CR}_i \to \text{SR}_k}^{j}$, thus resulting in reduced uncertainties on the background estimate in the signal regions. Both approaches of Equation 8.1.1 and Equation 8.1.2 are used in this work, with the first being employed in the $5.8\,\text{fb}^{-1}$ analysis and the second being used in the $20.3\,\text{fb}^{-1}$ analysis.

The extrapolation into the signal regions is validated by evaluating the background estimates obtained from the method described in *validation regions* (VRs) located between the control and signal regions in E_T^miss: $180 < E_T^\text{miss} < 250$ GeV. The definition of the validation regions is summarised in Table 8.2. The same requirements as in the signal regions are used in m_eff^incl and in m_T. The validation regions thus show a similar event population as the signal regions, but with negligible signal contamination (as shown in [199]). The statistics in the validation regions is increased by requiring more moderate values of the transverse momenta of the third and fourth jet (jets are always ordered in decreasing transverse momenta).

The location of all regions in the m_eff^incl-E_T^miss plane of all regions is presented in Figure 8.2.
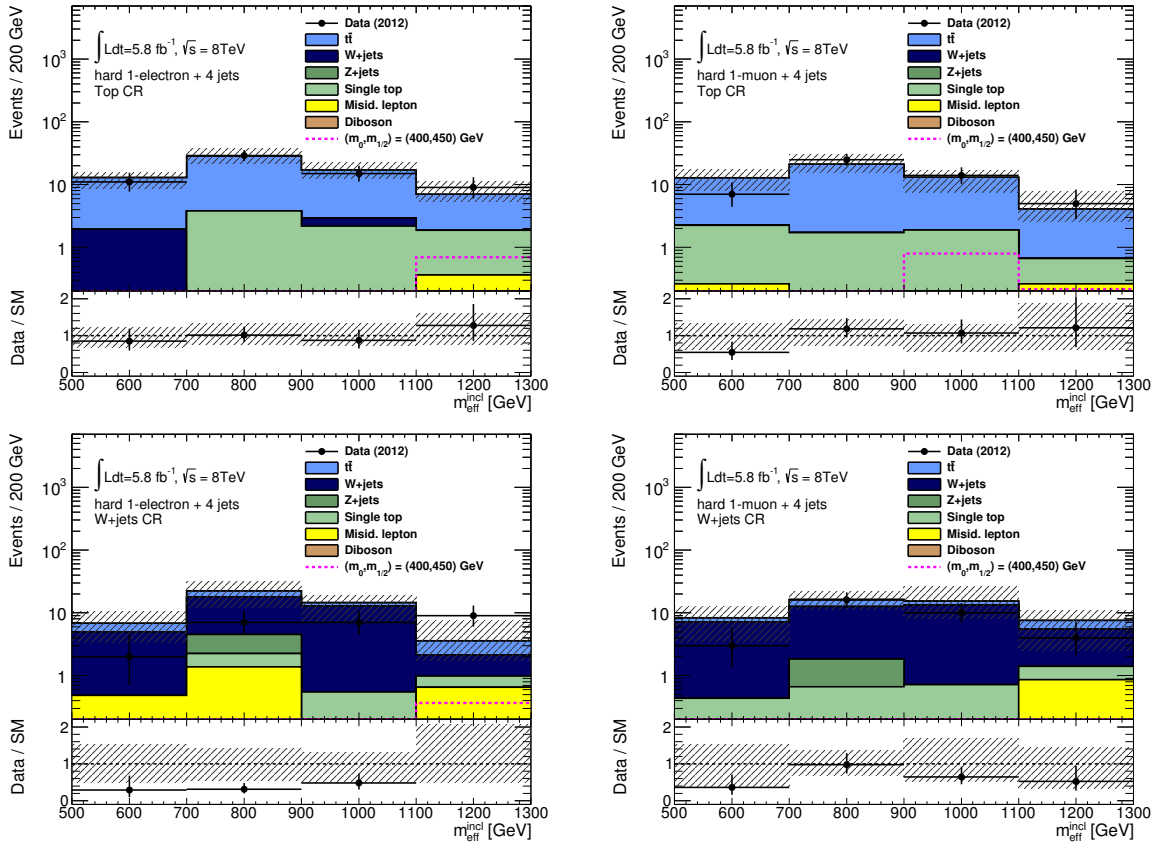
Figure 8.1: The $m_{\text{eff}}^{\text{incl}}$ distributions are shown in the Top control region in the electron channel (top left) and in the muon channel (top right) as well as in the W+jets control regions (electron channel: bottom left, muon channel: bottom right). A good agreement between data and Monte Carlo predictions is observed in the Top control regions, a poorer agreement is seen in the W+jets control regions, where the shape of the Monte Carlo prediction does not match the shape of the data distributions. The shape of the Monte Carlo prediction is corrected in the simultaneous fit described in Chapter 10 for the extrapolation into the signal regions. A MSUGRA/CMSSM signal point with coordinates $(m_0, m_{1/2}) = (400, 450)$ GeV is overlaid.

8.2 QCD multi-jet background estimation

The QCD multi-jet background is estimated by using an entirely data-driven method (referred to as matrix method in the following) instead of taking the Monte Carlo simulation, because the generators may introduce large systematic uncertainties when modelling the background in the regions interesting for this analysis. Furthermore, it is difficult to generate QCD multi-jet events in a sufficient statistics in these regions.

The QCD multi-jet background contribution in the signal regions is estimated by using *loose* control samples containing events with exactly one *loose* electron or muon as defined in Tables 4.1 and 4.2 with $p_{\text{T}} > 25$ GeV. Leptons in the loose control samples differ from *tight* leptons (corresponding to a signal electron or a signal muon as defined in Tables 4.1 and 4.2) as they are not required to satisfy the track isolation criteria $p_{\text{T}}^{\text{cone20}} < 1.8$ GeV in the muon channel and the relative track isolation criteria $p_{\text{T}}^{\text{cone20}}/p_{\text{T}} < 0.1$ in the electron channel. Loose electrons are also only required to be of `medium++` quality instead of `tight++` for tight electrons. All leptons in the loose control samples are still isolated from any close jet with $\Delta R(\text{lepton}, \text{jet}) > 0.4$. Loose leptons are thus less isolated than tight leptons. The loose control samples are therefore enhanced in QCD multi-jet events, in which the lepton originates from heavy flavour decays,

77

	Validation regions
N_{lep}	== 1 (electron or muon)
$p_T^{\ell_1}$ (GeV)	> 25
$p_T^{\ell_2}$ (GeV)	< 10
N_{jet}	≥ 4
p_T^{jet} (GeV)	> 80, 80, 40, 40
E_T^{miss} (GeV)	$\in[180, 250]$
m_T (GeV)	> 100
$m_{\text{eff}}^{\text{incl}}$ (GeV)	>800
$E_T^{\text{miss}}/m_{\text{eff}}^{\text{excl}}$ (GeV)	> 0.2

Table 8.2: The validation regions (VRs) are defined to contain events with similar properties as in the signal regions. This is achieved by applying the same criteria as in the definition of the signal regions (see Table 7.2), but by relaxing the requirements on E_T^{miss} and also on the third and fourth jets in the event. The validation regions are defined in the electron and muon channels.

jets faking a lepton or - in case of the electron channel - photon conversions.

8.2.1 The principle of the matrix method

The number of events after any cut described in Section 7.2.2 can be written as composition of QCD multi-jet events and any other background or signal event (labelled as 'non-QCD' in the following). For the loose and the tight regions (containing events with a loose or tight lepton)[1]:

$$N_{\text{loose}} = N_{\text{loose}}^{\text{QCD}} + N_{\text{loose}}^{\text{non-QCD}} \tag{8.2.3}$$
$$N_{\text{tight}} = N_{\text{tight}}^{\text{QCD}} + N_{\text{tight}}^{\text{non-QCD}} \tag{8.2.4}$$

Any tight region is a subset of the loose region with the same selection criteria (the only difference between loose and tight regions is the isolation criteria for the lepton). Thus, efficiencies can be defined as the probability that a lepton belonging to the loose sample also satisfies the tighter isolation criteria of the tight sample:

$$\epsilon_{\text{fake}} = \frac{N_{\text{tight}}^{\text{QCD}}}{N_{\text{loose}}^{\text{QCD}}}, \qquad \epsilon_{\text{real}} = \frac{N_{\text{tight}}^{\text{non-QCD}}}{N_{\text{loose}}^{\text{non-QCD}}} \tag{8.2.5}$$

where leptons in QCD multi-jet events are less likely to satisfy the tighter isolation criteria (thus the probability is denoted as ϵ_{fake} and is expected to be small) than well-isolated leptons from other backgrounds (the probability for this is denoted by ϵ_{real} and expected to be close to 1).

Equation 8.2.3 is rewritten by using these efficiencies:

$$N_{\text{loose}} = \frac{1}{\epsilon_{\text{fake}}} N_{\text{tight}}^{\text{QCD}} + \frac{1}{\epsilon_{\text{real}}} N_{\text{tight}}^{\text{non-QCD}} \tag{8.2.6}$$

---

[1]The following set of equations can be written in the form $\mathbf{y} = A \cdot \mathbf{x}$ with A being a matrix. The vector $\mathbf{y}$ contains the number of loose and tight events, the vector $\mathbf{x}$ the number of QCD multi-jet and non-QCD events. The QCD multi-jet estimate can thus be obtained via $\mathbf{x} = A^{-1} \cdot \mathbf{y}$ where the matrix A was inverted. The name of the method originates from this approach.
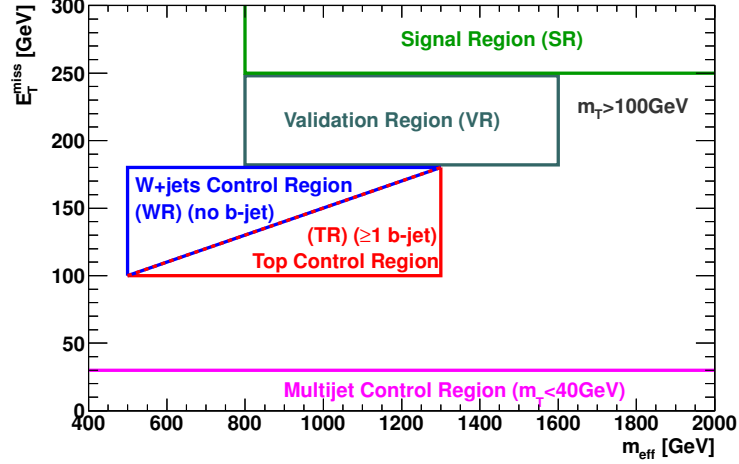
Figure 8.2: The location of all control, validation and signal regions in the $m_{\text{eff}}^{\text{incl}}$-$E_{\text{T}}^{\text{miss}}$ plane [199]. All regions indicated exist both in the electron and in the muon channel. The control regions are located at lower values in $E_{\text{T}}^{\text{miss}}$ and in $m_{\text{eff}}^{\text{incl}}$ with respect to the signal regions. The validation regions are located just between the control and the signal regions, aiming at controlling the extrapolation from the control to the signal regions. The multi-jet control regions are described in Section 8.2.2.

The system of Equations 8.2.4 and 8.2.6 can be solved for $N_{\text{tight}}^{\text{QCD}}$:

$$N_{\text{tight}}^{\text{QCD}} = \frac{\epsilon_{\text{fake}}}{\epsilon_{\text{real}} - \epsilon_{\text{fake}}} \left(\epsilon_{\text{real}} N_{\text{loose}} - N_{\text{tight}} \right) \tag{8.2.7}$$

The number of QCD multi-jet events in the signal regions, $N_{\text{tight}}^{\text{QCD}}$, can thus be evaluated by the efficiencies of an event in the loose sample also passing the tighter isolation criteria and the number of events in the loose and in the tight samples. Since the tight sample is a subset of the loose sample:

$$N_{\text{loose}} = N_{\text{loose}-\text{but}-\text{not}-\text{tight}} + N_{\text{tight}} \tag{8.2.8}$$

where *loose-but-not-tight* denotes all events being only in the loose sample. Using this, Equation 8.2.7 can be re-expressed:

$$
\begin{aligned}
N_{\text{tight}}^{\text{QCD}} &= \frac{\epsilon_{\text{fake}}}{\epsilon_{\text{real}} - \epsilon_{\text{fake}}} \left(\epsilon_{\text{real}} (N_{\text{loose}-\text{but}-\text{not}-\text{tight}} + N_{\text{tight}}) - N_{\text{tight}} \right) \\
&= \frac{\epsilon_{\text{fake}} \epsilon_{\text{real}}}{\epsilon_{\text{real}} - \epsilon_{\text{fake}}} N_{\text{loose}-\text{but}-\text{not}-\text{tight}} + \frac{\epsilon_{\text{fake}} (\epsilon_{\text{real}} - 1)}{\epsilon_{\text{real}} - \epsilon_{\text{fake}}} N_{\text{tight}} \\
&=: w_1 N_{\text{loose}-\text{but}-\text{not}-\text{tight}} + w_2 N_{\text{tight}} \\
&= \sum_{\text{loose}-\text{but}-\text{not}-\text{tight}} w_1 + \sum_{\text{tight}} w_2
\end{aligned} \tag{8.2.9}
$$

The QCD multi-jet background can thus be constructed from the loose control sample by assigning every loose-but-not-tight event the weight $w_1 = \frac{\epsilon_{\text{fake}} \epsilon_{\text{real}}}{\epsilon_{\text{real}} - \epsilon_{\text{fake}}}$ and every tight event the weight $w_2 = \frac{\epsilon_{\text{fake}} (\epsilon_{\text{real}} - 1)}{\epsilon_{\text{real}} - \epsilon_{\text{fake}}}$ and by taking the sum over these weights. Since the efficiencies have values between 0 and 1 and $\epsilon_{\text{real}} > \epsilon_{\text{fake}}$ due to the definitions of the efficiencies, the weight w_1 is

positive and the weight w_2 negative. The QCD multi-jet background estimate may be negative, for example if N_{tight} is significantly larger than $N_{\text{loose}-\text{but}-\text{not}-\text{tight}}$. In such cases, which may occur in low statistics signal regions, the QCD multi-jet background estimate is assumed to be zero with an upper limit given by the systematic and statistical uncertainties on the estimate (these uncertainties are evaluated from Equation 8.2.7 by using error propagation).

8.2.2   Efficiencies

The QCD multi-jet background estimate with the matrix method requires the knowledge of the efficiencies. Their determination is described in this section. Since the author worked on the QCD multi-jet estimation in the muon channel, only the results in the muon channel will be described in detail, while the corresponding results in the electron channel are only summarised.

Fake efficiencies

The fake efficiencies, ϵ_{fake}, are determined in control regions dominated by QCD multi-jet events at low $E_{\text{T}}^{\text{miss}}$ values.

QCD multi-jet control region in the muon channel: Events in this region are required to have a loose muon with $p_{\text{T}} > 25$ GeV, at least one jet with $p_{\text{T}} > 60$ GeV and $E_{\text{T}}^{\text{miss}} < 30$ GeV.

QCD multi-jet control region in the electron channel: Events in this region have a loose electron with $p_{\text{T}} > 25$ GeV as well as $E_{\text{T}}^{\text{miss}} < 30$ GeV, $m_{\text{T}} < 40$ GeV and at least one jet with $p_{\text{T}} > 25$ GeV.

The fake efficiencies in the muon channel are determined as a function of the muon transverse momentum, $p_{\text{T}}(\text{muon})$, as shown in Figure 8.3. The $p_{\text{T}}(\text{muon})$ distributions are shown in loose and in tight events for data and for the $t\bar{t}$, W+jets, Z+jets and single top backgrounds. The discrepancy between these backgrounds and the data at low $p_{\text{T}}(\text{muon})$ values is due to QCD multi-jet events. For $p_{\text{T}}(\text{muon}) > 70$ GeV the data agrees well with the background expectations from the $t\bar{t}$, W+jets, Z+jets and single top backgrounds alone. In the determination of the fake efficiency, these backgrounds are subtracted in order to only select QCD multi-jet events. Due to the negligible QCD multi-jet contribution for $p_{\text{T}} > 70$ GeV, the determination of the fake rates is only possible for smaller values of $p_{\text{T}}(\text{muon})$. The resulting efficiencies are shown in Figure 8.3 and vary between 0.23 for $33 < p_{\text{T}}(\text{muon}) < 35$ GeV and 0.47 for $p_{\text{T}} > 50$ GeV. The statistical uncertainties on the fake rates are shown by black bars and reach 1.5 %. The yellow error band denotes the systematic uncertainties arising from assuming a flat uncertainty of 20% for the total background yields by non-QCD backgrounds in the control regions, to be considered in the subtraction of these backgrounds. These uncertainties are small in the parts of the control region dominated by QCD multi-jet events, but reach $\sim 20\% - 40\%$ for large $p_{\text{T}}(\text{muon})$ values. The fake rates for $p_{\text{T}} > 50$ GeV are thus consistent with zero within the systematic uncertainties.

The dependency of the fake efficiencies on other variables was checked and was found to be only weakly dependent on $\eta(\text{muon})$ or the number of jets as shown in Figure 8.4. Therefore, the fake rates are only used in dependence on $p_{\text{T}}(\text{muon})$ in this analysis.

The fake rates in the electron channel were estimated by a similar method and were found to depend on $p_{\text{T}}(\text{electron})$ and $\eta(\text{electron})$. They vary between 0.02 and 0.3 for large and low $p_{\text{T}}(\text{electron})$ values, respectively [199].

(a)

(b)

(c)
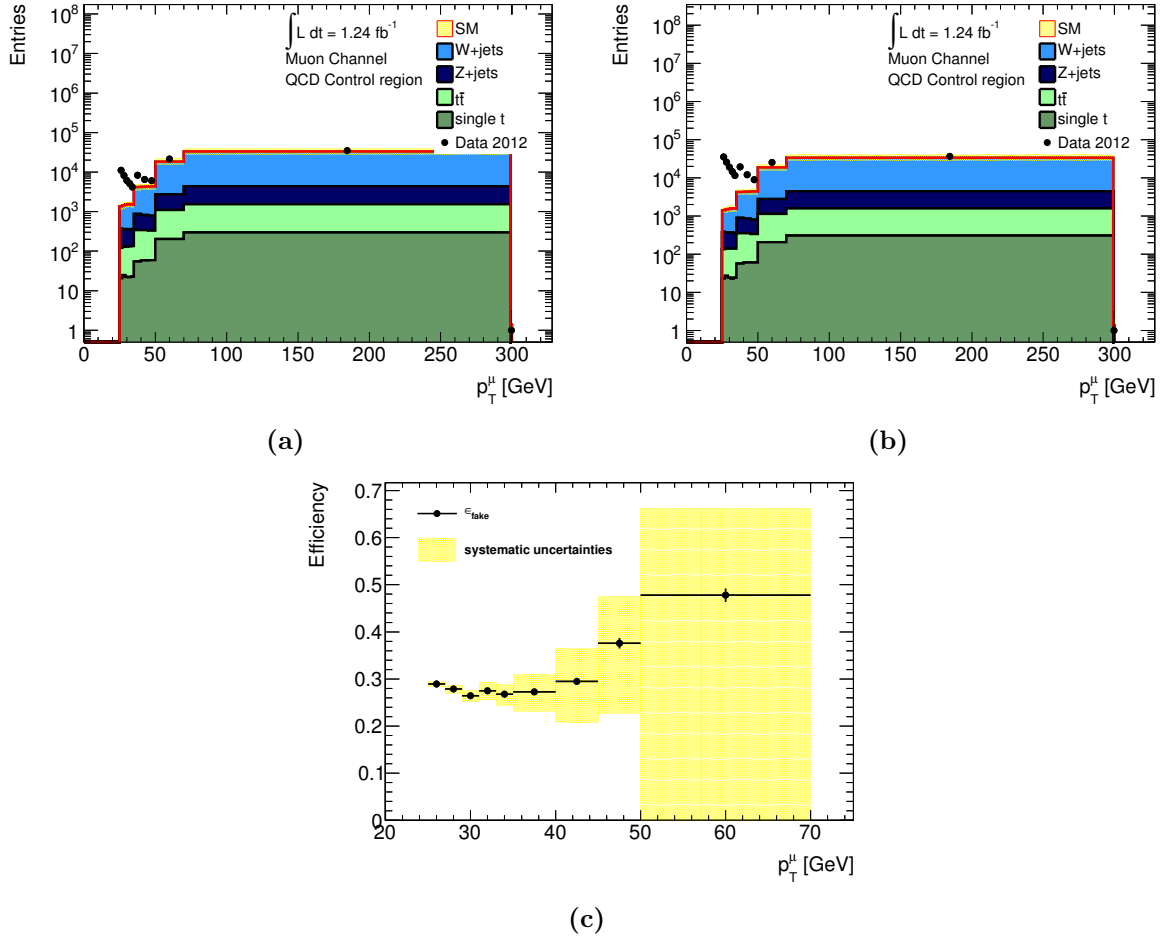
Figure 8.3: The fake efficiency ϵ_{fake} in dependence on $p_{\text{T}}(\text{muon})$ is shown in (c). The contributing tight and loose samples are shown in (a) and (b), respectively. The first five bins have a width of $2-3$ GeV, while for $p_{\text{T}}(\text{muon}) > 35$ GeV the bin width is enlarged to 5 GeV and to more than 20 GeV for $p_{\text{T}}(\text{muon}) > 50$ GeV. This irregular binning was chosen to reduce statistical and systematic uncertainties on ϵ_{fake} for higher values of $p_{\text{T}}(\text{muon})$ for which the number of QCD multi-jet events is smaller than for lower $p_{\text{T}}(\text{muon})$ values.
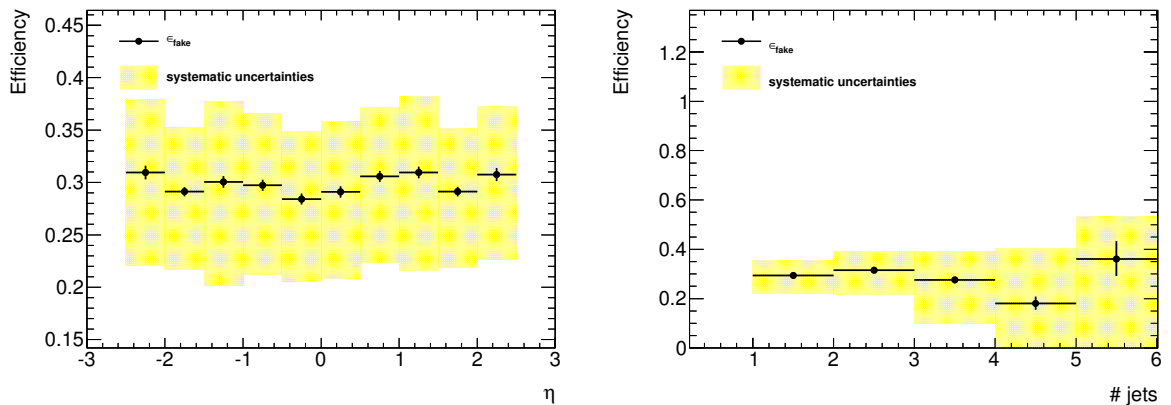
Figure 8.4: The fake efficiency ϵ_{fake} is shown as function of $\eta(\text{muon})$ in the left plot and of the jet multiplicity in the right plot. The efficiencies show only a weak dependence which is within the uncertainties on $\eta(\text{muon})$ and the jet multiplicity.
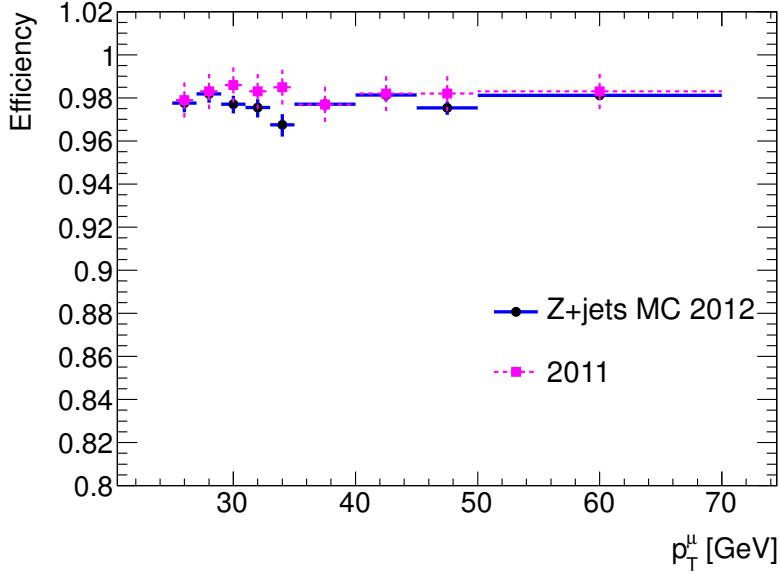
Figure 8.5: The real efficiency ϵ_{real} has been evaluated in Z+jets Monte Carlo in the QCD control region (blue curve) and is compared to the real efficiencies as evaluated in a Z Tag and Probe method in 2011 data (2011 graph from [200]). A reasonable agreement mostly within the statistical uncertainties is visible.

Real efficiencies ϵ_{real}

The real efficiencies, ϵ_{real}, are estimated in Z+jets events selected by a Tag & Probe method[2]. In this method, events with two leptons with the invariant mass of the di-lepton system being in a window around the Z-mass, $80 < m_{ll} < 100$ GeV, are selected. A cut on $E_{\mathrm{T}}^{\mathrm{miss}} < 30$ GeV is imposed to reject W+jets events. The leading lepton (in transverse momentum) needs to fulfil the tight criteria. The real efficiency is measured on the second lepton. This method was applied in a previous analysis of 7 TeV data [200]. The results obtained were compared to the Z+jets Monte Carlo sample at 8 TeV in a control region requiring one lepton and $E_{\mathrm{T}}^{\mathrm{miss}} < 30$ GeV. As shown in Figure 8.5 as function of $p_{\mathrm{T}}(\mathrm{muon})$, the efficiencies evaluated from the Z+jets Monte Carlo sample are consistent within uncertainties with the values obtained from the Tag & Probe method. Therefore, the real rates evaluated for the analysis in [200] were reused for this analysis. The real rates are with an average value of 0.98 very close to 1. The real efficiencies do not show a notable dependence on other kinematic variables.

---

[2]In a second possibility the real efficiencies are directly taken from Monte Carlo in a control region. This is possible, because the $t\bar{t}$, W+jets and Z+jets backgrounds can accurately be simulated. The control region contains events with a lepton, multiple jets and moderate $E_{\mathrm{T}}^{\mathrm{miss}}$ and m_{T} ($30 < E_{\mathrm{T}}^{\mathrm{miss}} < 80$ GeV and $40 < m_{\mathrm{T}} < 80$ GeV). It is dominantly populated by $t\bar{t}$ and W+jets events with a topology close to the signal regions. This method was used in [184].

Chapter 9

The trigger strategy in the 1-lepton channel with high instantaneous luminosities

Lepton triggers are preferred over the use of triggers only based on the missing transverse energy (E_T^{miss}) in this analysis to avoid high E_T^{miss} requirements in control and signal regions. The same triggers can therefore be used in the Top and W+jets control regions at lower E_T^{miss} values and in the signal regions at higher E_T^{miss} values.

In 2011, the 7 TeV analysis [131] used triggers only requiring one lepton, where no isolation requirements were imposed on the lepton. The triggers were usable in every region in the analysis. The luminosity and thus the pile-up increased steadily between 2010 and 2012. The rates of most triggers increased in consequence. The trigger rates of electron and muon triggers were found to increase linearly, whereas the rate increase for jet and E_T^{miss} triggers was faster than linear due to these triggers using information of the whole calorimeter. The latter triggers are thus more affected by pile-up. The rate increase during the course of 2012 is illustrated in Figure 9.1. In order to stay within the required 400 Hz output rate[1] of the EF, the requirements for the triggers had to be tightened and the algorithms had to be optimised. The 400 Hz output rate is dominated by lepton triggers as detailed in Table 9.1.

The detailed optimisation of electron and muon triggers is described below, but the most challenging change for physics analysis was the introduction of an isolation criterion for the lowest unprescaled[2] lepton triggers with a cut on the relative track isolation with $\frac{p_T^{cone20}}{p_T} < 0.1(0.12)$ for electrons (muons). The loose control sample in the QCD multi-jet background estimation contains events with relaxed isolation criteria for the lepton where the track isolation is not applied. As this is the same requirement (or similar for the muon case) as introduced for the lowest unprescaled lepton triggers, those lepton triggers are not usable for selecting events in the loose control sample. An alternative would be the use of a prescaled trigger requiring a lepton without isolation criteria imposed. The statistics in the *loose-but-not-tight* sample (as defined in the previous chapter) corresponding to a signal region is however usually very small with $O(1)$ event so that already a prescale of 10 would often result in the trigger not accepting any event

---

[1]The triggers were designed to stay within this rate limit. The rates are however affected by the instantaneous luminosity and the pile-up during data-taking. Depending on the available (computing) resources, the rates allowed during data-taking may be higher than the design rates.

[2]A prescaled trigger is a trigger only accepting a pre-defined fraction of events passing the trigger thresholds. Triggers may have a constant prescale, e.g. only accepting every 10th event, or a prescale depending on the instantaneous luminosity. Unprescaled triggers accept any event passing the trigger threshold.
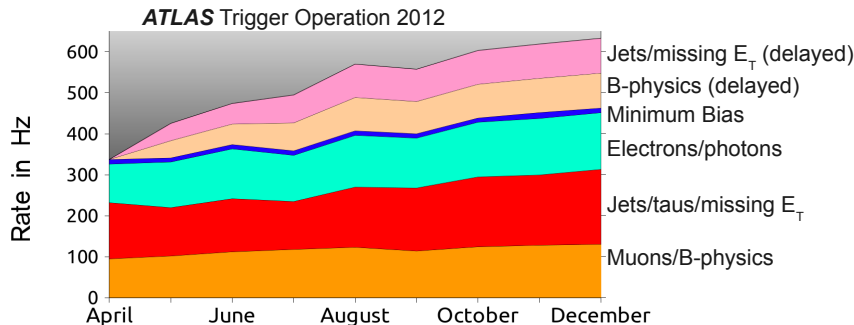
Figure 9.1: The evolution of the trigger rates at the Event Filter in 2012 [201]. The rates increased steadily due to increasing instantaneous luminosity and pile-up. To increase the output rate not all events were processed instantaneously, but some events were recorded in delayed streams to be processed after data-taking.

Category	Average EF rate [Hz]
Electron & Photon	140
Muon	100
Tau	35
Jets	35
$E_{\mathrm{T}}^{\mathrm{miss}}$	30
b-jets	45
B-physics	20
Total	400

Table 9.1: The average Event Filter rates for 2012 are broken down into categories. The unique rate of the categories is given so that an overlap in the rates exists between the categories. The triggers requiring electrons, photons and muons contribute with the highest rates to the total EF rate of 400 Hz. These rates are given after having optimised the triggers for the higher luminosity and pile-up environments of 2012. These values have to be understood as reference values and depend on the instantaneous luminosities and pile-up during data-taking. The evolution of the rates is shown in Figure 9.1. This table is composed with information from [202].

in the *loose-but-not-tight* sample. This would increase the uncertainties on the QCD multi-jet estimate in the concerned signal region significantly. Therefore, the use of prescaled triggers for this purpose was not considered to be possible. Instead, the usage of multi-object triggers was studied, as detailed in Section 9.2. Triggers requiring a lepton and $E_{\mathrm{T}}^{\mathrm{miss}}$ were found to best comply with the needs and were therefore used in the analyses in this work. The trigger strategy of the analyses is summarised in Section 9.5.

9.1 Electron and muon trigger chains

As being relevant for this analysis, the electron and muon trigger algorithms at the three levels (see Section 3.2.7) are summarised in the following. The subsequent execution of algorithms at the different trigger levels with given thresholds and criteria to accept an event is called trigger chain. A more detailed summary of the overall trigger performance and algorithm as used in 2012 can be found in [203, 204].

9.1.1 Electron trigger chains

Electron triggers at Level 1 only use calorimeter information. A sliding window algorithm [106] based on 4 trigger towers (each covering $\Delta\eta \times \Delta\phi = 0.1 \times 0.1$) is used to identify RoIs in the calorimeter [205]. Level 1 accepts an event if a pre-defined number of RoIs with a transverse energy (the transverse energy is evaluated in the RoI) exceeding a pre-defined threshold is found. For electron and photon triggers, further requirements have been introduced at Level 1 to limit the rates. The 'V' criterion indicates different L1 thresholds in the transverse energy (E_T) as function of $|\eta|$. This allows to consider the different amount of material in front of the calorimeters and to enable higher thresholds in E_T in regions with sufficiently high recording efficiencies. The 'H' criterion requires the electromagnetic shower energy deposit in the hadronic calorimeter to be below 1 GeV. Isolation criteria ('I') can be introduced by requiring the transverse energy to be less than 5 GeV within a defined region. As the L1 is hardware-based, a strictly limited number of L1 thresholds exists. Examples are EM18VH (the transverse energy in the RoI needs to exceed 18 GeV and V and H criteria are used) or EM30 (the transverse energy in the RoI needs to exceed 30 GeV).

Level 2 refines the RoI obtained from L1 in order to distinguish between electrons and photons. The positions of the L1 clusters are recalculated. Calorimeter information is combined with tracking information which is first available at L2. The tracks are obtained by using a fast and specialised tracking algorithm. The tracking information is limited to the RoI.

The Event Filter uses algorithms resembling the offline reconstruction.

To cope with higher rates in 2012, the electron and photon trigger algorithms took multiple measures. The distances between L1, L2 and EF thresholds were reduced by introducing various additional criteria on L1 (V and H) but also by optimising the L2 and EF algorithms. In particular, at EF, the quality criteria `loose1`, `medium1` and `tight1` were introduced to better cope with high pile-up environments. These quality criteria mimic the offline electron quality criteria `loose++`, `medium++` and `tight++` and are linked to the cluster and track variables used in the electron identification as detailed in Table B.1 in Appendix B. In addition, the rates of the lowest unprescaled electron and photon triggers were reduced by raising the E_T thresholds of these triggers. The E_T thresholds for the single electron triggers evolved for example from 20 GeV to 22 GeV and finally to 24 GeV[3]. A further rate reduction was obtained for the lowest unprescaled single electron trigger by introducing an isolation criterion at the Event Filter as discussed above.

9.1.2 Muon trigger chains

Signals from the RPCs in the barrel and TGCs in the endcap as well as information of the Inner Detector are used to trigger muons. A detailed overview can be found in [206].

At L1, RPCs and TGCs define the RoI by providing the detector region and the transverse momentum of the muon candidate. The p_T value is evaluated by comparing the hits on the muon trajectory to a straight line as expected for a muon with infinite momentum. The geometrical coverage of muon chambers define the efficiency of muon triggers. In the barrel, muon triggers are less efficient, as only 80 % is covered by the L1 trigger due to the service infrastructure and the feet and elevators of the detector at $\eta = 0$. The geometrical coverage in the endcap is 99 % [206].

Level 2 also uses information of the MDTs and tracking information from the Inner Detector

---

[3]This threshold in E_T defines the p_T cut used for the lepton in this work.

to refine the L1 muon candidate. Fast muon reconstruction algorithms and look-up tables are used to limit the processing times while obtaining reasonable resolutions [206].

The Event Filter uses algorithms similar to offline and full detector information.

Similarly to the electron triggers, the muon triggers needed to be re-optimised for the 2012 data-taking. This resulted in an increased p_T threshold of 24 GeV for the lowest unprescaled single muon trigger and in the introduction of isolation criteria for this trigger as described above.

9.1.3 Trigger nomenclature

Triggers are named according to the following nomenclature:

(trigger level)_(number of objects)(type of object)(threshold)_(quality criteria)

The trigger level may be L1, L2 or EF. The type of the trigger object is 'e' for electrons, 'mu' for muons, 'j' for jets and 'xe' for $E_\mathrm{T}^\mathrm{miss}$. The quality criteria depend on the triggered object, for example 'medium1' is used for electron triggers requiring `medium++` electrons. An example for this naming is `EF_e24ivh_medium1` indicating a trigger defined at EF (following the L1 and L2 algorithms) requiring one electron which needs to be isolated ('i') at EF and needs to satisfy the 'V' and 'H' criteria at L1 ('v' and 'h' in the trigger name). The electron needs to fulfil $E_\mathrm{T} > 24$ GeV and `medium++`. A list of the triggers used in this chapter with their technical names is given in Table 9.2.

9.2 Rate reduction by multi-object triggers

As the usage of the lowest unprescaled single lepton triggers[4] with isolation requirements and thresholds $E_\mathrm{T}(e) > 24$ GeV and $p_\mathrm{T}(\mu) > 24$ GeV is not suitable for this analysis as discussed above, options for multi-object triggers are presented in the following. Any multi-object trigger needs to possess only a small rate so that running this trigger in addition to the lowest unprescaled single lepton trigger is possible within the rate constraints of EF.

The studied multi-object triggers rely on a lepton and a further object. A rate reduction of approximately a factor 5 is required with respect to the single lepton trigger without isolation.

Rate reduction by a geometrical isolation criterion: As the loose control sample in the QCD multi-jet background estimation requires already geometrically isolated leptons, i.e. leptons with a distance of $\Delta R(\text{lepton}, \text{jet}) > 0.4$ from any jet with $p_\mathrm{T} > 20$ GeV in the event, a trigger requiring geometrically isolated leptons would be usable for the QCD multi-jet background estimation. The rate reduction of such a muon trigger with respect to a reference single muon trigger - here the single muon trigger with a requirement for $p_\mathrm{T}(\mu) > 20$ GeV is used[5] - is shown in Figure 9.2. The left plot in this figure shows the reduction obtained by a geometrical isolation cut with $\Delta R(\mu, \text{jet}) > 0.4$. The p_T of the jets used in the calculation of $\Delta R(\mu, \text{jet})$ is varied from 10 to 100 GeV (electromagnetic scale)[6]. If considering all jets with $p_\mathrm{T} > 10$ GeV,

---

[4]Technical names: `EF_e24vhi_medium1` and `EF_mu24i_tight`.

[5]Technical name: `EF_mu20`.

[6]These values are given at electromagnetic scale, not at hadronic scale. These values are thus not corrected for the lower response of the calorimeter to jets. The use of the electromagnetic scale for jets was the default in the trigger at the time of these studies which were performed before the trigger algorithms were improved to include hadronic calibrations.

Technical name	Requirements
	Single lepton triggers
`EF_mu20`	A muon with $p_{\mathrm{T}}(\mu) > 20$ GeV.
`EF_mu24i_tight`	A `tight` and isolated muon with $p_{\mathrm{T}}(\mu) > 24$ GeV. Isolation criteria: $p_{\mathrm{T}}^{\mathrm{cone20}}/p_{\mathrm{T}} < 0.12$.
`EF_e20_medium1`	A `medium++` electron with $E_{\mathrm{T}}(e) > 20$ GeV.
`EF_e24vh_medium1`	A `medium++` electron with $E_{\mathrm{T}}(e) > 24$ GeV, 'V' and 'H' criteria at L1 applied.
`EF_e24vhi_medium1`	As `EF_e24vh_medium1`, but the electron needs to be isolated in addition: $p_{\mathrm{T}}^{\mathrm{cone20}}/p_{\mathrm{T}} < 0.1$.
	Muon+jet trigger
`EF_mu24_j65_a4tchad`	A muon with $p_{\mathrm{T}}(\mu) > 24$ GeV and a jet with $p_{\mathrm{T}}(\mathrm{jet}) > 65$ GeV. The component 'a4tchad' indicates that anti-k_t jets with $R = 0.4$ and jet energy scale calibration are used. The jets may also be outside the RoI.
	Lepton(+jet)+$E_{\mathrm{T}}^{\mathrm{miss}}$ trigger
`EF_e24vh_medium1_EFxe30`	Electron component `EF_e24vh_medium1` and $E_{\mathrm{T}}^{\mathrm{miss}} > 30$ GeV. The calculation of $E_{\mathrm{T}}^{\mathrm{miss}}$ is based on cells in the calorimeter.
`EF_e24vh_medium1_EFxe35_tcem`	Electron component `EF_e24vh_medium1` and $E_{\mathrm{T}}^{\mathrm{miss}} > 35$ GeV. Calculation of $E_{\mathrm{T}}^{\mathrm{miss}}$ based on topological clusters with electromagnetic scale ('`tcem`').
`EF_e24vh_medium1_EFxe35_tclcw`	Electron component `EF_e24vh_medium1` and $E_{\mathrm{T}}^{\mathrm{miss}} > 35$ GeV. Calculation of $E_{\mathrm{T}}^{\mathrm{miss}}$ based on topological clusters with local cluster weighting ('`tclcw`').
`EF_mu24_j65_a4tchad_EFxe40_tclcw`	Muon+jet component `EF_mu24_j65_a4tchad` and $E_{\mathrm{T}}^{\mathrm{miss}} > 40$ GeV. Calculation of $E_{\mathrm{T}}^{\mathrm{miss}}$ based on topological clusters with local cluster weighting ('`tclcw`').

Table 9.2: Explanation of the technical names of the triggers used in this chapter. All threshold values are given at Event Filter. The criteria in $E_{\mathrm{T}}^{\mathrm{miss}}$ are explained in Section 9.3 and are only applied at EF.

a reduction of a bit more than a factor 2 can be obtained with respect to the reference trigger. The obtained rate reduction is thus smaller than the required factor of 5.

The reduction can be increased if the event is required to contain a certain number of additional jets. In the right plot in Figure 9.2, a geometrical isolation of $\Delta R(\mu, \mathrm{jet}) > 0.2$ is applied. The p_{T} of the jets used in this calculation is again varied between 10 and 100 GeV (electromagnetic scale). In addition, the event is required to contain at least one jet with $p_{\mathrm{T}} > 10$ GeV, $p_{\mathrm{T}} > 30$ GeV or two jets with $p_{\mathrm{T}} > 10$ GeV. A rate reduction of more than a factor 5 can be obtained for the cases in which at least one jet with $p_{\mathrm{T}} > 30$ GeV or two jets with $p_{\mathrm{T}} > 10$ GeV are requested, if $\Delta R(\mu, \mathrm{jet})$ is constructed with low p_{T} jets.

Resulting in a smaller rate reduction than the other options discussed below, while being less flexible in use, options with geometrical isolation criteria were not further pursued.

Rate reduction by adding additional jets: The rate can be reduced with respect to a single electron trigger when further requirements for multiple high p_{T} jets are added. Figure 9.3 presents the rate reduction with respect to the single electron trigger[7] with the criterion $E_{\mathrm{T}}(e) > 20$ GeV when requiring between one or five additional jets in the event. The transverse momenta of the jets is varied between 10 and 70 GeV (all at electromagnetic scale). A rate reduction of a factor 5 is obtained when requiring at least four or more jets with $p_{\mathrm{T}} > 10$ GeV. Alternatively,

---

[7]Technical name: `EF_e20_medium1`.
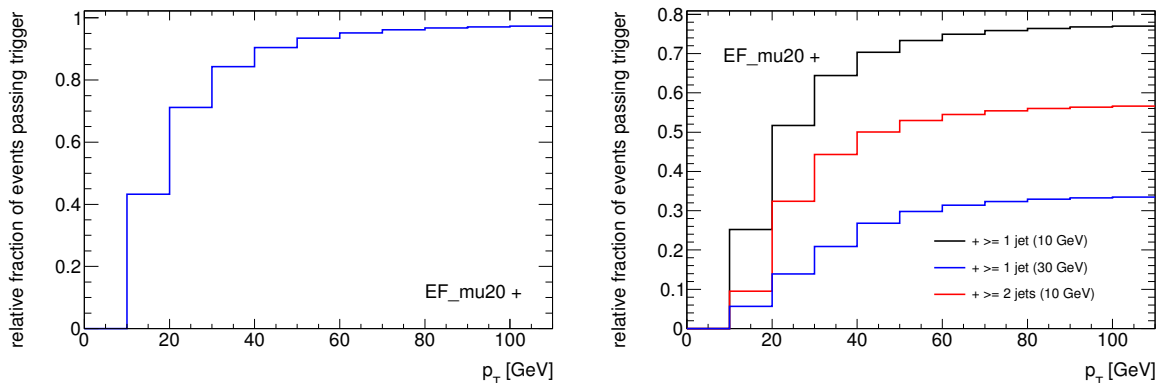
Figure 9.2: Rate reduction with respect to the single muon trigger requiring a muon with $p_T(\mu) > 20$ GeV when adding a geometrical isolation criterion. The left plot shows the reduction when requiring the muon to be geometrically isolated from any jet with a distance $\Delta R(\mu, \text{jet}) > 0.4$. Only jets with $p_T > x$ (as given on the x-axis) are considered in the calculation of $\Delta R(\mu, \text{jet})$. Muons are required to be separated from jets by $\Delta R(\mu, \text{jet}) > 0.2$ in the right plot. In this plot, a further rate reduction with respect to the single muon trigger is obtained by additionally requiring the event to contain at least one jet with $p_T > 10$ GeV (electromagnetic scale, black curve), at least one jet with $p_T > 30$ GeV (electromagnetic scale, blue curve) or at least two jets with $p_T > 10$ GeV (electromagnetic scale, red curve).

requiring additionally three jets results in a sufficient rate reduction if the p_T threshold of the jets is more than 15 GeV (electromagnetic scale). The p_T of jets at the hadronic scale is higher than at the electromagnetic scale. This forces an analysis using these triggers to select events with accordingly high p_T jets. Following these studies, triggers requiring an electron and jets or a muon and jets were implemented (as for example triggers requiring an electron with $p_T > 24$ GeV and three or four jets with a transverse momentum of 45 GeV at hadronic scale).

The analysis presented in this work considers final states with many jets, but not necessarily jets with high transverse momentum. Events with a low number of high p_T jets can equally occur. For a multi-jet trigger, it is difficult to accommodate these different needs due to fixed p_T thresholds for the jets. Additionally, the analysis uses a requirement on a high inclusive effective mass, $m_{\text{eff}}^{\text{incl}}$, which includes the sum over the transverse momenta of the jets in the event. Therefore, the rate reduction by adding a requirement of $H_T = \sum_{\text{jets}} p_T$ to the trigger was studied. For this, first the single electron trigger was applied and then the H_T requirement. The rates are calculated relatively to the events passing the single electron trigger. Figure 9.4 shows the possible rate reductions with respect to the single electron trigger with the criterion $E_T(e) > 20$ GeV when adding H_T requirements. Jets with $p_T > 10, 15$ or 20 GeV (electromagnetic scale) are used in the calculation of H_T. The black line corresponds effectively to a pure H_T requirement in addition to the electron requirement (the requirement of at least one jet is identical to requiring $H_T > 0$). A rate reduction of 80 % can be obtained by cutting on $H_T \sim 80$ GeV for all H_T definitions. Adding the additional criterion that the event should contain at least two, three or four jets with $p_T > 10, 15$ or 20 GeV helps suppressing the rates below 10 % also for small values of H_T. Although these trigger options were not used in 2012, they are continued to be studied for the LHC Run 2.

Rate reduction by an additional criterion on E_T^{miss}: Triggers including electron/muon and E_T^{miss} requirements are particular useful for this analysis as all regions, but the QCD multi-jet control regions at low E_T^{miss} values in which a sufficient statistics is collected by prescaled triggers, impose E_T^{miss} cuts of at least 100 GeV. The fractions of events also passing a E_T^{miss} cut after having been accepted by the single electron trigger with the criterion $E_T(e) > 20$ GeV are
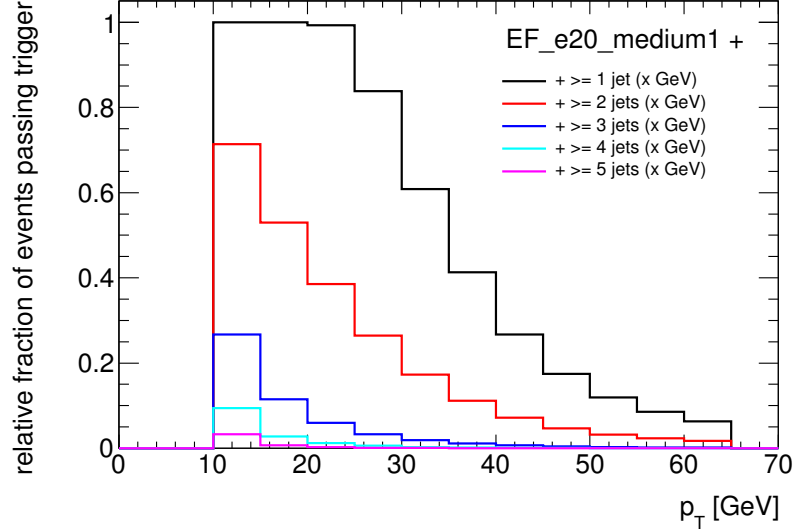
Figure 9.3: A rate reduction with respect to the single electron trigger with the criterion $E_T(e) > 20$ GeV can be achieved if requiring additional jets: The black curve indicates the possible rate reduction when requiring one additional jet in the event with $p_T > x$, where x is indicated on the x-axis. The rate can be further suppressed when requiring the event to contain at least two jets (red curve), three jets (blue curve), four jets (cyan curve) or five jets (magenta curve) with $p_T > x$ as indicated on the x-axis. The jet p_T values are given at electromagnetic scale.

given in Figure 9.5. A rate reduction to 10 % is already achieved by a E_T^{miss} cut of 35 GeV. Given the high possible rate reduction at relatively moderate E_T^{miss} values, multi-object triggers composed of electron, muon and E_T^{miss} trigger requirements are the most interesting option for this analysis. Such triggers were implemented to run in the 2012 trigger menu and define the trigger strategy of this analysis.

9.3 Performance of electron+E_T^{miss} triggers

Implemented trigger chains: Three different electron+E_T^{miss} triggers were available for the 2012 data-taking. The electron component of these triggers requires a `medium++` electron with $E_T(e) > 24$ GeV[8]. The electron component is thus similar to the lowest unprescaled single electron trigger, but without the isolation criteria on the electron at EF. The three triggers with different E_T^{miss} requirements are:

- Electron+E_T^{miss} trigger based on calorimeter cells[9]:

  The E_T^{miss} component requires a cut of 30 GeV in E_T^{miss} at the Event Filter only. No E_T^{miss} cuts are applied at L1 or L2, assuring that the E_T^{miss} component is not affected by L1 resolutions effects. The definition of E_T^{miss} used in this trigger is calorimeter cell based. Here, E_T^{miss} is constructed as the sum over E_T of all calorimeter cells with E_T exceeding 3σ where σ is the noise threshold. This E_T^{miss} definition is pile-up sensitive.

- Electron+E_T^{miss} trigger based on topological clusters with electromagnetic calibration[10]:

  This trigger contains a E_T^{miss} component based on topological clusters in the calorimeters. A 3-D cluster is built around a seed with an energy deposit exceeding 4σ by sequentially

---

[8]The electron component corresponds to the single electron trigger `EF_e24vh_medium1`.

[9]Technical name: `EF_e24vh_medium1_EFxe30`.

[10]Technical name: `EF_e24vh_medium1_EFxe35_tcem`.
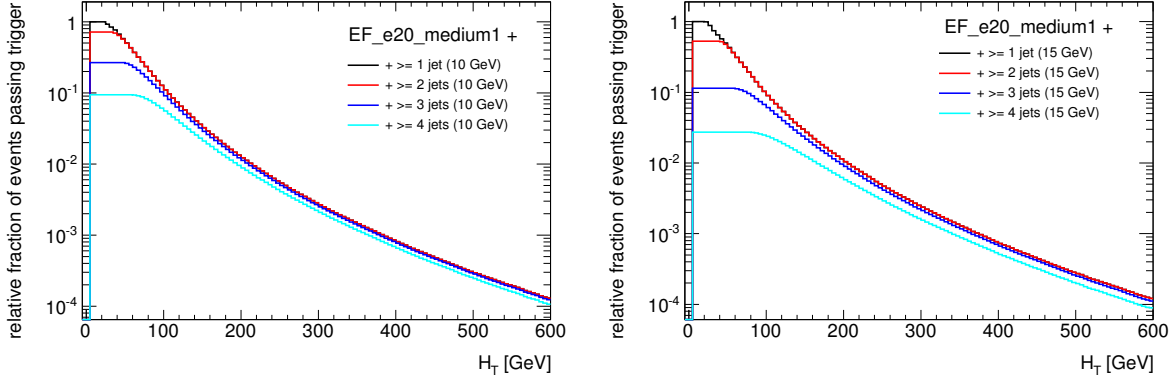
(a) H_T including jets with $p_T > 10$ GeV

(b) H_T including jets with $p_T > 15$ GeV
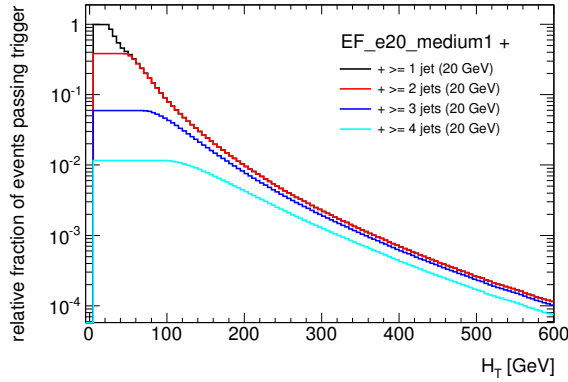
(c) H_T including jets with $p_T > 20$ GeV

Figure 9.4: The rate of the single electron trigger with the criterion $E_T(e) > 20$ GeV can be further reduced when requiring the presence of $H_T > x$ GeV (the value on the x-axis at the electromagnetic scale) in the event. Here, H_T is constructed including all jets with $p_T > 10$ GeV in the event (a), or including all jets with $p_T > 15$ GeV (b) or with $p_T > 20$ GeV (c). The rate can be further reduced by also requiring the presence of at least one (black curve), two (red curve), three (blue curve) or four jets(s) (cyan curve) (with $p_T > 10, 15, 20$ GeV depending on the jets included in the H_T calculation).

adding all neighbour cells with energy deposits exceeding 2σ and then adding all neighbour cells of these, regardless of the deposited energy. The E_T^{miss} is constructed as sum over E_T of the clusters at electromagnetic scale. This trigger requires $E_T^{\mathrm{miss}} > 35$ GeV. Being less pile-up affected, the E_T^{miss} component of this trigger reaches the full efficiency at lower E_T^{miss} values than the previous trigger.

- Electron+E_T^{miss} trigger based on topological clusters with local cluster weighting[11]:

  This trigger also uses a E_T^{miss} definition based on topological clusters, but in contrast to the previous one, the clusters are classified as being electromagnetic like or hadronic like according to their cluster shape, energy density etc. The clusters are weighted according to this (local cluster weighting). This trigger also requires $E_T^{\mathrm{miss}} > 35$ GeV as the previous trigger. Similar to the previous trigger, this trigger is fully efficient in its E_T^{miss} component for relatively lower values compared to the electron+E_T^{miss} trigger based on calorimeter cells.

---

[11]Technical name: `EF_e24vh_medium1_EFxe35_tclcw`.
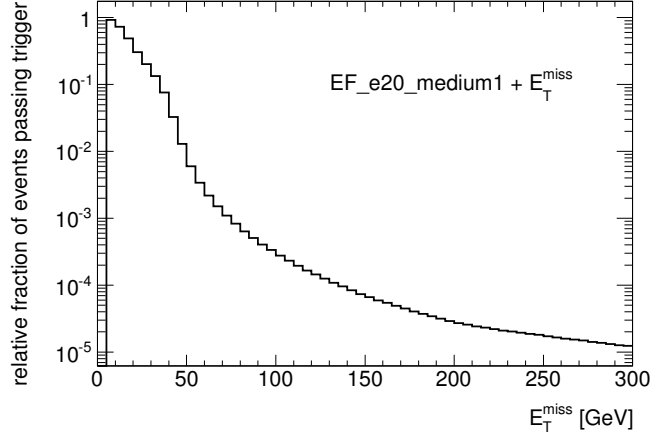
Figure 9.5: The rate reduction with respect to the single electron trigger with the criterion $E_T(e) > 20$ GeV when also requiring a cut on $E_T^{miss} > x$ GeV (given by the value on the x-axis).

Bootstrap method: The efficiencies of these triggers are determined by using the 'bootstrap' method which calculates the efficiencies with respect to a reference trigger. The efficiency $\epsilon(\text{electron} + E_T^{miss} \text{ trigger})$ is thus given by:

$$\epsilon(\text{electron} + E_T^{miss} \text{ trigger}) = \epsilon(\text{electron} + E_T^{miss} \text{ trigger}|\text{reference trigger}) \cdot \epsilon(\text{reference trigger})$$
(9.3.1)

where $\epsilon(\text{electron} + E_T^{miss} \text{ trigger}|\text{reference trigger})$ is the efficiency of the electron+E_T^{miss} trigger evaluated in events passing the reference trigger and $\epsilon(\text{reference trigger})$ is the efficiency of the reference trigger.

The obvious reference trigger for the electron+E_T^{miss} triggers is the single electron trigger with $E_T(e) > 24$ GeV which allows the separation of the electron and E_T^{miss} components. Thus, only the efficiency of the E_T^{miss} component with respect to this reference trigger remains to be calculated, while the efficiency of the single electron trigger with $E_T(e) > 24$ GeV needs to be calculated by other methods (usually by a Tag & Probe method, see [207]). To be close to the selection cuts of the analysis presented in this work, the efficiencies were measured in events containing an isolated electron and satisfying the same preselection cuts as described in Section 7.2.1. In addition, the reconstructed electron is matched to the reference single electron trigger by requiring the distance between the selected reconstructed electron and the single electron trigger objects (which caused the single electron trigger to be passed) to be small: $\Delta R(\text{electron}, \text{trigger electron}) < 0.15$. This requirement ensures that the reconstructed electron and the electron trigger object are the same objects. After these cuts, the fraction of events also having passed the electron+E_T^{miss} trigger is evaluated in dependence on the E_T^{miss} present in the event.

Turn-on and plateau: The efficiency can be displayed as schematically shown in Figure 9.6. The curve in this figure can be separated into three regions. For low values of E_T^{miss}, the trigger does not record any events, because the E_T^{miss} present in the event is not sufficient to pass the trigger requirements. In the second region, the efficiency curve raises from an efficiency of zero to the maximal efficiency possible for this trigger. The part of the curve in this region is called *turn-on*. The precise form of the turn-on curve partly depends on the correlation between the reconstructed quantity on the x-axis and the corresponding quantity used in the trigger definition, in this case on the correlation between reconstructed E_T^{miss} and the E_T^{miss} definition
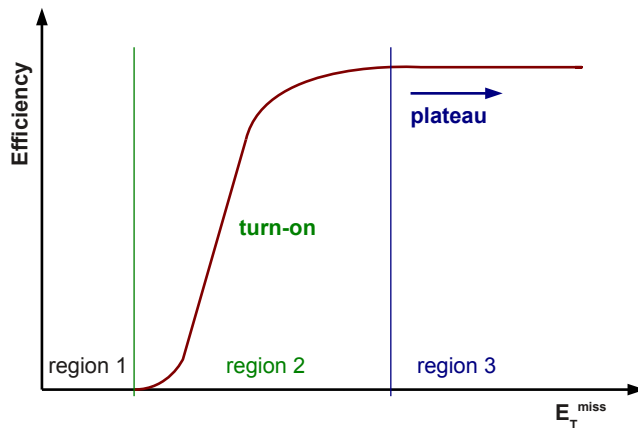
Figure 9.6: The trigger efficiency as function of the reconstructed E_T^{miss} is shown schematically. For very low E_T^{miss} values (region 1) the trigger is inefficient, as the events contain too low E_T^{miss} values as to pass the trigger. In region 2, the efficiency curve raises from very low efficiency values to the maximal possible efficiencies. This part is the turn-on region. The third region, called plateau, refers to the region where the trigger is maximally efficient with respect to the reconstructed E_T^{miss}.

used by the trigger. The slope of the turn-on curve is further influenced by resolution effects of the trigger quantities. The third region in which the trigger is maximally efficient with respect to the variable on the x-axis is called *plateau*.

Efficiencies: The efficiency curves of the three electron+E_T^{miss} triggers are shown in dependence on three different definitions of (offline) E_T^{miss} in the event in Figure 9.7. The analysis corrected definition of E_T^{miss} corresponds to the default definition used in this work as defined in Section 4.4. MET_RefFinal, defined in the reconstruction paragraph of Section 4.4 in Equation 4.4.5, is similar, but not corrected for the objects appearing in the analysis. MET_LocHadTopo is calculated on cells in the hadronic calorimeter at hadronic scale (without using topological clusters). This definition is the closest to the E_T^{miss} definitions of the triggers and thus the turn-on curves for this E_T^{miss} definition are the sharpest. The turn-on curves for the other two E_T^{miss} definitions are very similar to each other and overall a bit flatter than for MET_LocHadTopo. All efficiency curves reach an efficiency plateau of 100 % showing that the E_T^{miss} component of the electron+E_T^{miss} triggers is fully efficient. Focusing on the E_T^{miss} definition of this analysis, the efficiency plateau of the electron+E_T^{miss} trigger based on calorimeter cells is reached at $E_T^{\mathrm{miss}} \sim 150$ GeV, of the electron+E_T^{miss} trigger based on topological clusters with electromagnetic calibration at $E_T^{\mathrm{miss}} \sim 130$ GeV and of the electron+E_T^{miss} trigger based on topological clusters with local cluster weighting at $E_T^{\mathrm{miss}} \sim 80$ GeV. The last trigger thus reaches the plateau the fastest and shows the steepest turn-on curves compared to the other two triggers. This is due to the trigger E_T^{miss} definition being the closest to the offline E_T^{miss} definition for this trigger. Therefore, this trigger is used in this work.

As the analyses in this work requires final states with multiple jets, the efficiency of the electron+E_T^{miss} trigger based on topological clusters with local cluster weighting is also checked in events where at least one or two jets are present as function of E_T^{miss} (shown in Figure 9.8). The slope of the turn-on curve is slightly flatter for events containing at least two jets and the analysis E_T^{miss} definition, causing the plateau to be reached at slightly higher E_T^{miss} values. At $E_T^{\mathrm{miss}} > 100$ GeV the efficiency plateau is also reached for these events.

92
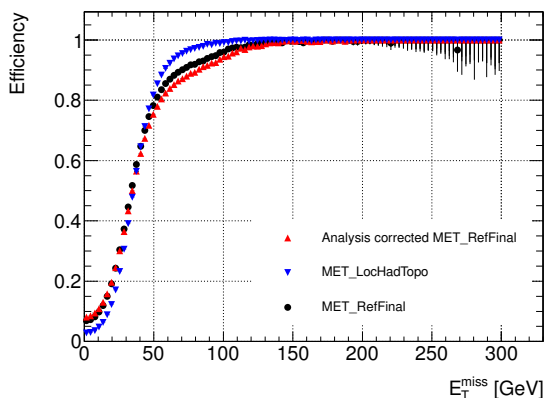
(a) Electron+E_T^{miss} trigger based on calorimeter cells
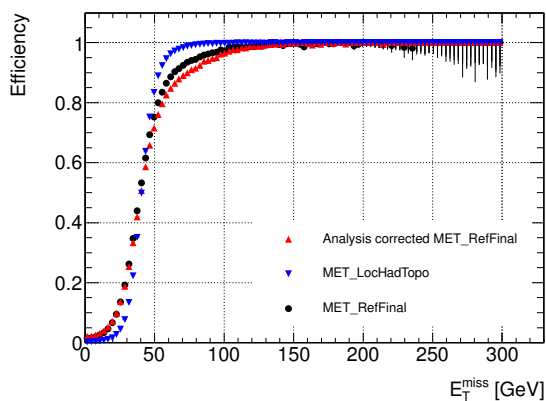
(b) Electron+E_T^{miss} trigger based on topological clusters with electromagnetic calibration
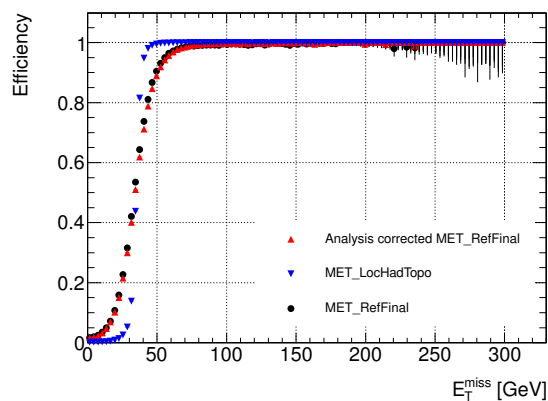
(c) Electron+E_T^{miss} trigger based on topological clusters with local cluster weighting

Figure 9.7: Efficiencies for different electron $+E_T^{\text{miss}}$ triggers (as defined in the text) with respect to offline E_T^{miss} definitions. The black curves reports the efficiencies with respect to the MET_RefFinal definition, the red curves with respect to the default E_T^{miss} definition in this work which is corrected by the objects used within the analysis and the blue curves give the efficiencies with respect to the MET_LocHadTopo definition, which is closest to the definition run online in the trigger algorithms (the different variants of E_T^{miss} are defined in the text).

9.4 Muon+jets+E_T^{miss} triggers

This work uses a muon+jet+E_T^{miss} trigger[12] with the thresholds $p_T(\mu) > 24$ GeV, $p_T(\text{jet}) > 65$ GeV and $E_T^{\text{miss}} > 40$ GeV which was introduced to avoid the lowest unprescaled single muon trigger with isolation requirements as in the electron case. The trigger uses as muon component a muon+jet trigger which requires in addition to a muon also a jet at L1. The jet requirement allows to use a lower L1 threshold for the muon, which increases the efficiency at L1 slightly. The efficiency of this trigger was evaluated by using the bootstrap method in context of [185]. The E_T^{miss} component of this trigger was shown to be fully efficient for $E_T^{\text{miss}} > 100$ GeV. However, since the E_T^{miss} definition used in this trigger is entirely based on calorimeter information and not corrected for the presence of the muon, the turn-on curve of this trigger is flatter than for the electron+E_T^{miss} triggers.

---

[12]Technical name: `EF_mu24_j65_a4tchad_EFxe40_tclcw`, see Table 9.2.
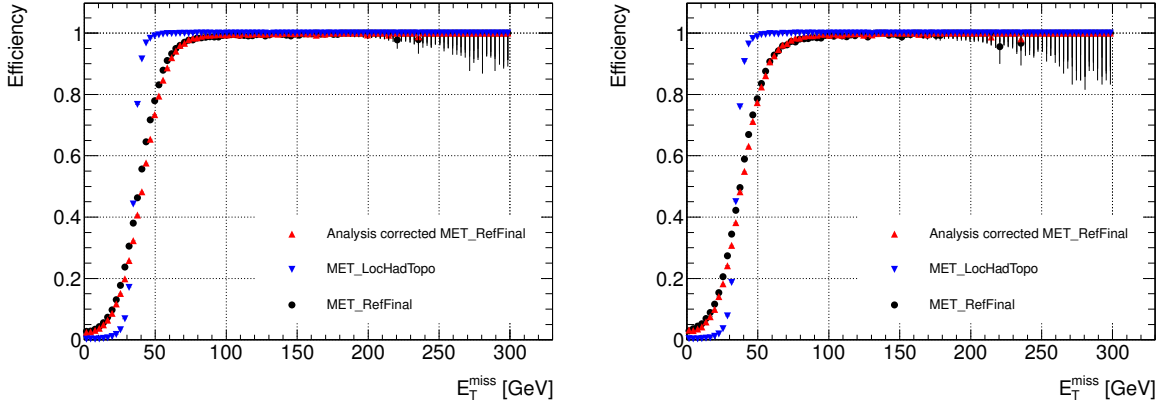
Figure 9.8: Efficiency of the electron+E_T^{miss} trigger based on topological clusters with local cluster weighting with respect to different definitions of E_T^{miss} in events containing at least one jet (left plot) or at least two jets (right plot).

Region	Trigger	Prescale
QCD multi-jet control regions	`EF_e24vh_medium1`	10
	`EF_mu24_tight`	10
$t\bar{t}$ control regions		
W+jets control regions	`EF_e24vh_medium1_EFxe35_tclcw || EF_e60_medium1`	-
Validation regions	`EF_mu24_j65_a4tchad_EFxe40_tclcw`	-
Signal regions		

Table 9.3: Summary of the trigger strategy as applied in this analysis. The names of the triggers have been explained in Table 9.2.

9.5 Summary: The trigger strategy in the 1-lepton channel

The trigger strategy as employed in this analysis is summarised in Table 9.3. Prescaled triggers with a prescale factor of 10 are used in the QCD multi-jet control regions. An electron+E_T^{miss} trigger with the thresholds $E_T(e) > 24$ GeV and $E_T^{miss} > 35$ GeV (with the E_T^{miss} calculation being based on topological clusters with local cluster weighting) in combination with a single electron trigger with the threshold $E_T(e) > 60$ GeV is used in all other control regions, validation regions and signal regions in the electron channel. The combination with the single electron trigger aims to recover inefficiencies of the electron+E_T^{miss} trigger introduced by the 'V' and 'H' requirements at L1 (see Section 9.1.1) used in this trigger. A muon+jet+E_T^{miss} trigger with thresholds $p_T(\mu) > 24$ GeV, $p_T(\text{jet}) > 65$ GeV and $E_T^{miss} > 40$ GeV is used in the muon channel for these regions.

The efficiencies of the various triggers may be different for data and Monte Carlo. This concerns in particular the electron and muon components and less the E_T^{miss} components, as these are fully efficient at the plateau. Inefficiencies in the electron trigger often arise from the reconstruction and matching of tracks [207]. Efficiencies for the single electron triggers are usually between 90 and 95%. Inefficiencies in the muon trigger particularly arise from the incomplete coverage by muon trigger chambers as described in Section 9.1.2. The efficiencies are usually $\sim 70 - 80\%$ for single muon triggers. To account for the different efficiencies in data and in Monte Carlo, scale factors are derived as ratio of the efficiencies in data and in Monte Carlo in $Z \rightarrow ee$ or $Z \rightarrow \mu\mu$ events. These scale factors are then used to correct the efficiencies in any Monte Carlo sample.

Chapter 10

Simultaneous fit for the background and signal estimation

The estimation of the $t\bar{t}$ and W+jets backgrounds presented in Section 8.1 requires the simultaneous normalisation of Monte Carlo samples to data in multiple control regions. This normalisation also needs to take into account the contribution of other, smaller backgrounds in the control regions, as for example of the QCD multi-jet background.

The simultaneous normalisation of the $t\bar{t}$ and the W+jets Monte Carlo samples in the control regions is achieved by fitting a statistical model describing all backgrounds and their systematic uncertainties to data. This model is represented by a parametrised probability density function constructed from binned histograms. This probability density function also defines the likelihood used in this analysis. The general format of the probability density function is explained in Section 10.2 and its specific construction for the $5.8\,\mathrm{fb}^{-1}$ analysis in Section 10.3.1. Background estimates in control, validation and signal regions are obtained by maximising the likelihood in Section 10.3.2.

Taking the model constructed with a signal contribution added, limits on new physics without model assumption or in the MSUGRA/CMSSM framework are derived in hypothesis tests by using the CL_s method as detailed in Section 10.4. The limits are presented at the end of this chapter.

The $5.8\,\mathrm{fb}^{-1}$ analysis (and similarly the $20.3\,\mathrm{fb}^{-1}$ analysis) makes use of a shape fit. In a shape fit, a signal or control region is divided into subregions in dependence on a discriminating variable. These subregions are fitted simultaneously. In the case of signal regions, this allows to explicitly consider the distinct shapes of background and signal distributions and thus to improve the sensitivity of the analysis to new physics. In the case of control regions, a shape fit allows to correct the shapes of background Monte Carlo samples to the shapes observed in data in order to improve the agreement between the Monte Carlo expectation and the data in the control regions. The correction of the shape of the W+jets Monte Carlo sample will be required in this analysis due to the disagreement between data and Monte Carlo prediction which was seen in the W+jets control regions in Figure 8.1.

The idea of the shape fit is motivated below in Section 10.1 and its technical implementation in Sections 10.3.1 and 10.4.4. The concept of a shape fit also increases the sensitivity of the $20.3\,\mathrm{fb}^{-1}$ analysis to new physics as explained in Chapter 12.
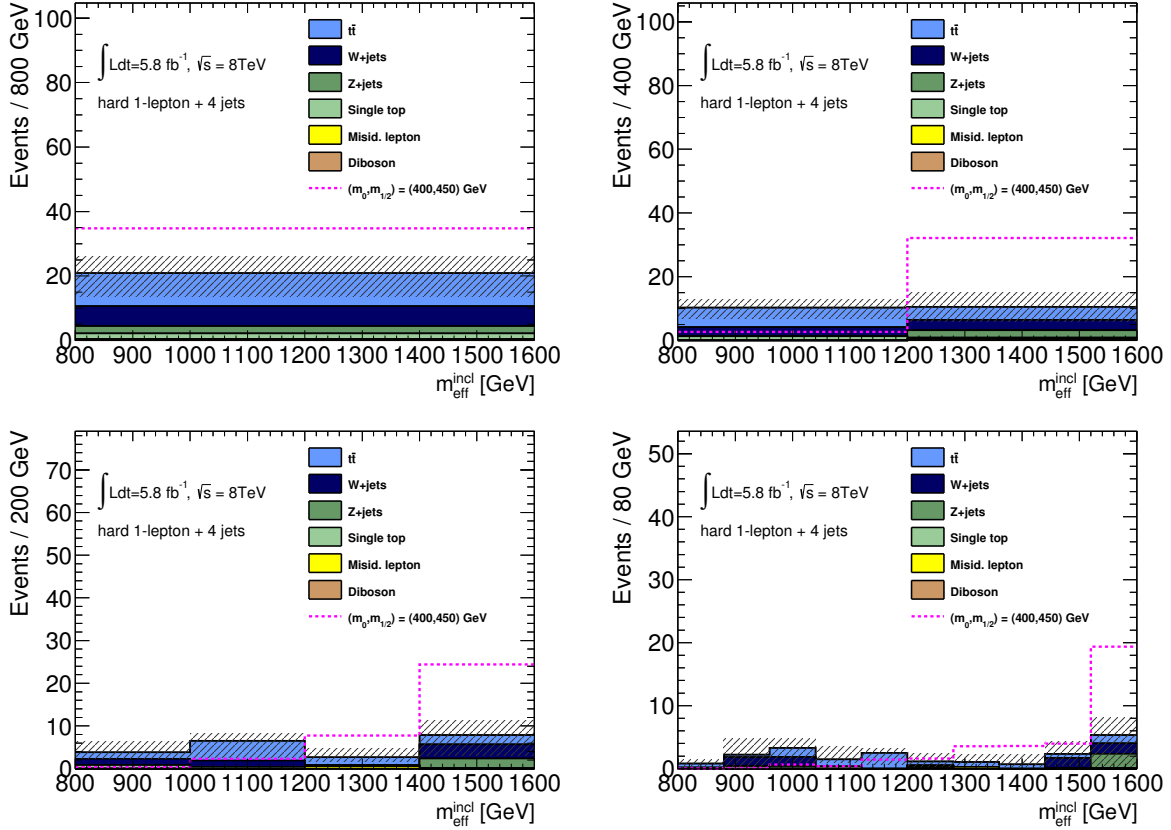
Figure 10.1: The $m_{\text{eff}}^{\text{incl}}$ distribution is shown in a signal region in which the electron and muon channels were combined. The signal region is not sub-divided into subregions in the top left plot. This corresponds to the "cut-and-count" approach. When dividing the signal region into two subregions with $m_{\text{eff}}^{\text{incl}} \in [800, 1200)$ GeV and $m_{\text{eff}}^{\text{incl}} \in [1200, \infty)$ GeV, the MSUGRA/CMSSM signal model with coordinates $(m_0, m_{1/2}) = (400, 450)$ GeV peaks in the bin with larger $m_{\text{eff}}^{\text{incl}}$ values, The shapes of background and signal distributions are thus very distinctive (top right). This feature is more pronounced when dividing the signal region into four subregions as shown in the bottom left plot or ten subregions as shown in the plot bottom right. The relative statistical uncertainties on the background estimate however increase if choosing a finer binning. Any event having a $m_{\text{eff}}^{\text{incl}}$ value larger than the range plotted will be added to the last bin displayed.

10.1 Using the shape of background and signal distributions

Previous analyses targeting final states with a lepton [3, 133] interpreted the results by using a "cut-and-count" approach without profiting from distinct shapes of background and signal distributions in the signal regions. Examples which illustrate the differences between both approaches in a signal region (in which the events in the electron and muon channels were combined) are shown in Figure 10.1. An analysis in "cut-and-count" style only compares the number of background to signal events in the signal regions. Analyses also considering the shapes of background and signal distributions divide the signal regions (or any other region) into subregions. For example, the signal regions of this analysis are divided into four subregions with $m_{\text{eff}}^{\text{incl}} \in [800, 1000)$ GeV, $m_{\text{eff}}^{\text{incl}} \in [1000, 1200)$ GeV, $m_{\text{eff}}^{\text{incl}} \in [1200, 1400)$ GeV or $m_{\text{eff}}^{\text{incl}} \in [1400, \infty)$ GeV in the electron and in the muon channel. In the case of the specific signal model in Figure 10.1, the regions with smaller $m_{\text{eff}}^{\text{incl}}$ values have a lower signal to background ratio in contrast to the regions with higher $m_{\text{eff}}^{\text{incl}}$ values which are largely dominated by signal. All of these subregions are fitted simultaneously with the signal (and the background) being constrained in all subregions. This simultaneous fit of multiple regions is called *shape fit* in the

following.

A shape fit in the signal regions has various advantages:

- More regions imply more constraints on the signal (and on the background, although the background is mostly constrained in the control regions) due to more measurements.

- The different characteristics of the distributions of signal and background are explicitly considered.

- Due to the different properties of different signal models, a given signal region cannot be optimal for all models. Dividing a signal region into subregions effectively means using more than one signal region. These can be chosen such that different subregions are optimal for different signal models.

The last point is extensively used in the $20.3\,\text{fb}^{-1}$ analysis, detailed in the next part of this work.

The $5.8\,\text{fb}^{-1}$ analysis also divides the control regions into subregions as detailed in Section 10.3.1. Originally introduced to reduce the size of systematic uncertainties, considering shapes in control regions is used in this analysis mainly to correct shapes of backgrounds to match the data. For such a correction, it is essential that every background is constrained in a control region dominated by this background with negligible signal contamination. The control regions used in the $5.8\,\text{fb}^{-1}$ analysis have been checked for possible signal contamination in [199]. The signal contamination was found to be below 10% in all control regions.

Shape fits in control and signal regions were used in [15] for the first time. The usage of a shape fit resulted in an increase of the sensitivity of around 50 GeV in $(m_0, m_{1/2})$ in the MSUGRA/CMSSM grid. The same binning as employed in [15] is used for the signal regions presented here (four bins with a width of 200 GeV between 800 and 1600 GeV).

The technical implementation of the shape fits relies on the construction of a parametrised probability density function based on binned histograms which is detailed in the next section.

10.2 The likelihood

This section describes the format of the statistical model which is fitted to data to obtain background estimates in the signal regions and to derive limits on new physics.

The model describing backgrounds including uncertainties (and signal, see Sections 10.4 and 10.4.4) in all control (and validation or signal) regions is based on a parametrised probability density function[1] (pdf) which is constructed from binned `ROOT` histograms. The pdf has the following form[2] consisting of Poisson terms (representing counting experiments in histogram bins) and constraint terms (constraining statistical and systematic uncertainties by external

---

[1]The pdf is built by using the tool `histfactory` [208] which is based on `RooStats` [209] and `RooFit` [210]. The pdf is created in a format which eases further processing with `RooStats` and `RooFit` tools. This analysis is based on the tool `HistFitter` [186], which is a wrapper around the `histfactory` tool. In particular, `HistFitter` builds the histograms needed as input for `histfactory` and provides information about the regions and backgrounds including uncertainties to be used by `histfactory`. It also organises the further processing of the pdf produced by `histfactory` by providing functions and classes to fit the model with various options, to evaluate p-values and to perform hypothesis tests of the model and the data (through appropriate calls of the `RooStats` and `RooFit` tools).

[2]The rest of this section follows closely the documentation of `histfactory` [208] in conventions and content.

measurements):

$$P(n_{cb}, a_p | \phi_p, \alpha_p, \gamma_b) = (\underbrace{ \prod_{c \in \text{channels}} \prod_{b \in \text{bins}} \text{Pois}(n_{cb} | \nu_{cb}) }_{\text{Poisson terms}}) \cdot \underbrace{ G(L_0 | \lambda, \Delta_L) \cdot \prod_{p \in S+\Gamma} f_b(a_p | \alpha_p) }_{\text{Constraint terms}} \quad (10.2.1)$$

with:

- $c \in$ channels. The channels comprise all regions appearing in the analysis: control, validation and signal regions.

- $b \in$ bins of the histograms used in the construction of the pdf.

- $p \in$ parameters (comprising normalisation parameters and nuisance parameters related to systematic uncertainties, see below).

- $S = \{\alpha_p\}$: the set of all parameters associated to systematic uncertainties with external constraint.

- $\Gamma = \{\gamma_{csb}\}$: the set of all bin-by-bin uncertainties with constraint (detailed below).

In addition the variable $s \in$ samples is required below. The samples include all backgrounds, data and possibly a signal.

The data in channel c and bin b is given by n_{cb}. The pdf is equivalent to the likelihood L if taking n_{cb} as fixed.

The constraint term $f_b(a_p | \alpha_p)$ in 10.2.1 describes the auxiliary measurements a_p for systematic uncertainties represented by the nuisance parameters α_p. An example is the uncertainty on the jet energy scale, which is constrained by measurements outside this analysis.

The Poisson terms $\text{Pois}(n_{cb} | \nu_{cb}) = \frac{\nu_{cb}^{n_{cb}} e^{-\nu_{cb}}}{n_{cb}!}$ give the probability to observe n_{cb} events when ν_{cb} events are expected in channel c and bin b.

The expected number of events ν_{cb} is given by:

$$\nu_{cb}(\phi_p, \alpha_p, \gamma_b) = \lambda_{cs} \gamma_{cb}(\alpha_p) \phi_{cs} \eta_{cs}(\alpha_p) \sigma_{csb}(\alpha_p) \quad (10.2.2)$$

This expression includes the luminosity parameter λ_{cs} for a given channel c and sample s which can be fixed to the nominal luminosity L_0 or can float as common luminosity parameter for all samples in all channels. In this case, the luminosity is constrained by the Gaussian term $G(L_0 | \lambda, \Delta_L)$ in the Likelihood 10.2.1. In this, Δ_L gives the uncertainty on the luminosity.

The parameter γ_{cb} is related to bin-by-bin scale factors for the statistical uncertainties or bin-by-bin shape systematic uncertainties. This corresponds to the first two types of systematic uncertainties detailed in Table 10.1. In the case where it is related to statistical uncertainties, the uncertainty in one bin includes all statistical uncertainties for all samples in a channel in this bin.

The parameters ϕ_{cs} are a product of all unconstrained normalisation factors for channel c and sample s: $\phi_{cs} = \prod_{p \in N_c} \phi_p$ with N_c being the set of all normalisation parameters of channel c. In particular, ϕ_{cs} can include free normalisation factors for the $t\bar{t}$ and $W+$jets backgrounds as well as for the signal.

The parameter $\eta_{cs}(\alpha_p)$ controls the overall normalisation of a nominal histogram in channel c and for sample s. It is constrained by a Gaussian term and is used for systematic uncertainties

Type	Description
shapeSys	• unconstrained uncertainty of Gaussian form • may vary in each bin independently from other bins
Statistical error on MC	• bin-by-bin variation, independent from any other bin • used for the Poisson statistical error on the sum of all Monte Carlo contributions in a bin • omitted in a particular bin when its statistical error does not exceed 5%

overallSys	• used for systematic uncertainties that only vary the scale
	  and not the shape
	• Gaussian with mean $1 \pm \alpha$ and width $\sigma \cdot E$,
	  E is the uncertainty before the fit, α and σ are fit parameters

histoSys	• variations of the shape and the scale with respect to a nominal histogram • up and down variations with respect to nominal given by histograms • variation parametrised as $\alpha \pm \sigma \cdot E_i$ where α and σ fit parameters and E_i the uncertainty in each bin • the bins in the histograms are correlated
normHistoSys	• similar to histoSys • only variation of the shape and not of the overall normalisation • the normalisation is absorbed into a floating background yields parameter

overallNormHistoSys	• for uncertainties on the transfer factor between control and signal regions
	• the nominal, up and down histograms are normalised to the yields
	  in a normalisation region, typically the control regions
	• the shape variations of the normalised histograms are handled with
	  the type histoSys, the overall normalisation by the type overallSys
	• the background topology needs to be similar in control and signal regions

Table 10.1: Description of the different implementations for uncertainties. The interpolation methods between the variations and the nominal values are explained in [208].

that only vary the scale of a nominal histogram, but not the shape (described by the type overallSys in Table 10.1).

The parameter σ_{csb} is used for systematic uncertainties that vary both the scale and the shape (as for example the type histoSys in Table 10.1) of a nominal histogram with bins b for sample s and in channel c.

In summary, systematic uncertainties are included as nuisance parameters in the likelihood. Their inclusion is possible in different ways as summarised in Table 10.1. In particular, systematic uncertainties can be included as uncertainty on the shape of the original nominal histogram or on the normalisation depending on the origin and purpose of the systematic uncertainty. Mixtures are also possible. The jet energy scale can for example vary both the normalisation and the shape of distributions (in particular for $m_{\mathrm{eff}}^{\mathrm{incl}}$) and is therefore implemented as type histoSys or overallNormHistoSys. The detailed implementation is discussed below.

10.3   Background-only fit

Background estimates in the signal and validation regions are obtained in the *background-only fit*, which does not incorporate signal contributions in control, validation or signal regions. Normalisations and systematic uncertainties are determined in the control regions and extrapolated to signal and validation regions.

The first part of this section, Subsection 10.3.1, details how the background-only fit is designed for this analysis. The results obtained, in particular the background yields in the signal regions, are detailed the second part, Subsections 10.3.2, 10.3.3 and 10.3.4.

Systematic uncertainty	Name	Type	Comment
Shape and scale variations			
Jet energy scale	α_{JLow}	`histoSys`	For jets with $p_{\text{T}} < 40$ GeV
	α_{JMedium}	`histoSys`	For jets with $40 < p_{\text{T}} < 100$ GeV
	α_{JHigh}	`histoSys`	For jets with $p_{\text{T}} > 100$ GeV
Jet energy resolution	α_{JER}	`histoSys`	No down variation
Scale of soft term of $E_{\text{T}}^{\text{miss}}$	α_{SCALEST}	`histoSys`	
Resolution of soft term of $E_{\text{T}}^{\text{miss}}$	α_{RESOST}	`histoSys`	
Scale varations			
Trigger scale factor	α_{TEel}	`overallSys`	Electron channel
	α_{TEmu}	`overallSys`	Muon channel
Lepton identification scale factor	α_{LEel}	`overallSys`	Electron channel
	α_{LEmu}	`overallSys`	Muon channel
Muon energy resolution	α_{LRImu}	`overallSys`	Inner detector (muon channel)
	α_{LRMmu}	`overallSys`	Muon spectrometer (muon channel)
Electron energy scale	α_{LESel}	`overallSys`	Electron channel
b-tagging scale factors	α_{BT}	`overallSys`	Only regions where b-tagging used
Theoretical uncertainties on $t\bar{t}$ and W+jets backgrounds, only in the signal regions			
Generator uncertainties	α_{GenW}	`overallSys`	On W/Z+jets background
	α_{GenTop}	`overallSys`	On $t\bar{t}$ background

Table 10.2: The systematic uncertainties as included for the backgrounds are summarised together with their parameter names and types. Two different groups of uncertainties are used, the first group varying the shape and scale of the nominal histograms, the second group only the scale.

10.3.1 Implementation

All four control regions (Top and W+jets control regions in the electron and the muon channels) are fitted simultaneously in a shape fit. Each of the control regions is divided in four subregions along $m_{\text{eff}}^{\text{incl}}$ with $m_{\text{eff}}^{\text{incl}} \in [500, 700)$ GeV, $m_{\text{eff}}^{\text{incl}} \in [700, 900)$ GeV, $m_{\text{eff}}^{\text{incl}} \in [900, 1100)$ GeV and $m_{\text{eff}}^{\text{incl}} \in [1100, 1300)$ GeV (the reasoning for a shape fit in $m_{\text{eff}}^{\text{incl}}$ is given below in Section 10.3.2.).

In each of these four control regions (and equivalently in the signal and validation regions) the following samples are defined:

- $t\bar{t}$ background: This background is assigned a free normalisation parameter μ_{Top} initially with a value of 1. This parameter may change the scale of the $t\bar{t}$ background.

- W/Z+jets backgrounds: The Z+jets background is negligible for this analysis, but its topology is similar to the W+jets background. Therefore, both the W+jets and Z+jets backgrounds are fitted together and have a common free normalisation parameter μ_{WZ} assigned.

- QCD-multijet background: This background is included in the fit with the estimates obtained by the matrix method. This background is only allowed to vary within the uncertainties of this estimate.

- Other backgrounds: Consisting of single t and diboson backgrounds. These backgrounds do not obtain a free normalisation factor, instead their scale may vary within 20 % which covers the theoretical uncertainties for these backgrounds. This uncertainty is added as `overallSys` type with parameter α_{errBG}.

- Data.

Each of these samples obtains systematic uncertainties as described in Table 10.2 and statistical

uncertainties on the Monte Carlo prediction. The origin of the systematic uncertainties was described in Chapter 4. The systematic uncertainties include uncertainties that vary the shape or the scale of the nominal distributions or both. The most important uncertainties are the uncertainties on the jet energy scale and resolution, which can modify the normalisation and the shape, the uncertainties on the b-tagging scale factors and the theoretical uncertainties. The latter two uncertainties can only modify the normalisation.

The uncertainty on the jet energy scale depends on the jet transverse momentum and is therefore split into three categories. It is described by three parameters. The first category includes all low p_T jets with $p_T < 40$ GeV, the second category all medium p_T jets with $40 < p_T < 100$ GeV and the last category all high p_T jets with $p_T > 100$ GeV. As the uncertainties on the jet energy scale for low, medium or high p_T jets are derived from different data samples, they are uncorrelated. This separation is motivated by the assumption that the control regions are populated mainly by medium p_T jets and the signal regions mainly by high p_T jets. By using this fit configuration, medium p_T jets cannot constrain the uncertainties on the jet energy scale for high p_T jets.

The theoretical uncertainties for the $t\bar{t}$ and the W+jets background were evaluated as uncertainties due to the generator used. For this, distributions produced by using the generator were compared to the appropriate distributions with the parameters of the generator (as for example the renormalisation and factorisation scale) varied in a truth level study.

Further systematic uncertainties are added when including a signal in the exclusion fit as described in Section 10.4.4.

10.3.2 Simultaneous fit in the control regions

The simultaneous fit to data in the control regions aims to correct the normalisation of the two main backgrounds, $t\bar{t}$ and W+jets, and to correct the shapes of those backgrounds to data. As shown in Section 8.1 in Figure 8.1, the $m_{\text{eff}}^{\text{incl}}$ distribution as obtained from the sum of all Monte Carlo distribution does not match the data in W+jets control regions. The $m_{\text{eff}}^{\text{incl}}$ distribution was therefore chosen as variable for the shape fit. The control regions after the background-only fit are shown in Figures 10.2 and 10.3 (along with the distributions before the fit which are the same distributions as in Figure 8.1 but with the background summarised as used in the fit). The agreement of the background estimates with data is considerably improved with respect to the agreement before the fit in Figure 8.1, in particular in the W+jets control regions. The remaining differences between data and background estimates are within the uncertainties.

The detailed comparison between data and background estimates is shown in Table 10.3. This table shows in the lower part the background yields before the fit (marked with 'expected'). The QCD multi-jet background estimate is obtained by the matrix method as described, the other backgrounds are given with their Monte Carlo prediction. The middle part gives the background estimates after fit.

The $t\bar{t}$ and W+jets backgrounds were allowed to vary with free normalisation parameters. These normalisation parameters were fitted to

$$
\begin{aligned}
\mu_{\text{Top}} &= 1.1 \pm 0.3 \\
\mu_{\text{WZ}} &= 0.7 \pm 0.3
\end{aligned}
\tag{10.3.3}
$$

The $t\bar{t}$ background yield is only slightly changed after the fit as its normalisation factor is close to 1. The W/Z+jets background in contrast is scaled down by 30 %. The difference between
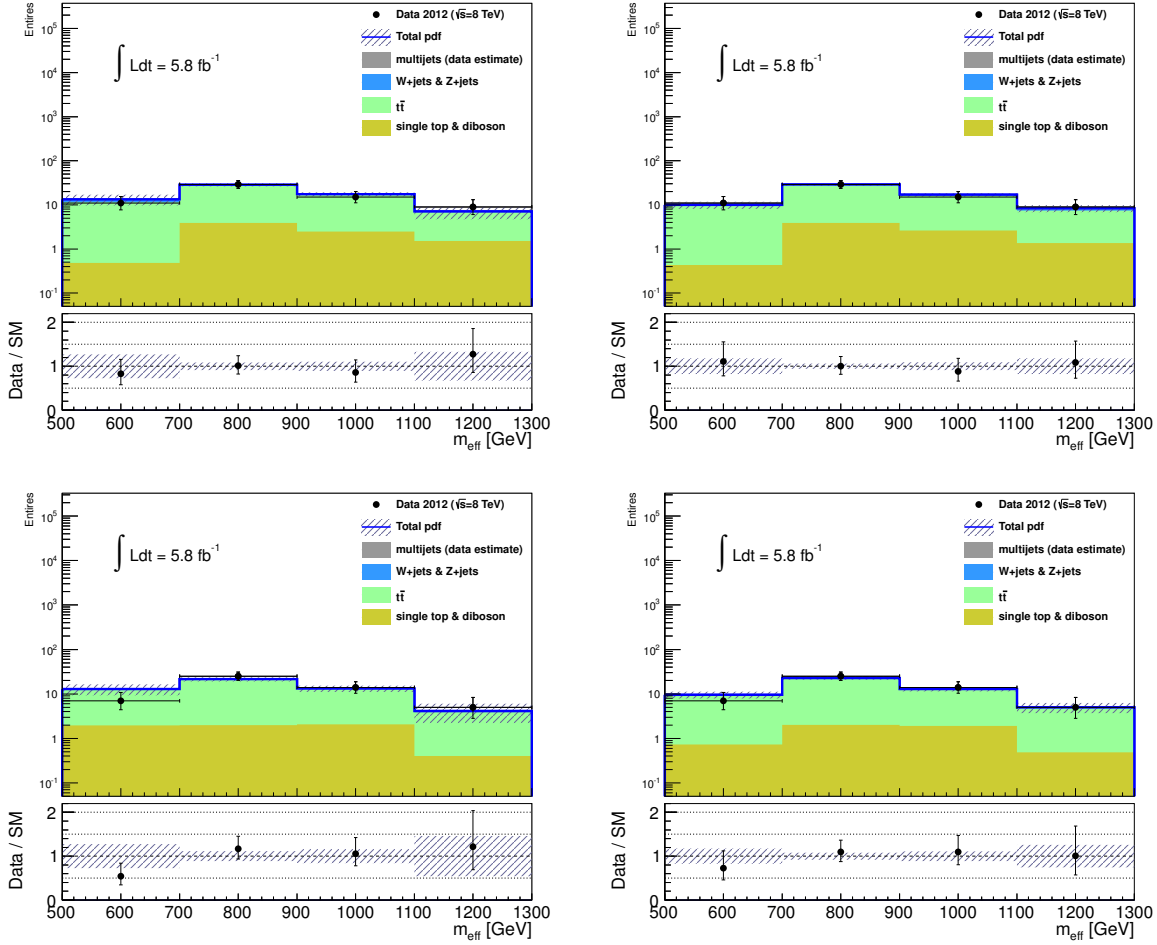
Figure 10.2: The $m_{\mathrm{eff}}^{\mathrm{incl}}$ distributions are shown in the Top control regions in the electron (top) and muon channel (bottom) before (left) and after the fit (right). The agreement between data and background estimates is improved after the fit. The author contributed similar plots to [199].

before and after fit yields for the W/Z+jets background in the W+jets control regions is larger than this 30 %, but within the statistical and systematic uncertainties. The total background estimate after correction by the fit agrees well with the observed data as shown in the upper part of the table. The agreement is visualised in the pull plot in Figure 10.4, where the difference of the observed data subtracted by the number of expected events is normalised to the total uncertainty (including statistical and systematic uncertainties). It should be noted however, that the good agreement between background estimates and observed data comes by construction of the fit in the control regions.

Table 10.3 also shows that while the Top control regions are almost pure in $t\bar{t}$ events, the W+jets control regions show a relatively high $t\bar{t}$ background contribution between 20 and 30 %. This contribution by $t\bar{t}$ events arises from the cut on $m_{\mathrm{T}} > 100$ GeV for the control regions, which suppresses the W+jets background effectively. This cut was introduced in order to move the control regions as close to the signal regions as possible. However, since the main background in the signal regions is composed of $t\bar{t}$ events, the purity of the W+jets control regions is considered to be sufficient.
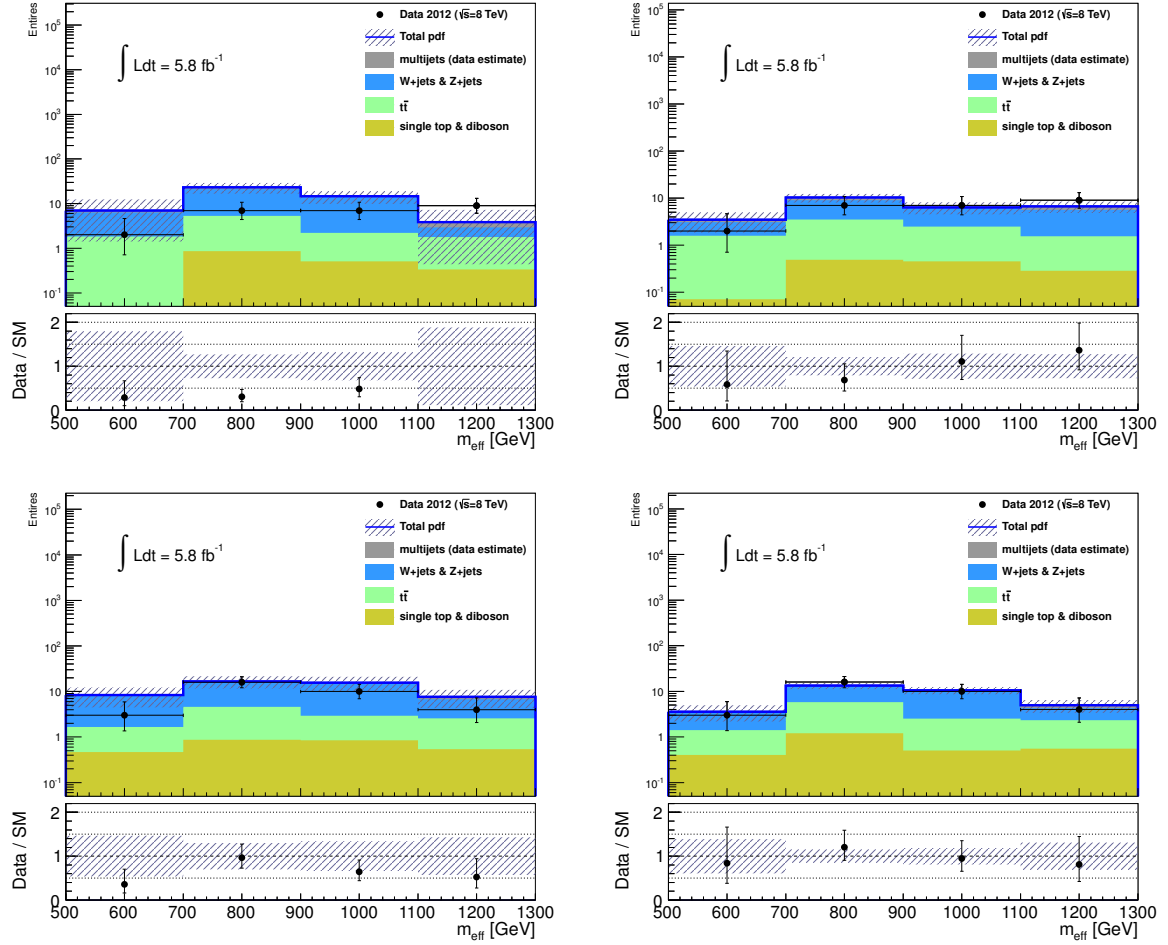
Figure 10.3: The $m_{\text{eff}}^{\text{incl}}$ distributions are shown in the W+jets control regions in the electron (top) and muon channel (bottom) before (left) and after the fit (right). The shape of the background estimates match the data within uncertainties after the fit. The author contributed similar plots to [199].

10.3.3 Extrapolation to the validation regions

The validation regions, placed between the control and signal regions in $E_{\text{T}}^{\text{miss}}$, are used to check the extrapolation to the signal regions from the control regions. The values of the normalisation and nuisance parameters as obtained in the background-only fit in the control regions are applied to the input Monte Carlo predictions. The detailed yields after the background-only fit as well as the Monte Carlo prediction before the background-only fit are summarised in Table 10.4. The background estimates in the validation regions after the fit are slightly higher than the observed number of data. However, the fitted background estimates are in agreement with observed data within 1σ, as shown in the pull plot in Figure 10.5.

10.3.4 Extrapolation to the signal regions

Similarly to the case of the validation regions, the results of the background-only fit in the control regions are extrapolated to the signal regions. The fitted background estimate yields 9.0 ± 2.8 events in the electron channel and 7.7 ± 3.2 events in the muon channel, while 10 events are observed in the electron channel and 4 events in the muon channel. While the background estimates in both channels are comparable, the data shows an underfluctuation in

| | Top control region | | W+jets control region | |
	Electron	Muon	Electron	Muon
Observed events	64	51	25	33
Fitted background events	64 ± 6	50 ± 5	27 ± 5	32 ± 5
Fitted $t\bar{t}$ events	54 ± 7	45 ± 6	7.8 ± 2.0	9.4 ± 2.1
Fitted W/Z+jets events	1.3 ± 1.2	$0.0^{+1.8}_{-0.0}$	15 ± 4	20 ± 5
Fitted other background events	8.3 ± 1.9	5.1 ± 1.9	1.3 ± 0.7	2.7 ± 0.7
Fitted multijet events	$0.5^{+1.5}_{-0.5}$	$0.5^{+0.7}_{-0.5}$	$2.6^{+3.0}_{-2.6}$	$0.6^{+0.8}_{-0.6}$
MC expected SM events	67	52	48	48
MC expected $t\bar{t}$ events	55	45	9.5	9.0
MC expected W/Z+jets events	2.6	0.0	34	36
MC expected other background events	8.4	6.4	1.7	2.7
Data-driven multijet events	0.4	0.5	3.5	0.9

Table 10.3: Background-only fit results for the Top and W+jets control regions, for an integrated luminosity of 5.8 fb^{-1}. The lower part of the table gives the nominal Monte Carlo expectations for comparison. The uncertainties shown include statistical and systematic uncertainties. The author contributed a similar table to [199, 185].
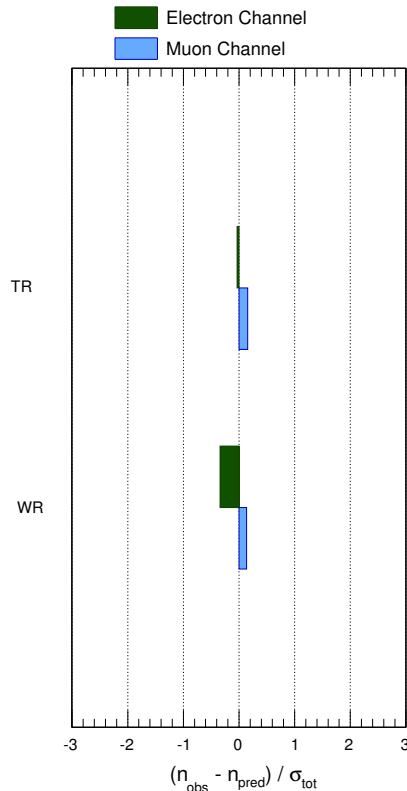
Figure 10.4: The pull, defined as the number of observed events subtracted by the number of fitted background events divided by the total uncertainty on the fitted number of background events, is shown for the control regions (TR indicates the Top control regions and WR the W+jets control regions). The good agreement with zero is obtained by construction of the background-only fit.

	Validation region	
	Electron	Muon
Observed events	32	30
Fitted background events	40 ± 7	40 ± 8
Fitted $t\bar{t}$ events	27 ± 6	22 ± 5
Fitted W/Z+jets events	5.7 ± 2.2	14 ± 6
Fitted other background events	5.5 ± 1.3	4.9 ± 2.0
Fitted multijet events	$1.5^{+1.9}_{-1.5}$	0.0 ± 0.0
MC expected SM events	43	46
MC expected $t\bar{t}$ events	25	20
MC expected W/Z+jets events	10	20
MC expected other background events	5.8	5.5
Data-driven multijet events	1.5	0.0

Table 10.4: Background-only fit results for the validation regions in the electron and in the muon channel, for an integrated luminosity of 5.8 fb^{-1}. The uncertainties shown include the statistical and systematic uncertainties. The author contributed a similar table to [199, 185].
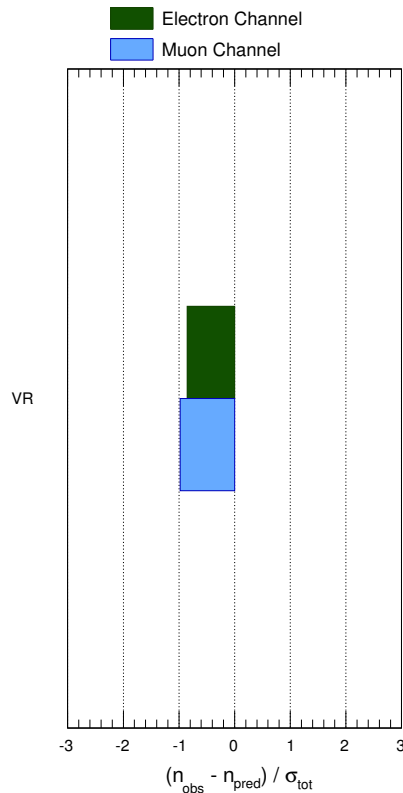
Figure 10.5: The pulls are shown for the two validation regions (indicated as VR in the plot) in the electron (green) and in the muon channel (blue). The fitted background estimates slightly overestimate the observed data, therefore the pulls are shifted to negative values. However, the discrepancies are within 1σ when considering all uncertainties.

| | Signal region | |
	Electron	Muon
Observed events	10	4
Fitted background events	9.0 ± 2.8	7.7 ± 3.2
Fitted $t\bar{t}$ events	6.0 ± 2.2	2.6 ± 1.9
Fitted W/Z+jets events	1.5 ± 0.7	4.2 ± 2.3
Fitted other background events	1.0 ± 0.7	0.88 ± 0.31
Fitted multijet events	0.4 ± 0.6	0.0 ± 0.0
MC expected SM events	9.5	12
MC expected $t\bar{t}$ events	5.7	4.6
MC expected W/Z+jets events	2.4	6.0
MC expected other background events	1.0	0.8
Data-driven multijet events	0.4	0.0

Table 10.5: Background-only fit results for the signal regions in the electron and in the muon channel, for an integrated luminosity of 5.8 fb^{-1}. The lower part of the table shows the background estimates as obtained from Monte Carlo or from the matrix method before the background-only fit, the upper part the corrected values after the fit. The uncertainties shown include statistical and systematic uncertainties. The author contributed a similar table to [199, 185].

the muon channel. Agreement between data and fitted background estimates is seen in the electron channel. In the muon channel, the agreement is also within 1σ as shown in the pull plot in Figure 10.6. In summary, this analysis does not observe an excess of events beyond Standard Model expectations.

The uncertainties on the background estimates contain both systematic and statistical uncertainties. A break-down into the various components is given in Table 10.6. The values for any given single floating parameter in this table is derived by setting all other parameters to constant and propagating the uncertainties due to this parameter only. Due to correlations between the single floating parameters, the final uncertainties do not necessarily match to the squared sum of the single uncertainties. The correlations are given in the Appendix C.1. The largest correlations are between the parameters related to the jet energy scale or those related to the b-tagging scale factors and the normalisation parameters of the $t\bar{t}$ or W+jets backgrounds.

The statistical uncertainties have the largest contribution to the total uncertainty in both channels. The second most important uncertainty is due to the error on the normalisation parameter of the $t\bar{t}$ background (W/Z+jets background) in the electron (muon) channel. Large uncertainties also arise from the theoretical uncertainties on the Monte Carlo generator for the W/Z+jets background in the muon channel and the $t\bar{t}$ background in the electron channel. Further important contributions are the uncertainties due to the jet energy scale and resolution and due to the QCD multi-jet background estimation.

The $m_{\mathrm{eff}}^{\mathrm{incl}}$ distributions in the signal regions after the background-only fit are shown in Figure 10.7. In general, a reasonable agreement between data and fitted background estimates is visible, although no data event was observed for high values of $m_{\mathrm{eff}}^{\mathrm{incl}}$ in the muon channel.

10.4 Limits

Limits are evaluated by hypothesis testing in which the background-only assumption is compared to a signal plus background assumption. In the following section, the test statistics used in
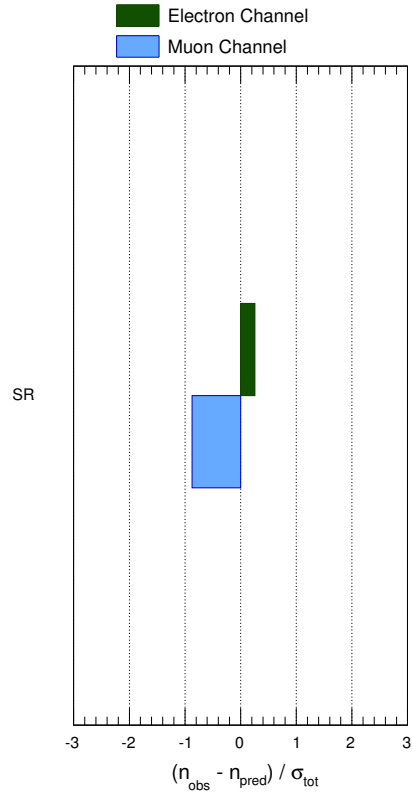
Figure 10.6: The pull after the background-only fit is shown for the signal regions in the electron (blue) and the muon channel (green) (the signal regions are abbreviated with SR). Discrepancies between observed data and the fitted background estimates are within 1σ.
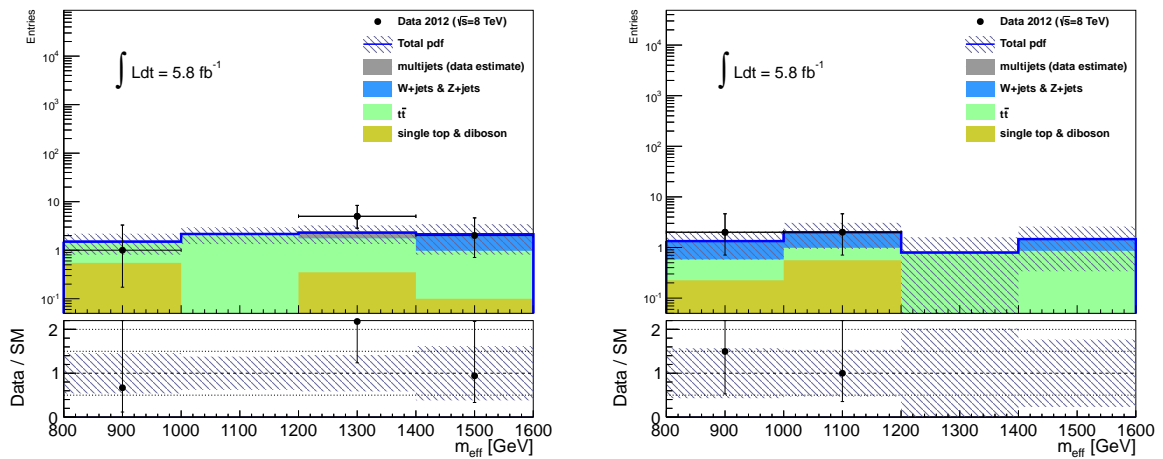
Figure 10.7: The $m_{\mathrm{eff}}^{\mathrm{incl}}$ distributions are shown in the signal regions in the electron channel (left) and in the muon channel (right) after the background-only fit.

Signal region	electron channel	muon channel
Total statistical ($\sqrt{N_{\mathrm{obs}}}$)	±3.2	±2.0
Total background systematic	±2.8	±3.2
MC generator ($t\bar{t}$, α_{GenTop})	±0.9	±0.4
MC generator (W+jets, α_{GenW})	±0.30	±0.9
Jet energy resolution (α_{JER})	±0.5	±1.5
Jet energy scale (high p_{T} jets, α_{JHigh})	±0.6	±0.4
Jet energy scale (low p_{T} jets, α_{JLow})	±0.05	±0.09
Jet energy scale (medium p_{T} jets, $\alpha_{\mathrm{JMedium}}$)	±0.23	±0.9
Electron energy scale (α_{LESel})	±0.4	±0.00
Electron identification (α_{LEel})	±0.11	±0.00
Muon energy resolution (muon spectrometer, α_{LRMmu})	±0.00	±0.14
QCD multi-jet estimate ($\alpha_{\mathrm{QCD\ multi-jet}}$)	±0.6	±0.00
Resolution of soft term in $E_{\mathrm{T}}^{\mathrm{miss}}$ (α_{RESOST})	±0.6	±0.018
Scale of the soft term in $E_{\mathrm{T}}^{\mathrm{miss}}$ ($\alpha_{\mathrm{SCALEST}}$)	±0.05	±0.04
Trigger scale factors (electron channel, α_{TEel})	±0.05	±0.00
Uncertainties on small backgrounds (α_{errBG})	±0.20	±0.17
Statistical uncertainties (γ_{stat})	±2.0	±2.2
W/Z+jets yield	±0.6	±1.8
$t\bar{t}$ yield	±1.5	±0.6

Table 10.6: Breakdown of the dominant systematic uncertainties on background estimates in the signal region in the electron and muon channels. Note that the individual uncertainties can be correlated, and do not necessarily add up quadratically to the total background uncertainty. The correlation between the parameters are given in the Appendix. The author contributed a similar table to [199, 185].

the hypothesis testing is introduced. In standard hypothesis testing, signal plus background assumptions could mistakenly be excluded if the signal contribution is very small and thus the background-only and signal plus background assumptions are very similar. Using the CL_s method, this can be avoided as explained in Section 10.4.2. Model independent upper limits on the visible cross section and limits in the MSUGRA/CMSSM model are derived based on this method at the end of this section.

10.4.1 Test statistics

To distinguish between a pure background model b and a model including signal and background $s + b$ the definition of a test statistics is necessary.

Starting with the pdf in Equation 10.2.1, the number of expected events in this pdf is rewritten as[3] $\nu = \mu s + b$ with b the number of background events expected, s the number of signal events expected and $\mu = \frac{\sigma}{\sigma_{\mathrm{SIG}}}$ the signal strength with σ_{SIG} being the theoretical signal cross section and σ the assumed cross section to be tested. For $\mu = 1$ the signal plus background model $s + b$ is obtained, for $\mu = 0$ the background-only model b. The likelihood $L(\mu, \boldsymbol{\theta})$ which depends on the signal strength μ and a vector $\boldsymbol{\theta}$ of nuisance parameters is equivalent to the pdf in Equation 10.2.1 if considering the number of observed events n in the pdf as fixed. The nuisance parameters in the vector $\boldsymbol{\theta}$ contain both the normalisation parameters related to backgrounds, systematic and statistical uncertainties described in Sections 10.2 and 10.3.1.

---

[3]Indices referring to channels and bins are omitted in the following.

Based on the likelihood L, the *profile likelihood ratio* is defined as [211][4]:

$$\lambda(\mu) = \frac{L(\mu, \hat{\hat{\boldsymbol{\theta}}})}{L(\hat{\mu}, \hat{\boldsymbol{\theta}})} \qquad (10.4.4)$$

where $\hat{\mu}$ and $\hat{\boldsymbol{\theta}}$ maximise the likelihood L (they are the Maximum Likelihood Estimators). For a given μ, $\hat{\hat{\boldsymbol{\theta}}}$ maximises the likelihood L; $\hat{\hat{\boldsymbol{\theta}}}$ is therefore a function of μ.

The profile likelihood ratio $\lambda(\mu)$ takes values between 0 and 1 by definition. Values of 1 are obtained when there is a good agreement between the observed data and the tested value of μ.

The test statistics t_μ is defined by:

$$t_\mu = -2 \ln \lambda(\mu) \qquad (10.4.5)$$

Large values of t_μ correspond to a bad agreement between the tested μ and the observed data. The p-value provides a measure for the agreement between data and the assumed model. A p-value is defined as the probability to find values of the test statistics equally or less compatible with the observed test statistics:

$$p_\mu = \int_{t_{\mu,\mathrm{obs}}}^{\infty} f(t_\mu|\mu) dt_\mu \qquad (10.4.6)$$

where $f(t_\mu|\mu)$ is the probability density function. The test statistics in Equation 10.4.5 is modified for special cases as discussed in the following. The signal strength is always taken to be 0 or positive. Therefore, the test statistics takes the following form:

$$\tilde{t}(\mu) = -2 \ln \tilde{\lambda}(\mu) \qquad (10.4.7)$$

with

$$\tilde{\lambda}(\mu) = \begin{cases} \dfrac{L(\mu, \hat{\hat{\boldsymbol{\theta}}}(\mu))}{L(\hat{\mu}, \hat{\boldsymbol{\theta}})} & \text{for } \hat{\mu} \geq 0 \\[3mm] \dfrac{L(\mu, \hat{\hat{\boldsymbol{\theta}}}(\mu))}{L(0, \hat{\boldsymbol{\theta}}(0))} & \text{for } \hat{\mu} < 0 \end{cases} \qquad (10.4.8)$$

This test statistics is further modified for the calculation of upper limits (as used in the discovery and exclusion fits described below), because, in Equation 10.4.8, an upward fluctuation of the data with $\hat{\mu} > \mu$ (e.g. a case in which the data is much larger than expected by the model $\mu s + b$) could result in a rejection of the assumed μ (but upward fluctuations of the data should not be regarded as incompatible with the tested μ in the following). Thus, the test statistics $\tilde{q}_\mu$ is defined as:

$$\tilde{q}_\mu = \begin{cases} -2 \ln \tilde{\lambda}(\mu) & \text{for } \hat{\mu} \leq \mu \\ 0 & \text{for } \hat{\mu} > \mu \end{cases} \qquad (10.4.9)$$

---

[4]This section follows closely in notation and argumentation [211].
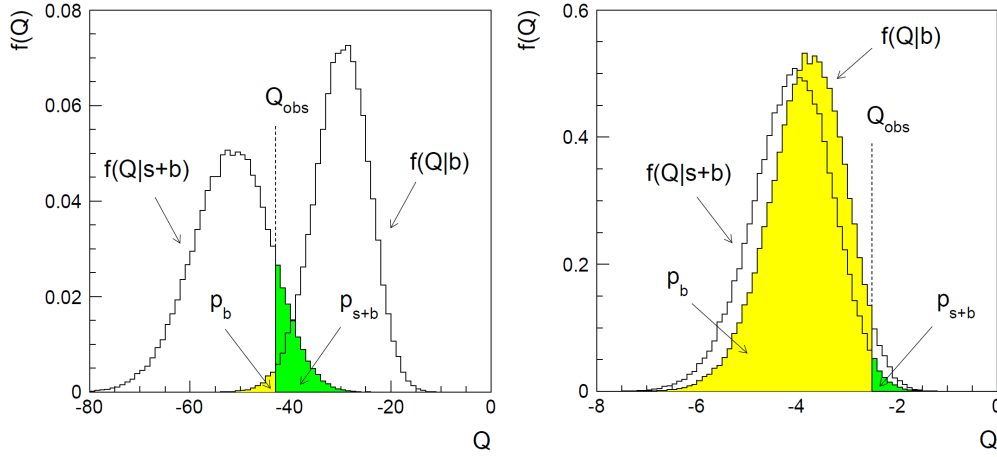
Figure 10.8: The distribution of the probability density functions for the background model ($f(Q|b)$) and signal+background model ($f(Q|s+b)$) are shown in cases where the two models can cleanly be distinguished (left) or are very close together due to a very small signal contribution (right). The test statistics is denoted by Q in these plots. The plots are taken from [214].

The probability density function $f(\tilde{q}_\mu|\mu)$ which constitutes the basis of the hypothesis test can be obtained by building pseudo experiments. In the large sampling limit (so in regions with sufficient statistics), however, an *asymptotic* expression is valid following results [211] by Wilks [212] and Wald [213]. This formulation is used in the second part of this work to derive the exclusion limits. It is given by:

$$
\tilde{q}_\mu = \begin{cases} \dfrac{\mu^2}{\sigma^2} - \dfrac{2\mu\hat{\mu}}{\sigma^2} & \text{for } \hat{\mu} < 0 \\ \dfrac{(\mu - \hat{\mu})^2}{\sigma^2} & \text{for } 0 \leq \hat{\mu} \leq \mu \\ 0 & \text{for } \hat{\mu} > \mu \end{cases} \tag{10.4.10}
$$

where σ is the standard variation of $\hat{\mu}$. The probability density function $f(\tilde{q}_\mu|\mu)$ can be derived from this expression and thus also the p-values.

10.4.2 CL_s method

A model consisting of the background b and with some signal contribution μs can be expressed as $\mu s + b$. For $\mu = 0$, a model without signal and only with background is obtained. This will be compared to the case where the signal is added with a signal strength of $\mu = 1$. The test statistics $\tilde{q}_\mu$ defined in the previous section is used to distinguish between background-only b and signal+background $s + b$ hypotheses by calculating the p-value for both cases.

The test statistics for both cases are visualised in Figure 10.8 for a case where the signal+background distribution is clearly distinguishable from the background only distribution and in a case where the signal expectation is very small and thus both distributions are very similar.

The p-value for the model $s + b$ is [215]:

$$
p_{s+b} = P(\tilde{q} \geq \tilde{q}_{obs}|s+b) = \int_{\tilde{q}_{obs}}^{\infty} f(\tilde{q}|s+b)d\tilde{q} \tag{10.4.11}
$$

110

	$\langle\epsilon\sigma\rangle^{95}_{\text{obs}}$[fb]	S^{95}_{obs}	S^{95}_{exp}	CL_b
Electron	1.69	9.9	$9.3^{+3.3}_{-2.6}$	0.59
Muon	1.09	6.4	$8.3^{+3.4}_{-2.3}$	0.19

Table 10.7: 95% CL upper limits on the visible cross section ($\langle\epsilon\sigma\rangle^{95}_{\text{obs}}$) and on the observed ($S^{95}_{\text{obs}}$) and expected ($S^{95}_{\text{exp}}$) number of signal events for the electron channel and the muon channel. The last column indicates the CL_b value, which is the confidence level observed for the background-only hypothesis. This table is taken from [185, 199].

and similarly for the background model:

$$p_b = P(\tilde{q} \leq \tilde{q}_{\text{obs}}|b) = \int_{-\infty}^{\tilde{q}_{\text{obs}}} f(\tilde{q}|b)d\tilde{q} \tag{10.4.12}$$

In the CL_{s+b} method, a signal model s is excluded if $p_{s+b} < \alpha$ where α is given by the desired confidence level, in this work: CL $= 1 - \alpha = 95\%$. Values of s which are not excluded are therefore in the confidence interval with the confidence level CL: The true value of s is covered by the interval $[0, s_{\text{up}}]$ with 95% probability, where s_{up} (upper limit on s) is the largest not excluded value of s.

The CL_{s+b} method allows to exclude models with very small signal strengths to which the analysis might not have a sensitivity. Such a case is shown in Figure 10.8 (right), where the test statistics of $s + b$ and b are very similar. This behaviour is avoided by multiplying a penalty term [216]:

$$CL_s = \frac{p_{s+b}}{1 - p_b} \tag{10.4.13}$$

In the case that $f(\tilde{q}|b)$ and $f(\tilde{q}|s + b)$ are widely separated, p_b will be small, and thus the term $1 - p_b$ close to 1. Therefore, the CL_s value will be close to the CL_{s+b} value. If, however, $f(\tilde{q}|b)$ and $f(\tilde{q}|s + b)$ are close together, the term p_b will be large and thus the CL_s value will be much larger than the CL_{s+b} value. Therefore, the CL_s method is more conservative than the CL_{s+b} method. A model is excluded according to the CL_s method, if the CL_s value falls below 5%. Only this method is used in the further course of this work.

10.4.3   Model independent upper limits

Upper limits on the visible cross section for physics beyond the Standard Model (i.e. the cross section evaluated inside a given signal region) are derived without any model dependence from the background-only fit results in Table 10.5, using observed data and the fitted background estimate in the signal regions.

For this, a special fit configuration is used in which no signal contamination in the control regions is allowed (thus the background estimates in the signal regions are the same as obtained in the background-only fit), but signal may present in the signal regions. The signal strength is scanned from $\mu = 0$ to high values of μ (μ is allowed to take values greater than 1 and for each assumed value of μ a hypothesis test as described is performed). The upper limit on the number of present signal events S^{95}_{obs} is given by the μ value for which the CL_s value (as defined in the last section) falls below 5%. The upper limit on the observed cross section $\langle\epsilon\sigma\rangle^{95}_{\text{obs}}$ is obtained by dividing this number of events by the integrated luminosity of 5.8 fb^{-1}.
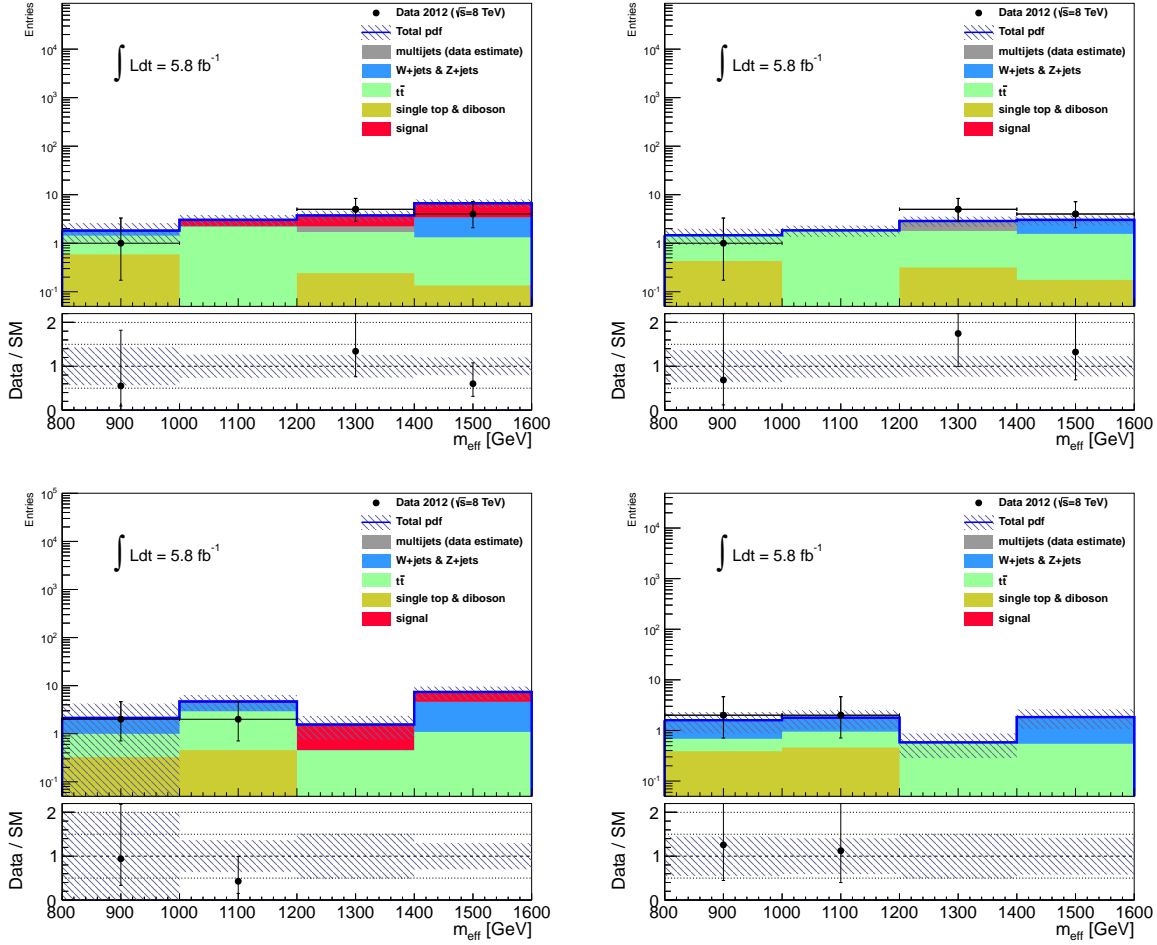
Figure 10.9: The $m_{\text{eff}}^{\text{incl}}$ distribution is shown before (left) and after (right) the exclusion fit in the electron (top) and the muon (bottom) channel. The exclusion fit is performed here by considering the point in the MSUGRA/CMSSM grid with coordinates $(m_0, m_{1/2}) = (2400, 350)$ GeV. The signal contribution is negligible after the fit to data.

The upper limits for this analysis are given in Table 10.7. In the electron channel, an upper limit of 9.9 signal events is obtained, which is in good agreement with the expected upper limit under background-only assumption. In the muon channel, an upper limit of 6.4 signal events is calculated, which is also in agreement with the expected upper limit within the uncertainties. The upper limits on the visible cross sections are 1.69 and 1.09 fb for the electron and muon channels, respectively.

10.4.4 Exclusion fit and interpretation

Limits in the MSUGRA/CMSSM grid are calculated by performing hypothesis tests using the CL_s method with the signal model defined by every grid point in the MSUGRA/CMSSM grid.

The fit setup of the *exclusion fit* differs from the background-only fit by allowing for signal presence in both the control and signal regions. Therefore, a further sample for the signal is introduced in the fit. The signal strength is a free floating parameter μ_{SIG}. This signal sample has the same systematic uncertainties assigned as the background samples with the exception of the jet energy scale. For the jet energy scale, a new parameter is added only to the signal sample to avoid that the background (through the jet energy scale parameters assigned to the
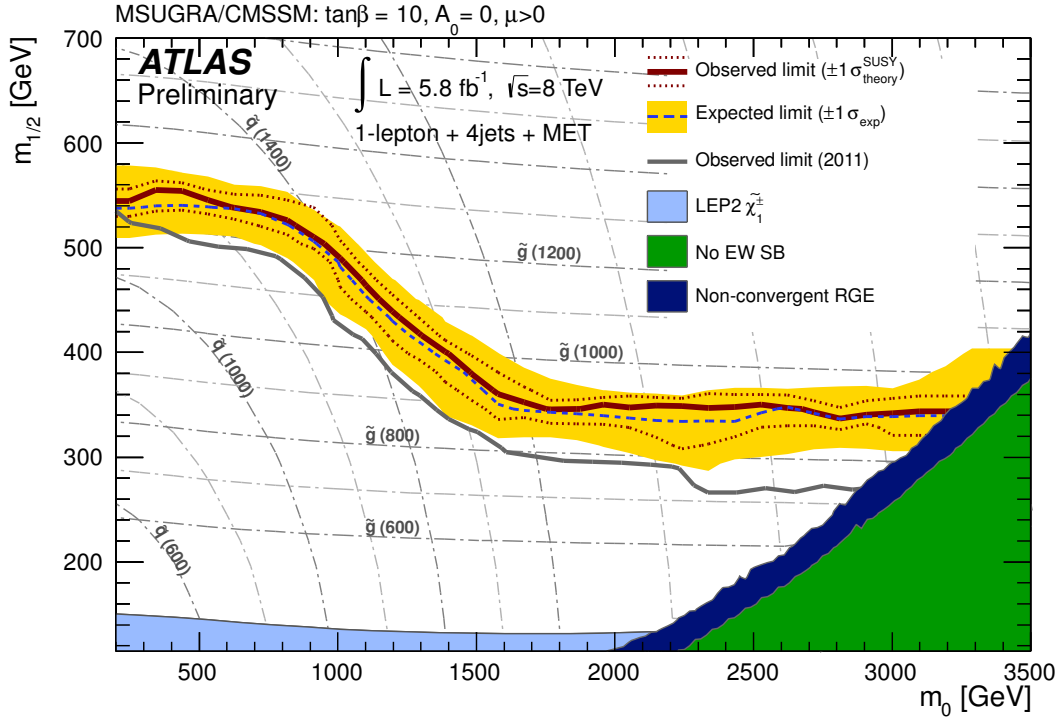
Figure 10.10: The analysis result is interpreted in the MSUGRA/CMSSM grid, defined by $\tan\beta = 10$, $A_0 = 0$, $\mu > 0$ [199, 185]. The limits are given as function of m_0 and $m_{1/2}$. Squark and gluino mass lines are also indicated. For small m_0 values, $m_{1/2}$ values smaller or equal to 530 GeV are excluded and $m_{1/2}$ values less than 320 GeV are excluded for any m_0 value. For equal squark and gluino masses, gluinos and squarks with a mass less than 1.2 TeV are excluded. All limits are given at 95 % confidence level. The author was involved in the production of this plot.

background samples) could constrain the jet energy scale uncertainty of the signal, because this could result in too small uncertainties on the signal component.

In addition, a nuisance parameter for the uncertainty on the signal cross section is added. For the MSUGRA/CMSSM grid, the signal cross sections are calculated at next-to-leading order and include the resummation effects of soft gluon emission at next-to-leading-logarithmic accuracy [185, 217, 218, 219, 220, 221]. The uncertainties on the cross sections are evaluated by varying the PDF sets and the factorisation and renormalisation scale [185] according to the method described in [222].

As described in Section 10.1, the signal regions are sub-divided into four regions along $m_{\text{eff}}^{\text{incl}}$ with four bins of equal distance (200 GeV) between 800 GeV and 1600 GeV. Any events - background, signal or data - with values larger than $m_{\text{eff}}^{\text{incl}} = 1600$ GeV are added to the last bin between $1400 < m_{\text{eff}}^{\text{incl}} < 1600$ GeV.

Figure 10.9 shows the $m_{\text{eff}}^{\text{incl}}$ distribution for the point $(m_0, m_{1/2}) = (2400, 350)$ GeV (in the MSUGRA/CMSSM grid) with nominal starting values and with optimised values for the normalisation and nuisance parameters after fit in the electron and in the muon channel. The signal, displayed in red, tends to peak at large values of $m_{\text{eff}}^{\text{incl}}$ before the fit and shows therefore a very different shape compared to the background. After the fit, the signal is reduced to a signal strength of less than 10^{-4} and is therefore not visible in the plots.

10.4.5 Interpretation in the MSUGRA/CMSSM grid

Evaluating the CL_s values for all points in the MSUGRA/CMSSM grid, the exclusion limit in Figure 10.10 is obtained. For this plot, the probability density functions used in the CL_s calculation have been evaluated by pseudo experiments.

The red curve in the plot shows the observed limit. This curve has been calculated by using the nominal signal cross sections. When modifying the signal cross sections (up or down) by their theoretical uncertainties, evaluated as described in the last subsection, the dotted red lines are obtained. They thus show the uncertainty on the observed limit due to variations of the signal cross section. The blue dashed line shows the expected limit in the background only hypothesis. The yellow band indicates the $\pm 1\sigma$ variations on the expected limit. All lines are given at 95% confidence level.

The squark and gluino masses are visualised by the light grey dotted-dashed lines. The observed limit crosses the squark mass line of 1400 GeV and follows the gluino mass line of 900 GeV at medium to large m_0 values.

The light blue area at low $m_{1/2}$ values is excluded by the LEP experiments [223]. Regions at low $m_{1/2}$ and high m_0 values are not allowed by theory due to the non-existence of electroweak symmetry breaking for the points inside the green area, or since the renormalisation group equations did not converge numerically for the points inside the dark blue area.

Values of $m_{1/2}$ less than ~ 320 GeV can be excluded for any m_0 value[5]. For small m_0 values, the exclusions reaches up to $m_{1/2}$ values of ~ 530 GeV. Squark and gluino masses of ~ 1.2 TeV are excluded for equal gluino and squark masses. For high m_0 values, gluino masses of 850 GeV are excluded for most regions.

The limits are compared to the limit obtained in the previous analysis focusing on final states with a lepton with 4.7 fb^{-1} of 7 TeV data in [224] which is shown by the grey curve. In comparison to the previous analysis, the limit is improved by ~ 50 GeV for equal gluino and squark masses, and by ~ 150 GeV for high m_0 values. This improvement is obtained because of the luminosity and energy increase with respect to the analysis in [224]. A re-optimisation of the signal regions has not taken place. Since the signal regions in use for this analysis have been designed for lower centre-of-mass energies and luminosities, the next part of this work will present a re-optimisation with the aim to obtain sensitivity also at higher gluino and squark masses.

---

[5]The reference for the excluded limit is the -1σ line.

Part IV

Results with the full dataset of 2012

Chapter 11

Overview

This part presents an analysis of the complete dataset of pp collisions at 8 TeV taken between April and December in 2012. The signal regions were re-optimised for this center-of-mass energy and for the increased statistics of $20.3\,\mathrm{fb}^{-1}$. The re-optimisation is discussed in Chapter 12.

The re-optimised signal regions target a different phase space. The signal regions are required to focus on the regions not yet excluded by previous analyses [131, 132], including the one described in the last part. This implies to assess higher squark or gluino masses which often requires harder criteria on $m_{\mathrm{eff}}^{\mathrm{incl}}$, m_{T} and $E_{\mathrm{T}}^{\mathrm{miss}}$ in the signal regions. Furthermore, the re-optimised signal regions are required to cover different topologies ranging from short decay chains originating from squark pair production to longer decay chains stemming from gluino pair production. Taking all the requirements together, the re-optimised signal regions are clustered in three groups with different jet multiplicities. One group, requiring at least three high energetic jets, is sensitive to squark pair production. The other groups with requirements for at least five or six jets are focusing on gluino pair production, including scenarios with longer decay chains. The sensitivity of these signal regions is discussed in Section 12.3. The shape fit, introduced in its principles in the previous part, turns out to be an important ingredient to cover as large a phase space as possible.

All of these signal regions impose tighter criteria on $m_{\mathrm{eff}}^{\mathrm{incl}}$, m_{T} and $E_{\mathrm{T}}^{\mathrm{miss}}$. Although the background estimation methods of the previous part, explained in Chapter 8, are also used for the analysis presented in this part, the re-optimised signal regions require the re-definition of the control and validation regions. Furthermore, the Monte Carlo samples used were adapted. The modifications are summarised in Chapter 13.1.

The fit setup increases in complexity to accommodate the three groups of signal regions with different jet multiplicities and their dedicated control regions. Three background-only fits are performed, one for each jet multiplicity. Each of these background-only fits is similar to the fit setup described in the last part. However, as it turned out to be the area in which the most modifications were necessary in comparison to the analysis presented before, a detailed description is given in Chapter 14.1.

All different groups of signal and control regions are combined in the exclusion fit to derive limits in a variety of models. These models include simplified models with one and two intermediate steps. Limits are also presented in the 'Higgs aware' MSUGRA/CMSSM grid. The results of the exclusion fit and the limits are presented in Section 16.2.

This part closes with a comparison to the limits derived in analyses targeting other final states in Section 16.3.

The results of this analysis were made public in [179].

Chapter 12

Signal region optimisation

As mentioned before, the signal regions used in the $5.8\,\mathrm{fb}^{-1}$ analysis were first defined for the 7 TeV pp analysis [131, 132]. They were thus not only optimised for a center-of-mass energy of 7 TeV and for an integrated luminosity of $\sim 5\mathrm{fb}^{-1}$, but also for being sensitive to squark and gluino masses that are now already excluded by these analyses. In addition, they were optimised only for the MSUGRA/CMSSM grid and not for other supersymmetric models.

A re-optimisation for a center-of-mass energy of 8 TeV and an integrated luminosity of $20.3\,\mathrm{fb}^{-1}$ was thus necessary. A particular focus in this re-optimisation[1] was placed on simplified models with one step, which are the most attractive simplified models for analyses targeting final states with a lepton.

The re-optimisation procedure consisted of three parts, which are discussed in the following sections:

- **Sensitivities of existing signal regions at higher luminosities and at a center-of-mass energy of 8 TeV:**

  The first part calculates the sensitivity of the existing signal regions used in the 7 TeV analyses at an assumed[2] integrated luminosity of $25\,\mathrm{fb}^{-1}$ at 8 TeV. This part will illustrate the regions in the signal grids in which each of the signal regions is most powerful. It will also illustrate that no sensitivity to higher squark and gluino masses can be obtained if using these signal regions.

- **Determination of the optimal signal region for selected signal models:**

  The second part presents a re-optimisation carried out as a scan in variables known for their good discriminating power between signal and background. The sensitivity of approximately 30000 cut combinations as candidate signal regions was evaluated for a selection of around 9 points in each of the simplified models with one step and in the MSUGRA/CMSSM grid. A set of three signal regions was proposed based on this. Due to the high number of variations tested, some approximations needed to be made regarding statistical and systematic uncertainties, but also regarding the definition of significance used.

- **Improvement of the sensitivity by a shape fit:**

---

[1]The description in this chapter uses material provided by the author for an ATLAS internal analysis documentation [225].

[2]The signal region optimisation was mainly performed before the precise accumulated statistics collected in pp collisions at 8 TeV was known. The statistics was assumed to be $25\,\mathrm{fb}^{-1}$. The re-calculated sensitivity in the third optimisation step below was evaluated with the actual luminosity taken.

The third optimisation step re-calculates the sensitivity of the proposed signal regions and of some of their variations with the correct statistical treatment implemented in the HistFitter package [186]. Furthermore, the gain in sensitivity by the simultaneous fitting of various signal regions and by the inclusion of shape information was investigated in this step.

12.1 Sensitivity of the 2011 signal regions extrapolated to $25\,\mathrm{fb}^{-1}$

Three sets of signal regions requiring a lepton (electron or muon) with $p_\mathrm{T} > 25$ GeV were used in the analysis of the 2011 data in [131, 132] as shown in Table 12.1. Their main difference is the jet multiplicity requirement. The signal regions requiring three or four jets also focus on squark pair production (where at least four jets can be expected from the two decay cascades of the squarks as discussed in Section 2.4.3), whereas the signal regions requiring seven jets only focuses on gluino pair production or long decay chains.

The sensitivity of these signal regions was calculated for every grid point in the simplified models with one step for an integrated luminosity of $25\,\mathrm{fb}^{-1}$. The significance is defined as follows for these studies[3]:

$$\text{Significance} = \frac{S}{\sqrt{1 + B + (0.3 \cdot B)^2}} \qquad (12.1.1)$$

where S is the number of signal events and B the number of background events. The systematic uncertainty of the background is approximated by 30% for all values of B which results in the term $(0.3 \cdot B)^2$. The '1' in the denominator avoids a pole for zero background events B. The formula is a more sophisticated version of the well-known $S/\sqrt{B}$ description for the significance[4]. It provides a rough measure of the significance, which is however sufficient for this analysis. Using this simplified version allows the testing of many different candidate cut combinations for a signal region, which would be too CPU intensive otherwise. The significance calculated with the full statistical treatment is presented at the end of this chapter.

The signal region (without separation into electron and muon channels) resulting in the largest significance is indicated for every grid point in the simplified models with one step in Figure 12.1 for gluino pair production and in Figure 12.2 for squark pair production. In each of the grids, only grid points where at least one signal region results in a sensitivity greater than 1.64σ are shown - this value is chosen as approximate threshold for an exclusion limit with a 95%CL. The limit of the 2011 analysis in [131] is shown in grey as reference.

For gluino pair production, at least six jets are expected in pure final states with a lepton and further jets can arise from initial or final state radiation. The signal region requiring seven jets provides the highest sensitivity to low and medium gluino masses, whereas the signal region requiring four jets dominates for high gluino masses and low to medium x values. Close to the diagonal line with $m_{\tilde{g}} = m_{\tilde{\chi}_1^0}$ in the grid with fixed $x = 1/2$ and for high x values in the grid with variable x, the signal region requiring three jets dominates due to the softness of the jets emerging from the decay of the gluino to the $\tilde{\chi}_1^\pm$ due to the small mass differences between the gluino and the $\tilde{\chi}_1^\pm$.

---

[3]As simplification, the events in the electron and muon channels were added together in the following calculation, so that the 3-jets, 4-jets and 7-jets signal regions were not divided into electron and muon channels for this optimisation step. Electron and muon channels were also combined in the second step of the optimisation in Section 12.2. The third optimisation step in Section 12.3 again uses the signal regions divided into an electron and a muon channel.

[4]More precise formula for the significance are given in [226].

	3-jets	**4-jets**	**7-jets**
N_{lep}		$== 1$	
p_{T}^{l} (GeV)		> 25	
$p_{\mathrm{T}}^{l_2}$ (GeV)		< 10	
N_{jet}	≥ 3	≥ 4	≥ 7
$p_{\mathrm{T}}^{\mathrm{jet}}$ (GeV)	$> 100, 40, 40$ $p_{\mathrm{T}}^{\mathrm{jet}\ 4} < 80$ GeV	$> 80, 80, 80, 80$	$> 80, 25, 25, 25, 25, 25, 25$
$E_{\mathrm{T}}^{\mathrm{miss}}$ (GeV)	> 250	> 250	> 180
m_{T} (GeV)	> 100	> 100	> 120
$E_{\mathrm{T}}^{\mathrm{miss}}/m_{\mathrm{eff}}^{\mathrm{excl}}$	> 0.3	> 0.2	-
$m_{\mathrm{eff}}^{\mathrm{incl}}$ (GeV)	> 1200	> 800	> 750

Table 12.1: Signal regions requiring a lepton with $p_{\mathrm{T}} > 25$ GeV used in the 2011 analyses [131, 132]. These signal regions serve as starting point for the re-optimisation.
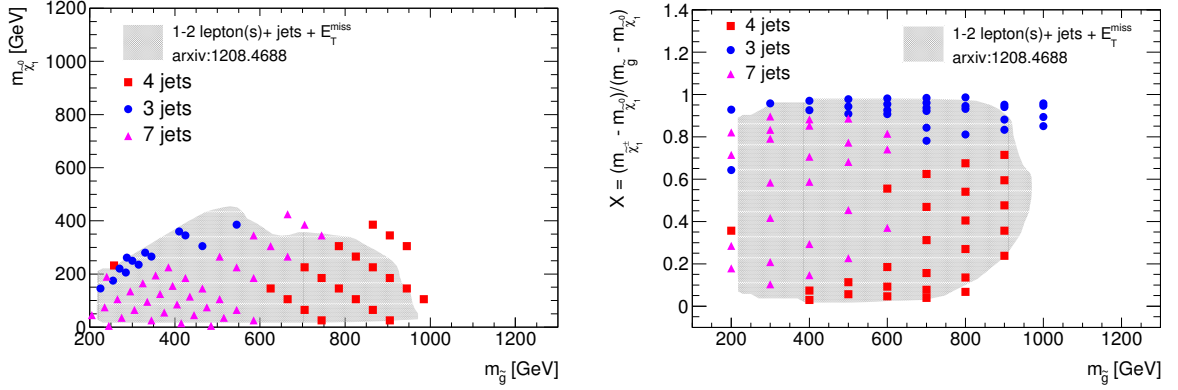
Figure 12.1: The signal regions resulting in the largest significance in the simplified models with one step and initial gluino pair production, where only points for which at least one signal region shows a significance greater than 1.64σ are displayed. The signal regions are defined as in Table 12.1 without separation into electron or muon channels, with the red rectangle standing for the 4-jets signal region, the blue dots for the 3-jets signal region and the pink triangles for the 7-jets signal region. The area excluded in the 2011 analyses is indicated by the grey shaded area. The left plot shows the grid with fixed $x = 1/2$, the right plot the grid with variable x.
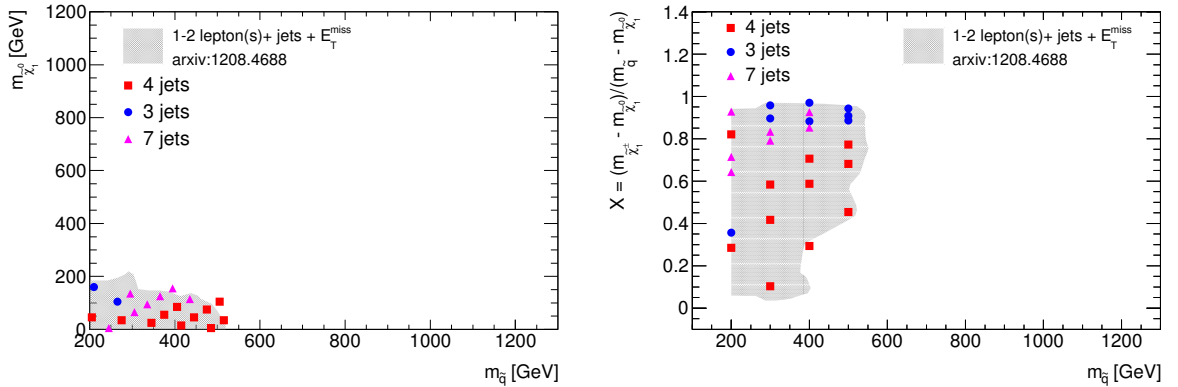
Figure 12.2: Similarly to Figure 12.1 the two simplified models with one step and initial squark pair production are shown, with the grid with fixed $x = 1/2$ on the left and the grid with variable x on the right.

At least four jets (plus additional jets from initial and final state radiation) are expected in the final state for simplified models with one step and initial squark pair production. The signal region requiring four jets is thus showing the largest sensitivity for most grid points, only complemented by the signal region requiring three jets for very large x values, where some of the four jets are expected to be of lower energy. The signal region requiring seven jets provides the best sensitivity for some of the grid points with medium x values.

In none of the plots a significance sufficient to increase the exclusion assuming an integrated luminosity of $25\,\text{fb}^{-1}$ can be achieved by the signal regions of the 2011 analyses. The exclusion limits could be extended by 100 GeV at most compared to the limits obtained in $4.7\,\text{fb}^{-1}$ of 7 TeV pp collisions [131]. This underlines the need for a re-optimisation of these signal regions.

12.2   Scan of discriminating variables

The sensitivity needs to be extended particularly to the regions in the simplified models with one step not yet excluded and characterised by higher gluino, squark or $\tilde{\chi}_1^0$ masses. Between eight and ten representative and not yet excluded points are chosen in each of the grids, some of them being closely to the already excluded regions, others being at some distance. The significance is calculated for ~ 30000 different cut variations, candidates for signal regions, by using the simplified definition for significance used above. The variations include a scan in the following variables[5]:

- **jet multiplicity ($\mathbf{N_{jet}}$)**: 3 - 7 jets, the lowest energetic jet needs to satisfy $p_T > 30\,\text{GeV}$[6],

- **transverse momentum of leading jet ($\mathbf{p_T^{1st\ jet}}$)**: $p_T > 80$, 120 or 160 GeV,

- **transverse momentum of subleading jet ($\mathbf{p_T^{2nd\ jet}}$)**: $p_T > 30$, 50 or 80 GeV,

- **missing transverse energy ($\mathbf{E_T^{miss}}$)**: 150 - 400 GeV in steps of 50 GeV (and in addition also 500 GeV),

- **transverse mass ($\mathbf{m_T}$)**: 100 - 350 GeV in steps of 50 GeV,

- **ratio of missing transverse energy and truncated effective mass ($\mathbf{E_T^{miss}/m_{eff}^{excl}}$)**: 0.2, 0.3 or not applied,

- **inclusive effective mass ($\mathbf{m_{eff}^{incl}}$)**: 600 - 1600 GeV in steps of 200 GeV,

where all variables are varied together, so that correlations between variables are taken into account. To penalise options with no background event remaining and thus large systematic and statistical uncertainties, a signal region candidate is only accepted if at least one background event passes.

Tables 12.2-12.5 indicate the combinations of criteria resulting in the largest significance for every of the chosen points in the one-step simplified models. Sometimes, multiple variations result in the same significance. In this case, all possible values are summarised by giving an enclosing interval.

In general, the signal region candidates often show higher values in E_T^{miss}, m_T and m_{eff}^{incl} in comparison to previous analyses. High jet multiplicities (six or seven jets) are also preferred.

---

[5]The variables were defined in Chapter 5.

[6]The results of the optimisation procedure were also cross-checked based on a requirement of $p_T > 40$ GeV for the jet with lowest transverse momentum.

$(m_{\tilde{g}},m_{\tilde{\chi}^\pm},m_{\tilde{\chi}^0_1})$ [GeV]	(1025, 625, 225)	(1025, 705, 385)	(825, 625, 425)	(505,465,425)	(625, 545, 465)	(1105, 705, 305)	(1025, 865, 705)	(1145,1025,905)
$E_\mathrm{T}^\mathrm{miss}$ [GeV]	200	200	350	[350,400]	350	300	350	350
m_T [GeV]	350	350	150	150	150	300	150	150
$p_\mathrm{T}^{(\mathrm{1st\ jet})}$ [GeV]	[80,120]	[80,120]	80	160	[80,160]	80	80	80
$p_\mathrm{T}^{(\mathrm{2nd\ jet})}$ [GeV]	[30,50]	[30,50]	30	50	[30,50]	[30,80]	[30,50]	[30,50]
# jets	6	6	7	3	7	5	7	7
$E_\mathrm{T}^\mathrm{miss}/m_\mathrm{eff}^\mathrm{excl}$	-	-	-	0.3	0.3	0.2	-	-
$m_\mathrm{eff}^\mathrm{incl}$ [GeV]	1400	1400	600	1400	1000	1400	600	[600,800]
Significance	7.98	3.61	5.29	2.35	9.09	4.23	0.64	0.14

Table 12.2: The variations resulting in the largest significance for eight selected points in the simplified model with one step and initial gluino pair production and fixed $x = 1/2$. If more than one variation results in the same significance value, all cut combinations are noted by giving an interval of all possible cut combinations.

$(m_{\tilde{g}},m_{\tilde{\chi}^\pm},m_{\tilde{\chi}^0_1})$ [GeV]	(800, 70, 60)	(800,750,60)	(900,260,60)	(900, 760, 60)	(1000,460,60)	(1100, 70, 60)	(1100, 960, 60)	(1200, 260, 60)	(1200,660,60)
$E_\mathrm{T}^\mathrm{miss}$ [GeV]	350	400	150	[150,350]	200	[150,400]	[150,400]	350	350
m_T [GeV]	100	350	200	300	350	100	300	150	250
$p_\mathrm{T}^{(\mathrm{1st\ jet})}$ [GeV]	[80,160]	80	[80,120]	80	[80,120]	[80,160]	80	[80,160]	[80,120]
$p_\mathrm{T}^{(\mathrm{2nd\ jet})}$ [GeV]	[30,80]	30	[30,80]	80	[30,80]	80	80	[30,80]	80
# jets	7	4	6	4	6	4	4	7	5
$E_\mathrm{T}^\mathrm{miss}/m_\mathrm{eff}^\mathrm{excl}$	0.2	0.3	-	0.3	-	0.3	0.3	-	0.2
$m_\mathrm{eff}^\mathrm{incl}$ [GeV]	1600	800	1400	1400	1400	1600	1400	1600	1600
Significance	1.61	20.64	8.65	18.68	8.77	0.63	6.15	1.42	3.72

Table 12.3: The variations resulting in the largest significance for nine selected points in the simplified model with one step, initial gluino pair production and variable x. If more than one variation results in the same significance value, all cut combinations are noted by giving an interval of all possible criteria.

$(m_{\tilde{q}}, m_{\tilde{\chi}^\pm}, m_{\tilde{\chi}^0_1})$ [GeV]	(385, 305, 225)	(300,275,250)	(505, 385, 265)	(585,305,25)	(705, 465, 225)	(625, 545, 465)	(825,465,105)	(825,625,425)	(1025, 545, 65)
$E_{\mathrm{T}}^{\mathrm{miss}}$ [GeV]	400	[150,250]	350	150	350	[150,350]	[150,300]	400	[150,350]
m_{T} [GeV]	150	300	150	200	250	150	300	200	250
$p_{\mathrm{T}}^{(\mathrm{1st\ jet})}$ [GeV]	[80,160]	[80,160]	80	[80,120]	80	[80,160]	[80,120]	80	[80,160]
$p_{\mathrm{T}}^{(\mathrm{2nd\ jet})}$ [GeV]	80	[30,80]	[30,50]	[30,80]	80	80	80	80	80
# jets	7	7	7	6	5	4	3	5	3
$E_{\mathrm{T}}^{\mathrm{miss}}/m_{\mathrm{eff}}^{\mathrm{excl}}$	0.3	0.2	0.2	-	0.2	0.3	0.3	0.3	0.3
$m_{\mathrm{eff}}^{\mathrm{incl}}$ [GeV]	1000	1400	600	1400	1000	1400	1400	[600,800]	1600
Significance	3.34	2.12	2.00	2.53	1.26	0.41	1.31	0.33	0.52

Table 12.4: The variations resulting in the largest significance for nine selected points in the simplified model with one step, initial squark pair production and fixed $x = 1/2$. If more than one variation results in the same significance value, all cut combinations are noted by giving an interval all possible criteria.

$(m_{\tilde{q}}, m_{\tilde{\chi}^\pm}, m_{\tilde{\chi}^0_1})$ [GeV]	(500, 110, 60)	(500, 490, 60)	(600, 260, 60)	(600, 460, 60)	(700, 70, 60)	(700, 690, 60)	(900,70,60)	(900, 260, 60)	(900,560,60)	(900,890,60)
$E_{\mathrm{T}}^{\mathrm{miss}}$ [GeV]	[150,400]	400	400	350	[150,400]	[150,350]	[150,350]	[150,400]	[150,300]	[150,350]
m_{T} [GeV]	100	300	150	350	100	300	100	150	300	350
$p_{\mathrm{T}}^{(\mathrm{1st\ jet})}$ [GeV]	[80,160]	80	[80,120]	80	[80,160]	[80,120]	[80,160]	[80,120]	80	80
$p_{\mathrm{T}}^{(\mathrm{2nd\ jet})}$ [GeV]	80	80	[30,50]	[30,50]	80	80	80	80	80	50
# jets	4	4	6	5	4	3	4	3	3	3
$E_{\mathrm{T}}^{\mathrm{miss}}/m_{\mathrm{eff}}^{\mathrm{excl}}$	0.3	0.3	-	0.3	0.3	0.3	0.3	0.3	0.3	0.3
$m_{\mathrm{eff}}^{\mathrm{incl}}$ [GeV]	1600	[600,800]	1000	800	1600	1400	1600	1600	1400	1400
Significance	1.42	6.78	2.07	4.92	0.53	2.00	0.32	0.60	0.14	0.72

Table 12.5: The cut combinations resulting in the largest significance for ten selected points in the simplified model with one step, initial squark pair production and variable x. If more than one variation results in the same significance value, all variations are noted by giving an interval of all possible criteria.

	3-jets (tight)	5-jets (tight)	6-jets (tight)
N_{lep}	== 1 (electron or muon)		
p_T^l (GeV)	> 25		
$p_T^{l_2}$ (GeV)	< 10		
N_{jet}	≥ 3	≥ 5	≥ 6
p_T^{jet} (GeV)	> 80, 80, 30	> 80, 50, 40... ,40	> 80, 50, 40... ,40
E_T^{miss} (GeV)	> 500	> 300	> 350
m_T (GeV)	> 150	> 200	> 150
$E_T^{\text{miss}}/m_{\text{eff}}^{\text{excl}}$	> 0.3	-	-
$m_{\text{eff}}^{\text{incl}}$ (GeV)	> 1400	> 1400	> 600

Table 12.6: The three sets of tight signal regions require three, five or six jets and are further separated into electron and muon channels. They are used to derive limits on the visible cross section without model dependence.

Only a small number of signal regions is practical for the use in this analysis. Therefore, a compromise between the optimal criteria for each of the single points needs to be found. Table 12.2 suggests for example signal regions with requirements for six or seven jets and cuts on E_T^{miss} and on m_T around 300 GeV. An additional optimisation step is added in which for each signal region candidate the expected number of excluded signal points is evaluated. This helps in identifying the option with a large sensitivity to large parts of the grids. Based on this, three *tight* signal regions with different requirements on the jet multiplicity are selected as presented in Table 12.6. Each of the three signal regions is defined in the electron and in the muon channel. These signal regions are not orthogonal to each other and will therefore be re-defined for the use in a simultaneous fit of all signal regions below. The signal regions will later be used to derive limits on the visible cross section without model dependence.

The 3-jets signal regions target the decay of pair-produced squarks and short decay chains in general, whereas the 5-jets or 6-jets signal regions are sensitive to the decay of pair-produced gluinos and long decay chains. All of the signal regions show higher cuts on E_T^{miss}, on m_T and on $m_{\text{eff}}^{\text{incl}}$ than the signal regions of 2011 (with exception of the $m_{\text{eff}}^{\text{incl}}$ criterion in the 6-jets signal regions). This is due to the considerably higher squark and gluino masses for which the signal regions are sensitive. In particular the cut on m_T is useful in rejecting the W+jets background events, but it also selects some supersymmetric signal models with considerably higher m_T values than the background. This is illustrated for two examples in Figure 12.3.

This optimisation step was also performed for both MSUGRA/CMSSM grids. Similar results as in the simplified models with one step were obtained.

The sensitivity of the newly optimised signal regions is evaluated by using the package HistFitter and thus by a statistically correct calculation in the next section.

12.3   Loose signal regions for the exclusion fit

The tight signal regions in Table 12.6 are not disjoint and can therefore not be used in a simultaneous fit to multiple signal regions. Furthermore, these signal regions have a too low statistics due to too tight selection criteria so that they cannot be subdivided into more regions. Therefore, shapes of background and signal distributions cannot be taken into account in a shape fit[7] in these signal regions.

---

[7]The idea of a shape fit was introduced in Section 10.1.
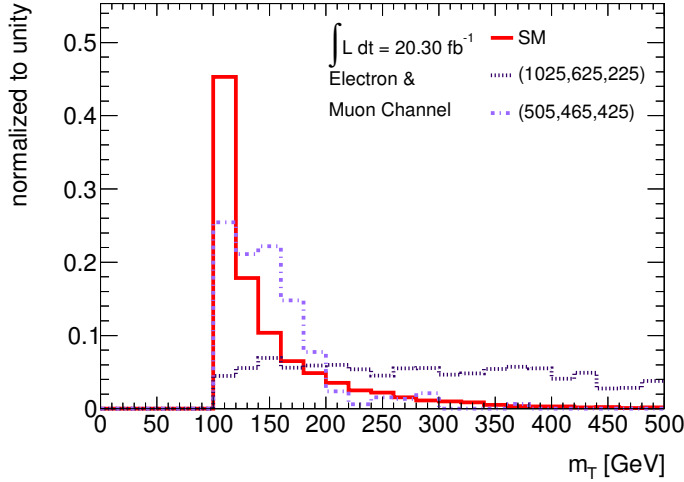
Figure 12.3: The normalised m_T distributions are shown for the total Standard Model background (in solid red) and for two signal models from the simplified models with one step and initial gluino pair production with the parameters $(m_{\tilde{g}}, m_{\tilde{\chi}_1^\pm}, m_{\tilde{\chi}_1^0}) = (505, 465, 425)$ GeV (in dashed-dotted light blue) and $(1025, 625, 225)$ GeV (in dotted dark blue). Preselection cuts as defined in Section 7.2.1 were applied as well as cuts on $E_T^{miss} > 100$ GeV, $p_T^{1nd\ jet} > 80$ GeV and $m_T > 100$ GeV. Electron and muon channel were combined. The m_T distribution of the signal point $(1025, 625, 225)$ GeV is flat and shows a long tail, which provides discriminating power against the Standard Model background. The other signal point with parameters $(505, 465, 425)$ GeV shows a less dominant tail, but still peaks at larger values than the background. This analysis is more sensitive to models with a medium or large mass distance between the gluino and the $\tilde{\chi}_1^0$ like point $(1025, 625, 225)$ GeV and less to models with a small mass difference like point $(505, 465, 425)$ GeV.

This section will thus introduce signal regions with relaxed selection criteria (loose signal regions) which are orthogonal to each other. These signal regions can be fitted simultaneously and a shape fit can be performed in them. It will be shown that the sensitivity of the loose signal regions is larger than the sensitivity of the tight signal regions in all simplified models studied. This increase is obtained by both the combination of signal regions and the consideration of background and signal shapes.

The third step of the optimisation procedure discussed in this section is performed by using the package `HistFitter`, which allows the correct statistical calculation of the significances in contrast to the second step. Systematic uncertainties arise from different sources, but for simplicity also for this optimisation step a background uncertainty of 30% is assumed, although the impact of this assumption is checked at the end of this section.

Procedure: For this optimisation step a similar setup as for the exclusion fit as described in Section 10.4.4 is used and the 95% CL expected limit calculated. However, the background is taken directly from the Monte Carlo simulation and no control regions are used to constrain it. An impact of the control regions on the sensitivity can hence be avoided, as for example by constraining some systematic uncertainties. So, only signal regions are used in this fit setup. Backgrounds and signal have statistical uncertainties assigned. The backgrounds receive a flat systematic uncertainty of 30 %. The signal receives only a systematic uncertainty on initial and final state radiation.

For the simultaneous fitting of regions, it is essential that these do not overlap, but are orthogonal. This is not the case for the tight signal regions in Table 12.6, as the 5-jets and 6-jets signal regions are partly a subset of the 3-jets signal regions. A veto on the fifth jet with $p_T > 40$ GeV

	3-jets (loose, proposed)	**5-jets (loose, proposed)**	**6-jets (loose, proposed)**
N_{lep}		== 1 (electron or muon)	
p_{T}^{l} (GeV)		> 25	
p_{T}^{l2} (GeV)		< 10	
N_{jet}	≥ 3	≥ 5	≥ 6
$p_{\mathrm{T}}^{\mathrm{jet}}$ (GeV)	> 80, 80, 30	> 80, 50, 40... ,40	> 80, 50, 40... ,40
	$p_{\mathrm{T}}^{\text{5th jet}} < 40$ GeV	$p_{\mathrm{T}}^{\text{6th jet}} < 40$ GeV	
$E_{\mathrm{T}}^{\mathrm{miss}}$ (GeV)	> 500	> 300	> 200
m_{T} (GeV)	> 250	> 200	> 150
$E_{\mathrm{T}}^{\mathrm{miss}}/m_{\mathrm{eff}}^{\mathrm{excl}}$	> 0.3	-	-
$m_{\mathrm{eff}}^{\mathrm{incl}}$ (GeV)	> 800	> 800	> 600
Shape fit	In $m_{\mathrm{eff}}^{\mathrm{incl}}$ In four bins $\in [800, 1600]$ GeV		In $E_{\mathrm{T}}^{\mathrm{miss}}$ In three bins $\in [200, 500]$

Table 12.7: Three sets of loose signal regions with different jet multiplicities, further divided into an electron and a muon channel, are proposed based on the tight signal regions in Table 12.6 by adding vetoes on further jets in the 3-jets and 5-jets signal regions.

is thus added for the 3-jets signal regions and on the sixth jet with $p_{\mathrm{T}} > 40$ GeV in the 5-jets signal regions. Different variables as $E_{\mathrm{T}}^{\mathrm{miss}}$, m_{T} and $m_{\mathrm{eff}}^{\mathrm{incl}}$ have been studied for a shape fit, as well as different cut values in these variables and different binning in a shape fit. The selection criteria and the shape fits resulting in the highest sensitivities are outlined in Table 12.7 (and are referred to as default configuration in the following). A shape fit in $m_{\mathrm{eff}}^{\mathrm{incl}}$ with four bins between 800 and 1600 GeV is found to be most effective among all options for the 3-jets and 5-jets signal regions, although a shape fit in $E_{\mathrm{T}}^{\mathrm{miss}}$ results in nearly the same sensitivity for the 3-jets signal regions. To make this shape fit possible in both signal regions, the cut on $m_{\mathrm{eff}}^{\mathrm{incl}}$ needed to be lowered to 800 GeV compared to the tight signal regions (to ensure an acceptable statistics in the single bins used in the shape fit). Similarly, a shape fit in $E_{\mathrm{T}}^{\mathrm{miss}}$ carried out in three bins between 200 and 500 GeV provided the best sensitivity in the 6-jets signal regions.

Sensitivity of loose and tight signal regions: The sensitivity of the loose signal regions (in default configuration) is evaluated in simplified models with one and two step(s) as shown in Figure 12.4 in the blue line by fitting the signal regions simultaneously. This figure shows the two simplified models with one step and initial gluino production on the top (fixed $x = 1/2$ left, variable x right), followed by the two simplified models with one step and initial squark pair production in the next row (again fixed $x = 1/2$ left, variable x right). The two last rows present the sensitivity in the simplified models with two steps with the gluino grids in the third row and the squark grids in the last row. The simplified models with two steps and with a decay via sleptons and sneutrinos are shown on the left side of these two rows, the simplified models with two steps and with the decay involving W and Z bosons on the right side.

In the two simplified models with one step and initial gluino pair production, a sensitivity to gluino masses up to 1.2 TeV can be reached for vanishing $\tilde{\chi}_1^0$ masses (grid with fixed $x = 1/2$) or medium x values (grid with variable x), whereas the sensitivity to squark masses extends up to 700 or 800 GeV for vanishing $\tilde{\chi}_1^0$ masses or high x values, respectively, in simplified models with one step and initial squark pair production. For the gluino simplified models with two steps, the sensitivity is similar as in the corresponding simplified models with one step. This is also the case for the squark simplified model with two steps with the decay through sleptons and sneutrinos, but no sensitivity is obtained in the simplified model with two steps and with the decay involving W and Z bosons. This is due to various reasons. First, the signal regions have not been optimised for simplified models with two steps. Second, as shown in Figure A.3, most low squark mass points have not been generated in this grid as being in a region already

excluded by the analysis in [131]. Third, the signal regions impose a veto on the second lepton reducing the acceptance in a grid with many leptons to expect in the final state. The veto on the second lepton is imposed to make this analysis complementary to another analysis requiring at least two leptons [180].

In the simplified models with two steps the limits do not extend to low gluino or squark masses and small $\tilde{\chi}_1^0$ masses. This is because no points were generated in these regions as visualised in Figure A.3 in Appendix A. These or similar regions are already excluded by the analysis in [131].

The sensitivity of the loose signal regions, fitted simultaneously, is compared to the sensitivity obtained with the tight signal regions. To make a fair comparison, a shape fit is also used in these signal regions with four bins in $m_{\mathrm{eff}}^{\mathrm{incl}}$ between 800 and 1600 GeV in the signal regions requiring three or five jets and three bins in $E_{\mathrm{T}}^{\mathrm{miss}}$ between 350 and 500 GeV in the signal regions requiring six jets. The main differences between the loose and tight signal regions is thus that no veto on additional jets is applied for the tight signal regions, a higher cut on $E_{\mathrm{T}}^{\mathrm{miss}}$ in the tight signal regions requiring three or six jets and on m_{T} in the signal regions requiring five jets. Also the tight signal regions are not fitted simultaneously, but one after the other.

The sensitivity of the tight signal regions is shown in Figure 12.4. In comparison to the loose signal regions, their sensitivities are lower in all regions. The tight 6-jets signal regions result in a comparable sensitivity compared to the simultaneously fitted loose signal regions at higher gluino masses in the simplified models with one step. The tight 5-jets signal regions are providing sensitivity to a similar phase space as the tight 6-jets signal regions, but not to equally high gluino masses. Instead these signal regions also extend to lower gluino masses. The tight 3-jets signal regions complement the other signal regions in the simplified models with one step and variable x at large x values.

In summary, a significant gain in sensitivity can be obtained by the simultaneous fitting of the loose signal regions in comparison to the sensitivity of the tight signal regions.

Comparison between shape fit and inclusive signal regions: Considering only the loose signal regions with default configuration, which include a shape fit in $m_{\mathrm{eff}}^{\mathrm{incl}}$ and in $E_{\mathrm{T}}^{\mathrm{miss}}$ for the 3-jets, 5-jets and 6-jets signal regions, respectively, this configuration is compared to signal regions without shape fit in Figure 12.5. The default configuration is again indicated by the solid blue line. Fitting the three signal regions simultaneously but without shape fit, the red dotted curve is obtained. This is compared to the green dashed line giving the sensitivity of a tighter version of the signal regions, fitted simultaneously, where the cut on $m_{\mathrm{eff}}^{\mathrm{incl}}$ is increased from 800 GeV to 1400 GeV for the 3-jet and 5-jets signal regions and the cut on $E_{\mathrm{T}}^{\mathrm{miss}}$ is increased from 200 GeV to 350 GeV for the 6-jet signal regions. Again, for this version, no shape fit is used.

The default configuration of signal regions results into the largest sensitivity in all grids, but the tighter version of the signal regions without shape fit (green dashed) is able to reach almost the sensitivity of the default configuration for high gluino or squark masses while loosing sensitivity to smaller squark and gluino masses. In contrast, the looser signal regions without shape fit (red dotted) show almost the same reach at low squark or gluino masses, but not at higher gluino or squark masses.

Hence, the signal regions of the default configuration with shape fit combine the benefits of both looser and tighter versions of signal regions without shape fit. This can be understood by the observation, that the looser version of the signal regions would be optimal for lower squark and gluino masses, the tight version for higher masses, but both options are included as subregions in the signal regions with default configuration and shape fit.
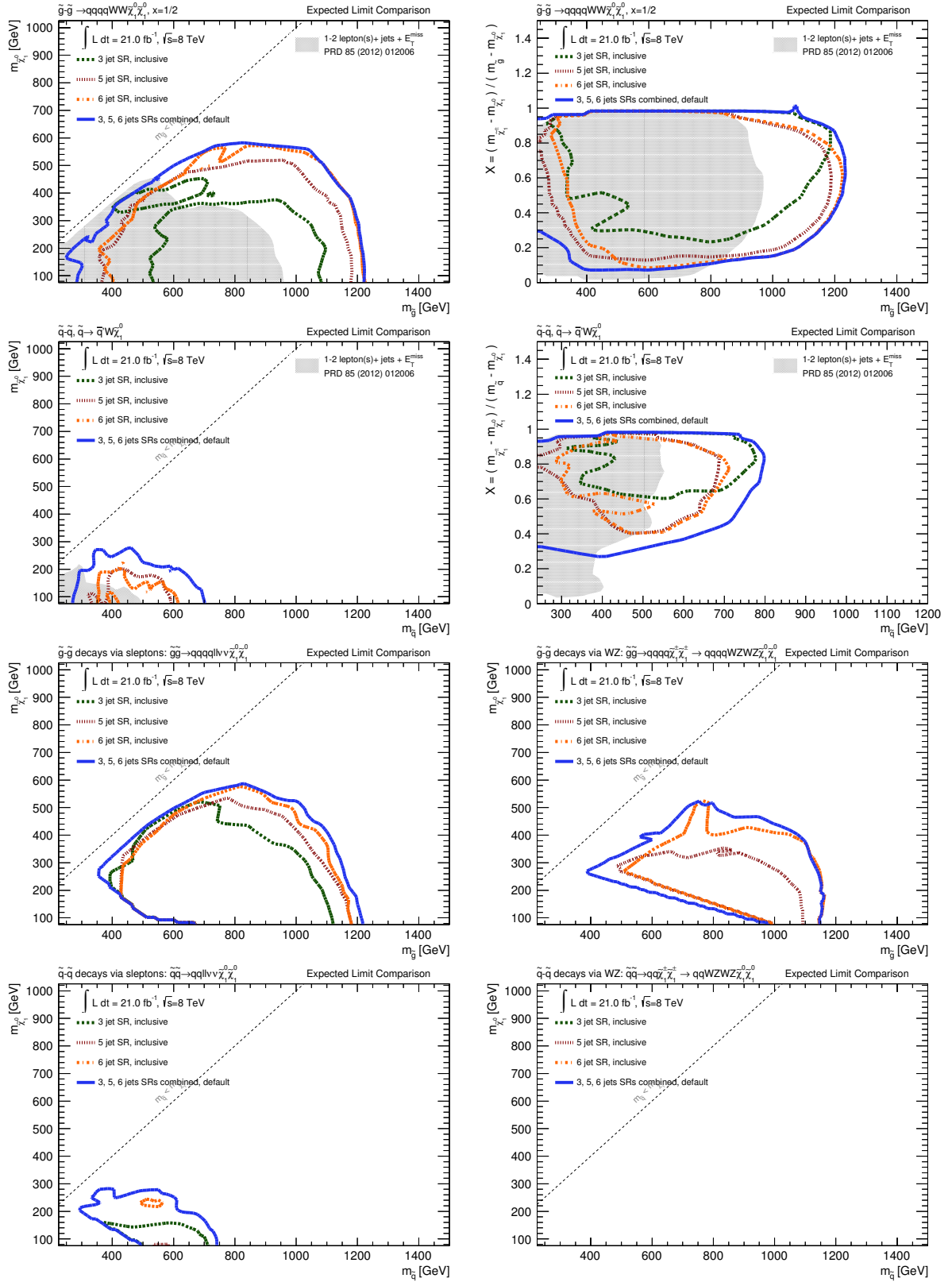
Figure 12.4: The sensitivity of the simultaneously fitted loose signal regions (default version, in blue) is compared to the sensitivity of the tight signal regions (in a binned version, see text) requiring six jets (orange dotted-dashed), requiring five jets (red dotted) and three jets (dark green dashed) in simplified models with one step (top two rows) and in simplified models with two steps (bottom two rows).

	3-jets (loose)	5-jets (loose)	6-jets (loose)
N_{lep}		== 1 (electron or muon)	
p_T^l (GeV)		> 25	
p_T^{l2} (GeV)		< 10	
N_{jet}	≥ 3	≥ 5	≥ 6
p_T^{jet} (GeV)	> 80, 80, 30	> 80, 50, 40... ,40	> 80, 50, 40... ,40
	$p_T^{\text{5th jet}} < 40$ GeV	$p_T^{\text{6th jet}} < 40$ GeV	
E_T^{miss} (GeV)	> 300	> 300	> 250
m_T (GeV)	> 150	> 150	> 150
$E_T^{\text{miss}}/m_{\text{eff}}^{\text{excl}}$	> 0.3	-	-
$m_{\text{eff}}^{\text{incl}}$ (GeV)	> 800	> 800	> 600
Shape fit	In $m_{\text{eff}}^{\text{incl}}$ In four bins $\in [800, 1600]$ GeV		In E_T^{miss} In three bins in $\in [250, 550]$

Table 12.8: These loose signal regions, derived from the signal regions in 12.7 and defined in the electron and muon channels are used to derive limits in simplified models and in the 'Higgs aware' MSUGRA/CMSSM grid. The signal regions requiring three (five, six) jets provide sensitivity to models with squark (gluino) pair production.

In summary, Figures 12.5 and 12.4 show that the sensitivity of this analysis is improved by using a shape fit:

- The signal strength is constrained by more regions which are fitted simultaneously in the shape fit, thus the sensitivity obtained is larger. This is in particular visible in Figures 12.5 and 12.4 in the simplified models with one step and squark pair production. In these grids, the sensitivity of the loose signal regions with default configuration is notable larger than of any other option tested.

- Each point in the various grids would demand a specific signal region. The signal regions for the various points are often very different (see Tables 12.2-12.5). A shape fit can balance these different requirements. This is can be seen in particular from Figure 12.4.

Impact of systematic uncertainties: A background systematic uncertainty of 30% was assumed in the evaluation of the sensitivity. Figure 12.6 compares this default configuration to configurations where a flat uncertainty of 20% (green dashed), 50% (red dotted) or 80% (orange dotted-dashed) was assumed. The sensitivities of all these configurations are very close to each other, although showing the expected tendency of an increased reach with lower uncertainties. Hence, the value assumed for the systematic uncertainties has only little impact on the limit.

Loose signal regions used in this analysis The loose signal regions of the default configuration are modified by relaxing the E_T^{miss} and m_T criteria in the 3-jets and 5-jets signal regions and by tightening the E_T^{miss} criteria in the signal regions requiring six jets. The lower criteria on E_T^{miss} and on m_T in the 3-jets and 5-jets signal regions reduce statistical fluctuations in the backgrounds caused by low Monte Carlo statistics. The higher criterion on E_T^{miss} for the 6-jets signal regions was shown to provide a slightly better sensitivity. The resulting loose signal regions are shown in Table 12.8. They are used in this analysis to derive limits in simplified models and in the 'Higgs aware' MSUGRA/CMSSM grid. In these signal regions, similar shape fits as described for the loose signal regions in the default configuration are used, although the range for the shape fit in the signal regions requiring six jets is modified to 250 and 550 GeV. In all shape fit configurations, events exceeding the highest bin are projected back into this bin, so that this bin also includes the overflow events.
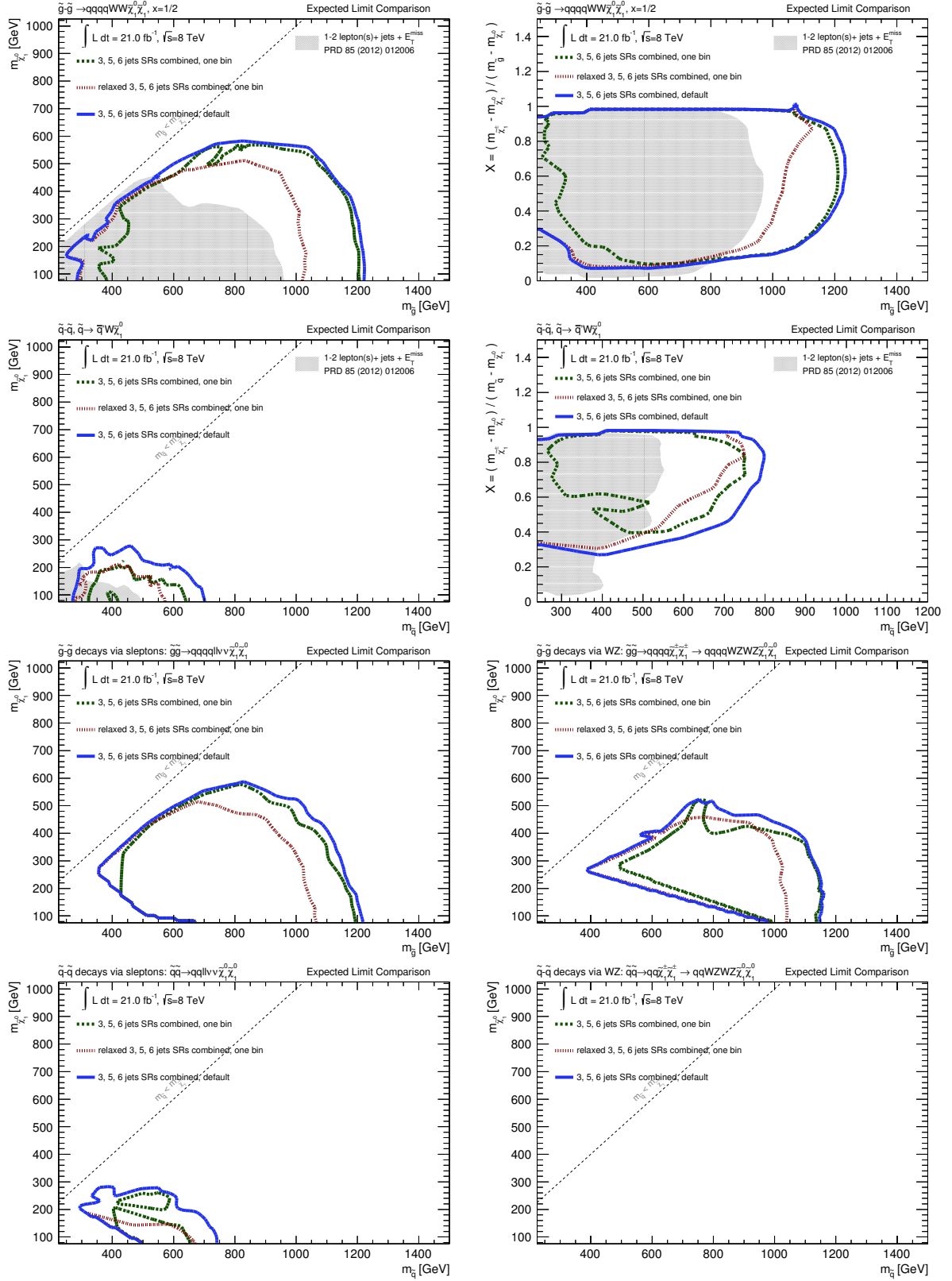
Figure 12.5: The 3-jets, 5-jets and 6-jets signal regions in the default configuration (in blue) are compared to a fit configuration with only one bin. In red dotted, the sensitivity of a version of signal regions with one bin and loose cuts in $m_{\text{eff}}^{\text{incl}}$ for the 3-jets and 5-jets signal regions and in $E_{\text{T}}^{\text{miss}}$ for the 6-jet signal regions is shown. In green dashed the sensitivity of signal regions with tight cuts in $m_{\text{eff}}^{\text{incl}}$ and $E_{\text{T}}^{\text{miss}}$ is given. The sensitivities in simplified models with one step are given in the top two rows, in simplified models with two steps in the bottom two rows. Again no sensitivity to the simplified model with two steps, initial squark pair production and the decay involving W and Z bosons is obtained.
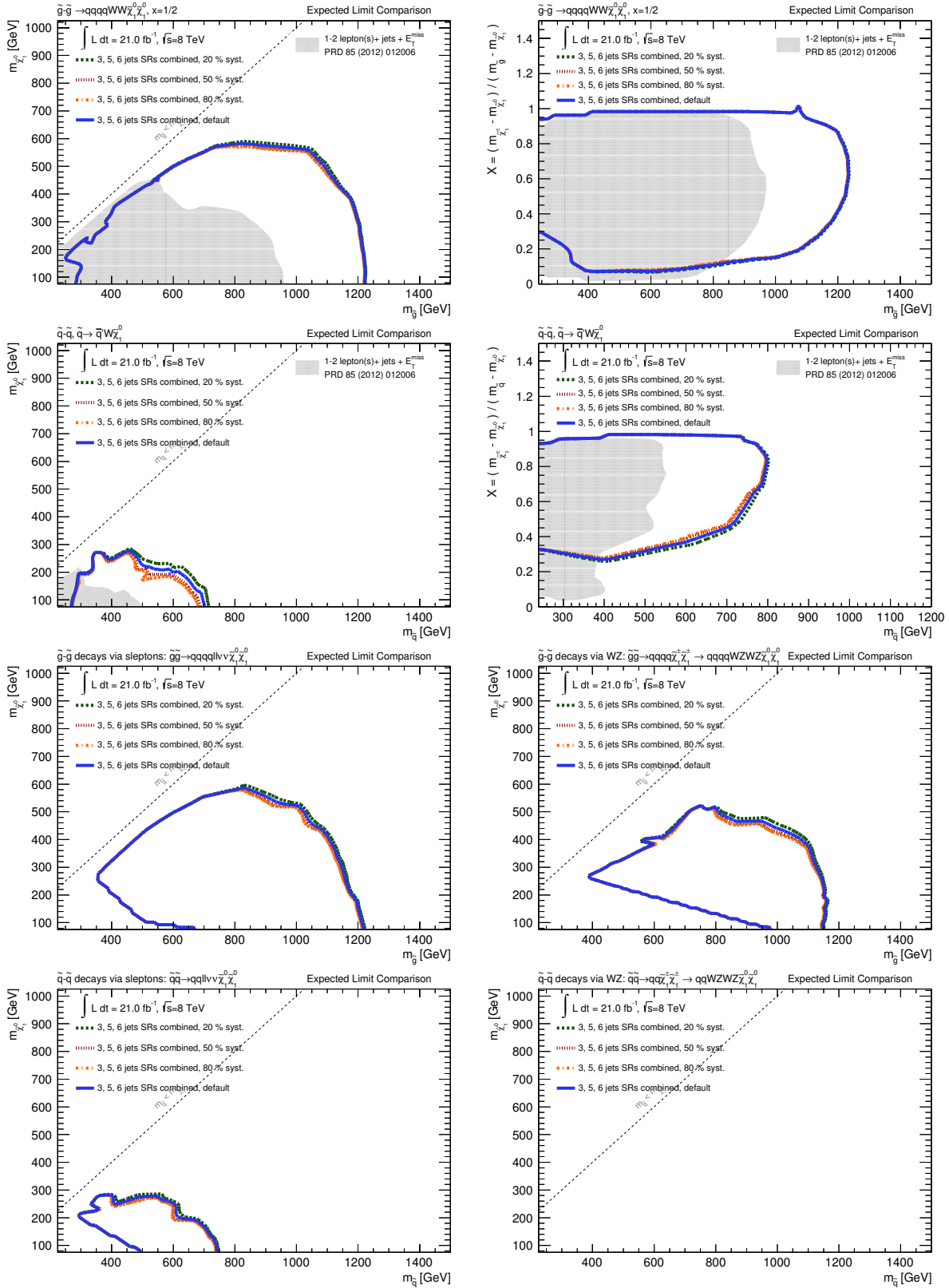
Figure 12.6: The size of the flat systematic uncertainty is varied from 30 % (blue, default) to 20 % (dark green), 50 % (red) and 80 % (orange) in one step (top two rows) and two step simplified models (bottom two rows).

Chapter 13

Backgrounds and control regions

This analysis uses the background estimation techniques introduced in Chapter 8. Due to the re-optimised signal regions, the control (and validation) regions of the analysis in the previous part were adapted in the estimation of the $t\bar{t}$ and W+jets backgrounds. They were moved to higher values in $E_\mathrm{T}^\mathrm{miss}$, m_T and $m_\mathrm{eff}^\mathrm{incl}$ in order to resemble the background kinematics in the signal regions as closely as possible.

This chapter first summarises the changes in the background estimation methods, including a summary of the Monte Carlo samples used, before it describes the definition of the control regions used in the $t\bar{t}$ and W+jets background estimation. Finally, the validation regions, used to validate the extrapolation from the control regions to the signal regions, are defined.

The trigger strategy remains unchanged and is therefore not further mentioned.

13.1 Changes with respect to the $5.8\,\mathrm{fb}^{-1}$ analysis

13.1.1 QCD multi-jet background estimation

The QCD mutli-jet background is estimated by the same method as described in Section 8.2. Only the fake and real efficiencies have been re-evaluated using the same or similar[1] control regions with the full statistics of the 2012 data. The fake and real efficiencies did not change significantly.

13.1.2 $t\bar{t}$ and W+jets background estimation

The estimation of the $t\bar{t}$ and W+jets backgrounds follows the same semi-data-driven method as described in Section 8.1. The control regions were re-defined and are described below. The normalisation is done in a simultaneous fit in all control regions of which the details are given in Section 14.1. By using transfer factors, the background estimates are extrapolated from the control to the signal regions. Also the systematic uncertainties on the $t\bar{t}$ and the W+jets backgrounds were revisited - a short summary is given below.

In contrast to the $5.8\,\mathrm{fb}^{-1}$ analysis, the Z+jets background is not estimated together with the W+jets background. Given the considerably tighter signal regions, the Z+jets background is

---

[1]The QCD control region in the muon channel is identical. In the electron channel at least one jet with $p_\mathrm{T} > 60$ GeV is required in the QCD control region, instead of 25 GeV previously.

negligible and is taken directly from Monte Carlo, as the other smaller backgrounds: single t, $t\bar{t}$ + vector boson and diboson production (WW, WZ and ZZ).

13.2 Monte Carlo samples

For nearly all background processes, different Monte Carlo samples were used compared to the $5.8\,\mathrm{fb}^{-1}$ analysis. All background processes along with their Monte Carlo generator are summarised in Table 13.1.

Newly produced Monte Carlo samples were used for the W+jets background. As for the analysis presented in the previous part, the generator is `AlpGEN` with `HERWIG` for the simulation of the parton shower and the fragmentation process and `JIMMY` for the underlying event. In contrast to the previous analysis, these samples provide a higher statistics as the low statistics inclusive sample are complemented by filtered high statistics samples. The filter conditions are applied at truth level: a truth jet of $p_\mathrm{T} > 80$ GeV and a true $E_\mathrm{T}^\mathrm{miss} > 100$ GeV are required. As the inclusive and filtered samples overlap, any event satisfying the filter criteria in the inclusive sample is discarded. Due to resolution effects (as the filter criteria cut on truth variables), some events of the inclusive sample enter the control and signal regions at high $E_\mathrm{T}^\mathrm{miss}$ values. These events carry a large weight due to the low statistics of the inclusive sample and thus large statistical uncertainties. This will affect some of the results in the control regions. Despite of these inaccuracies due to low Monte Carlo statistics, the usage of the Monte Carlo samples generated with `AlpGEN` is mandatory for this analysis because of the high jet multiplicity regions requiring at least five or six jets. Alternative Monte Carlo samples based on the `SHERPA` generator exist, but those provide only four additional partons in the matrix element. For the `AlpGEN` samples six additional partons are added in the calculation of the matrix element.

The Monte Carlo generator for the $t\bar{t}$ samples was changed to `POWHEG` [227] and `PYTHIA`. This is motivated by the high jet multiplicities used in this analysis, for which the samples based on `POWHEG/PYTHIA` show a better agreement between Monte Carlo and data than the previously used `MC@NLO` samples.

The Monte Carlo generator for the diboson samples was changed from `HERWIG` to `SHERPA` [228], as the kinematic distributions in `HERWIG` were found to be too soft compared to data.

In this analysis, another small background is considered: $t\bar{t}$+vector boson production[2]. The Monte Carlo samples are generated by `MadGraph5` [77] for the hard scattering and `PYTHIA` for the parton shower simulation.

13.3 Theoretical uncertainties on the $t\bar{t}$ and W+jets Monte Carlo samples

The systematic uncertainties on the $t\bar{t}$ and W+jets Monte Carlo samples are evaluated as uncertainty on the transfer factor [225] used for the extrapolation between control and signal regions.

For the W+jets background, the uncertainties due to the PDF set used was evaluated by comparing to other PDF sets. The uncertainties due to the factorisation and renormalisation scales are evaluated by varying these scales up and down by a factor of 2. To derive the uncertainty on

---

[2]As this background is usually very small, it was considered to be negligible in comparison to other backgrounds in the $5.8\,\mathrm{fb}^{-1}$ analysis. Due to the tighter control and signal regions, the $t\bar{t}$+vector boson production is added in the $20.3\,\mathrm{fb}^{-1}$ analysis.

Physics process	Generator	Cross section (pb)	Cross section calculation	
$W(\to \ell\nu)$ + jets	AlpGEN 2.14 [147]	1.22×10^4	NNLO	[194]
$W(\to \ell\nu) + b\bar{b}$ + jets	AlpGEN 2.14 [147]	153	LO×K	
$W(\to \ell\nu) + c\bar{c}$ + jets	AlpGEN 2.14 [147]	461	LO×K	
$W(\to \ell\nu) + c$ + jets	AlpGEN 2.14 [147]	1.29×10^3	LO×K	
$Z/\gamma^*(\to \ell\ell)$ + jets ($m_{\ell\ell} > 60\,\mathrm{GeV}$)	AlpGEN 2.14 [147]	1.15×10^3	NNLO	[194]
$Z/\gamma^*(\to \ell\ell)$ + jets ($10 < m_{\ell\ell} < 60\,\mathrm{GeV}$)	AlpGEN 2.14 [147]	4.37×10^3	NNLO	[194]
$Z/\gamma^*(\to \ell\ell) + b\bar{b}$ + jets ($m_{\ell\ell} > 60\,\mathrm{GeV}$)	AlpGEN 2.14 [147]	15.2	NNLO	[194]
$t\bar{t}$	POWHEG r1556[227]	238	NLO+NLL	[193]
Single-top (t-channel)	AcerMC 3.8 [146]	9.46	NLO+NLL	[195]
Single-top (s-channel)	MC@NLO 4.06 [148]	0.61	NLO+NLL	[196]
Single-top (Wt-channel)	MC@NLO 4.06 [148]	22.4	NLO+NLL	[197]
WW	SHERPA 1.4.1 [228]	5.88	NLO	[192]
WZ	SHERPA 1.4.1[228]	10.34	NLO	[192]
ZZ	SHERPA 1.4.1[228]	10.26	NLO	[192]
$W\gamma$	SHERPA 1.4.1[228]	96.9	LO	
$Z\gamma$	SHERPA 1.4.1[228]	488	LO	
$t\bar{t} + W$	MadGraph5 [77]	0.232	NLO	[229]
$t\bar{t} + Z$	MadGraph5 [77]	0.208	NLO	[230]

Table 13.1: The Monte Carlo samples used in this analysis along with their cross section. For the W + light jets, the Z/γ^* + light jets, the $Z/\gamma^* + b\bar{b}$ and the single-top (in the s- and $t-$ channels) backgrounds, the cross section is listed for only one lepton flavour. Some processes are calculated at leading order but are corrected by a K-factor (to account for the differences between LO and NLO). This is denoted by LO×K. This table was taken from [179] and slightly modified.

the minimum p_T threshold used, below which additional jets are calculated by using the matrix element and above which they are calculated by the Parton Shower algorithm, the threshold is varied from 25 to 40 GeV.

For the uncertainties on the $t\bar{t}$ background, the uncertainties on the PDF set used and on the renormalisation and factorisation scales are derived similarly to the W+jets background. Additionally, the uncertainty due to the parton showering is evaluated by comparing the POWHEG/ PYTHIA sample to a POWHEG/JIMMY sample and thus the parton showering algorithm of PYTHIA and HERWIG. Uncertainties due to initial and final state radiation are studied by comparing to ACER/PYTHIA samples with a different amount of parton showering.

13.4 Control regions

The control regions (CRs) were designed following the same reasoning as in Section 8.1. Their definition is chosen such that they are as close to the signal regions as possible. The definition of the control regions is given in Table 13.2 and their location in the $E_\mathrm{T}^\mathrm{miss}$-$m_\mathrm{T}$ phase space is shown relatively to the signal regions in Figure 13.1.

The control regions have very similar cuts compared to the loose signal regions. In particular, the $m_\mathrm{eff}^\mathrm{incl}$ criteria are the same, so that an extrapolation in $m_\mathrm{eff}^\mathrm{incl}$ between control and signal regions is only necessary for the tight signal regions. The jet criteria in the control regions are similar to the ones of the signal regions, because the control regions require the same jet multiplicity as the corresponding signal regions, but the criteria on p_T for the jet with lowest transverse momentum is relaxed to 30 GeV instead of 40 GeV in the signal regions. Consequently, the vetoes on the fourth jet and the sixth jet in the control regions requiring three or five jets, respectively, are correspondingly relaxed. The reduction of the p_T threshold increases the statistics in the control

	3-jets	**5-jets**	**6-jets**
	W+jets / Top		
N_ℓ	1 (electron or muon)		
$p_{\rm T}^\ell({\rm GeV})$	> 25		
$p_{\rm T}^{{\rm add.}\ \ell}\ ({\rm GeV})$	< 10		
$N_{\rm jet}$	≥ 3	≥ 5	≥ 6
$p_{\rm T}^{\rm jet}({\rm GeV})$	> 80, 80, 30	> 80, 50, 30, 30, 30	> 80, 50, 30, 30, 30, 30
$p_{\rm T}^{{\rm add.\ jets}}(\ {\rm GeV})$	$p_{\rm T}^{\rm 5th\ jet} < 30$	$p_{\rm T}^{\rm 6th\ jet} < 30$	$-$
$N_{b-{\rm tag}}$	$0\ /\geq 1$		
$E_{\rm T}^{\rm miss}\ ({\rm GeV})$	[150,300]		[100,200] / [150,250]
$m_{\rm T}\ ({\rm GeV})$	[80,150]	[60,150]	[40,80] / [40,150]
$m_{\rm eff}^{\rm incl}\ ({\rm GeV})$	> 800		> 600

Table 13.2: Definition of the control regions (as contributed to [179] by the author). The background in the signal regions is estimated with the help of the control regions with the same jet multiplicity as the signal regions, respectively. For each jet multiplicity two different types of control regions are required which differ by their b-jet requirements: In the first type any event containing b-tagged jets is rejected and thus these control regions are dominated by W+jets events. In the control regions belonging to the second type at least one b-tagged jet among the leading three jets is required, consequently, these regions are dominated by $t\bar{t}$ events.

regions, which is beneficial due to the generally tight cuts in the control regions.

Only the $m_{\rm T}$ and the $E_{\rm T}^{\rm miss}$ criteria are considerably different between signal and control regions - therefore, the extrapolation to the signal regions happens mainly in $m_{\rm T}$ and in $E_{\rm T}^{\rm miss}$. The upper edge of the $E_{\rm T}^{\rm miss}$ and $m_{\rm T}$ cuts defining the control regions correspond to the cuts of the loose signal regions in $E_{\rm T}^{\rm miss}$ and $m_{\rm T}$.

For every jet multiplicity, four control regions exist similarly to Section 8.1: The requirement of a b-tagged jet defines the Top control region and the veto on any b-tagged jet the W+jets control region. These are further separated into electron and muon channels.

Cuts on $150 < E_{\rm T}^{\rm miss} < 300$ GeV are required for the 3-jets or 5-jets control regions. The transverse mass is required to be between 80 and 150 GeV for the 3-jets control regions and between 60 and 150 GeV for the 5-jets control regions. The lower cut in $m_{\rm T}$ for the 5-jets control regions with respect to the 3-jets control regions is to enhance the statistics. The 6-jets control region require $150 < E_{\rm T}^{\rm miss} < 250$ GeV ($100 < E_{\rm T}^{\rm miss} < 200$ GeV) and $40 < m_{\rm T} < 80$ GeV ($40 < m_{\rm T} < 150$ GeV) for the Top (W+jets) control regions. For W+jets events, high jet multiplicities are less likely due to reduced cross sections. Therefore, all 6-jets control regions are dominated by $t\bar{t}$ events, even the W+jets control regions with a fraction of ~ 30 % W+jets events. The reduced cuts in $m_{\rm T}$ and in $E_{\rm T}^{\rm miss}$ in the W+jets control regions increase this fraction. This low fraction of W+jets events will be reflected by a large uncertainty on the W+jets background estimate in the signal regions requiring six jets, but this background is negligible in these signal regions.

Similarly, the 3-jets W+jets control regions are more dominated by W+jets events ($\sim 80\%$) than the corresponding 5-jets control regions ($\sim 55\%$), despite of the looser cut in $m_{\rm T}$ in the 5-jets regions.

The fraction of $t\bar{t}$ events in Top control regions is the lowest in the 3-jets Top control regions with $\sim 60\%$, while it is $\sim 85\%$ in both the 5-jets and 6-jets Top control regions.

Considering the closeness of the control and signal regions, the signal contamination needs to be
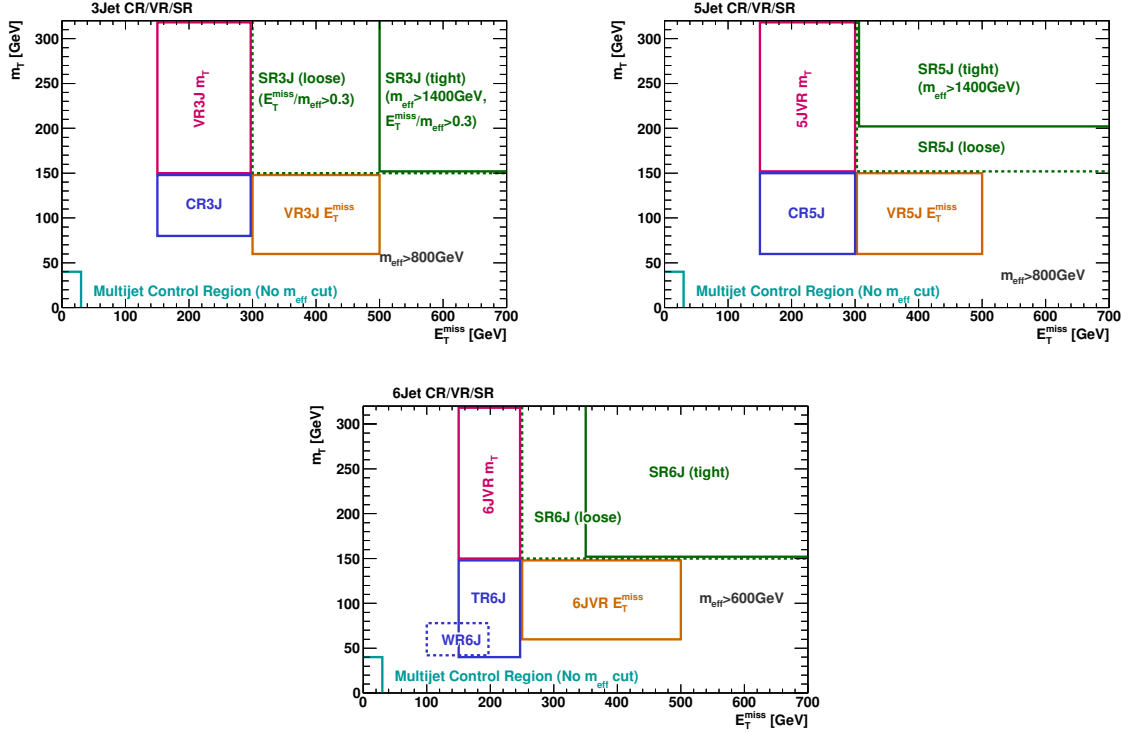
Figure 13.1: The definition and position of the control regions requiring three jets (top left), five jets (top right) and six jets (bottom) with respect to the signal regions with the same jet multiplicity in the E_T^{miss}-m_T-plane. The position of the validation regions is also given. The suffixes '3J', '5J' and '6J' indicate the jet multiplicities. The plots were slightly modified with respect to [179].

carefully checked in the control regions. This has been done in [225] for different signal models close to the expected sensitivity as evaluated in Chapter 12. The signal contamination has been found to be negligible for the control regions and also for the validation regions defined below.

The extrapolation between the control and the signal regions is mostly in m_T and in E_T^{miss}, but also in m_{eff}^{incl} for the discovery signal regions. It is checked that the background estimates and distributions describe the data well enough to perform this extrapolation safely. As examples, Figures 13.2, 13.3 and 13.4 show the E_T^{miss} distributions in the 3-jets control regions in the electron channel (the E_T^{miss} cut was not applied for these plots), the m_{eff}^{incl} distributions in the 5-jets control regions in the electron channel and the m_T distributions in the 6-jets control regions in the electron channel (the cut on m_T was not applied for these plots). A reasonable agreement can mostly be seen, although the W+jets background contribution is too high in the 3-jets and 5-jets W+jets control regions.

13.5   Validation regions

Validation regions are defined to check the extrapolation between control regions and signal regions. As the control regions close directly on the signal regions in m_T and in E_T^{miss}, it is not possible to place the validation regions at values of E_T^{miss} and m_T between the control and signal regions. Instead, the validation regions are defined to control the extrapolation in m_T or in E_T^{miss} independently.

For each set of control and signal regions with the same jet multiplicity, four validation regions are defined, as detailed in Table 13.3. All of these validation regions use the same cuts on the
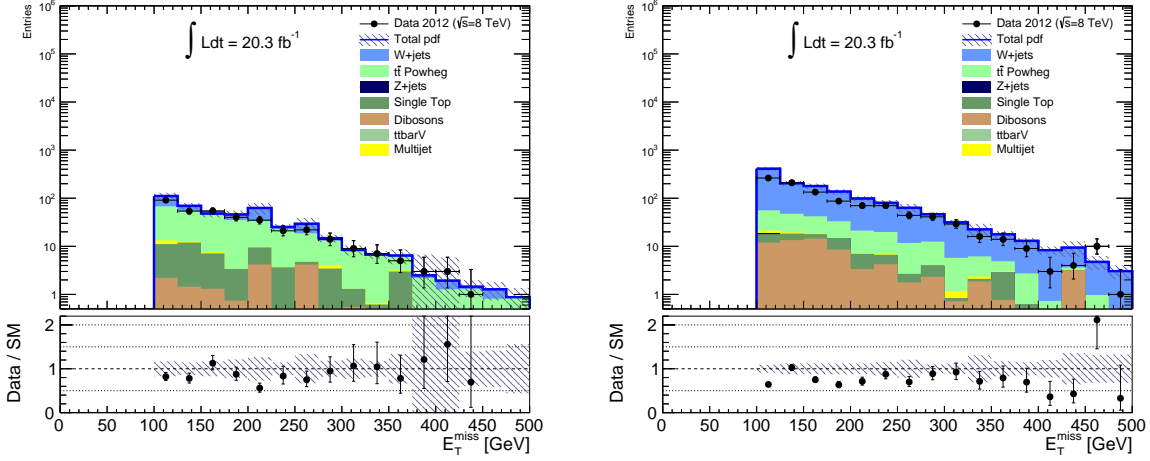
Figure 13.2: The E_T^{miss} distributions are shown in the 3-jets Top control region (left) and in the 3-jets W+jets control region (right) in the electron channel without imposing the E_T^{miss} cuts of the control regions. (The lower cut on $E_T^{miss} > 100$ GeV is applied due to the trigger.)
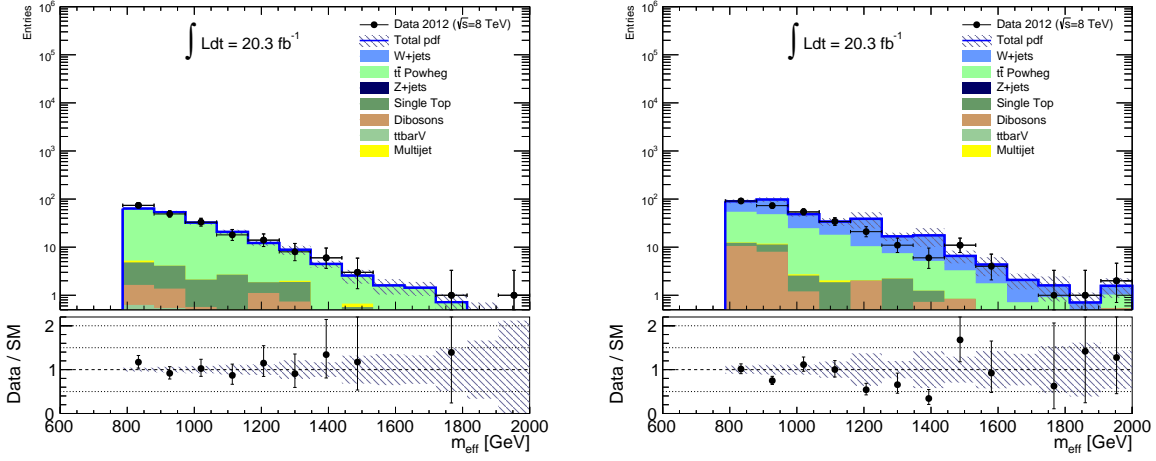
Figure 13.3: The m_{eff}^{incl} distributions are shown in the 5-jets Top control region (left) and in the 5-jets W+jets control regions (right) in the electron channel.
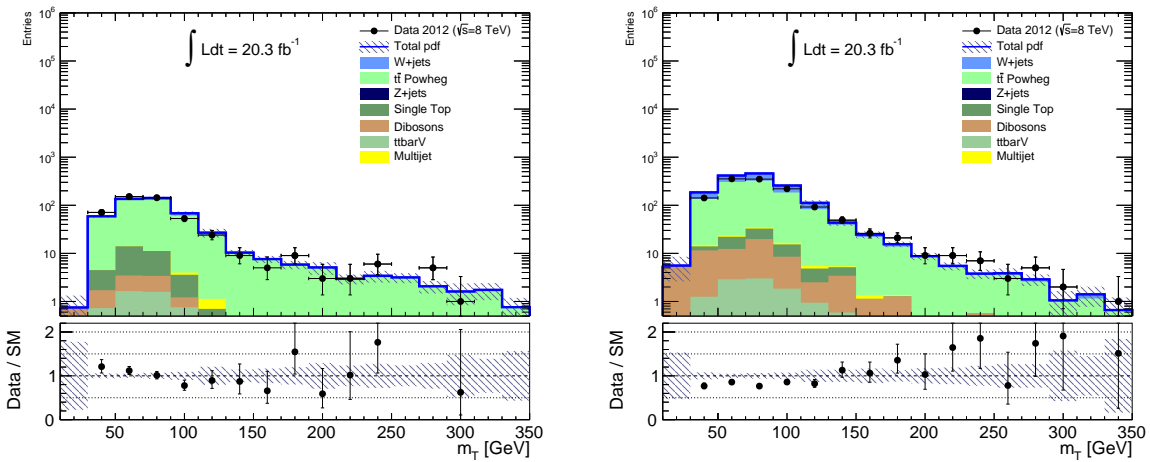
Figure 13.4: The m_T distributions are shown in the 6-jets Top control regions (left) and in the W+jets control regions (right) in the electron channel. The cut on m_T was not applied for these plots.

	3-jet		5-jet		6-jet	
	$E_{\mathrm{T}}^{\mathrm{miss}}$ **region**	m_{T} **region**	$E_{\mathrm{T}}^{\mathrm{miss}}$ **region**	m_{T} **region**	$E_{\mathrm{T}}^{\mathrm{miss}}$ **region**	m_{T} **region**
$p_{\mathrm{T}}^{\mathrm{jet}}$(GeV)	> 80, 80, 30		> 80, 50, 40, 40, 40		> 80, 50, 40, 40, 40, 40	
$p_{\mathrm{T}}^{\mathrm{add.\ jets}}$(GeV)	$p_{\mathrm{T}}^{\mathrm{5th\ jet}} < 40$		$p_{\mathrm{T}}^{\mathrm{6th\ jet}} < 40$		$-$	
$E_{\mathrm{T}}^{\mathrm{miss}}$ (GeV)	[300,500]	[150,300]	[300,500]	[150,300]	[250,500]	[150,250]
m_{T} (GeV)	[60,150]	[150,320]	[60,150]	[150,320]	[60,150]	[150,320]
$m_{\mathrm{eff}}^{\mathrm{incl}}$ (GeV)	> 800				> 600	

Table 13.3: Definition of the validation regions. The extrapolation (see text) from the control regions to the signal regions is cross-checked in validation regions with the same jet multiplicity as the corresponding control and signal regions. The validation regions are located at higher m_{T} or $E_{\mathrm{T}}^{\mathrm{miss}}$ values compared to the control regions.

jets as the corresponding signal regions and are therefore tighter than the control regions. Two validation regions are defined at larger $E_{\mathrm{T}}^{\mathrm{miss}}$ values than the control regions in the electron and in the muon channel; the other two are defined at larger values in m_{T} than the control regions in the electron or muon channel.

Distributions in the validation regions are presented after the background-only fit in Section 15.2.

Chapter 14

Fit strategy

14.1 Fit strategy

For the $20.3\,\mathrm{fb}^{-1}$ analysis, the fit strategy needs to be changed with respect to the $5.8\,\mathrm{fb}^{-1}$ analysis due to the presence of more control and signal regions with different jet multiplicities. As described in Section 13, a set of four control regions is defined for the two signal regions in the electron and muon channels with the same jet multiplicity. All control regions with the same jet multiplicity as the corresponding signal (or validation) regions are fitted together in one background-only fit to obtain the background estimates. In the following, all regions with the same jet multiplicity will be referred to as 'tower'. In total, three background-only fits are executed, one for each tower. Parameters related to background samples in one tower are not correlated with the parameters in another tower. The background-only fit in one tower can be compared to the fit setup presented in Section 10.3.1.

This implementation accounts for the possibility that regions with different jet multiplicities are dominated by different background processes. Usually, the jet energy scale and theoretical uncertainties are correlated with the normalisation parameters of the W+jets and $t\bar{t}$ background, as both uncertainties also affect the normalisation. Separating the towers from each other, it is assured that no uncertainties or normalisation parameters of one tower can constrain the parameters of another tower. The separation of the towers in the fits was also introduced to avoid constraining the usually large errors (due to low Monte Carlo statistics) on the normalisation parameters in the tower containing the 6-jets regions by the towers with lower jet multiplicities and thus higher Monte Carlo statistics.

In contrast to the background-only fits, the towers are correlated in the exclusion fit by the signal. The signal sample has the same normalisation parameter, the signal strength μ_{SIG}, and the same systematics parameters related to signal specific systematics in every region.

A schematic sketch of the background-only fits and the exclusion fit is given in Figure 14.1, indicating the three towers, the extrapolations between the control and signal regions and the addition of the signal sample.

14.2 Implementation

The technical design of the three background-only fits is determined by the towers and by the requirement that systematics uncertainties assigned to backgrounds should not notably be modified in the fit in both their shape and their size. Systematic uncertainties could for
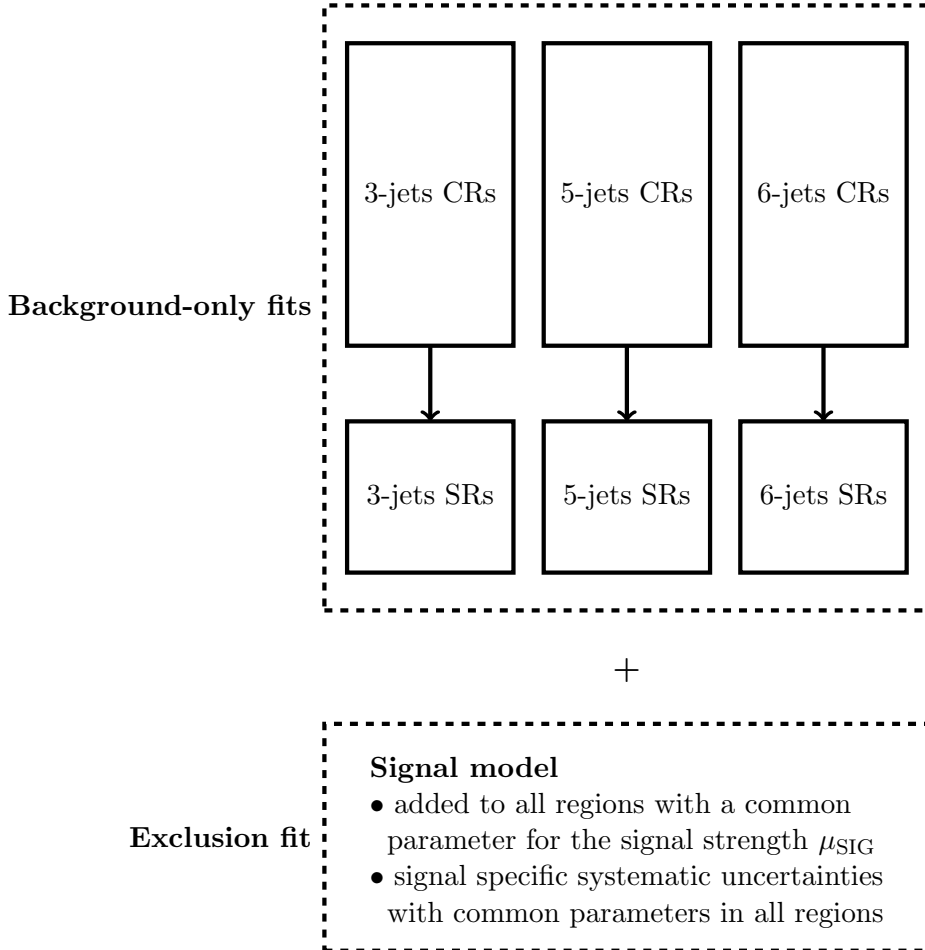
Figure 14.1: Schematic sketch of the fit strategy. All control regions (CRs) with the same jet multiplicity are fitted simultaneously. The background estimates in the signal regions (SRs) are obtained by extrapolation from the control regions with the same jet multiplicity. Control and signal regions with the same jet multiplicity form a 'tower'. Parameters related to backgrounds are only defined per tower. Thus, the towers are completely independent in the background-only fits. In the exclusion fit, a signal is added to all regions, which has the same normalisation parameter (the signal strength μ_{SIG}) in all regions. Signal specific systematic uncertainties have the same parameters in all regions. Hence, in the exclusion fit, the towers are correlated due to the signal sample.

example be modified due to large correlations to the normalisation parameters assigned to the backgrounds.

The reduction of systematic uncertainties in the fit is avoided by not using a shape fit in the control regions. Thus, the background-only fit has mainly the power to change normalisations of backgrounds. Shapes of systematic uncertainties can only be changed by comparisons between the control regions within one tower. This implementation is in contrast to the implementation of the background-only fit in Section 10.3.1, where the shape of the $m_{\mathrm{eff}}^{\mathrm{incl}}$ distribution in the control regions was explicitly used and corrected in the background fit.

Similarly to the fit setup in Section 10.3.1, the following samples are defined in every region (in addition to the data sample):

- The $t\bar{t}$ background with three free normalisation parameters $\mu_{\mathrm{Top\_xJ}}$ (x indicates the number of jets in the tower), one per tower

- The W+jets background with three free normalisation parameters $\mu_{\mathrm{W\_xJ}}$ (x indicates the number of jets in the tower), one per tower

  Systematic uncertainties are only assigned to the $t\bar{t}$ and W+jets backgrounds. The other smaller backgrounds receive an overall uncertainty on their normalisation.

- The Z+jets background is taken from Monte Carlo and is thus allowed to vary within its statistical uncertainties. Additionally, a systematic uncertainty of 30 % on this background is included by the type `overallSys`[1] with parameters $\alpha_{\mathrm{errBG\_3J}}$, $\alpha_{\mathrm{errBG\_5J}}$ and $\alpha_{\mathrm{errBG\_6J}}$

- The single top background is allowed to vary within its statistical uncertainties and an assumed systematic uncertainty of 50%. The systematic uncertainty is implemented as type `overallSys` with parameters $\alpha_{\mathrm{errST\_3J}}$, $\alpha_{\mathrm{errST\_5J}}$ and $\alpha_{\mathrm{errST\_6J}}$

- The $t\bar{t}$ plus an additional vector boson background is allowed to vary within the statistical uncertainties and a systematic uncertainties of 30% (`overallSys`). This background is correlated with the Z+jets background.

- The diboson background is poorly known, but very small, thus this background receives a systematic uncertainty of 50% implemented as `overallSys` with parameters $\alpha_{\mathrm{errDB\_3J}}$, $\alpha_{\mathrm{errDB\_5J}}$ and $\alpha_{\mathrm{errDB\_6J}}$. The background is also allowed to vary within its statistical uncertainties.

- The QCD multi-jet background is taken from the matrix method and may vary within the uncertainties calculated from this method.

14.3   Systematic uncertainties

Detailed systematic uncertainties are only assigned to the two major backgrounds $t\bar{t}$ and W+jets. Table 14.1 lists all the systematic uncertainties used in the fit along with the names of their parameters, their size and their implementation type.

The jet energy scale and resolution uncertainties are the largest contributions and exceed 100% in some regions. These uncertainties are implemented as uncertainties on the transfer factor. In contrast to the analysis presented in the last part, only one parameter for the jet energy scale is used for every tower and no separation into low, medium or high p_{T} jets is made. This was found not to be necessary, as the jet energy scale is not constrained significantly with the current setup.

---

[1]Systematic uncertainties can be implemented in different ways as described in Chapter 10

Systematic uncertainty	Parameter names	Size (in control regions)	Type
Jet energy resolution	$\alpha_{\text{JER\_3J}}$, $\alpha_{\text{JER\_5J}}$, $\alpha_{\text{JER\_6J}}$	1 - 350%	`overallNormHistoSys`, no down variation
Jet energy scale	$\alpha_{\text{JES\_3J}}$, $\alpha_{\text{JES\_5J}}$, $\alpha_{\text{JES\_6J}}$	2 - 214%	`overallNormHistoSys`
Resolution of soft term of $E_{\text{T}}^{\text{miss}}$	$\alpha_{\text{RESOST\_3J}}$, $\alpha_{\text{RESOST\_5J}}$, $\alpha_{\text{RESOST\_6J}}$	< 50%	`overallNormHistoSys`, no down variation
Scale of soft term of $E_{\text{T}}^{\text{miss}}$	$\alpha_{\text{SCALEST\_3J}}$, $\alpha_{\text{SCALEST\_5J}}$, $\alpha_{\text{SCALEST\_6J}}$	< 50%	`overallNormHistoSys`
Pile-up	$\alpha_{\text{pileup\_3J}}$, $\alpha_{\text{pileup\_5J}}$, $\alpha_{\text{pileup\_6J}}$	< 47%	`overallNormHistoSys`
b-tagging - efficiency on b-jets	$\alpha_{\text{BT\_3J}}$, $\alpha_{\text{BT\_5J}}$, $\alpha_{\text{BT\_6J}}$	< 14%	`overallNormHistoSys`
b-tagging - efficiency on c-jets	$\alpha_{\text{CT\_3J}}$, $\alpha_{\text{CT\_5J}}$, $\alpha_{\text{CT\_6J}}$	< 6%	`overallNormHistoSys`
b-tagging - light jets	-	mostly below < 3%	not used
Electron Energy Scale	-	< 2 %	not used
Muon Energy Resolution	-	< 2 %	not used
Lepton Scale Factors	-	< 2 %	not used
Trigger Efficiency	-	< 2 %	not used
Theoretical uncertainties			
Factorisation scale - $t\bar{t}$	$\alpha_{\text{topTheoFacSc\_3J}}$, $\alpha_{\text{topTheoFacSc\_5J}}$, $\alpha_{\text{topTheoFacSc\_6J}}$	< 20%	`overallSys`
Factorisation scale - W+jets	$\alpha_{\text{qfac\_3J}}$, $\alpha_{\text{qfac\_5J}}$, $\alpha_{\text{qfac\_6J}}$	< 15%	`overallNormHistoSys`
Renormalisation scale - $t\bar{t}$	$\alpha_{\text{topTheoRenSc\_3J}}$, $\alpha_{\text{topTheoRenSc\_5J}}$, $\alpha_{\text{topTheoRenSc\_6J}}$	< 36%	`overallSys`
Renormalisation scale - W+jets	$\alpha_{\text{ktfac\_3J}}$, $\alpha_{\text{ktfac\_5J}}$, $\alpha_{\text{ktfac\_6J}}$	< 43%	`overallNormHistoSys`
Minimum p_{T} threshold[2] - W+jets	$\alpha_{\text{WTheoPtMin\_3J}}$, $\alpha_{\text{WTheoPtMin\_5J}}$, $\alpha_{\text{WTheoPtMin\_6J}}$	< 46%	`overallSys`
Initial and final state radiation - $t\bar{t}$	$\alpha_{\text{topTheoPS\_3J}}$, $\alpha_{\text{topTheoPS\_5J}}$, $\alpha_{\text{topTheoPS\_6J}}$	< 23%	`overallSys`
PDF	$\alpha_{\text{pdfIntra\_3J}}$, $\alpha_{\text{pdfIntra\_5J}}$, $\alpha_{\text{pdfIntra\_6J}}$	< 9%	`overallNormHistoSys`
	$\alpha_{\text{pdfInter\_3J}}$, $\alpha_{\text{pdfInter\_5J}}$, $\alpha_{\text{pdfInter\_6J}}$	< 9%	combined with $\alpha_{\text{pdfIntra\_X}}$ parameters

Table 14.1: Summary of the systematic uncertainties on the $t\bar{t}$ and W+jets backgrounds included in the fit. The sizes of the systematic uncertainties are given before the fit and only in the control regions. They are often larger in the signal regions.

---

[2]See Section 13.3

The theoretical uncertainties are also large with up to 50% depending on the region. They are implemented as uncertainties on the transfer factor.

Further uncertainties include the uncertainties on the scale and resolution of low energy topological clusters entering the $E_\mathrm{T}^\mathrm{miss}$ computation which are not associated with reconstructed objects (soft term of $E_\mathrm{T}^\mathrm{miss}$, resolution and scale), and uncertainties related to b-tagging efficiencies on b-jets and c-jets, all of them implemented as uncertainties on the transfer factor.

The b-tagging uncertainty on light jets is below 3% in all regions apart from one region where it is 6% (5-jets Top control region in the electron channel). In comparison with theoretical uncertainties, the jet energy scale and resolution, this uncertainty is small. Therefore, it is not included in the fit in the following. The uncertainties on trigger scale factors, electron energy scale and muon energy resolution, as well as on the lepton scale factors, are below 2% in all regions. They are therefore not used in the fit in order to simplify the fit setup.

14.4   Setup of the exclusion fit

In the exclusion fit, a signal sample is added in all signal and control regions. A common free normalisation factor, the signal strength μ_SIG, is added to all regions. Thus, all three towers are connected by the signal sample in the exclusion fit. The signal sample receives the same systematics as the $t\bar{t}$ and W+jets backgrounds apart from the theoretical uncertainties and the jet energy scale. Concerning the jet energy scale, the signal sample is assigned its own parameter (implemented as `overallHistoSys`) so that the background cannot constrain the jet energy scale of the signal. Similar to the description in Section 10.4.4, a systematic uncertainty is added on the signal cross section.

In addition, for the simplified models, a further systematic uncertainty is added to take into account theoretical uncertainties on the signal event acceptance [231]. These uncertainties are evaluated from the shape uncertainties on the renormalisation and factorisation scales, the initial and final state radiation, the jet matching and the PDF sets used. The resulting combined systematic uncertainties were evaluated in [231] on 18 points with gluino pair production and seven points with squark pair production, all points belonging to simplified models with one step. The uncertainties depend on the mass difference ΔM between gluino/squark and $\tilde{\chi}_1^0$. They are parametrised for this analysis by an exponential function and are given by $\max(e^{-1.4-0.013\Delta M}, 0.06)$ for the signal regions requiring at least three jets and $e^{-1.2-0.005\Delta M}$ for the signal regions requiring at least five or six jets.

In the exclusion fit, the systematic uncertainties on the Z+jets, the single top and the $t\bar{t}+$ vector boson sample were handled differently from background-only fit setup[3]. In the exclusion fit, these backgrounds are correlated and obtain a common systematic uncertainty only varying the scale with a size of 20%.

To enhance the sensitivity in the exclusion fit, a shape fit in $m_\mathrm{eff}^\mathrm{incl}$ between 800 and 1600 GeV is performed in the signal regions requiring at least three or five jets (in four bins of equal width of 200 GeV) and in $E_\mathrm{T}^\mathrm{miss}$ between 250 and 550 GeV (in three bins of a width of 100 GeV) in the 6-jets signal regions. The motivation of this shape fit has been described in Section 12.3.

---

[3]This had purely historical reasons. The limits as shown in Section 16.2 were derived based on the exclusion fit setup as described here. Afterwards, the systematic uncertainties on the Z+jets/$t\bar{t}+$ vector boson and those on the single top sample were decorrelated in order to be more conservative in the results and not to constrain backgrounds. It was however checked that the difference between the background-only fit setup and the exclusion fit setup is negligible, and thus the CPU and time intensive re-calculation of the limits was not considered to be necessary.

Chapter 15

Background fit results

This chapter presents the results of the background-only fit for the full dataset of 2012[1]. In particular, the background estimates in the loose and tight signal regions are derived. The size of the systematic uncertainties for the loose signal regions is discussed at the end of this chapter.

15.1 Results in the control regions

The backgrounds are simultaneously fitted to the control regions in each of the three towers. Table 15.1 shows the results of the background-only fits. The top part of this table shows the results of the background-only fit in the 3-jets control regions, the middle part for the 5-jets control regions and the bottom part for the 6-jets control regions. Each of the parts is similarly constructed as Table 10.3, showing the background estimates obtained from Monte Carlo simulation or the matrix method at the bottom and the background estimates after the fit to the control regions in the upper part. At the top, the number of observed events is given, to be compared to the fitted total background expectation.

Due to its construction, the background-only fit leads to a good agreement between the total fitted background estimate and the data in all control regions. The $t\bar{t}$ background remains approximately of the same strength after fit, whereas the W+jets background is scaled down. The precise normalisation factors evaluated in the fit are[2]:

$$
\begin{aligned}
\mu_{\text{Top\_3J}} &= 1.02^{+0.23}_{-0.21}, & \mu_{\text{W\_3J}} &= 0.65^{+0.09}_{-0.12} \\
\mu_{\text{Top\_5J}} &= 1.04^{+0.14}_{-0.12}, & \mu_{\text{W\_5J}} &= 0.62^{+0.19}_{-0.21} \\
\mu_{\text{Top\_6J}} &= 1.00 \pm 0.13, & \mu_{\text{W\_6J}} &= 0.6 \pm 0.4
\end{aligned}
\tag{15.1.1}
$$

The relatively large uncertainty on the normalisation factor for the W+jets sample in the 6-jets control regions stems from the low purity of the W+jets control regions in W+jets events and from the large Monte Carlo statistical uncertainty on this background.

The table also shows that - depending on the control region - the single t or the diboson background is the third largest background contribution after the $t\bar{t}$ and W+jets background. The

---

[1]These results are slightly different from the results in [179, 225] as the author recalculated them with the same software version as used for the limits in Chapter 16.2, whereas the yields in the various regions and the break-up of the systematic uncertainties in [179, 225] were calculated with a slightly older software version.

[2]The precise fit results including the correlation matrices are given in Appendix D.

Control region	3-jets Top control region		3-jets W+jets control region	
Channel	Electron channel	Muon channel	Electron channel	Muon channel
Observed events	186	160	446	389
Fitted background events	192 ± 13	154 ± 11	446 ± 22	389 ± 21
Fitted $t\bar{t}$ events	129 ± 22	104 ± 19	89 ± 37	65 ± 28
Fitted W+jets events	31 ± 15	18 ± 10	303 ± 49	279 ± 42
Fitted Z+jets events	0.00 ± 0.00	0.00 ± 0.00	0.00 ± 0.00	0.00 ± 0.00
Fitted single t events	21 ± 10	23 ± 11	19 ± 9	11 ± 6
Fitted diboson events	9 ± 5	4.5 ± 2.3	33 ± 17	26 ± 13
Fitted $t\bar{t}$+V events	1.06 ± 0.33	0.97 ± 0.30	0.64 ± 0.19	0.52 ± 0.16
Fitted QCD multi-jet events	$0.53^{+1.16}_{-0.53}$	2.9 ± 2.4	$0.9^{+2.7}_{-0.9}$	8 ± 5
MC exp. SM events	225	156	602	534
MC exp. $t\bar{t}$ events	135	99	87	63
MC exp. W+jets events	57	28	462	426
MC exp. Z+jets events	0.00 ± 0.00	0.00 ± 0.00	0.00 ± 0.00	0.00 ± 0.00
MC exp. single t events	21	21	18	11
MC exp. diboson events	10	4.5	34	26
MC exp. $t\bar{t}$+V events	1.13	0.95	0.64	0.52
QCD multi-jet events	0.6	2.6	0.9	8

Control region	5-jets Top control region		5-jets W+jets control region	
Channel	Electron channel	Muon channel	Electron channel	Muon channel
Observed events	208	185	311	271
Fitted background events	207 ± 13	186 ± 11	305 ± 15	276 ± 15
Fitted $t\bar{t}$ events	186 ± 16	147 ± 14	151 ± 35	124 ± 30
Fitted W+jets events	2^{+4}_{-2}	7 ± 5	116 ± 38	117 ± 35
Fitted Z+jets events	0.00 ± 0.00	0.00 ± 0.00	0.00 ± 0.00	0.90 ± 0.27
Fitted single t events	12 ± 6	23 ± 11	11 ± 5	8 ± 4
Fitted diboson events	3.9 ± 2.0	6.8 ± 3.4	24 ± 12	20 ± 10
Fitted $t\bar{t}$+V events	2.2 ± 0.7	1.6 ± 0.5	1.5 ± 0.5	1.2 ± 0.4
Fitted QCD multi-jet events	$0.6^{+1.2}_{-0.6}$	0^{+1}_{-0}	$1.0^{+1.8}_{-1.0}$	4 ± 4
MC exp. SM events	202	187	361	348
MC exp. $t\bar{t}$ events	180	143	141	121
MC exp. W+jets events	3	13	184	192
MC exp. Z+jets events	0.00	0.00	0.00	0.92
MC exp. single t events	13	24	11	8.09
MC exp. diboson events	3.9	6.7	23	21
MC exp. $t\bar{t}$+V events	2.2	1.6	1.5	1.2
QCD multi-jet events	0.6	0.0	0.9	5

Control region	6-jets Top control region		6-jets W+jets control region	
Channel	Electron channel	Muon channel	Electron channel	Muon channel
Observed events	451	393	684	688
Fitted background events	449 ± 18	389 ± 16	709 ± 24	669 ± 24
Fitted $t\bar{t}$ events	395 ± 32	340 ± 27	522 ± 94	449 ± 91
Fitted W+jets events	18^{+21}_{-18}	18^{+25}_{-18}	132 ± 90	149 ± 100
Fitted Z+jets events	0.00 ± 0.00	0.00 ± 0.00	0.00 ± 0.00	4.5 ± 1.4
Fitted single t events	25 ± 12	17 ± 8	23 ± 11	26 ± 13
Fitted diboson events	4.7 ± 2.4	4.1 ± 2.1	23 ± 12	21 ± 11
Fitted $t\bar{t}$+V events	5.5 ± 1.6	4.5 ± 1.4	5.9 ± 1.7	5.4 ± 1.6
Fitted QCD multi-jet events	$0.5^{+1.9}_{-0.5}$	5 ± 4	3^{+4}_{-3}	13 ± 8
MC exp. SM events	440	375	850	757
MC exp. $t\bar{t}$ events	377	325	558	456
MC exp. W+jets events	28	21	238	237
MC exp. Z+jets events	0.00	0.00	0.00	4.2
MC exp. single t events	24	16	22	24
MC exp. diboson events	4.9	4.3	24	21
MC exp. $t\bar{t}$+V events	5.4	4.6	5.8	5.1
QCD mutli-jet events	0.5	4	3	11

Table 15.1: The yields before and after fit are shown in the control regions (see text).
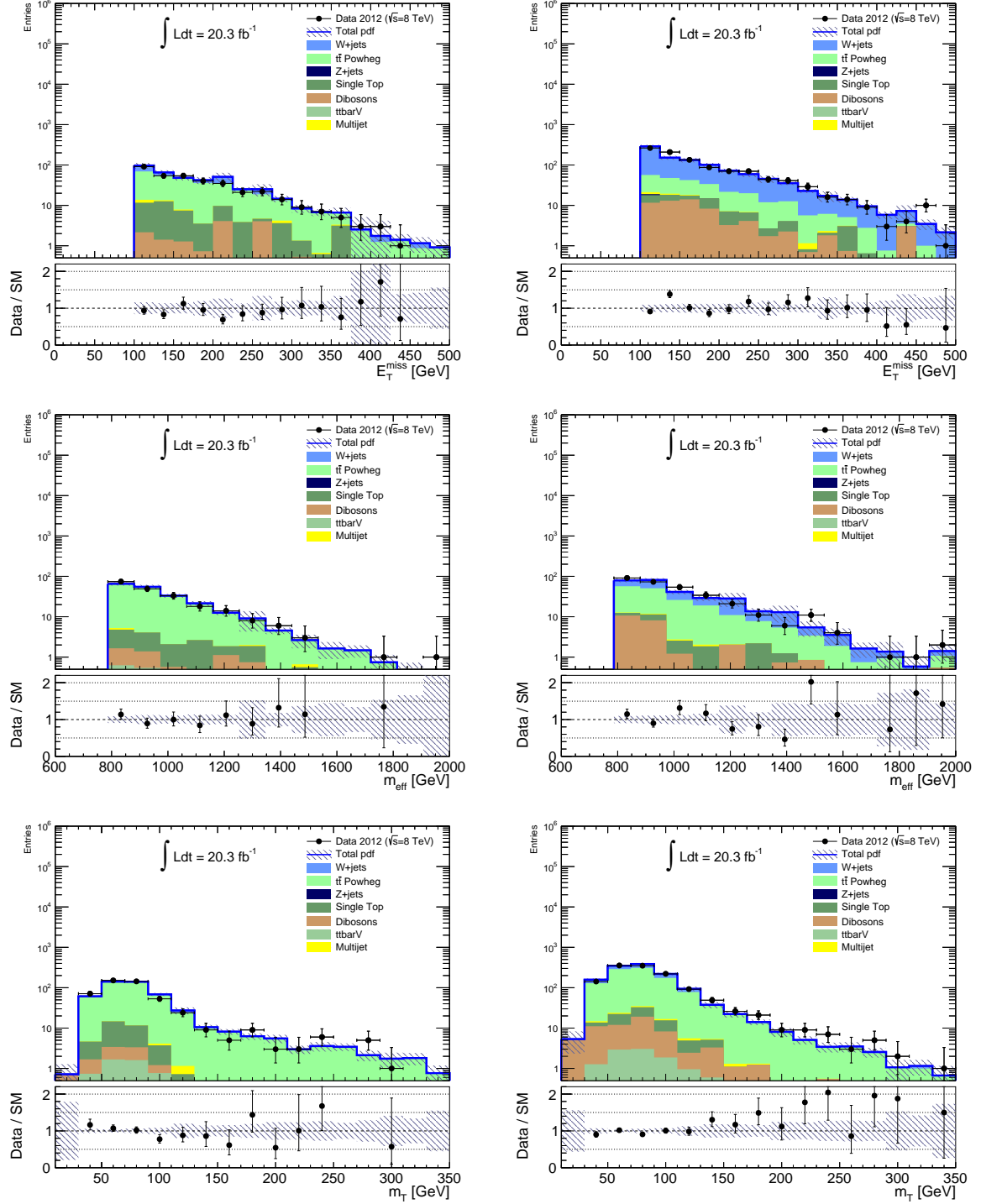
Figure 15.1: The E_T^{miss} distributions are shown in the 3-jets Top (top left) and in the W+jets (top right) control regions. The m_{eff}^{incl} distributions are shown in the 5-jets Top (middle left) and W+jets (middle right) control regions. The m_T distributions are shown in the Top (bottom left) and in the W+jets (bottom right) 6-jets control regions. All distributions are shown in the electron channel after the background-only fit and for 20.3 fb^{-1}. The uncertainty bands include the statistical and systematic uncertainties.
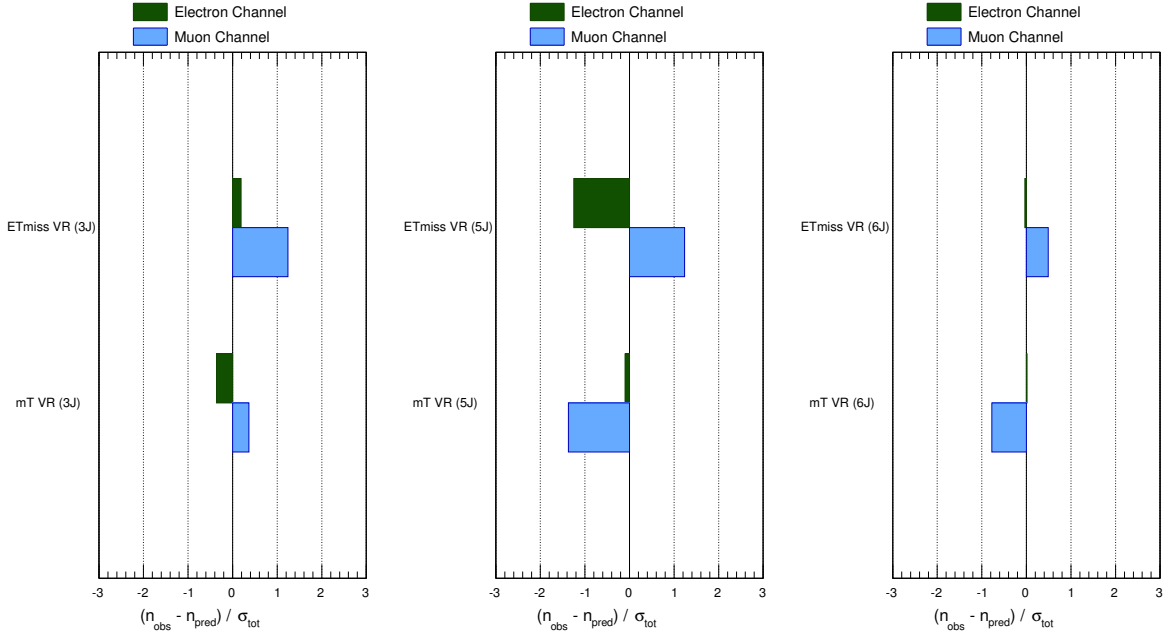
Figure 15.2: Pull plots for the validation regions requiring at least three jets (left), five jets (middle) and at least six jets (right).

Z+jets background is completely negligible, being zero in most regions. The other two backgrounds, the QCD multi-jet background and the $t\bar{t}$+vector boson background (abbreviated by $t\bar{t}$+V) are similarly small.

Figure 15.1 shows a selection of distributions in the control regions, all being from the electron channel (similar plots are found in the muon channel). These plots are the corresponding after-fit plots matching the before-fit plots shown in Figures 13.2, 13.3 and 13.4: The E_T^{miss} distributions are shown in the 3-jets, the $m_{\text{eff}}^{\text{incl}}$ distributions in the 5-jets and the m_T distributions in the 6-jets Top and W+jets control regions. As discussed in Chapter 14.1, the background-only fit is not allowed to change the shapes of distributions significantly. Consequently, the differences between the plots in Figure 15.1 and Figures 13.2, 13.3 and 13.4 are mainly the normalisation and the uncertainties on the background estimates, resulting in a better agreement after fit.

15.2 Results in the validation regions

The results of the background-only fit in the control regions are extrapolated to the validation regions in order to cross-check the extrapolation to larger m_T and E_T^{miss} values and thus to the signal regions. The background estimates after the background-only fit are shown together with the observed data and the background estimates before the fit in Table 10.4 for the validation regions requiring at least three, five or six jets. The agreement between fitted background estimates and observed data is also summarised in the pull plots in Figure 15.2. These plots are calculated as described in Section 10.3.2. Only four out of twelve validation regions show greater then 1σ differences between the background estimate and data: the 3-jets E_T^{miss} validation region in the muon channel, the 5-jets E_T^{miss} validation regions in both channels and the 5-jets m_T validation region in the muon channel. However, even in these regions the disagreement is well below 2σ and therefore considered acceptable. Thus, the agreement is in general good in the 3-jets and 6-jets validation regions, but less good (but considered to be acceptable) in the 5-jets validation regions.

| Validation region | 3-jets $E_{\mathrm{T}}^{\mathrm{miss}}$ region | | 3-jets m_{T} region | |
Channel	Electron channel	Muon channel	Electron channel	Muon channel
Observed events	378	367	147	124
Fitted background events	368 ± 46	310 ± 43	156 ± 22	116 ± 20
Fitted $t\bar{t}$ events	103.65 ± 23	75 ± 17	96 ± 24	79 ± 20
Fitted W+jets events	215 ± 58	187 ± 51	37 ± 13	19 ± 8
Fitted Z+jets events	0.00 ± 0.00	0.9 ± 0.3	0.00 ± 0.00	2.0 ± 0.6
Fitted single t events	20 ± 10	16 ± 8	12 ± 6	4.4 ± 2.1
Fitted diboson events	28 ± 14	27 ± 14	7 ± 3	8 ± 4
Fitted $t\bar{t}$+V events	1.3 ± 0.4	0.97 ± 0.29	1.9 ± 0.6	1.6 ± 0.5
Fitted QCD multi-jet events	$0.2^{+2.2}_{-0.2}$	$2.5^{+3.3}_{-2.5}$	$1.9^{+2.2}_{-1.9}$	$1.5^{+1.7}_{-1.5}$
MC exp. SM events	484	409	176	124
MC exp. $t\bar{t}$ events	101.9	74	94	77
MC exp. W+jets events	332	288	59	29
MC exp. Z+jets events	0.00	0.93	0.00	2.0
MC exp. single t events	19	15	12	4.2
MC exp. diboson events	29	28	7	9
MC exp. $t\bar{t}$+V events	1.3	1.0	1.9	1.6
QCD multi-jet events	0.22	2.5	1.9	1.5

| Validation region | 5-jets $E_{\mathrm{T}}^{\mathrm{miss}}$ region | | 5-jets m_{T} region | |
Channel	Electron channel	Muon channel	Electron channel	Muon channel
Observed events	43	50	43	25
Fitted background events	57 ± 8	40 ± 5	44 ± 5	36 ± 5
Fitted $t\bar{t}$ events	36 ± 8	26 ± 6	35 ± 6	31 ± 5
Fitted W+jets events	12.9 ± 5.8	7.6 ± 3.1	1.4 ± 0.8	1.0 ± 0.6
Fitted Z+jets events	0.00 ± 0.00	0.00 ± 0.00	0.00 ± 0.00	0.00 ± 0.00
Fitted single t events	4.1 ± 2.0	2.5 ± 1.2	4.6 ± 2.3	1.4 ± 0.7
Fitted diboson events	2.7 ± 1.4	2.0 ± 1.0	1.5 ± 0.8	1.4 ± 0.7
Fitted $t\bar{t}$+V events	0.66 ± 0.20	0.45 ± 0.14	1.04 ± 0.32	1.01 ± 0.31
Fitted QCD multi-jet events	0.00 ± 0.16	$1.0^{+1.1}_{-1.0}$	$0.05^{+0.25}_{-0.05}$	0.00 ± 0.12
MC exp. SM events	63	43	43	35
MC exp. $t\bar{t}$ events	35	25	33.8	29.7
MC exp. W+jets events	21	12.2	2.2	1.6
MC exp. Z+jets events	0.00	0.00	0.00	0.00
MC exp. single t events	4.2	2.6	4.7	1.4
MC exp. diboson events	2.7	1.9	1.5	1.4
MC exp. $t\bar{t}$+V events	0.66	0.45	1.04	1.01
QCD multi-jet events	0.00	1.0	0.05	0.00

| Validation region | 6-jets $E_{\mathrm{T}}^{\mathrm{miss}}$ region | | 6-jets m_{T} region | |
Channel	Electron channel	Muon channel	Electron channel	Muon channel
Observed events	53	50	25	16
Fitted background events	53 ± 5	45 ± 8	24 ± 6	20 ± 4
Fitted $t\bar{t}$ events	44 ± 7	33 ± 7	23 ± 6	18 ± 5
Fitted W+jets events	5 ± 4	8 ± 6	$0.29^{+0.33}_{-0.29}$	0.8 ± 0.8
Fitted Z+jets events	0.00 ± 0.00	0.00 ± 0.00	0.00 ± 0.00	0.00 ± 0.00
Fitted single t events	2.7 ± 1.3	1.8 ± 0.9	0.11 ± 0.05	0.8 ± 0.4
Fitted diboson events	0.9 ± 0.5	1.2 ± 0.7	0.42 ± 0.22	0.08 ± 0.04
Fitted $t\bar{t}$+V events	1.03 ± 0.31	0.71 ± 0.23	0.86 ± 0.26	0.73 ± 0.23
Fitted QCD multi-jet events	$0.00^{+0.16}_{-0.00}$	$0.3^{+0.7}_{-0.3}$	$0.19^{+0.24}_{-0.19}$	1.1 ± 1.0
MC exp. SM events	57	50	26	23
MC exp. $t\bar{t}$ events	45	33	24	19
MC exp. W+jets events	8	13	0.6	1.2
MC exp. Z+jets events	0.00	0.00	0.00	0.00
MC exp. single t events	2.6	1.7	0.10	0.8
MC exp. diboson events	1.0	1.3	0.44	0.08
MC exp. $t\bar{t}$+V events	1.02	0.70	0.85	0.72
QCD multi-jet events	0.00	0.3	0.19	1.1

Table 15.2: The yields before and after fit are shown in the validation regions (see text).

	Loose signal regions					
Region	**3-jets**		**5-jets**		**6-jets**	
Channel	Electron	Muon	Electron	Muon	Electron	Muon
Observed events	45	28	12	7	7	7
Fitted background events	46.3 ± 8.1	38.1 ± 5.8	12.2 ± 5.3	7.0 ± 1.6	9.7 ± 2.0	7.4 ± 1.7
Fitted $t\bar{t}$ events	23.8 ± 6.3	20.1 ± 5.0	7.4 ± 3.3	5.6 ± 1.5	8.0 ± 1.9	5.7 ± 1.5
Fitted W+jets events	15 ± 5	11 ± 4	3.1 ± 2.2	0.4 ± 0.4	$0.13^{+0.16}_{-0.13}$	$0.28^{+0.32}_{-0.28}$
Fitted Z+jets events	0.00 ± 0.00	0.00 ± 0.00	0.00 ± 0.00	0.00 ± 0.00	0.00 ± 0.00	0.00 ± 0.00
Fitted single t events	1.1 ± 0.5	2.2 ± 1.1	0.32 ± 0.20	0.31 ± 0.15	0.53 ± 0.26	0.19 ± 0.10
Fitted diboson events	4.4 ± 2.3	3.3 ± 1.7	0.9 ± 0.6	0.41 ± 0.21	0.52 ± 0.27	0.065 ± 0.034
Fitted $t\bar{t}$+V events	1.2 ± 0.4	0.96 ± 0.30	0.45 ± 0.22	0.34 ± 0.11	0.46 ± 0.15	0.38 ± 0.12
Fitted QCD multi-jet events	$0.4^{+0.5}_{-0.4}$	$0.8^{+0.9}_{-0.8}$	$0.01^{+0.08}_{-0.01}$	0.00 ± 0.03	$0.07^{+0.09}_{-0.07}$	0.9 ± 0.9
MC exp. SM events	54	43	14	7.0	10.1	7.9
MC exp. $t\bar{t}$ events	23	19.7	7.1	5.3	8.4	6.0
MC exp. W+jets events	24	16	5.3	0.6	0.18	0.5
MC exp. Z+jets events	0.00	0.00	0.00	0.00	0.00	0.00
MC exp. single t events	1.0	2.1	0.32	0.31	0.50	0.18
MC exp. diboson events	4.5	3.4	0.9	0.40	0.55	0.07
MC exp. $t\bar{t}$+V events	1.2	0.96	0.45	0.35	0.46	0.38
QCD multi-jet events	0.4	0.8	0.01	0.00	0.07	0.8

Table 15.3: The yields in the loose signal regions before and after fit for an integrated luminosity of 20.3 fb^{-1}. The uncertainties include statistical and systematic uncertainties.

The distributions of $E_{\mathrm{T}}^{\mathrm{miss}}$, m_{T} and of $m_{\mathrm{eff}}^{\mathrm{incl}}$ are shown in selected validation regions in Figure 15.3.

15.3 Results in the signal regions

The background estimates in the loose and tight signal regions are obtained by extrapolating the results of the background-only fit in the control regions to the signal regions. The observed data is compared to the fitted background estimates in Table 15.3 for the loose signal regions and in Table 15.4 for the tight signal regions. Both tables show the background estimates before the fit in the lower part and the background estimates after fit in the upper part.

Data and fitted background estimates agree in almost all signal regions within uncertainties, only the loose 3-jets signal region in the muon channel shows a larger data underfluctuation, which is also visible in the $m_{\mathrm{eff}}^{\mathrm{incl}}$ distribution in this signal region shown in the top right plot in Figure 15.4. This figure also shows further distributions in the loose signal regions, namely the $m_{\mathrm{eff}}^{\mathrm{incl}}$ distributions in the 3-jets and 5-jets signal regions and the $E_{\mathrm{T}}^{\mathrm{miss}}$ distribution in the 6-jets signal regions, both in the electron and muon channel. The shape fit in the exclusion fit uses these distributions with the binning shown. Therefore, the plots are useful in interpreting the results of the shape fit later on. Of particular importance is the data underfluctuation at larger $E_{\mathrm{T}}^{\mathrm{miss}}$ values in the 6-jets signal regions, because the signal would be expected to peak in these regions. As no data was observed in these bins, the limits in Section 16.2 will be tighter than expected.

The $t\bar{t}$ background is the dominant background in all signal regions. The W+jets background is only important in the loose 3-jets and 5-jets signal regions and negligible otherwise. Therefore, the large uncertainties on the W+jets background due to very limited Monte Carlo statistics do
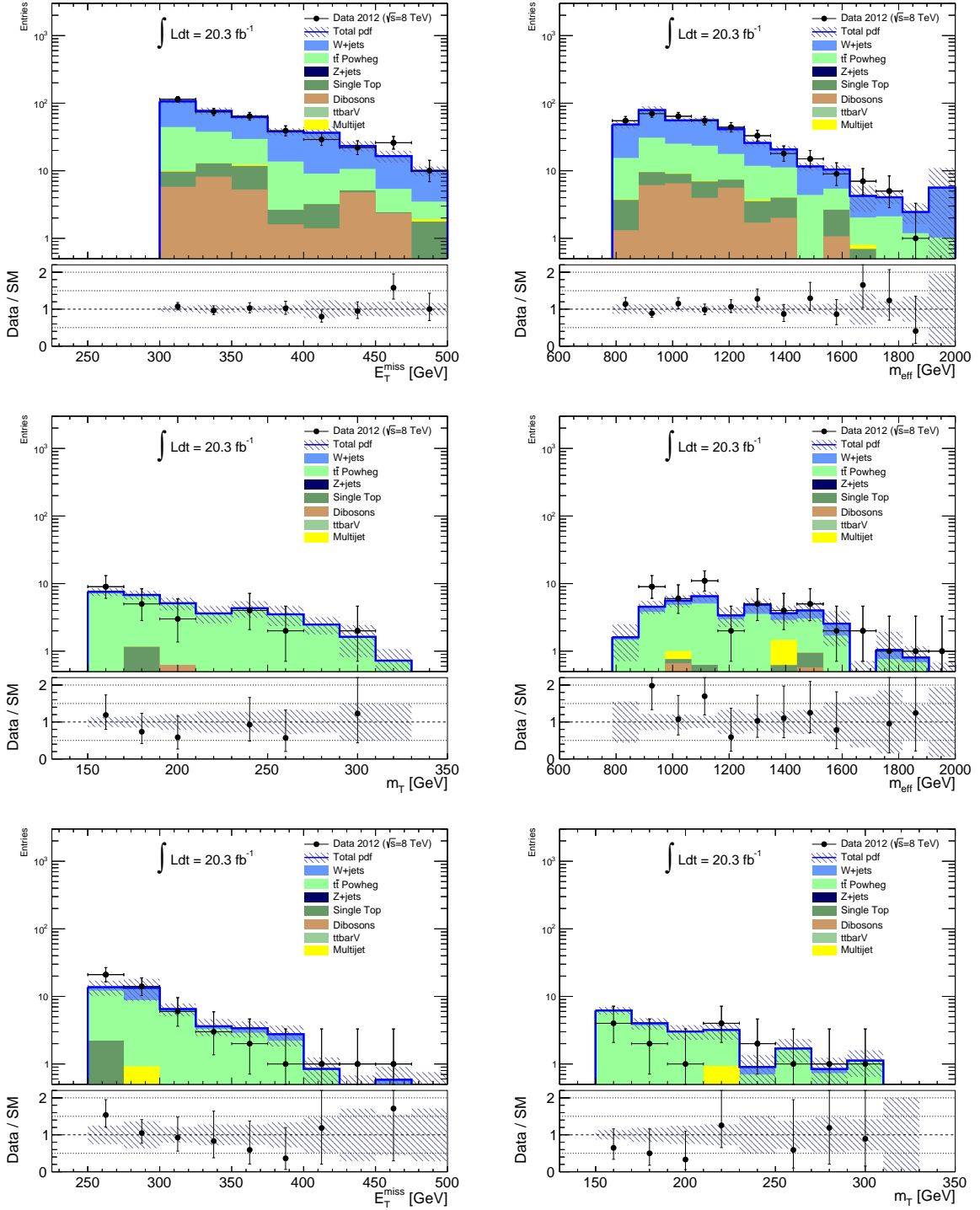
Figure 15.3: The E_T^{miss} (top left) and m_{eff}^{incl} (top right) distributions are shown in the 3-jets E_T^{miss} validation region in the electron channel. The m_T distribution (middle left) and the m_{eff}^{incl} distribution (middle right) are shown in the 5-jet m_T and E_T^{miss} validation regions, respectively, in the muon channel. In the 6-jets E_T^{miss} and m_T validation regions in the muon channel, the E_T^{miss} (bottom left) and the m_T (bottom right) distributions are shown, respectively. The integrated luminosity in all plots is 20.3 fb^{-1}.

	Tight signal regions					
Region	**3-jets**		**5-jets**		**6-jets**	
Channel	Electron	Muon	Electron	Muon	Electron	Muon
Observed events	4	5	4	2	2	0
Fitted background events	3.9 ± 1.0	2.6 ± 0.9	3.6 ± 1.0	2.5 ± 0.8	2.0 ± 0.7	1.7 ± 0.5
Fitted $t\bar{t}$ events	1.4 ± 0.5	1.6 ± 0.5	2.7 ± 0.8	2.0 ± 0.7	1.3 ± 0.5	1.3 ± 0.5
Fitted W+jets events	0.9 ± 0.4	0.6 ± 0.5	0.11 ± 0.08	$0.08^{+0.08}_{-0.08}$	0.00 ± 0.00	$0.07^{+0.14}_{-0.07}$
Fitted Z+jets events	0.00 ± 0.00	0.00 ± 0.00	0.00 ± 0.00	0.00 ± 0.00	0.00 ± 0.00	0.00 ± 0.00
Fitted single t events	0.6 ± 0.3	0.00 ± 0.00	0.00 ± 0.00	0.18 ± 0.09	0.5 ± 0.3	0.2 ± 0.1
Fitted diboson events	0.8 ± 0.5	0.38 ± 0.21	0.7 ± 0.4	0.10 ± 0.05	0.06 ± 0.04	0.00 ± 0.00
Fitted $t\bar{t}$+V events	0.086 ± 0.031	0.087 ± 0.032	0.13 ± 0.05	0.11 ± 0.04	0.12 ± 0.05	0.12 ± 0.05
Fitted QCD multi-jet events	$0.15^{+0.17}_{-0.15}$	0.00 ± 0.024	0.00 ± 0.010	0.00 ± 0.011	0.00 ± 0.00	0.00 ± 0.00
MC exp. SM events	4.2	2.9	3.6	2.4	2.1	1.9
MC exp. $t\bar{t}$ events	1.3	1.5	2.6	1.9	1.4	1.4
MC exp. W+jets events	1.3	0.9	0.18	0.12	0.00	$0.13^{+0.27}_{-0.13}$
MC exp. Z+jets events	0.00	0.00	0.00	0.00	0.00	0.00
MC exp. single t events	0.51	0.00	0.00	0.18	0.50	0.18
MC exp. diboson events	0.9	0.39	0.7	0.10	0.07	0.00
MC exp. $t\bar{t}$+V events	0.086	0.087	0.13	0.11	0.12	0.12
QCD multi-jet events	0.15	0.00	0.00	0.00	0.00	0.00

Table 15.4: The yields in the tight signal regions before and after fit for an integrated luminosity of 20.3 fb^{-1}. The uncertainties include statistical and systematic uncertainties.

not impact the result. The Z+jets background is zero everywhere. The single top and diboson backgrounds are subdominant compared to the $t\bar{t}$ background, but can reach each $\sim 25\%$ of the fitted total background depending on the region. The QCD multi-jet background is small as well.

The systematic uncertainties are deconstructed into components for the 3-jets signal regions in Table 15.5, for the 5-jets signal regions in Table 15.6 and for the 6-jets signal regions in Table 15.7. The procedure for this is as described in Section 10.3.4, fixing all parameters and studying the impact of varying only one parameter on the result. The names of most parameters in the tables are as defined in Section 14.1. Additionally, the parameter γ_{stat} indicates the impact due to statistical uncertainties of the Monte Carlo samples. This parameter only considers the Monte Carlo statistical uncertainties for the first bin in each histogram shown in Figure 15.4, as the statistical uncertainties due to the other bins are below the threshold value of 0.05. The parameter $\alpha_{QCD\ multi-jet}$ indicates the contribution of uncertainties due to the QCD multi-jet background estimate. The impact of the normalisation parameters for the $t\bar{t}$ and W+jets sample, $\mu_{\text{Top\_xJ}}$ and $\mu_{\text{W\_xJ}}$ with x indicating the number of jets, is also displayed. The systematic uncertainties are roughly ordered according to descending size.

In the loose 3-jets signal regions, the statistical uncertainties dominate, followed by the uncertainty due to the top normalisation factor. The largest systematic uncertainties are the uncertainties due to the minimum p_{T} value chosen in the generator for the W+jets samples and the systematic uncertainty assigned to the diboson background.

The statistical uncertainty also dominates in the loose 5-jets signal regions. The second largest uncertainties are the systematic uncertainties due variation of the factorisation scale for the $t\bar{t}$ background and again due to the variation of the minimum p_{T} value used in the W+jets background generator. The uncertainties due to the normalisation factors for the W+jets and $t\bar{t}$ backgrounds also contribute significantly.
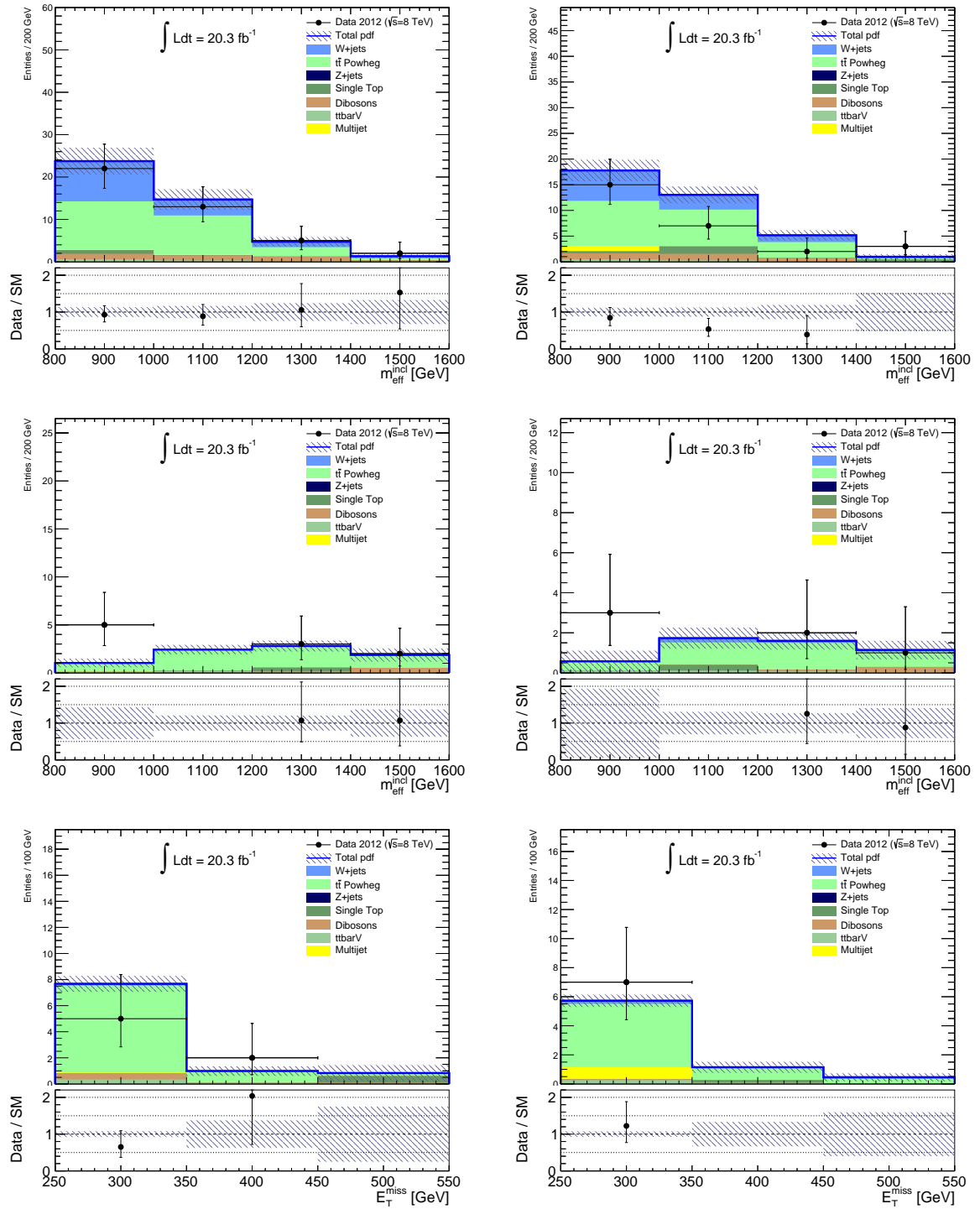
Figure 15.4: The $m_{\text{eff}}^{\text{incl}}$ distributions are shown in the loose 3-jets (top) and 5-jets (middle) signal regions and the $E_{\text{T}}^{\text{miss}}$ distributions in the loose 6-jets signal regions. Plots for the electron (muon) channel are shown on the left (right). Some data underfluctuations are visible in the 3-jets signal region in the muon channel in the middle bins and in the 6-jets signal regions in the bins at larger $E_{\text{T}}^{\text{miss}}$. The last bin in all distributions also includes events with $m_{\text{eff}}^{\text{incl}}$ and $E_{\text{T}}^{\text{miss}}$ values larger than the values on the x-axis.

Loose signal region	3-jets Electron	3-jets Muon
Total background expectation	46	38
Total statistical ($\sqrt{N_{\text{exp}}}$)	±7	±6
Total background systematic	±8 [17.48%]	±6 [15.18%]
Statistical uncertainties (γ_{stat})	±6 [13.0%]	±4 [9.5%]
$t\bar{t}$ yield ($\mu_{\text{Top\_3J}}$)	±5 [11.1%]	±4 [11.3%]
Minimum p_{T} threshold (W+jets, $\alpha_{\text{WTheoPtMin\_3J}}$)	±4 [8.8%]	±3 [7.4%]
W+jets yield ($\mu_{\text{W\_3J}}$)	±2.5 [5.5%]	±1.8 [4.6%]
Size of diboson background ($\alpha_{\text{errDB\_3J}}$)	±2.2 [4.8%]	±1.7 [4.4%]
Factorisation scale ($t\bar{t}$, $\alpha_{\text{topTheoFacSc\_3J}}$)	±2.0 [4.4%]	±1.7 [4.5%]
Renormalisation scale (W+jets, $\alpha_{\text{ktfacW\_3J}}$)	±0.7 [1.6%]	±0.22 [0.57%]
Pile-up ($\alpha_{\text{pileup\_3J}}$)	±0.7 [1.4%]	±1.6 [4.1%]
QCD multi-jet estimate ($\alpha_{\text{QCD multi-jet}}$)	±0.5 [1.2%]	±0.9 [2.4%]
Size of single t background ($\alpha_{\text{errST\_3J}}$)	±0.5 [1.1%]	±1.1 [2.8%]
Size of Z+jets and $t\bar{t}$+V backgrounds ($\alpha_{\text{errBG\_3J}}$)	±0.3 [0.75%]	±0.3 [0.75%]
PDF ($\alpha_{\text{pdfIntra\_3J}}$)	±0.31 [0.66%]	±0.15 [0.39%]
$E_{\text{T}}^{\text{miss}}$ soft term scale ($\alpha_{\text{SCALEST\_3J}}$)	±0.26 [0.57%]	±0.19 [0.50%]
Facorisation scale (W+jets, $\alpha_{\text{qfacW\_3J}}$)	±0.26 [0.55%]	±0.07 [0.17%]
Renormalisation scale ($t\bar{t}$, $\alpha_{\text{topTheoRenSc\_3J}}$)	±0.25 [0.53%]	±0.21 [0.55%]
Initial and final state radiation ($t\bar{t}$, $\alpha_{\text{topTheoPS\_3J}}$)	±0.24 [0.51%]	±0.20 [0.52%]
Jet energy resoultion ($\alpha_{\text{JER\_3J}}$)	±0.20 [0.43%]	±0.8 [2.1%]
$E_{\text{T}}^{\text{miss}}$ soft term resolution ($\alpha_{\text{RESOST\_3J}}$)	±0.15 [0.32%]	±0.06 [0.16%]
Jet energy scale ($\alpha_{\text{JES\_3J}}$)	±0.05 [0.11%]	±0.5 [1.3%]

Table 15.5: The size of the systematic uncertainties contributing to the total uncertainties are shown for the two loose 3-jets signal regions.

The systematic uncertainties due to the variations of the initial and final state radiation in the $t\bar{t}$ background are the largest in the loose 6-jets signal regions, followed by the statistical uncertainties on the Monte Carlo samples. The normalisation factor for the $t\bar{t}$ background is the third largest contribution. The impact of the normalisation parameter for the W+jets background is small in these regions. Instead, these regions are the only regions where the systematic uncertainties on the jet energy scale are relevant. This is in contrast to the systematic uncertainties initially shown in Table 14.1 and is due to the treatment of this systematic uncertainty as an uncertainty on the transfer factor.

In summary, the uncertainties in the signal regions are dominated by statistical uncertainties originating from limited Monte Carlo statistics and theoretical uncertainties on the $t\bar{t}$ and the W+jets background.

Loose signal region	5-jets Electron	5-jets Muon
Total background expectation	12	7.0
Total statistical ($\sqrt{N_{\mathrm{exp}}}$)	± 3	± 2.7
Total background systematic	± 5 [42.95%]	± 1.6 [22.90%]
Statistical uncertainties (γ_{stat})	± 4.8 [38.8%]	± 0.97 [13.8%]
Factorisation scale ($t\bar{t}$, $\alpha_{\mathrm{topTheoFacSc\_5J}}$)	± 1.2 [9.7%]	± 0.9 [12.6%]
Minimum p_{T} threshold (W+jets, $\alpha_{\mathrm{WTheoPtMin\_5J}}$)	± 1.2 [9.7%]	± 0.16 [2.3%]
W+jets yields ($\mu_{\mathrm{W\_5J}}$)	± 1.0 [8.1%]	± 0.13 [1.9%]
$t\bar{t}$ yields ($\mu_{\mathrm{Top\_5J}}$)	± 0.9 [7.7%]	± 0.7 [10.0%]
Jet energy scale ($\alpha_{\mathrm{JES\_5J}}$)	± 0.9 [7.1%]	± 0.6 [7.8%]
Renormalisation scale (W+jets, $\alpha_{\mathrm{ktfacW\_5J}}$)	± 0.8 [6.2%]	± 0.11 [1.6%]
Initial and final state radiation ($t\bar{t}$, $\alpha_{\mathrm{topTheoPS\_5J}}$)	± 0.6 [4.8%]	± 0.5 [6.3%]
Jet energy scale ($\alpha_{\mathrm{JER\_5J}}$)	± 0.5 [3.8%]	± 0.04 [0.51%]
Size of diboson background ($\alpha_{\mathrm{errDB\_5J}}$)	± 0.5 [3.8%]	± 0.20 [2.9%]
PDF ($\alpha_{\mathrm{pdfIntra\_5J}}$)	± 0.4 [3.0%]	± 0.018 [0.26%]
Factorisation scale (W+jets, $\alpha_{\mathrm{qfacW\_5J}}$)	± 0.27 [2.2%]	± 0.04 [0.53%]
Size of single t background ($\alpha_{\mathrm{errST\_5J}}$)	± 0.15 [1.3%]	± 0.15 [2.1%]
Size of Z+jets and $t\bar{t}$+V background ($\alpha_{\mathrm{errBG\_5J}}$)	± 0.13 [1.1%]	± 0.10 [1.5%]
$E_{\mathrm{T}}^{\mathrm{miss}}$ soft term scale ($\alpha_{\mathrm{SCALEST\_5J}}$)	± 0.12 [0.98%]	± 0.17 [2.5%]
Renormalisation scale ($t\bar{t}$, $\alpha_{\mathrm{topTheoRenSc\_5J}}$)	± 0.11 [0.86%]	± 0.08 [1.1%]
QCD multi-jet estimate ($\alpha_{\mathrm{QCD\ multi-jet}}$)	± 0.08 [0.69%]	± 0.03 [0.49%]
Pile-up ($\alpha_{\mathrm{pileup\_5J}}$)	± 0.06 [0.47%]	± 0.31 [4.4%]
$E_{\mathrm{T}}^{\mathrm{miss}}$ soft term resolution ($\alpha_{\mathrm{RESOST\_5J}}$)	± 0.00 [0.03%]	± 0.012 [0.17%]

Table 15.6: The size of the systematic uncertainties contributing to the total uncertainties are shown for the two loose 5-jets signal regions.

Loose signal region	6-jets Electron	6-jets Muon
Total background expectation	9.7	7.4
Total statistical ($\sqrt{N_{\text{exp}}}$)	± 3.1	± 2.7
Total background systematic	± 2.0 [20.58%]	± 1.7 [22.38%]
Initial and final state radiation ($t\bar{t}$, $\alpha_{\text{topTheoPS\_6J}}$)	± 1.2 [12.5%]	± 0.9 [11.6%]
Statistical uncertainties (γ_{stat})	± 1.2 [12.0%]	± 0.9 [11.9%]
$t\bar{t}$ yields ($\mu_{\text{Top\_6J}}$)	± 1.0 [10.6%]	± 0.7 [9.8%]
Jet energy scale ($\alpha_{\text{JES\_6J}}$)	± 0.4 [3.7%]	± 0.04 [0.60%]
Size of diboson background ($\alpha_{\text{errDB\_6J}}$)	± 0.27 [2.8%]	± 0.033 [0.45%]
Size of single t background ($\alpha_{\text{errST\_6J}}$)	± 0.26 [2.6%]	± 0.09 [1.3%]
Renormalisation scale ($t\bar{t}$, $\alpha_{\text{topTheoRenSc\_6J}}$)	± 0.24 [2.5%]	± 0.17 [2.3%]
$E_{\text{T}}^{\text{miss}}$ soft term scale ($\alpha_{\text{SCALEST\_6J}}$)	± 0.15 [1.5%]	± 0.10 [1.3%]
Size of Z+jets and $t\bar{t}$+V backgrounds ($\alpha_{\text{errBG\_6J}}$)	± 0.14 [1.4%]	± 0.11 [1.5%]
$E_{\text{T}}^{\text{miss}}$ soft term resolution ($\alpha_{\text{RESOST\_6J}}$)	± 0.12 [1.2%]	± 0.11 [1.4%]
Pile-up ($\alpha_{\text{pileup\_6J}}$)	± 0.10 [1.1%]	± 0.30 [4.1%]
W+jets yields ($\mu_{\text{W\_6J}}$)	± 0.09 [0.95%]	± 0.19 [2.6%]
QCD multi-jet estimate ($\alpha_{\text{QCD multi-jet}}$)	± 0.09 [0.90%]	± 0.87 [11.8%]
Minimum p_{T} threshold (W+jets, $\alpha_{\text{WTheoPtMin\_6J}}$)	± 0.08 [0.79%]	± 0.16 [2.2%]
Factorisation scale ($t\bar{t}$, $\alpha_{\text{topTheoFacSc\_6J}}$)	± 0.07 [0.74%]	± 0.05 [0.69%]
Renormalisation scale (W+jets, $\alpha_{\text{ktfacW\_6J}}$)	± 0.04 [0.45%]	± 0.007 [0.10%]
Jet energy resolution ($\alpha_{\text{JER\_6J}}$)	± 0.04 [0.37%]	± 0.05 [0.63%]
Factorisation scale (W+jets, $\alpha_{\text{qfacW\_6J}}$)	± 0.015 [0.15%]	± 0.00 [0.01%]
PDF ($\alpha_{\text{pdfIntra\_6J}}$)	± 0.013 [0.13%]	± 0.008 [0.11%]

Table 15.7: The size of the systematic uncertainties contributing to the total uncertainties are shown for the two loose 6-jets signal regions.

Chapter 16

Interpretation

As this analysis sees no excess beyond Standard Model expectations neither in the loose, nor in the tight signal regions, upper limits on the visible cross section are derived in Section 16.1. Limits in simplified models with one and two steps and in the 'Higgs aware' MSUGRA/CMSSM grid are derived in Section 16.2. At the end of this chapter, the results of this analysis, in particular the limits, are compared to similar analyses within ATLAS.

16.1   Upper limits on the visible cross section

Based on Table 15.4, which presented the yields in the tight signal regions, upper limits on the number of observed signal events, S_{obs}^{95}, are derived (following the same procedure as in Section 10.4.3). Upper limits on the visible cross section, $\langle \epsilon \sigma \rangle_{\text{obs}}^{95}$, are calculated by dividing this by the integrated luminosity of 20.3 fb^{-1}. These upper limits are shown in Table 16.1 for all signal regions. The upper limit on the visible cross section varies between 0.15 and 0.38 fb depending on the signal region, corresponding to an upper limit of 3.0 and 7.7 signal events.

16.2   Limits in different supersymmetric models

Limits in simplified models and in the 'Higgs aware' MSUGRA/CMSSM grid are derived by using the exclusion fit as described in Section 14.4. The models have been described in Section 2.4.3. Apart from the CL_s values calculated for every point in the signal grids, the upper limits on the excluded cross section are given for every point in simplified models. All limits shown in the following are based on a 95% CL.

16.2.1   Limits in simplified models with one step and fixed $x = 1/2$

The limits calculated in the two simplified models with initial gluino or squark pair-production and where each gluino or squark decays via an intermediate $\tilde{\chi}_1^{\pm}$ to the $\tilde{\chi}_1^0$ (with fixed $x = 1/2$) are shown in Figure 16.1 and in Figure 16.2. They are compared to the limits by the 7 TeV analysis of 4.7 fb^{-1} data [131] shown as grey area.

In both of these models the limits are given as function of the gluino or squark mass and the $\tilde{\chi}_1^0$ mass. Limits in these grids were also produced by a similar analysis requiring a low p_{T} lepton (an electron with $10 < p_{\text{T}} < 25$ GeV or a muon with $6 < p_{\text{T}} < 25$ GeV). This soft lepton analysis targets scenarios with very compressed decay chains, where the mass difference

Signal channel	$\langle\epsilon\sigma\rangle^{95}_{\mathrm{obs}}$[fb]	S^{95}_{obs}	S^{95}_{exp}	CL_b	$p(s=0)$
Tight signal regions					
3-jets (electron)	0.30	6.1	$5.8^{+2.0}_{-1.6}$	0.57	0.48
3-jets (muon)	0.38	7.7	$5.2^{+2.0}_{-1.5}$	0.89	0.13
5-jets (electron)	0.30	6.0	$5.4^{+2.3}_{-1.5}$	0.59	0.43
5-jets (muon)	0.22	4.6	$4.7^{+1.9}_{-1.2}$	0.44	0.50
6-jets (electron)	0.22	4.5	$4.3^{+1.9}_{-0.5}$	0.55	0.50
6-jets (muon)	0.15	3.0	$4.0^{+1.3}_{-1.1}$	0.13	0.50

Table 16.1: Upper limits on the visible cross section in the six tight signal regions. The second column gives the 95% CL upper limits on the visible cross section ($\langle\epsilon\sigma\rangle^{95}_{\mathrm{obs}}$), the third column the 95% CL upper limits on the number of signal events (S^{95}_{obs}). The fourth column (S^{95}_{exp}) shows the 95% CL upper limits on the number of signal events, given the expected number (and $\pm1\sigma$ variations) of background events. The last two columns indicate the CL_b values, which are the confidence levels observed for the background-only hypothesis, and the discovery p-values ($p(s=0)$). For an observed number of events lower than expected, the discovery p-values are truncated at 0.5. The numbers are calculated by using toy Monte Carlo pseudo-experiments. This table was recalculated with respect to [179].

between the gluino/squark and the $\tilde\chi^0_1$ or between the $\tilde\chi^\pm_1$ and the $\tilde\chi^0_1$ is small. The signal regions of this analysis [179] are summarised in Appendix E. The soft lepton analysis is interesting for the two grids shown in Figures 16.1 and 16.2, because it provides additional sensitivity 'close to the diagonal', i.e. in points close to the line defined by $m_{\tilde g/\tilde q} = m_{\tilde\chi^0_1}$.

This can be seen in Figure 16.1, where the limit of the analysis described in this work is shown in solid magenta for the observed limit and in dashed magenta for the expected limit. The observed limit reaches up to 1.24 TeV in the gluino mass for vanishing $\tilde\chi^0_1$ masses and up to gluino masses of ~ 840 GeV for $\tilde\chi^0_1$ masses of ~ 600 GeV. The sensitivity in regions with large gluino masses is entirely dominated by the signal regions requiring six jets in this grid. As in these signal regions the data shows an underfluctuation compared to the background estimates for large $E^{\mathrm{miss}}_{\mathrm{T}}$ values (see Figure 15.4) where the signal would dominate, the observed limits are stronger than the expected limit in this region of the grid. The limit calculated by the soft lepton analysis (shown in blue and blue dashed for the observed and the expected limits) does only reach gluino masses up to ~ 800 GeV for vanishing $\tilde\chi^0_1$ masses, but succeeds in obtaining sensitivity to a region close to the diagonal up to $m_{\tilde g} - m_{\tilde\chi^0_1} = 15$ GeV for gluino masses up to 600 GeV.

Given the complementarity of the limits obtained by the two analyses, a combination of the limits is beneficial. This combination is calculated on a point-by-point basis: For every point in the grid, the analysis which obtains the best expected limit is chosen. This analysis provides then the expected and the observed limit, as well as the uncertainties on these limits, for the particular point.

The combined limit follows the expected limits of both analyses and in the case of Figure 16.1 also the observed limit. Therefore, the combined limit is identical to the limits by the soft lepton analysis for regions close to the diagonal and identical to the analysis presented in this work for large gluino masses. A future work will be to combine these two analyses with a simultaneous fit including all signal regions, and thus to improve the limits by the single analyses in a combined limit.

An improvement of around 250 GeV in the gluino mass is obtained for medium to large gluino masses in comparison to the 7 TeV analysis in [131].

Figure 16.1: Interpretation in the simplified model with one step, initial gluino pair production and fixed $x = 1/2$. Gluino masses up to 1.18 TeV (-1σ observed line) are excluded for very small $\tilde{\chi}_1^0$ masses. Gluino masses up to 700 GeV are excluded for all $\tilde{\chi}_1^0$ masses with $m(\tilde{g}) - m(\tilde{\chi}_1^0) \geq 15$ GeV. The limit presented is a combination of the single limits of the analysis presented here (magenta curves) and a similar analysis requiring a soft lepton with $6(\mu)/10(e) < p_T < 25$ GeV (blue curves). In this combination, the analysis providing the best expected limit is chosen for every grid point. The author contributed this plot to [179].

The limit in the simplified model with one step, initial squark pair-production and fixed $x = 1/2$, shown in Figure 16.2, is less strong compared to the similar grid with gluino pair production. The limits for this analysis extend up to ~ 740 GeV for vanishing $\tilde{\chi}_1^0$ masses (again shown in magenta). The soft lepton analysis (limits shown in blue) extends the limits near the diagonal and is able to exclude squark masses below ~ 440 GeV for $\tilde{\chi}_1^0$ masses below ~ 350 GeV. The expected combined limit of both analyses follows the better one of the expected limits of the two analyses. The observed combined limit follows the limit of the analysis presented in this work in regions where the observed limit of the soft lepton analysis is stronger. This stems from points where the expected limit calculated by the soft lepton analysis is considerably weaker than its observed limit. In comparison to the 7 TeV analysis [131], an improvement of ~ 250 GeV in the squark mass exclusion is obtained.

A combination with the soft lepton analysis was only performed for the two grids discussed. For all the grids presented in the following, the limits by the soft lepton analysis are considerably weaker than the limits presented here.

16.2.2 Limits in simplified models with one step and variable x

Limits are evaluated in the two simplified models with one step, where the initial gluino or squark decays via a $\tilde{\chi}_1^\pm$ into a $\tilde{\chi}_1^0$ of mass $m_{\tilde{\chi}_1^0} = 60$ GeV and the gluino or squark mass and the parameter x are varied over the grid.

The limit for the case of initial gluino production is shown in Figure 16.3. Similarly to the grid with fixed $x = 1/2$, the limits on the gluino mass extend up to 1.2 TeV for medium x values. For small or large x values, the mass difference between the $\tilde{\chi}_1^\pm$ and the $\tilde{\chi}_1^0$ or the gluino and the $\tilde{\chi}_1^\pm$ is small and thus soft objects, either a soft lepton or soft jets (i.e. jets of low

Figure 16.2: Interpretation in the simplified model with initial squark pair production and decay of each squark via an intermediate $\tilde{\chi}_1^{\pm}$ into the $\tilde{\chi}_1^0$ (x is fixed to 1/2). Squark masses up to 700 GeV are excluded for very small $\tilde{\chi}_1^0$ masses (-1σ observed line). As in Figure 16.1 the limit is a combination of the single limits of this analysis (in magenta) and the analysis requiring a soft lepton (in light blue). The sensitivity at high squark masses and low $\tilde{\chi}_1^0$ masses is provided by this analysis, whereas the analysis requiring a soft lepton improves the sensitivity close to the diagonal. The author contributed this plot to [179].

transverse momentum) can be expected. This analysis has little sensitivity to these regions for large gluino masses, but succeeds excluding regions with low and large x values up to gluino masses of ~ 800 GeV and ~ 1000 GeV, respectively.

In Figure 16.4, the limit is presented for the case of initial squark pair production. In this case, squark masses up to ~ 780 GeV (observed limit) can be excluded for medium x values and up to ~ 680 GeV for large x values. The limit for small x values is considerably weaker and withdraws at low squark masses and $x = 0.2$. The grid points in this region were investigated closer and were found to have large statistical uncertainties, as only very few generated signal events survive the selection cuts of the signal regions.

In both grids, an improvement of about 250 GeV in squark/gluino mass exclusion is reached in comparison to the analysis presented in [131].

16.2.3 Limits in simplified models with two steps and the decay proceeding via sleptons and sneutrinos

The limits in simplified models with two steps and a decay of the initial gluino or squark via sleptons and sneutrinos are given in Figure 16.5 for initial gluino pair-production and in Figure 16.6 for initial squark pair-production. In both cases, some grid points for low squark or gluino masses were not generated. Hence, the limits are cut in proximity to the lowest generated points and not extrapolated to lower values.

In both models, similar limits are obtained as in the simplified models with one step with the observed limit reaching up to gluino masses of ~ 1.2 TeV and squark masses up to ~ 780 GeV
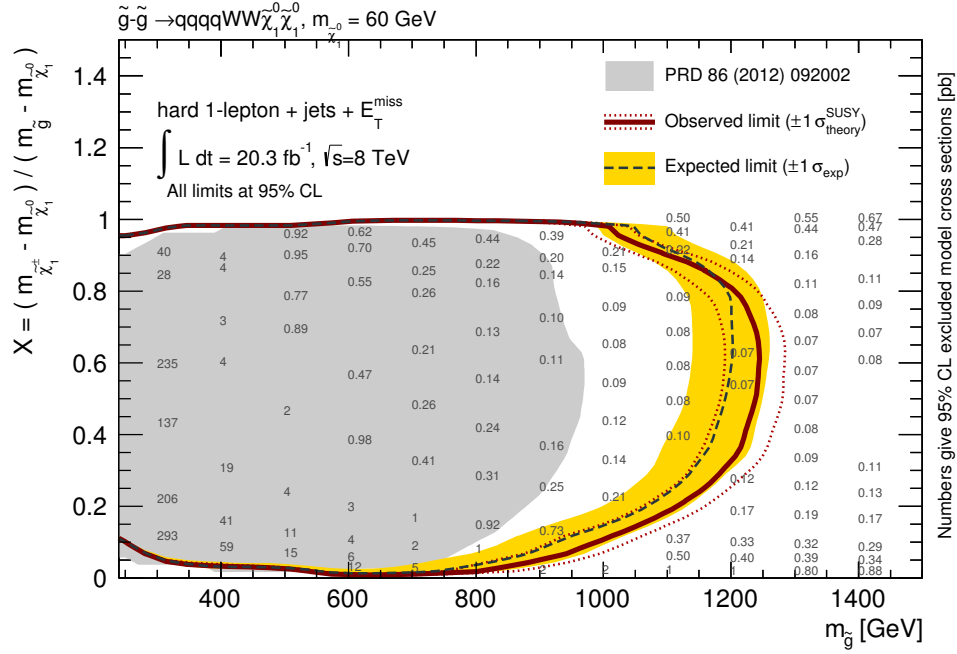
Figure 16.3: Interpretation in the simplified model with initial gluino pair production and decay of each gluino via an intermediate $\tilde{\chi}_1^\pm$ into the $\tilde{\chi}_1^0$. In this grid, the limit is given as function of $m(\tilde{g})$ and x, the mass of the $\tilde{\chi}_1^0$ is constant: $m(\tilde{\chi}_1^0) = 60$ GeV. Gluino masses up to ~ 1.2 TeV are excluded for medium x values (-1σ observed line). The author contributed a similar plot to [179].
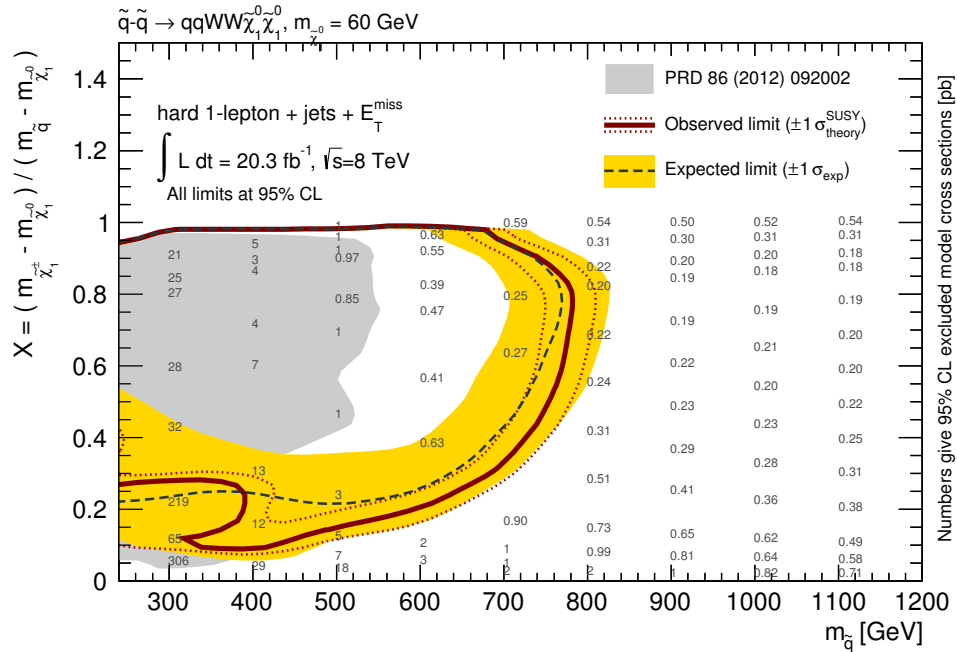
Figure 16.4: Interpretation in the simplified model with initial squark pair production and decay of each squark via an intermediate $\tilde{\chi}_1^\pm$ into the $\tilde{\chi}_1^0$. In this grid, the limit is given as function of $m(\tilde{q})$ and x, the mass of the LSP is constant: $m(\tilde{\chi}_1^0) = 60$ GeV. Squark masses up to 700 GeV are excluded for medium x values (-1σ observed line). The author contributed a similar plot to [179].
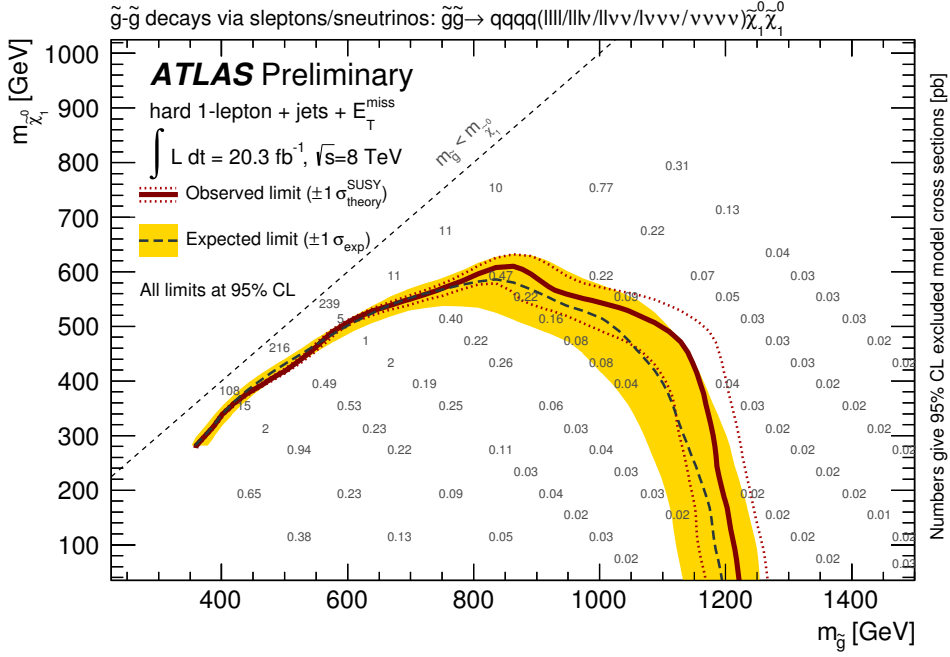
Figure 16.5: Interpretation in a simplified model with two steps, initial gluino pair production and decay through sleptons and sneutrinos. Similarly to the simplified models with one step, gluino masses up to ~ 1.2 TeV are excluded (by the observed limit) for vanishing $\tilde{\chi}_1^0$ masses. The author contributed this plot to [179].

for vanishing $\tilde{\chi}_1^0$ masses.

The 7 TeV analysis [131] did not interpret in precisely the same simplified models, therefore no comparison is made here.

16.2.4 Limits in simplified models with two steps and the decay involving W and Z bosons

The limits in simplified models with two steps where the initial gluino or squark decays via charginos and neutralinos into the $\tilde{\chi}_1^0$ and W and Z bosons are presented in Figure 16.7 for gluino pair production and in Figure 16.8 for squark pair production.

Similar limits as for the simplified models with one step are obtained for the gluino case, however slightly weaker in both the gluino and $\tilde{\chi}_1^0$ masses. Few grid points have been generated inside the area excluded by the 7 TeV analysis [131], thus, the observed limit of the analysis presented in this work is cut close to the previous limit for low gluino masses. For high gluino masses, the limit was only calculated for grid points with a $\tilde{\chi}_1^0$ mass of at least 65 GeV, thus the observed limit was not extrapolated to lower $\tilde{\chi}_1^0$ masses.

The signal region optimisation in Chapter 12 did not show a sensitivity to the squark grid. However, as the observed limit is stronger than the expected limit in Figure 16.8, one point at $(m_{\tilde{g}}, m_{\tilde{\chi}_1^0}) = (585, 25)$ GeV is excluded. This limit is considerably weaker than in [131]. However, the analysis presented in this work applies a veto on any second lepton in contrast to the previous analysis, which also included signal regions requiring at least two leptons. In this particular simplified model, multiple leptons may appear in the final state.

164
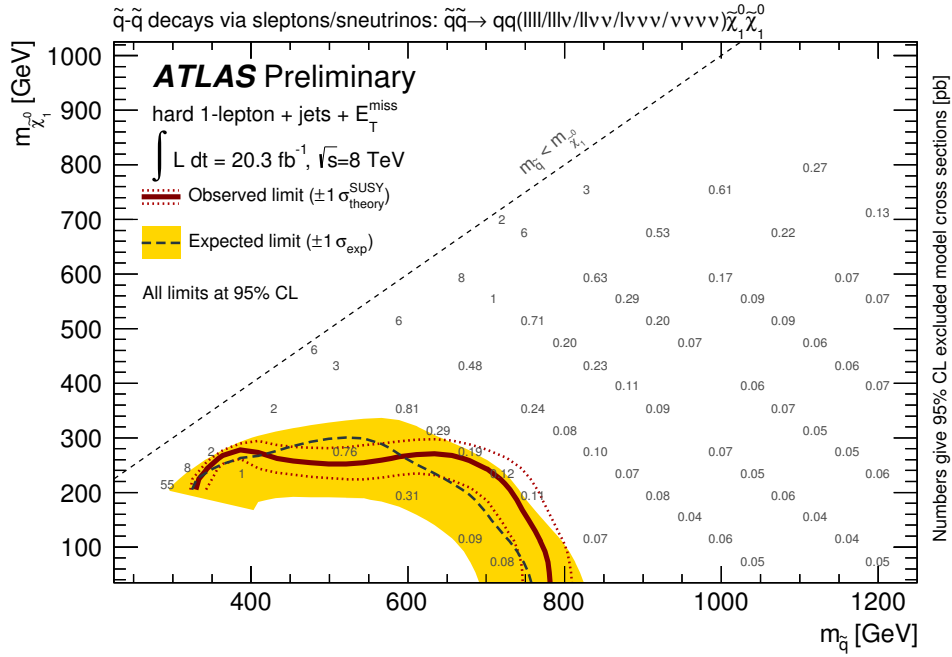
Figure 16.6: Interpretation in a simplified model with two steps and initial squark pair production and decay through sleptons and sneutrinos. Squark masses up to ~ 780 GeV are excluded by the observed limit for vanishing $\tilde{\chi}_1^0$ masses. The author contributed this plot to [179].
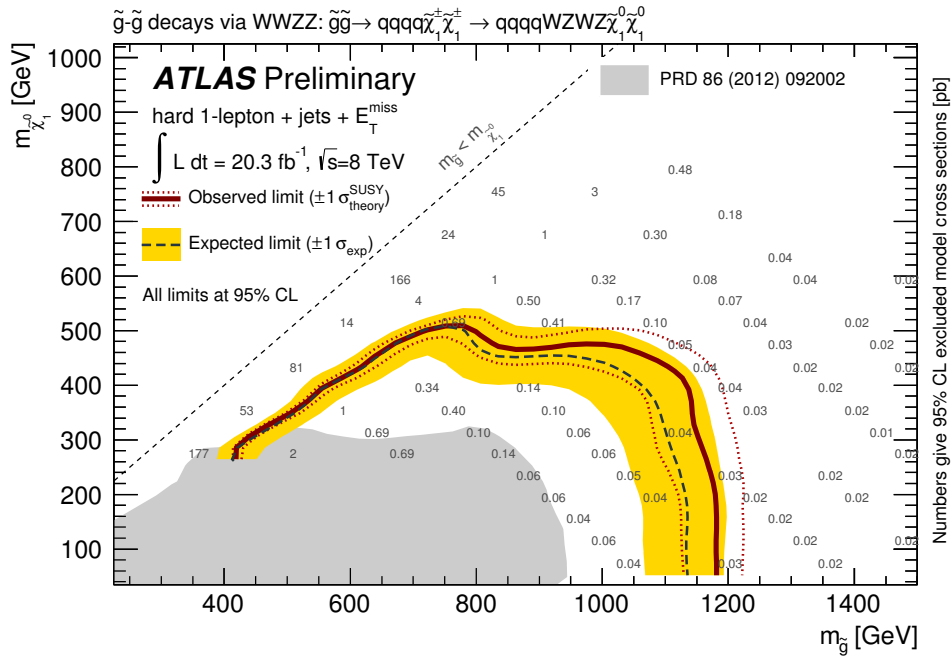
Figure 16.7: Interpretation in a simplified model with two steps and gluino pair production and the decay involving W and Z bosons. The limits are similar as in the simplified models with one step. The author contributed this plot to [179].
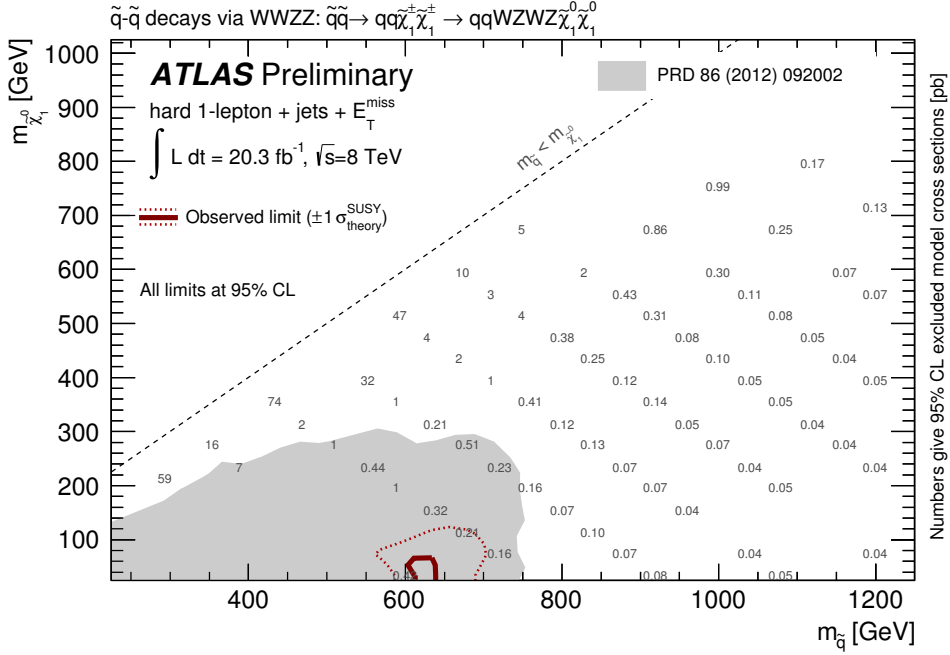
Figure 16.8: Interpretation in a simplified model with two steps and initial squark pair production and the decay involving W and Z bosons. The author contributed this plot to [179].

16.2.5 Limits in the 'Higgs aware' MSUGRA/CMSSM grid

Apart from simplified models, this analysis is also interpreted in the 'Higgs aware' MSUGRA/C-MSSM grid. The limits are shown in Figure 16.9. For low m_0 values the observed limit extends up to $m_{1/2} = 675$ GeV. For high m_0 values, $m_{1/2}$ reaches 480 GeV. Gluino masses up to 1.2 TeV are excluded for any m_0 value.

16.3 Comparison to other analyses

Various analyses in ATLAS search for gluino and squark production. They however target different final states with or without leptons. These analyses interpret their results in the same models as the analyses discussed in this work and thus complement the results obtained in this chapter. A complete summary of the limits on Supersymmetry obtained in different ATLAS analyses is given in Appendix F. Three examples in simplified models with one or two steps and in the 'Higgs aware' MSUGRA/CMSSM grid are discussed in the following.

Simplified models with one step The analysis focusing on final states with two to six jets, no lepton and a high E_T^{miss} (0-lepton analysis, [232]) profits from high cross sections for full hadronic states but consequently suffers from a large QCD multi-jet background. The analysis derived limits in a variety of simplified models, among those simplified models with one step. In the simplified model with one step, gluino pair production and fixed $x = 1/2$, this analysis excludes gluino masses below ~ 1.2 GeV for vanishing $\tilde{\chi}_1^0$ masses as shown in Figure 16.10. This limit is comparable with the limit obtained in this work. However, the 0-lepton analysis is able to reach closer to the diagonal as no lepton is required and thus its sensitivity in this region is larger than the one of the soft lepton analysis described earlier. However, the 0-lepton analysis excludes no $\tilde{\chi}_1^0$ masses beyond ~ 470 GeV in contrast to the limits derived in this chapter.
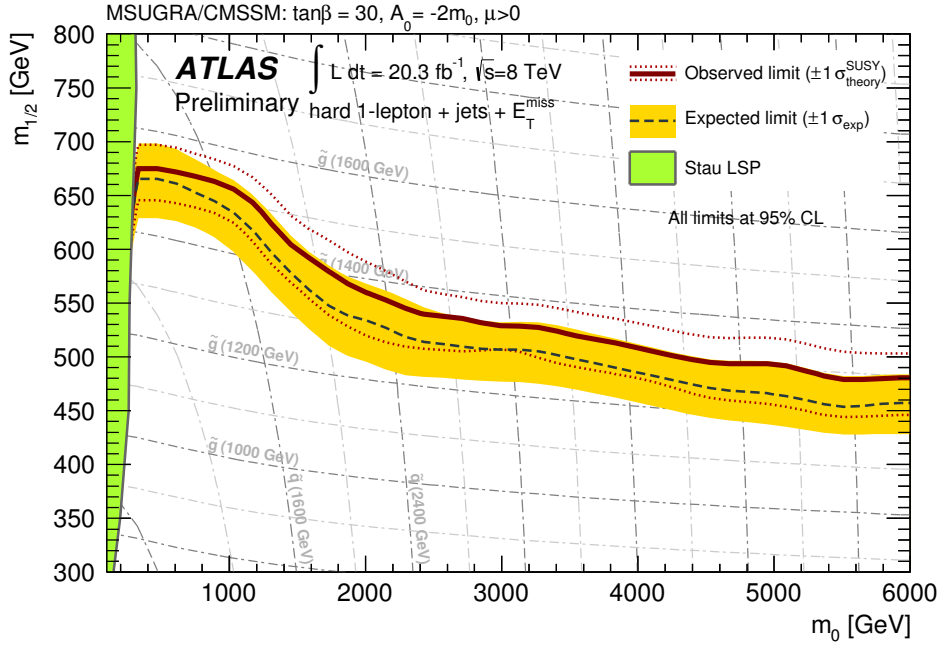
Figure 16.9: Interpretation in the 'Higgs aware' MSUGRA/CMSSM grid. The author contributed this plot to [179].

Simplified models with two steps   Analyses requiring more than one lepton are expected to provide particular sensitivity to simplified models with two steps or in general to any decay chain resulting in many leptons. The analysis requiring two leptons in the final states, large $E_{\mathrm{T}}^{\mathrm{miss}}$, jets and no b-jets (2-lepton analysis, [180]) derives limits in a variety of simplified models and is complementary to the analyses described in this work. Figure 16.11 shows the limits in the simplified model with two steps, gluino pair production and decay via sleptons or sneutrinos. The green solid (dashed) line indicates the observed (expected) limit derived in this chapter. The 2-lepton analysis is able to obtain sensitivity closer to the diagonal than the analysis discussed in this work, because it can allow for looser criteria on the transverse momenta of the two leptons. These looser criteria arise from the possibility to use di-lepton triggers in the 2-lepton analysis. The (expected) limits of the 2-lepton analysis and the $20.3\,\mathrm{fb}^{-1}$ analysis in this work are similar for high gluino masses, whereas the $20.3\,\mathrm{fb}^{-1}$ analysis can obtain sensitivity to higher $\tilde{\chi}_1^0$ masses than the 2-lepton analysis for medium gluino masses.

'Higgs aware' MSUGRA/CMSSM grid   All analyses searching for gluinos and squarks derived limits in the 'Higgs aware' MSUGRA/CMSSM grid as shown as summary in Figure 16.12. The $20.3\,\mathrm{fb}^{-1}$ analysis is represented by the red curves. The analysis requiring between two and six jets and no lepton, shown in magenta, is able to exclude m_0 values up to ~ 840 GeV for low m_0 values and thus provides the strongest limit in this area of all analyses. This region is dominated by squark pair production with possibly shorter decay chains. The 3-b-jet analysis, which requires three b-tagged jets and has different signal regions requiring either zero or one lepton [9], provides the largest sensitivity at high m_0 values. Gluino pair production dominates in this regions with decays similar to the ones discussed in Figure 2.6 (right), in which a gluino decays via a stop into the $\tilde{\chi}_1^0$. Due to the presence of stop quarks in the decay and top quarks in the final states, many b-jets can be expected in this region. The limit of the $20.3\,\mathrm{fb}^{-1}$ analysis discussed in this work is considerably weaker than the limit by the 0-lepton analysis at low values of m_0, but only slightly weaker than the limit by the 3 b-jets analysis. The $20.3\,\mathrm{fb}^{-1}$
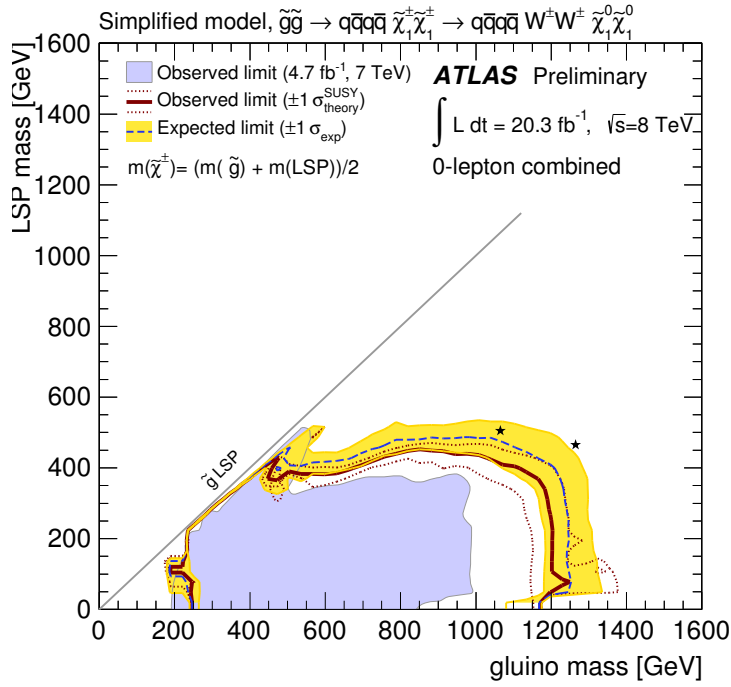
Figure 16.10: Limits by an analysis focusing on final states with two to six jets, no leptons and E_T^{miss} in the simplified model with one step, gluino pair production and fixed $x = 1/2$ [232].
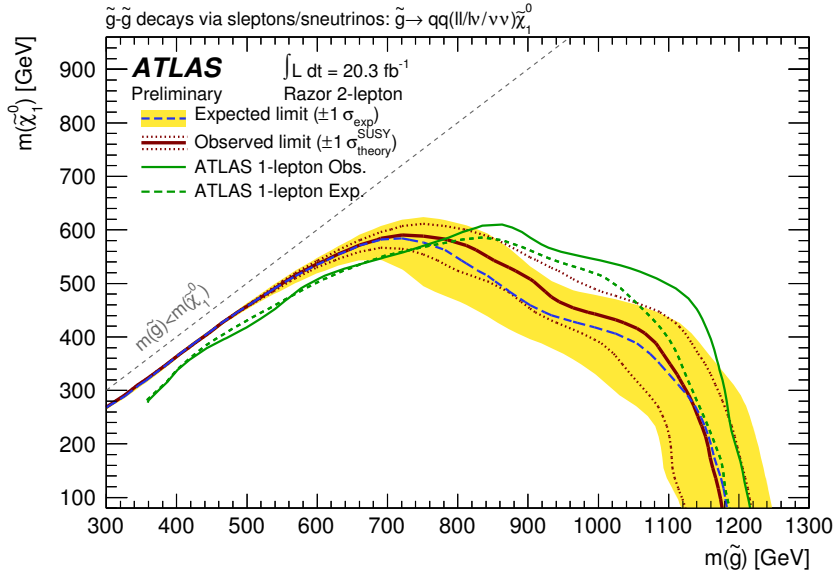
Figure 16.11: Limits in the simplified model with two steps, gluino pair production with the gluinos decaying via sleptons and sneutrinos are derived by the analysis requiring two leptons, large E_T^{miss}, jets and no b-jet in the final state [180].
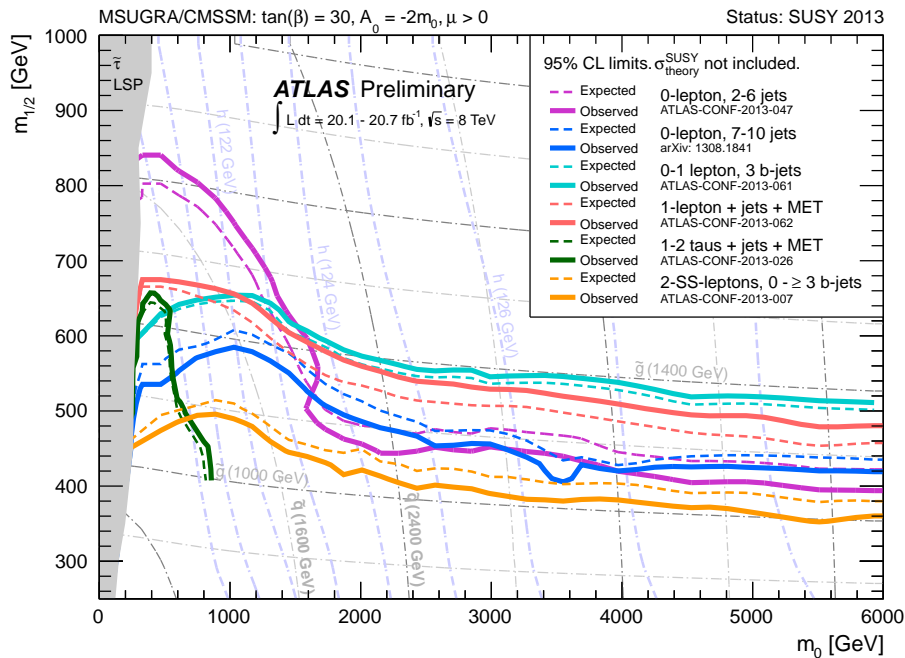
Figure 16.12: Observed and expected limits of various ATLAS analyses in the 'Higgs aware' MSUGRA/CMSSM grid [233]. The analysis developed in this work is shown by the red curves.

analysis does however not require *b*-tagged jets in its signal regions as discussed[1].

Summary: The various analyses searching for gluinos and squarks complement themselves, some being more sensitive to compressed scenarios, others for final states containing *b*-jets, others for particular high gluino masses. The $20.3 \, \text{fb}^{-1}$ analysis provides sensitivity in most models considered. In some simplified models with two steps, however, the limits by the $20.3 \, \text{fb}^{-1}$ analysis are sometimes considerably weaker. This is in particular the case for the simplified model with two steps, squark pair production and the decay involving W and Z bosons, which was discussed earlier in this chapter, possibly due to the veto on the second lepton which is not beneficial in grids where multiple leptons are expected in the final states. In summary, regardless of the specific model, gluinos with masses below 1.2 (simplified models) - 1.3 TeV ('Higgs aware' MSUGRA/CMSSM grid) can be excluded for negligible $\tilde{\chi}_1^0$ masses or all m_0 values. Limits on squarks are weaker and reach up to ~ 780 GeV in simplified models.

Comparison to analyses by the CMS Collaboration: The CMS Collaboration has currently no published analysis with 8 TeV data which targets the same final states as the analyses in this work. Limits in similar simplified models with one step are derived by an analysis considering final states with two isolated same-sign leptons and jets [234]. This analysis excludes gluino masses below ~ 920 GeV for vanishing $\tilde{\chi}_1^0$ masses. Limits on gluino and squark masses are also derived in an analysis requiring jets and E_T^{miss}, but no leptons [235]. Gluino (squark) masses below ~ 1.2 TeV (~ 840 GeV) are excluded for vanishing $\tilde{\chi}_1^0$ masses in simplified models with a direct decay of the gluino (squark) to the $\tilde{\chi}_1^0$.

In total, the CMS Collaboration obtains weaker or similar limits on the gluino and squark masses. The limits by the CMS Collaboration are summarised in Figure F.2 in Appendix F.

---

[1]This would have reduced the sensitivity in the simplified models considered, in which *b*-jets do not explicitly appear.

Part V

Summary and Outlook

Chapter 17

Summary and Outlook

Although no supersymmetric particles have been seen yet, the search for Supersymmetry remains interesting, as many popular models predict not too heavy supersymmetric particles which may still have evaded searches.

This work discussed two analyses searching for gluinos and squarks produced in pp collisions and decaying to final states with multiple jets, an isolated electron or muon and a large missing transverse energy. The dataset used in these analyses was recorded by the ATLAS detector in pp collisions at 8 TeV at the LHC in 2012. The first analysis was based on a partial statistics of $5.8\,\mathrm{fb}^{-1}$, the second analysis on the full dataset of $20.3\,\mathrm{fb}^{-1}$.

Standard Model backgrounds can mimic the topology of the signal. The dominant two backgrounds are $t\bar{t}$ and W+jets production. A semi-data-driven method to estimate these backgrounds has been described. This method relies on a good description of the backgrounds by Monte Carlo samples and on well-defined control regions close to the signal regions. The background estimates in the signal regions for these two backgrounds are obtained by an extrapolation from the control regions to the signal regions using transfer factors obtained from Monte Carlo simulation.

The QCD multi-jet background is small in the signal regions. It cannot be estimated by using Monte Carlo samples, because of the difficulty to generate a large enough statistics for these events in the regions of phase space interesting for this analysis. A entirely data-driven matrix method is therefore used instead with minimal reliance on Monte Carlo samples. This method uses control samples with identical criteria as the standard selection criteria of the signal and control regions but with relaxed isolation requirements for the selected electron or muon. The QCD multi-jet background estimate in each control or signal region is inferred from these control samples by assigning every event in it a weight depending on the probability that it is a QCD multi-jet event or not.

The data was selected by electron+$E_\mathrm{T}^\mathrm{miss}$ or muon+jet+$E_\mathrm{T}^\mathrm{miss}$ triggers in both analyses. The triggers have been proposed and validated in the context of this work. These triggers can also be used for collecting most of the control samples used in the QCD multi-jet background estimation. Thus, the analyses can avoid using prescaled triggers in any region with low statistics.

The $5.8\,\mathrm{fb}^{-1}$ analysis used signal regions proposed by the 7 TeV analysis [131] which were optimised for MSUGRA/CMSSM scenarios. These signal regions selected events with an isolated electron or muon, at least four highly energetic jets and a large missing transverse energy.

Being optimised for a lower center-of-mass energy and for only one model type and in particular for a grid which is not compatible with the recently observed scalar boson, the signal regions

were not optimal. The signal regions were thus thoroughly re-optimised for the full 2012 dataset with particular focus on simplified models with one step. In order to accommodate the different jet multiplicities arising from the cascade decays of pair produced gluinos or squarks, three sets of signal regions were proposed requiring at least three, five or six jets. These signal regions required higher E_T^{miss}, m_T and m_{eff}^{incl} values than the first analysis, reflecting the higher squark and gluino masses to which these signal regions are sensitive to. The combination of these signal regions provided the largest possible coverage in most models interesting for the final state considered.

The final background estimates in all signal regions are derived in a simultaneous profile log-likelihood fit in all control regions including all relevant systematic uncertainties. The uncertainties on the background estimates arise mainly from statistical uncertainties, the jet energy scale and resolution, and the theoretical uncertainties. No excess beyond Standard Model expectations has been seen in the signal regions.

For both analyses, upper limits on the visible cross section without signal model assumption have been derived. Depending on the signal region, these limits vary between 1.06 and 1.69 fb for the $5.8\,\text{fb}^{-1}$ analysis and between 0.15 and 0.38 fb for the $20.3\,\text{fb}^{-1}$ analysis.

Limits on gluino, squark and $\tilde{\chi}_1^0$ masses have been calculated in specific supersymmetric models. This calculation uses a special fit configuration which partially considers the shapes of background and signal distributions. This increases the sensitivity to the models studied.

The $5.8\,\text{fb}^{-1}$ analysis can exclude squarks and gluinos with a mass of 1.2 TeV for equal gluino and squark masses in a MSUGRA/CMSSM grid with parameters $A_0 = 0$, $\tan\beta = 10$ and $\mu > 0$. The $20.3\,\text{fb}^{-1}$ analysis places limits in the context of simplified models with one and two steps and in a MSUGRA/CMSSM grid with parameters $A_0 = -2m_0$, $\tan\beta = 30$ and $\mu > 0$. This MSUGRA/CMSSM grid is compatible with the recently discovered scalar boson. The limits in the different models are comparable. Gluino masses of ~ 1.2 TeV and squark masses of 750 GeV are excluded for vanishing $\tilde{\chi}_1^0$ masses. In the MSUGRA/CMSSM grid gluino masses below ~ 1.2 TeV can be excluded for all m_0 values.

The limits calculated are consistent with other analyses by the ATLAS Collaboration also searching for gluino and squark production. In particular for low $\tilde{\chi}_1^0$ masses, the $20.3\,\text{fb}^{-1}$ analysis obtains comparable or tighter limits. Some regions in the phase-space can however not be accessed by the analyses presented. This concerns in particular signal models with a very compressed spectra which rarely produce as highly energetic a lepton as required by the analyses presented or signal models predicting multiple leptons in the final state. Other analyses by the ATLAS Collaboration thus complement the $20.3\,\text{fb}^{-1}$ analysis in difficult regions.

The $20.3\,\text{fb}^{-1}$ analysis has only little assumptions on the type of supersymmetric models. The optimisation of the signal regions explicitly considered regions in the MSUGRA/CMSSM grid with parameters $A_0 = -2m_0$, $\tan\beta = 30$ and $\mu > 0$ where squarks of the first two generations are very heavy and the gluino decays via a stop quark into the $\tilde{\chi}_1^0$. The analysis is therefore also sensitive to models with stop quark production in the gluino decay. Furthermore, the $20.3\,\text{fb}^{-1}$ analysis has recently been shown to be also sensitive to models with R-parity violation [16]. The $20.3\,\text{fb}^{-1}$ analysis is thus very general.

The supersymmetric models discussed in this work contained only MSUGRA/CMSSM models as example for a complete supersymmetric model. The limits on the masses of gluinos and squarks are however very tight in this framework. Therefore, the attention has shifted to pMSSM models recently. Although few pMSSM models have already been studied for the $20.3\,\text{fb}^{-1}$ analysis, no systematic analysis has been performed of a broader class of pMSSM models so far. Efforts are currently undertaken within the ATLAS Collaboration and also in context of the analysis

presented in this work to classify the pMSSM models with respect to existing experimental constraints from e.g. searches for Dark Matter or searches for rare B-hadron decays. Models not excluded by these constraints will be further studied in the future.

Thus, notwithstanding the tight limits on sparticles, loop-holes within the current analyses are being identified both in the previously studied models but also in new, possibly more exotic models. This, together with novel methods, is hoped to provide best chances for a discovery of Supersymmetry in the data of LHC Run 2.

Part VI

Appendix

Appendix A

Grids for the simplified models

This chapter details the grids used for the simplified models that are defined in Section 2.4.3. Between 80 and 200 points were generated for each of the simplified models. The limits presented in Chapter 16 are sometimes influenced by the location of the points in the different grids, as detailed below.

A.1 Simplified models with one step
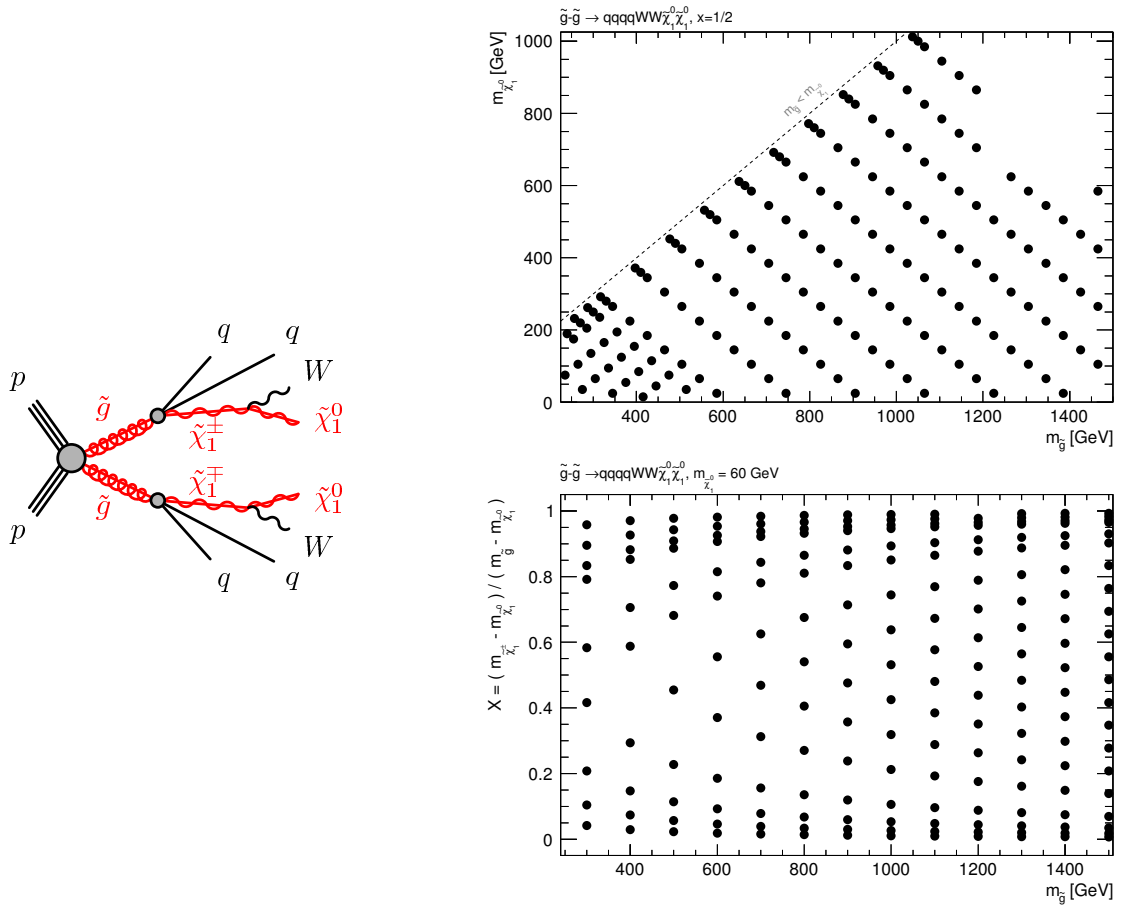
Figure A.1: Graph (left) and grids for simplified models with one step and initial gluino pair production (grid with fixed $x = 1/2$ at the top and with variable x at the bottom).
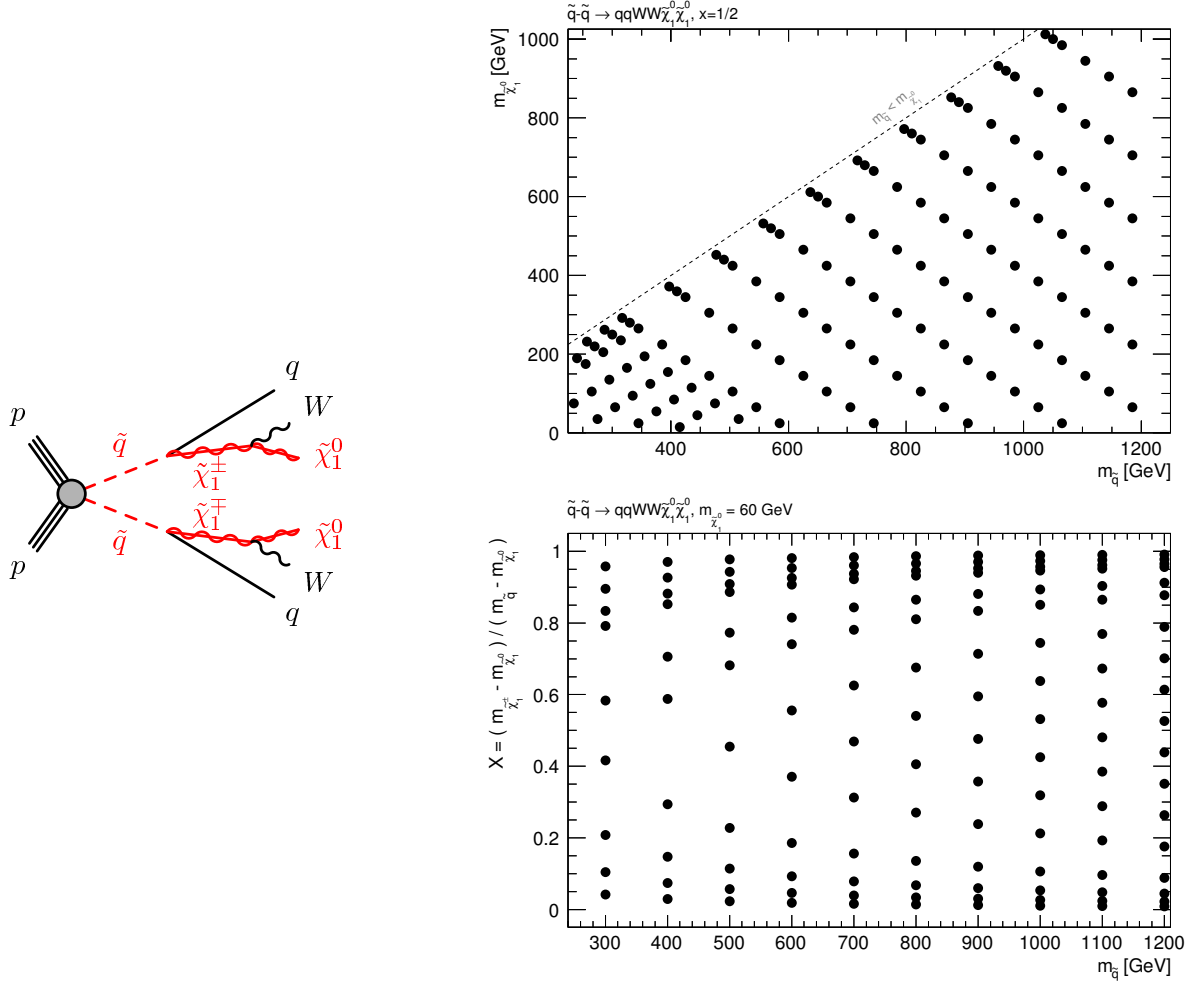
Figure A.2: Graph (left) and grids for simplified models with one step and initial squark pair production with $x = 1/2$ (top right) and variable x (bottom right).

The grids for the simplified models with one step and initial gluino pair production are shown in Figure A.1. Corresponding to the expected sensitivities in these grids, points with gluino masses up to 1.5 TeV were generated. Masses of the $\tilde{\chi}^0_1$ up to 1.2 TeV (the highest $\tilde{\chi}^0_1$ masses are outside the plot in Figure A.1) are considered in the case of the grid with fixed $x = 1/2$. Close to the diagonal with $m_{\tilde{\chi}^0_1} = m_{\tilde{g}}$ more points were generated to allow for a detailed limit in this region populated by models with small mass differences between the gluino and the $\tilde{\chi}^0_1$. Similarly for the grid with variable x, in which the density of points is larger for small or large x values than for medium x values.

The grids for the simplified models with one step and initial squark pair production are shown in Figure A.2. As the sensitivities in these two grids is smaller in comparison to the gluino grids, points were only generated for squark masses up to 1.2 TeV.

A.2 Simplified models with two steps

The grids for the simplified models with two steps and the decay involving W and Z bosons are shown in Figure A.3. Points with gluino (squark) masses up to 1.5 TeV (1.2 TeV) were generated for models with initial gluino (squark) pair production.
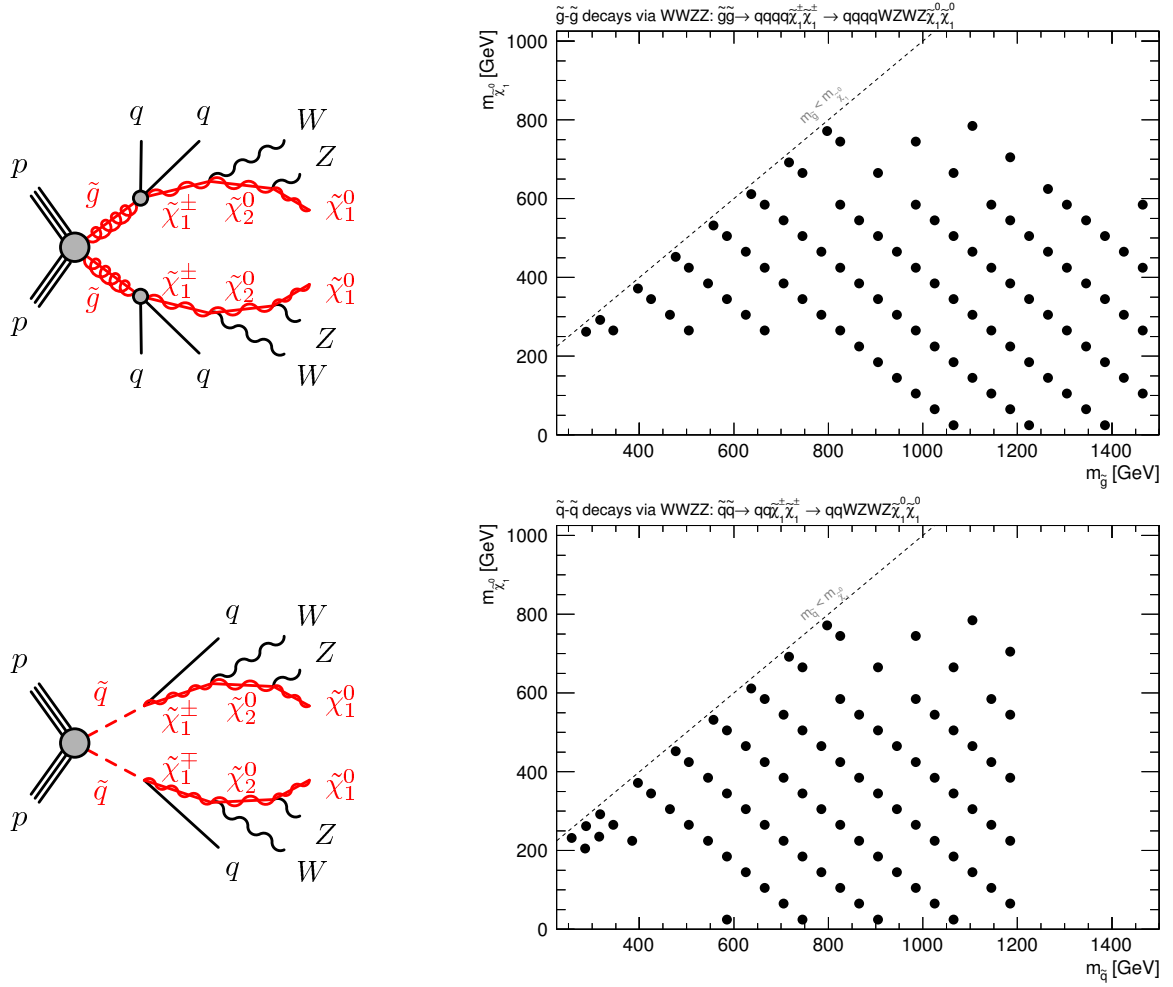
Figure A.3: Graphs and grids for the simplified models with two steps and initial gluino pair production (top row) or squark pair production (bottom row). The decay sequence includes W and Z bosons (as shown in the diagrams on the left) which decay further to jets and leptons. The precise location of the simulated signal points in the grids is show on the right

No or few points were generated in regions excluded by the 7 TeV analysis [131]. This analysis includes signal regions requiring a soft, a hard or two hard leptons. The $20.3\,\text{fb}^{-1}$ analysis fails to reach the sensitivity of this previous analysis in the squark grid and is only sensitive (with the observed limit) to the point with coordinates $(m_{\tilde{q}}, m_{\tilde{\chi}_1^0}) = (585, 25)$ GeV in this region. The sensitivity of the $20.3\,\text{fb}^{-1}$ analysis in the region with low squark and $\tilde{\chi}_1^0$ masses cannot be evaluated as no points are available.

The grids for the simplified models with two steps and the decay proceeding via sleptons and sneutrinos are shown in Figure A.4. Also in these grids, no or few points were generated for low $\tilde{\chi}_1^0$ and gluino/squark masses as these regions were excluded by the 7 TeV analysis.

In the case of all simplified models with two steps, the limits derived in Chapter 16 are not extended into regions where no point was generated.
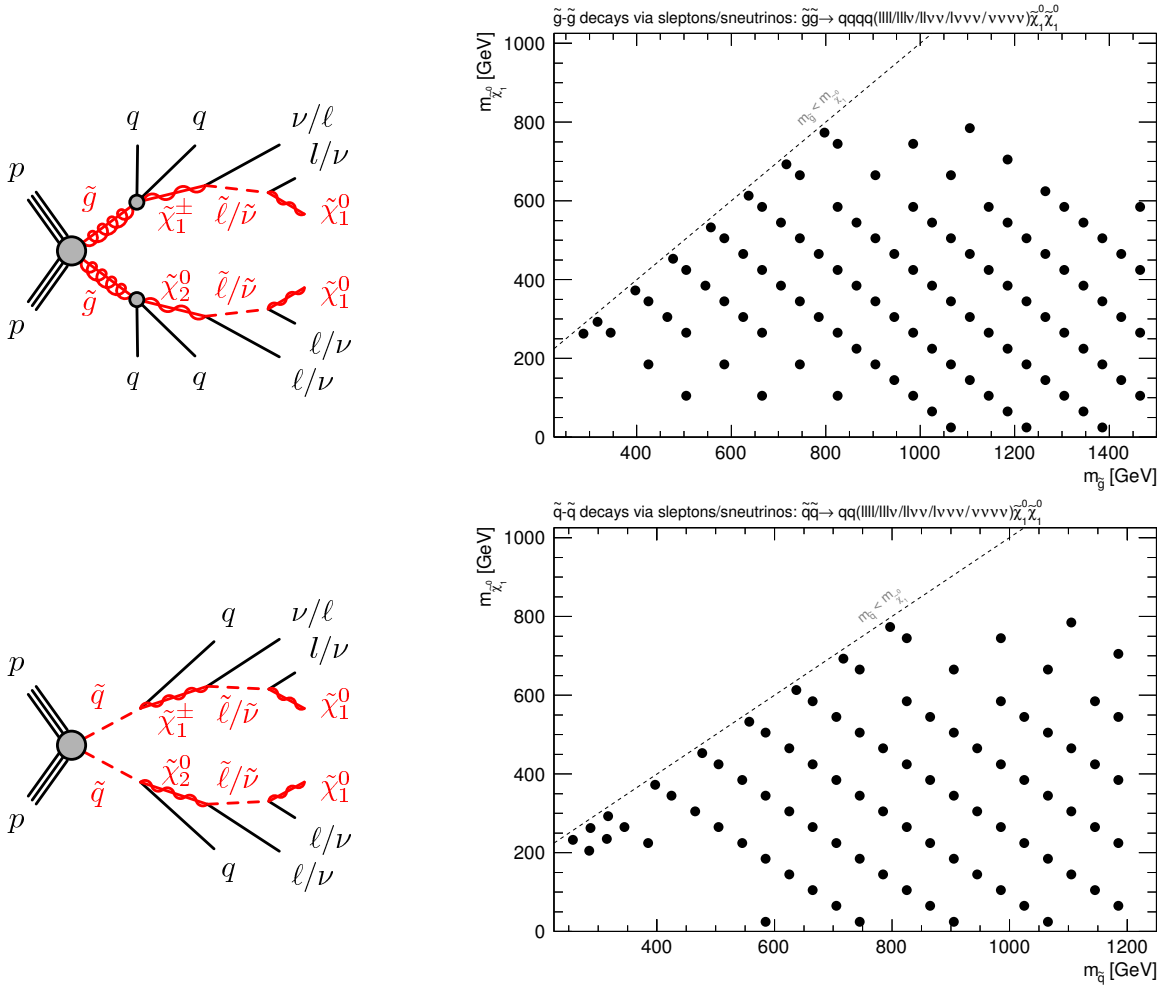
Figure A.4: Graphs (left) and grids (right) for simplified models with two steps and the decay proceeding via sleptons and sneutrinos. The graphs and grids for initial gluino (squark) pair production are shown in the top (bottom) row.

Appendix B

The quality of electrons in the offline identification and in the trigger

Different quality levels are defined for electrons in the the electron identification (see Section 4.1): `loose++`, `medium++` and `tight++` with increasing purity and background rejection. The criteria for the quality levels are detailed in Table B.1. The criteria use various variables which are explained in Table B.2.

Name	Cut-based		
	`loose++`	`medium++`	`tight++`
$R_{\mathrm{Had}(1)}$	✓	✓	✓
f_3		✓	✓
$W_{\eta 2}$	✓	✓	✓
R_η	✓	✓	✓
W_{stot}	✓	✓	✓
E_{ratio}	✓	✓	✓
n_{Blayer}		✓	✓
n_{Pixel}	✓	✓	✓
n_{Si}	✓	✓	✓
d_0		✓	✓
n_{TRT}		✓	✓
F_{HT}		✓	✓
$\Delta\eta_1$	✓	✓	✓
$\Delta\phi_2$			(✓)
E/p			(✓)
!isConv			(✓)

Table B.1: The quality levels for electrons as used in the trigger and in the offline identification are defined based on the variables explained in Table B.2. The analyses in this work use `medium++` and `tight++` electrons in the offline identification. The triggers used require `medium++` electrons. Quantities with the checkmark in brackets are only used in the offline identification, but not in the trigger. The table is taken from [150] with small modifications.

Type	Description	Name
Hadronic leakage	Ratio of E_T in the first layer of the hadronic calorimeter to E_T of the EM cluster (used over the range $|\eta| < 0.8$ and $|\eta| > 1.37$)	R_Had1
	Ratio of E_T in the hadronic calorimeter to E_T of the EM cluster (used over the range $|\eta| > 0.8$ and $|\eta| < 1.37$)	R_Had
Third layer of EM calorimeter	Ratio of the energy in the third layer to the total energy	f_3
Middle layer of EM calorimeter	Lateral shower width, $\sqrt{(\Sigma E_i \eta_i^2)/(\Sigma E_i) - ((\Sigma E_i \eta_i)/(\Sigma E_i))^2}$, where E_i is the energy and η_i is the pseudorapidity of cell i and the sum is calculated within a window of 3×5 cells	$W_{\eta 2}$
	Ratio of the energy in 3×3 cells over the energy in 3×7 cells centred at the electron cluster position	R_ϕ
	Ratio of the energy in 3×7 cells over the energy in 7×7 cells centred at the electron cluster position	R_η
Strip layer of EM calorimeter	Shower width, $\sqrt{(\Sigma E_i (i - i_\mathrm{max})^2)(\Sigma E_i)}$, where i runs over all strips in a window of $\Delta\eta \times \Delta\phi \approx 0.0625 \times 0.2$, corresponding typically to 20 strips in η, and i_max is the index of the highest-energy strip	W_stot
	Ratio of the energy difference between the largest and second largest energy deposits in the cluster over the sum of these energies	E_ratio
	Ratio of the energy in the strip layer to the total energy	f_1
Track quality	Number of hits in the b-layer (discriminates against photon conversions)	n_Blayer
	Number of hits in the pixel detector	n_Pixel
	Number of total hits in the pixel and SCT detectors	n_{Si}
	Transverse impact parameter	d_0
	Significance of transverse impact parameter defined as the ratio of d_0 and its uncertainty	σ_{d_0}
	Momentum lost by the track between the perigee and the last measurement point divided by original momentum	$\Delta p/p$
TRT	Total number of hits in the TRT	n_TRT
	Ratio of the number of high-threshold hits to the total number of hits in the TRT	F_HT
Track–cluster matching	$\Delta\eta$ between the cluster position in the strip layer and the extrapolated track	$\Delta\eta_1$
	$\Delta\phi$ between the cluster position in the middle layer and the extrapolated track	$\Delta\phi_2$
	Defined as $\Delta\phi_2$, but the track momentum is rescaled to the cluster energy before extrapolating the track to the middle layer of the calorimeter	$\Delta\phi_\mathrm{Res}$
	Ratio of the cluster energy to the track momentum	E/p
Conversions	Veto electron candidates matched to reconstructed photon conversions	!isConv

Table B.2: The variables used in the electron identification are defined. This table is taken from [149, 150].

Appendix C

Detailed fit results in the 5.8 fb^{-1} analysis

This chapter presents more results of the simultaneous fit in the analysis of the first $5.8\,\mathrm{fb}^{-1}$ of 2012. The fit configuration and yields in control, validation and signal regions are detailed in Chapter 10.

C.1 Background-only fit result

The values of the parameters (with names as defined in Subsection 10.3.1) after the fit are summarised in Table C.1. Variations of systematic uncertainties of the type `overallSys` are parametrised by a Gaussian with mean α and width $\sigma \cdot E$ where E is the uncertainty before the fit. Variations of uncertainties of the type `histoSys` are parametrised by $\alpha + \sigma \cdot E_i$ with E_i being the uncertainty in bin i. The different types of systematic uncertainties are detailed in Section 10.2. The initial value of α is zero and the initial value of σ is 1. Modified values of α after the fit imply a shifted mean for the systematic uncertainty after the fit. Values smaller than 1 for σ implies a reduction of the uncertainty with respect to before the fit. Values greater than 1 can also occur for the parameters σ. In these cases, the uncertainty concerned is larger after the fit compared to before the fit.

The normalisation parameters μ_{Top} and μ_{WZ} have an initial value of 1 and may be modified in the fit. A value of $\mu_{\mathrm{WZ}} = 0.70$ means for example that the W/Z+jets background is scaled down by 30%.

The sizes of the systematic uncertainties are mostly not modified in the background-only fit as can be seen in Table C.1. Exceptions are the uncertainties on the jet energy scale and resolutions and on the muon energy resolution in the muon spectrometer which are reduced by 40 to 75% after the fit. In particular the the uncertainty on the jet energy scale for jets with a low transverse momentum (parameter α_{JLow}) is significantly reduced by 75%. This systematic uncertainties would however be expected to be small, as only few jets with such a low transverse momentum are expected in the signal regions. Therefore, the reduction of this uncertainty in the background-only fit is considered to be acceptable. The reduction of the other components of the uncertainties on the jet energy scale motivates the introduction of an own parameter for the jet energy scale for the signal sample.

The mean values of the jet energy scale and jet energy resolution are shifted after the fit.

Parameter	Final Value	Uncertainty
α_{BT}	0.1	± 0.9
α_{JER}	-0.8	± 0.7
α_{JHigh}	0.3	± 0.6
α_{JLow}	-0.01	± 0.25
$\alpha_{\mathrm{JMedium}}$	-0.8	± 0.6
α_{LESel}	-0.06	± 0.98
α_{LEel}	-0.02	± 0.99
α_{LRImu}	0.00	± 0.99
α_{LRMmu}	0.00	± 0.61
$\alpha_{\mathrm{QCD\ multi-jet,\ TR\ (electron\ channel)}}$	0.00	± 0.96
$\alpha_{\mathrm{QCD\ multi-jet,\ TR\ (muon\ channel)}}$	-0.07	± 0.99
$\alpha_{\mathrm{QCD\ multi-jet,\ WR\ (electron\ channel)}}$	-0.11	± 0.97
$\alpha_{\mathrm{QCD\ multi-jet,\ WR\ (muon\ channel)}}$	-0.14	± 0.98
α_{RESOST}	-0.2	± 0.9
$\alpha_{\mathrm{SCALEST}}$	-0.2	± 0.9
α_{TEel}	-0.01	± 0.99
α_{errBG}	0.01	± 0.97
μ_{Top}	1.15	± 0.28
μ_{WZ}	0.70	± 0.30

Table C.1: Parameters after the background-only fit for the analysis of the first $5.8\,\mathrm{fb}^{-1}$. The parameters related to statistical uncertainties have been omitted.

The correlation matrix of the background-only fit is shown in Fig. C.1. The correlations between the uncertainties on the jet energy scale for jets with intermediate transverse momentum and the normalisation parameters μ_{Top} and μ_{WZ} are the largest, followed by the correlations between the parameter for the jet energy resolution and the normalisation parameters.

C.2 Distributions in the validation regions

The $E_{\mathrm{T}}^{\mathrm{miss}}$, $m_{\mathrm{eff}}^{\mathrm{incl}}$ distributions and the distribution of the jet multiplicities are shown after the background-only fit in the validation region in the electron and muon channels in Figures C.2, C.3 and C.4. Given the small statistics in the validation regions, the data agrees with the background predictions within the uncertainties.

C.3 Detailed exclusion fit result for one example signal point

The results of the exclusion fit for the MSUGRA/CMSSM model with parameters $(m_0, m_{1/2}) = (2400, 350)$ GeV are detailed in Table C.2. A signal is permitted in the control regions in the exclusion fit, therefore, the normalisation parameters for the Top and the W+jets background could be different from the values found in the background-only fit. The values for the normalisation parameters and for the systematic uncertainties are however consistent with the values obtained in the background-only fit. The signal strength is negligible after the exclusion fit.
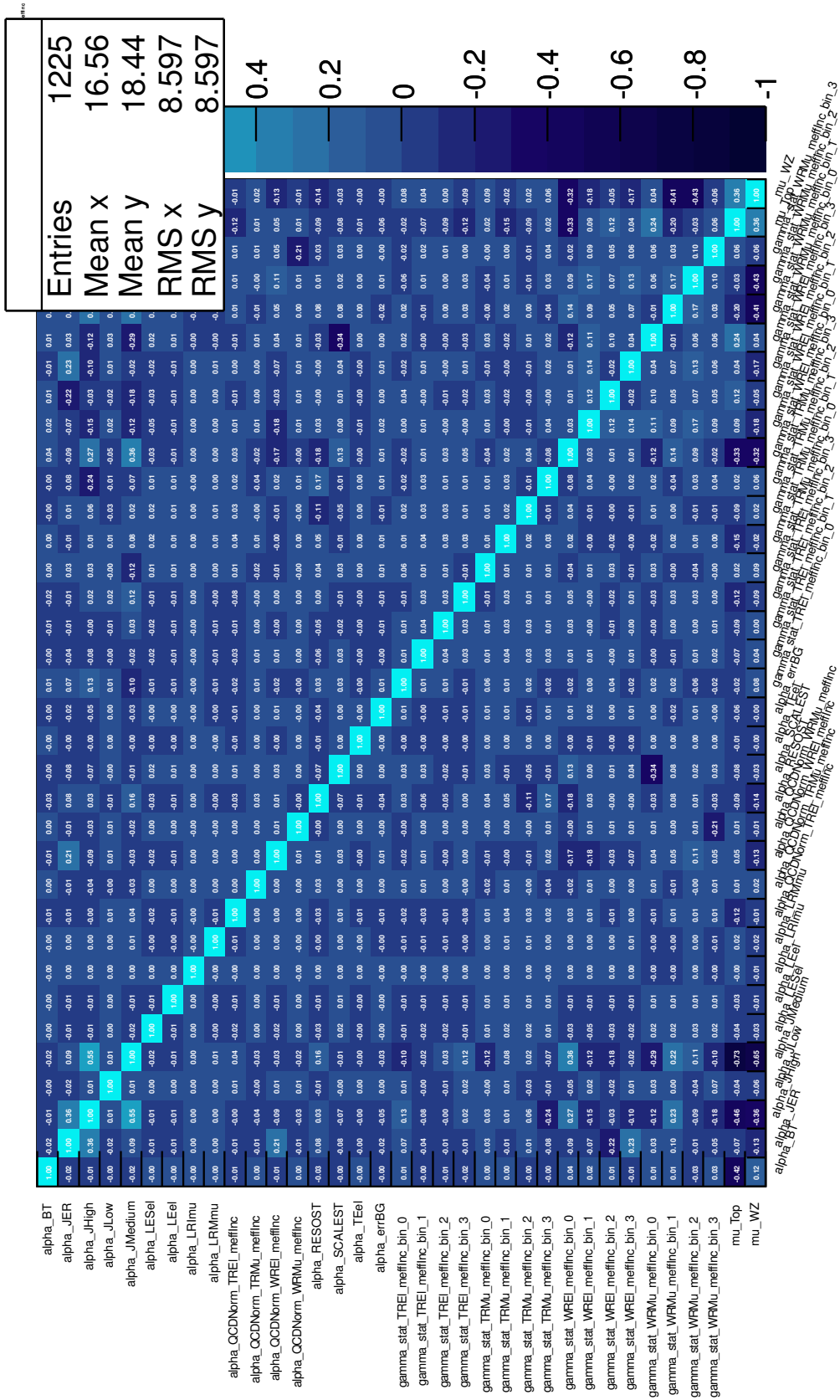
Figure C.1: Correlation matrix for the background-only fit.
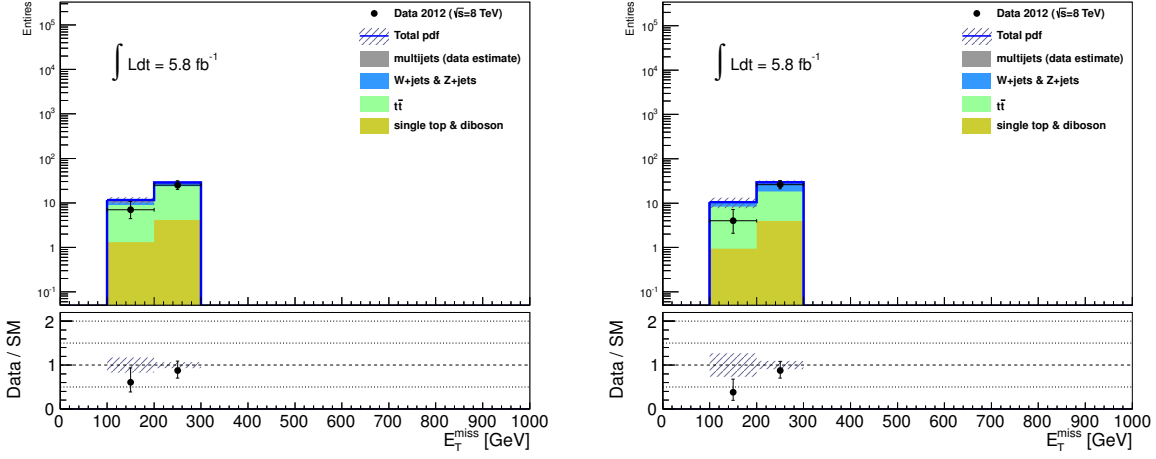
Figure C.2: The E_T^{miss} distributions after the background only fit in the validation region in the electron (left) and muon (right) channel.
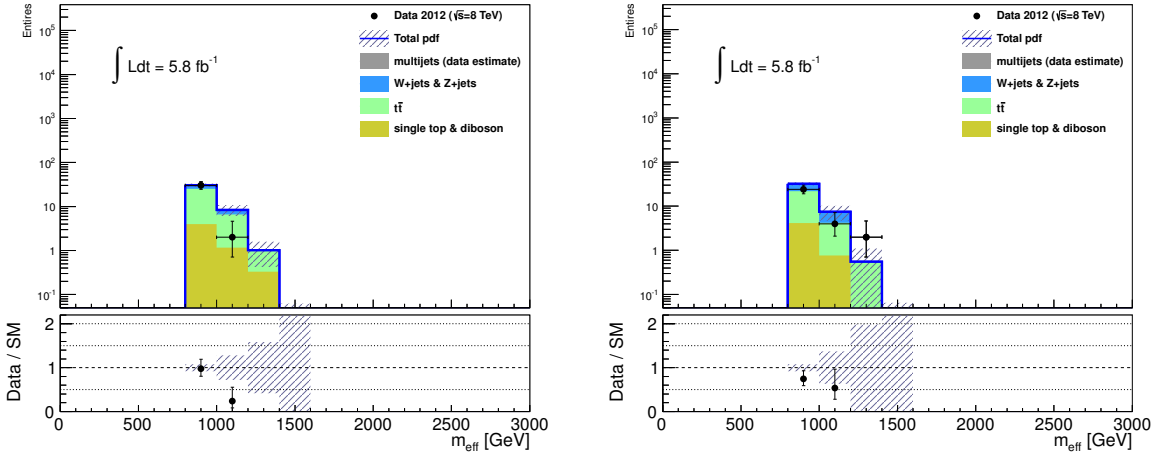
Figure C.3: The m_{eff}^{incl} distributions after the background only fit in the validation region in the electron (left) and muon (right) channel.
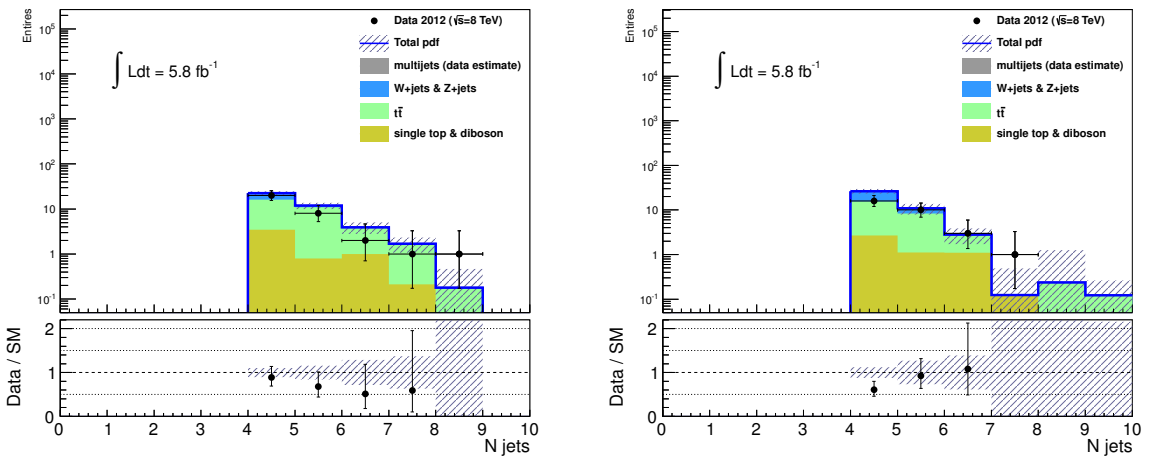
Figure C.4: The jet multiplicities after the background only fit in the validation region in the electron (left) and muon (right) channel.

Parameter	Final Value	Uncertainty
Luminosity	1.00	$\pm$ 0.04
α_{BT}	0.2	$\pm$ 0.8
α_{GenTop}	-0.2	$\pm$ 0.9
α_{GenW}	-0.1	$\pm$ 0.9
α_{JER}	-0.9	$\pm$ 0.6
α_{JHigh}	-0.12	$\pm$ 0.35
α_{JLow}	0.00	$\pm$ 0.34
α_{JMedium}	-0.7	$\pm$ 0.5
α_{JSig}	0.00	$\pm$ 0.08
α_{LESel}	-0.0	$\pm$ 0.9
α_{LEel}	-0.03	$\pm$ 0.97
α_{LEmu}	-0.04	$\pm$ 0.97
α_{LRImu}	0.0	$\pm$ 1.0
α_{LRMmu}	-0.12	$\pm$ 0.97
$\alpha_{\text{QCD multi}-\text{jet, SR (electron channel)}}$	0.6	$\pm$ 0.8
$\alpha_{\text{QCD multi}-\text{jet, TR (electron channel)}}$	0.1	$\pm$ 0.9
$\alpha_{\text{QCD multi}-\text{jet, TR (muon channel)}}$	-0.03	$\pm$ 0.98
$\alpha_{\text{QCD multi}-\text{jet, WR (electron channel)}}$	0.2	$\pm$ 0.9
$\alpha_{\text{QCD multi}-\text{jet, WR (muon channel)}}$	-0.1	$\pm$ 0.4
α_{RESOST}	0.3	$\pm$ 0.8
α_{SCALEST}	-0.2	$\pm$ 0.8
α_{SigXSec}	0.0	$\pm$ 0.9
α_{TEel}	-0.01	$\pm$ 0.99
α_{TEmu}	0.0	$\pm$ 1.0
α_{errBG}	0.1	$\pm$ 0.9
μ_{SIG}	0.0	$\pm$ 0.4
μ_{Top}	1.13	$\pm$ 0.22
μ_{WZ}	0.67	$\pm$ 0.26

Table C.2: Exclusion fit result for the MSUGRA/CMSSM model with parameters $(m_0, m_{1/2}) = (2400, 350)$ GeV.

Appendix D

Detailed fit results in the 20.3 fb^{-1} analysis

The detailed values of the parameters after the background-only fit for the 20.3 fb^{-1} analysis are shown in Table D.1 for the 3-jets tower, in Table D.2 for the 5-jets tower and in Table D.3 for the 6-jets tower. The parameters and the fit implementation is described in Section 14.1. The fitted parameters result in the yields in the control, validation and signal regions that are described in Chapter 15.

Most of the systematic uncertainties in the regions belonging to the 3-jets tower are not considerably constrained or shifted after the background-only fit (see Table D.1). The uncertainty on the jet energy resolution is slightly reduced after the background-only fit. The normalisation of the $t\bar{t}$ background remains comparable to before the background-only fit, the scale of the W+jets background is reduced by 35 %.

The systematic uncertainties attached to the 5-jets tower are not modified by the background-only fit (see Table D.2), again with exception of the jet energy resolution, which is increased after the fit (the *sigma* for this parameter is increased from 1 to 1.1 or 1.2). The normalisation of the $t\bar{t}$ background remains as before the fit, the W+jets background is reduced by 38 %. The uncertainty on the normalisation parameter of the W+jets sample increases with respect to the normalisation parameter for this background in the 3-jets regions.

The systematic uncertainties in the 6-jets region are more modified in the background-only fit (see Table D.3). The systematic uncertainties were sometimes large before the fit, as their estimation was affected by statistical variations due to a low statistics in some of the 6-jets regions. The uncertainties on the jet energy scale and on the factorisation scale of the $t\bar{t}$ sample are reduced after the background-only fit, the uncertainties on the pile-up increased. The uncertainties on the b-tagging scale factors and the pile-up are shifted. The scale of the $t\bar{t}$ background remains unchanged in the fit, the W+jets background is scaled down by 40%.

The matrices showing the correlation between the parameters are shown in Figure D.1 for the 3-jets background-only fit, in Figure D.2 for the 5-jets background-only fit and in Figure D.3 for the 6-jets background-only fit.

The b-tagging parameters are correlated (positively and negatively) by up to 50% with the normalisation parameters of the $t\bar{t}$ and the W+jets sample in the 3-jets regions (see Figure D.1). The parameters attached to the smaller backgrounds (single t, diboson) are correlated negatively to the normalisation parameters with a size of $\sim 40\%$. The theoretical uncertainties are sometimes correlated with the normalisation parameters.

Parameter	Final Value and Uncertainty
$\alpha_{\text{BT\_3J}}$	0.0 ± 1.0
$\alpha_{\text{CT\_3J}}$	$0.0^{+1.0}_{-0.99}$
$\alpha_{\text{JER\_3J}}$	$0.0^{+0.8}_{-1.0}$
$\alpha_{\text{JES\_3J}}$	$0.0^{+1.0}_{-0.9}$
$\alpha_{\text{QCD multi-jet, TR (electron channel)}}$	-0.04 ± 0.98
$\alpha_{\text{QCD multi-jet, TR (muon channel)}}$	0.1 ± 1.0
$\alpha_{\text{QCD multi-jet, WR (electron channel)}}$	0.0 ± 1.0
$\alpha_{\text{QCD multi-jet, WR (muon channel)}}$	$0.00^{+0.99}_{-0.99}$
$\alpha_{\text{RESOST\_3J}}$	$-0.01^{+0.91}_{-0.99}$
$\alpha_{\text{SCALEST\_3J}}$	$0.15^{+0.99}_{-1.11}$
$\alpha_{\text{WTheoPtMin\_3J}}$	0.1 ± 1.0
$\alpha_{\text{errBG\_3J}}$	0.0 ± 1.0
$\alpha_{\text{errDB\_3J}}$	$0.05^{+1.00}_{-0.99}$
$\alpha_{\text{errST\_3J}}$	$0.13^{+0.99}_{-0.99}$
$\alpha_{\text{ktfacW\_3J}}$	$-0.14^{+0.98}_{-0.97}$
$\alpha_{\text{pdfIntra\_3J}}$	0.0 ± 1.0
$\alpha_{\text{pileup\_3J}}$	$0.32^{+0.95}_{-0.97}$
$\alpha_{\text{qfacW\_3J}}$	0.1 ± 1.0
$\alpha_{\text{topTheoFacSc\_3J}}$	0.0 ± 1.0
$\alpha_{\text{topTheoPS\_3J}}$	0.0 ± 1.0
$\alpha_{\text{topTheoRenSc\_3J}}$	0.0 ± 1.0
$\mu_{\text{Top\_3J}}$	$1.02^{+0.23}_{-0.21}$
$\mu_{\text{W\_3J}}$	$0.65^{+0.08}_{-0.12}$

Table D.1: Background-only fit results in the tower with 3-jets regions

The correlations in the 5-jets background-only fit are similar, but the (anti-)correlation between the b-tagging parameter $\alpha_{\text{BT\_5J}}$ and the normalisation parameters is larger. This (anti-)correlation is again larger for the 6-jets regions between the $\alpha_{\text{BT\_6J}}$ and the normalisation parameters (up to 80%). The two normalisation parameters for the $t\bar{t}$ and the W+jets backgrounds are correlated in all towers. The correlation is the largest for the 6-jets regions and amounts to -91%.
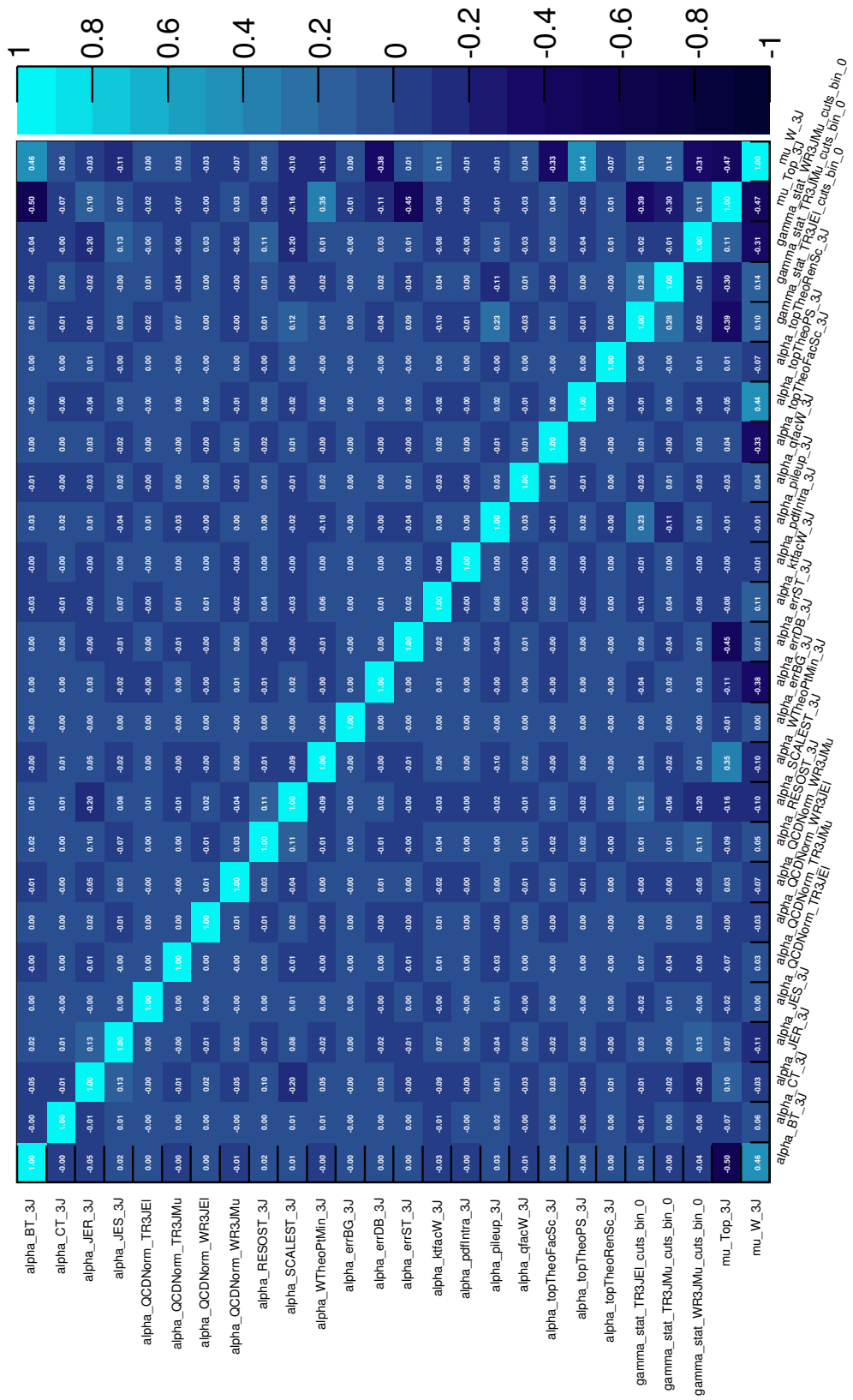
Figure D.1: Correlation matrix for the background-only fit in the 3-jet tower

Parameter	Final Value and Uncertainty
$\alpha_{\text{BT\_5J}}$	-0.1 ± 1.0
$\alpha_{\text{CT\_5J}}$	0.0 ± 1.0
$\alpha_{\text{JER\_5J}}$	0.0 ± 1.0
$\alpha_{\text{JES\_5J}}$	$0.1^{+1.1}_{-1.2}$
$\alpha_{\text{QCD multi-jet, TR (electron channel)}}$	0.0 ± 1.0
$\alpha_{\text{QCD multi-jet, TR (muon channel)}}$	$0.00^{+0.98}_{-1.00}$
$\alpha_{\text{QCD multi-jet, WR (electron channel)}}$	0.0 ± 1.0
$\alpha_{\text{QCD multi-jet, WR (muon channel)}}$	$-0.07^{+0.99}_{-1.00}$
$\alpha_{\text{RESOST\_5J}}$	$-0.01^{+0.98}_{-0.99}$
$\alpha_{\text{SCALEST\_5J}}$	0.0 ± 0.9
$\alpha_{\text{WTheoPtMin\_5J}}$	0.02 ± 0.99
$\alpha_{\text{errBG\_5J}}$	0.0 ± 1.0
$\alpha_{\text{errDB\_5J}}$	0.0 ± 1.0
$\alpha_{\text{errST\_5J}}$	$-0.02^{+0.95}_{-0.97}$
$\alpha_{\text{ktfacW\_5J}}$	-0.12 ± 0.99
$\alpha_{\text{pdfIntra\_5J}}$	0.0 ± 1.0
$\alpha_{\text{pileup\_5J}}$	0.0 ± 1.0
$\alpha_{\text{qfacW\_5J}}$	0.0 ± 1.0
$\alpha_{\text{topTheoFacSc\_5J}}$	0.0 ± 1.0
$\alpha_{\text{topTheoPS\_5J}}$	0.0 ± 1.0
$\alpha_{\text{topTheoRenSc\_5J}}$	0.0 ± 1.0
$\mu_{\text{Top\_5J}}$	$1.04^{+0.14}_{-0.12}$
$\mu_{\text{W\_5J}}$	$0.62^{0.19}_{-0.21}$

Table D.2: Background-only fit results in the tower with 5-jets regions
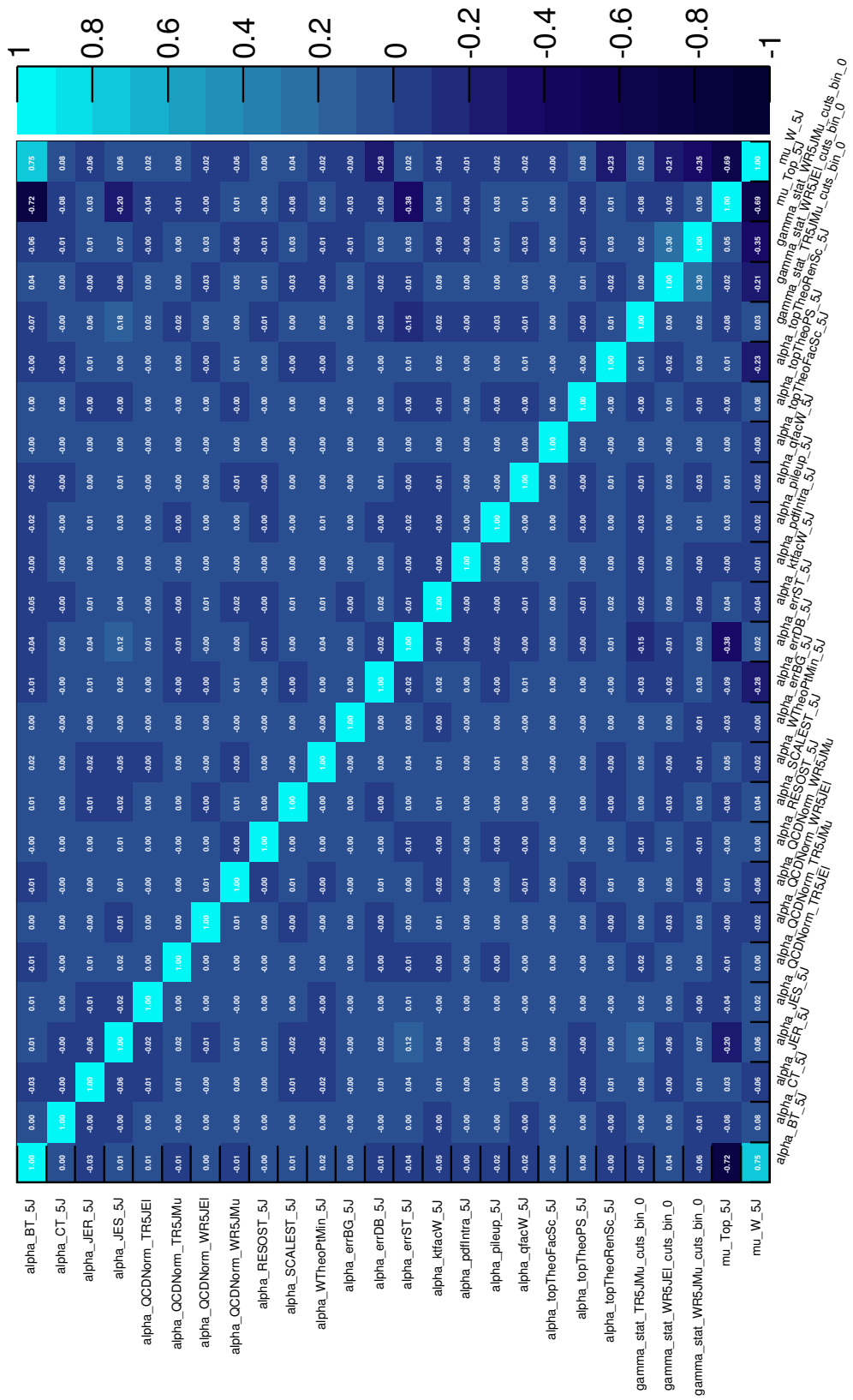
Figure D.2: Correlation matrix for the background-only fit in the 5-jet tower

Parameter	Final Value and Uncertainty
$\alpha_{\text{BT\_6J}}$	0.7 ± 0.9
$\alpha_{\text{CT\_6J}}$	$0.99^{+0.99}_{-1.01}$
$\alpha_{\text{JER\_6J}}$	-0.1 ± 0.9
$\alpha_{\text{JES\_6J}}$	$0.0^{+0.7}_{-0.9}$
$\alpha_{\text{QCD multi-jet, TR (electron channel)}}$	0.0 ± 1.0
$\alpha_{\text{QCD multi-jet, TR (muon channel)}}$	0.04 ± 0.99
$\alpha_{\text{QCD multi-jet, WR (electron channel)}}$	$-0.14^{+0.93}_{-0.96} \pm 0.9$
$\alpha_{\text{QCD multi-jet, WR (muon channel)}}$	$0.23^{+0.99}_{-1.00}$
$\alpha_{\text{RESOST\_6J}}$	-0.1 ± 0.9
$\alpha_{\text{SCALEST\_6J}}$	0.1 ± 0.9
$\alpha_{\text{WTheoPtMin\_6J}}$	-0.2 ± 1.0
$\alpha_{\text{errBG\_6J}}$	0.0 ± 1.0
$\alpha_{\text{errDB\_6J}}$	$-0.08^{+1.00}_{-0.99}$
$\alpha_{\text{errST\_6J}}$	$0.1^{+0.99}_{-1.0}$
$\alpha_{\text{ktfacW\_6J}}$	-0.2 ± 1.0
$\alpha_{\text{pdfIntra\_6J}}$	-0.1 ± 1.0
$\alpha_{\text{pileup\_6J}}$	$-0.5^{+1.2}_{-0.9}$
$\alpha_{\text{qfacW\_6J}}$	-0.1 ± 1.0
$\alpha_{\text{topTheoFacSc\_6J}}$	0.0 ± 0.8
$\alpha_{\text{topTheoPS\_6J}}$	0.2 ± 1.0
$\alpha_{\text{topTheoRenSc\_6J}}$	$0.00^{+0.97}_{-0.93}$
$\mu_{\text{Top\_6J}}$	0.99 ± 0.13
$\mu_{\text{W\_6J}}$	0.6 ± 0.4

Table D.3: Background-only fit results in the tower with 6-jets regions
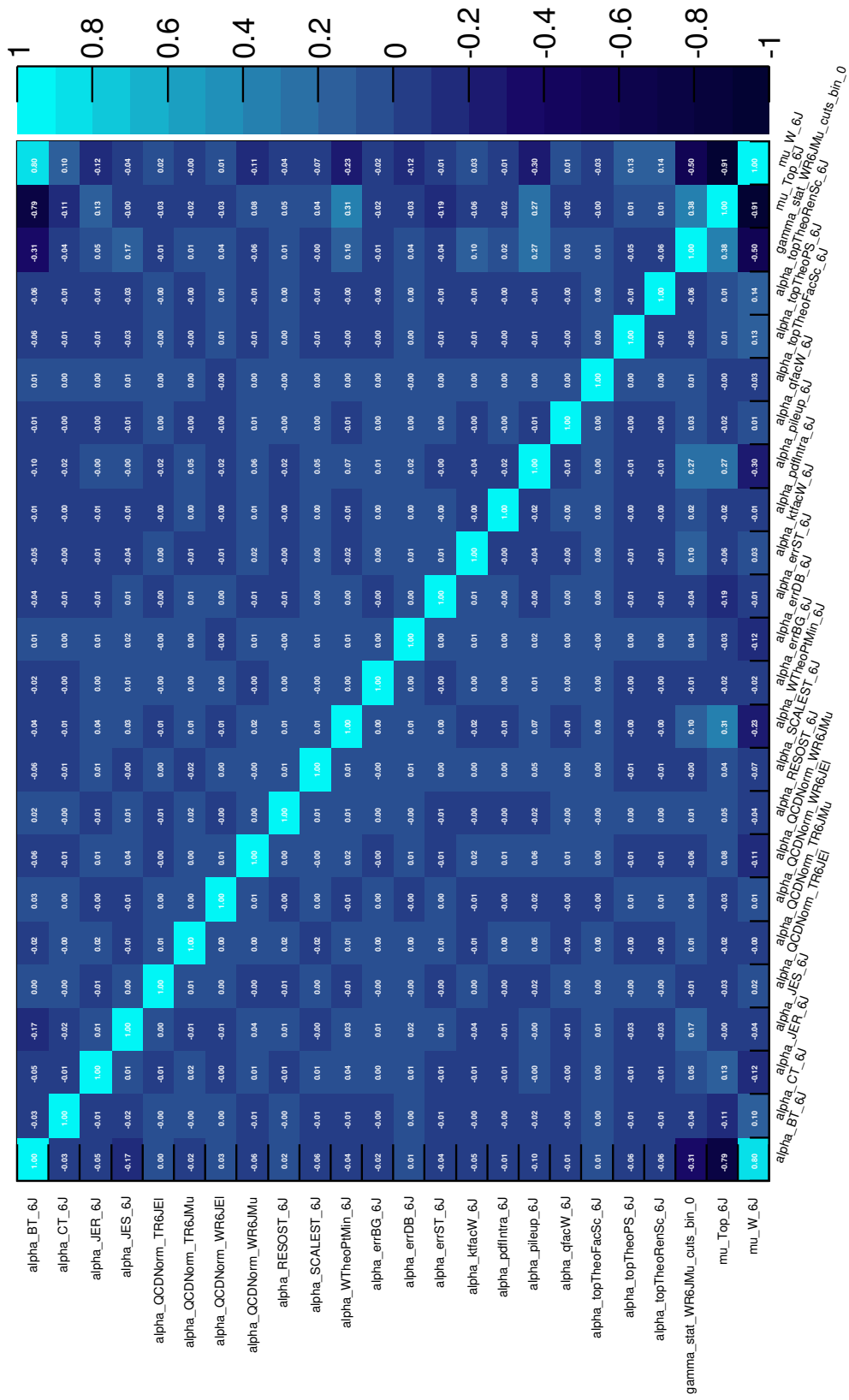
Figure D.3: Correlation matrix for the background-only fit in the 6-jet tower

Appendix E

The soft lepton signal regions

A similar analyses to the ones presented in this work considers final states with a lepton of low transverse momentum (therefore 'soft') [179]. It particularly targets 'compressed' scenarios, in which the mass difference between the gluino/squark or the $\tilde{\chi}_1^\pm$ and the $\tilde{\chi}_1^0$ is small. The two signal regions relevant in comparison to the analyses in this work are given in Table E.1. The signal regions are not further separated into electron and muon channel, because this analysis uses triggers without lepton requirements and similar isolation criteria for electrons and muons. More signal regions were used, as for example a signal region requiring two soft muons. These signal regions are however not interpreted in models discussed in this work.

	soft single-lepton	
	3-jets	**5-jets**
N_ℓ	1 (electron or muon)	
p_T^ℓ(GeV)	[10,25] (electron) , [6,25] (muon)	
$p_T^{\text{add. }\ell}$ (GeV)	< 7 (electron), < 6 (muon)	
N_{jet}	[3,4]	≥ 5
$p_T^{\text{leading jet}}$(GeV)	> 180	
$p_T^{\text{subleading jets}}$(GeV)	> 25	
E_T^{miss} (GeV)	>400	>300
m_T (GeV)	> 100	
$E_T^{\text{miss}}/m_{\text{eff}}^{\text{incl}}$	> 0.3	
$\Delta R_{\min}(\text{jet}, \ell)$	> 1.0	−

Table E.1: The soft lepton analysis uses signal regions with requirements for three or four jets or at least five jets. Adapted from [179].

Appendix F

Limits on Supersymmetry by the ATLAS and CMS experiments

Both the ATLAS and the CMS collaborations pursue a broad programme of analyses searching for Supersymmetry. Apart from the searches for strong production like the analyses presented in this work, this programme includes searches for sparticles of the third generation (stops and sbottoms in particular), for direct production of gauginos, for sleptons and for supersymmetric models not conserving parity.
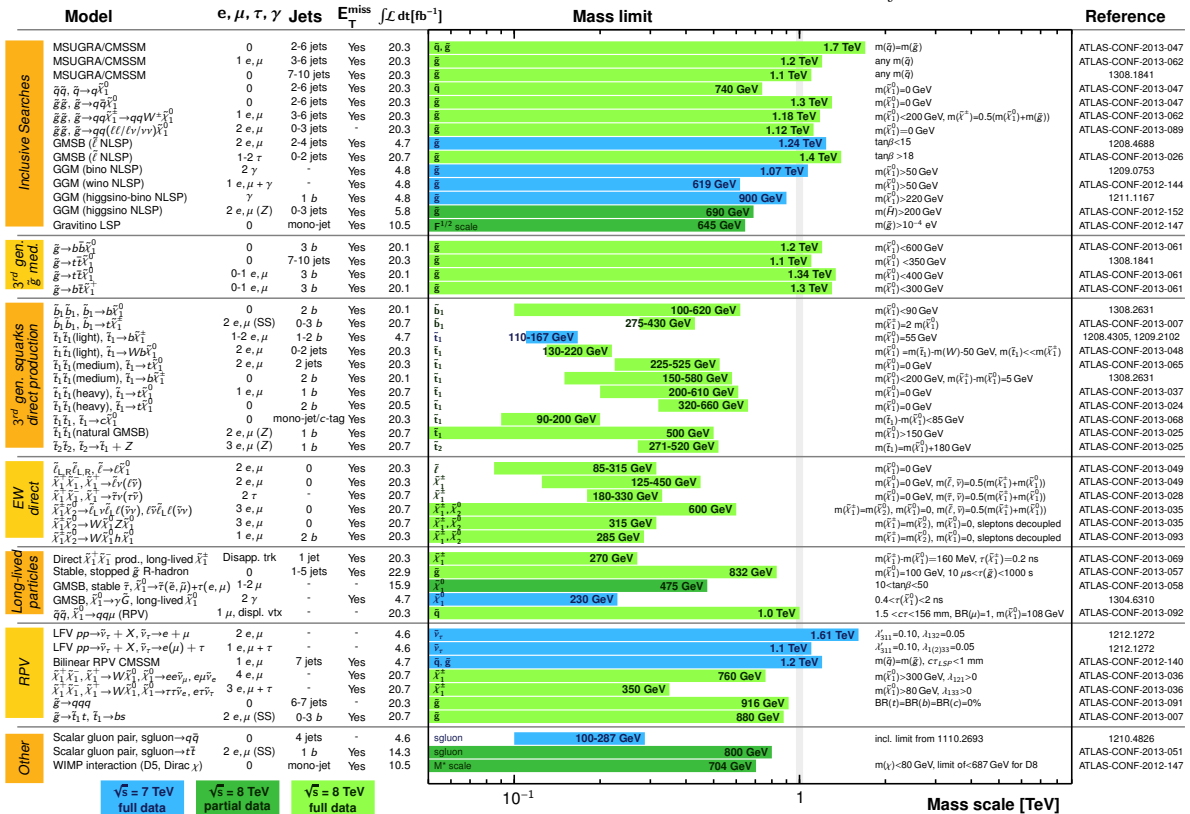
Figure F.1: Limits on Supersymmetry by the ATLAS Collaboration [236].

The most stringent limits by the ATLAS collaboration are summarised in Figure F.1. Similar
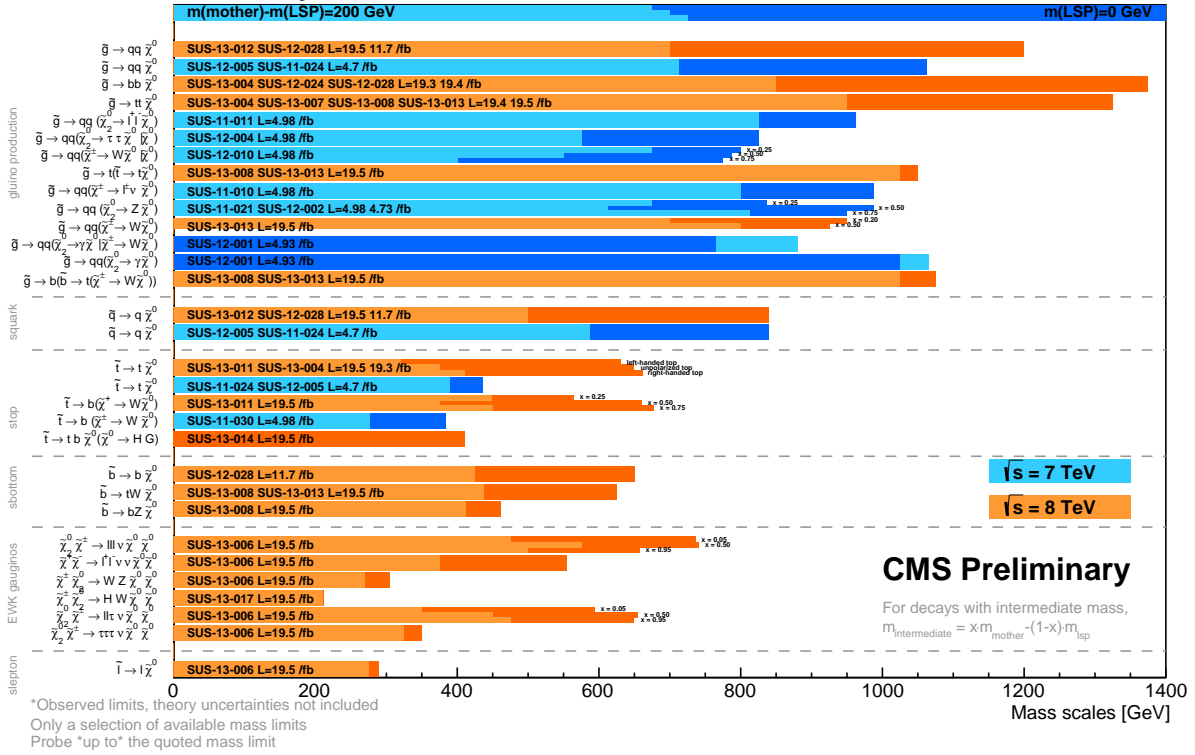
Figure F.2: Limits on Supersymmetry by the CMS Collaboration [237].

limits are obtained by the CMS collaboration. They are summarised in Figure F.2.

List of Figures

204

List of Tables

Bibliography

[1] G. L. Kane et al., *Upper bounds in low-energy SUSY*, arXiv:hep-ph/9405364 [hep-ph].

[2] H. K. Dreiner, *Hide and seek with supersymmetry*, arXiv:hep-ph/9902347 [hep-ph].

[3] ATLAS Collaboration, *Search for supersymmetry using final states with one lepton, jets, and missing transverse momentum with the ATLAS detector in $\sqrt{s} = 7$ TeV pp Collisions*, Phys.Rev.Lett. **106** (2011) 131802, arXiv:1102.2357 [hep-ex].

[4] ATLAS Collaboration, *Search for squarks and gluinos using final states with jets and missing transverse momentum with the ATLAS detector in $\sqrt{s} = 7$ TeV proton-proton collisions*, Phys.Lett. **B701** (2011) 186–203, arXiv:1102.5290 [hep-ex].

[5] CMS Collaboration, *Search for Supersymmetry in pp Collisions at 7 TeV in Events with Jets and Missing Transverse Energy*, Phys. Lett. B **698** no. arXiv:1101.1628. CMS-SUS-10-003. CERN-PH-EP-2010-084, (2011) 196–218. 32 p.

[6] ATLAS Collaboration, *Search for direct production of the top squark in the all-hadronic $t\bar{t} + E_\mathrm{T}^\mathrm{miss}$ final state in 21 fb^{-1} of pp collisions at $\sqrt{s} = 8$ TeV with the ATLAS detector*, Tech. Rep. ATLAS-CONF-2013-024, CERN, Geneva, Mar, 2013.

[7] ATLAS Collaboration, *Search for direct top squark pair production in final states with one isolated lepton, jets, and missing transverse momentum in $\sqrt{s} = 8\,TeV$ pp collisions using 21 fb^{-1} of ATLAS data*, Tech. Rep. ATLAS-CONF-2013-037, CERN, Geneva, Mar, 2013.

[8] ATLAS Collaboration, *Search for direct top squark pair production in final states with two leptons in $\sqrt{s} = 8$ TeV pp collisions using 20fb^{-1} of ATLAS data*, Tech. Rep. ATLAS-CONF-2013-048, CERN, Geneva, May, 2013.

[9] ATLAS Collaboration, *Search for strong production of supersymmetric particles in final states with missing transverse momentum and at least three b-jets using 20.1 fb^{-1} of pp collisions at $\sqrt{s} = 8$ TeV with the ATLAS Detector*, Tech. Rep. ATLAS-CONF-2013-061, CERN, Geneva, Jun, 2013.

[10] ATLAS Collaboration, *Search for supersymmetry in events with four or more leptons in 21fb^{-1} of pp collisions at $\sqrt{s} = 8\,TeV$ with the ATLAS detector*, Tech. Rep. ATLAS-CONF-2013-036, CERN, Geneva, Mar, 2013.

[11] ATLAS Collaboration, *Search for direct production of charginos and neutralinos in events with three leptons and missing transverse momentum in 21 fb^{-1} of pp collisions at $\sqrt{s} = 8\,TeV$with the ATLAS detector*, Tech. Rep. ATLAS-CONF-2013-035, CERN, Geneva, Mar, 2013.

[12] ATLAS Collaboration, *Search for direct-slepton and direct-chargino production in final states with two opposite-sign leptons, missing transverse momentum and no jets in*

$20 \mathrm{fb}^{-1}$ *of pp collisions at* $\sqrt{s} = 8$ TeV *with the ATLAS detector*, Tech. Rep. ATLAS-CONF-2013-049, CERN, Geneva, May, 2013.

[13] ATLAS Collaboration, *Search for electroweak production of supersymmetric particles in final states with at least two hadronically decaying taus and missing transverse momentum with the ATLAS detector in proton-proton collisions at* $\sqrt{s} = 8$ *TeV*, Tech. Rep. ATLAS-CONF-2013-028, CERN, Geneva, Mar, 2013.

[14] J. L. Feng, *Naturalness and the Status of Supersymmetry*, arXiv:1302.6587 [hep-ph].

[15] ATLAS Collaboration, *Further search for supersymmetry at* $\sqrt{s} = 7$ *TeV in final states with jets, missing transverse momentum and one isolated lepton*, Tech. Rep. ATLAS-CONF-2012-041, CERN, Geneva, Mar, 2012.

[16] ATLAS Collaboration, "Search for strongly produced supersymmetric particles in decays with leptons at $\sqrt{s} = 8$ TeV." Paper in preparation. Internal documentation: ATL-COM-PHYS-2013-1517, Nov, 2013.

[17] R. Mohapatra and A. Smirnov, *Neutrino Mass and New Physics*, Ann.Rev.Nucl.Part.Sci. **56** (2006) 569–628, arXiv:hep-ph/0603118 [hep-ph].

[18] B. Povh et al., *Teilchen und Kerne: Eine Einführung in die physikalischen Konzepte.* Springer-Verlag GmbH, 2006.

[19] Particle Data Group Collaboration, J. Beringer et al., "Review of particle physics and 2013 partial update for the 2014 edition." http://pdg.lbl.gov/2013/listings/rpp2013-list-higgs-boson.pdf.

[20] ATLAS Collaboration, *Observation of a new particle in the search for the Standard Model Higgs boson with the ATLAS detector at the LHC*, Phys.Lett. **B716** (2012) 1–29, arXiv:1207.7214 [hep-ex].

[21] CMS Collaboration, *Observation of a new boson at a mass of 125 GeV with the CMS experiment at the LHC*, Physics Letters B **716** no. 1, (2012) 30 – 61.

[22] Particle Data Group Collaboration, J. Beringer et al., *Review of Particle Physics*, Phys. Rev. D **86** (2012) 010001.

[23] V. D. Barger et al., *Collider Physics.* Westview Press, 1991.

[24] D. Griffiths, *Introduction to Elementary Particles.* John Wiley & Sons, 2008.

[25] I. Aitchison and A. Hey, *Gauge Theories in Particle Physics, two volumes.* Taylor & Francis, 2003 and 2004.

[26] M. Maggiore, *A Modern Introduction to Quantum Field Theory.* Oxford University Press, 2010.

[27] E. Fermi, *An attempt of a theory of beta radiation. 1.*, Z.Phys. **88** (1934) 161–177.

[28] S. Glashow, *Partial Symmetries of Weak Interactions*, Nucl.Phys. **22** (1961) 579–588.

[29] S. Weinberg, *A Model of Leptons*, Phys. Rev. Lett. **19** (1967) 1264–1266.

[30] F. Englert and R. Brout, *Broken Symmetry and the Mass of Gauge Vector Mesons*, Phys. Rev. Lett. **13** (1964) 321–323.

[31] P. W. Higgs, *Broken Symmetries and the Masses of Gauge Bosons*, Phys. Rev. Lett. **13** (1964) 508–509.

[32] P. W. Higgs, *Spontaneous Symmetry Breakdown without Massless Bosons*, Phys. Rev. **145** (1966) 1156–1163.

[33] M. Bustamante, L. Cieri, and J. Ellis, *Beyond the Standard Model for Montaneros*, arXiv:0911.4409 [hep-ph].

[34] P. Binetruy, *Supersymmetry: Theory, Experiment, and Cosmology*. Oxford Graduate Texts. OUP Oxford, 2012.

[35] ATLAS Collaboration, *Measurements of Higgs boson production and couplings in diboson final states with the ATLAS detector at the LHC*, Physics Letters B **726** no. 1–3, (2013) 88 – 119.

[36] CMS Collaboration, *Study of the Mass and Spin-Parity of the Higgs Boson Candidate via Its Decays to Z Boson Pairs. On the mass and spin-parity of the Higgs boson candidate via its decays to Z boson pairs*, Phys. Rev. Lett. **110** (2012) 081803. 25 p.

[37] ATLAS Collaboration, *Evidence for the spin-0 nature of the Higgs boson using ATLAS data*, Physics Letters B **726** no. 1–3, (2013) 120 – 144.

[38] ATLAS Collaboration, *Combined coupling measurements of the Higgs-like boson with the ATLAS detector using up to 25 fb^{-1} of proton-proton collision data*, Tech. Rep. ATLAS-CONF-2013-034, CERN, Geneva, Mar, 2013.

[39] CMS Collaboration, "Higgs public results." https://twiki.cern.ch/twiki/bin/view/CMSPublic/PhysicsResultsHIG.

[40] H. Baer and X. Tata, *Weak Scale Supersymmetry: From Superfields to Scattering Events*. Cambridge University Press, 2006.

[41] F. Zwicky, *Die Rotverschiebung von extragalaktischen Nebeln*, Helv.Phys.Acta **6** (1933) 110–127.

[42] D. Perkins, *Particle Astrophysics*. Oxford University Press, 2009.

[43] G. F. Smoot et al., *Structure in the COBE differential microwave radiometer first year maps*, Astrophys.J. **396** (1992) L1–L5.

[44] C. L. Bennett et al., *Four-Year COBE DMR Cosmic Microwave Background Observations: Maps and Basic Results*, The Astrophysical Journal Letters **464** no. 1, (1996) L1.

[45] WMAP Collaboration, *Nine-Year Wilkinson Microwave Anisotropy Probe (WMAP) Observations: Final Maps and Results*, Astrophys.J.Suppl. **208** (2013) 20, arXiv:1212.5225 [astro-ph.CO].

[46] WMAP Collaboration, *Nine-Year Wilkinson Microwave Anisotropy Probe (WMAP) Observations: Cosmological Parameter Results*, Astrophys.J.Suppl. **208** (2013) 19, arXiv:1212.5226 [astro-ph.CO].

[47] Planck Collaboration, *Planck 2013 results. I. Overview of products and scientific results*, arXiv:1303.5062 [astro-ph.CO].

[48] L. E. Strigari, *Galactic searches for dark matter*, Physics Reports **531** no. 1, (2013) 1 – 88. Galactic searches for dark matter.

[49] S. P. Martin, *A Supersymmetry primer*, arXiv:hep-ph/9709356 [hep-ph].

[50] M. Muhlleitner, "Supersymmetrie an Collidern." http://www.itp.kit.edu/~maggie/susycolliders11/aktuell.pdf, 2011.

[51] D. Kazakov, *Beyond the standard model: In search of supersymmetry*, `arXiv:hep-ph/0012288 [hep-ph]`.

[52] S. Coleman and J. Mandula, *All Possible Symmetries of the S Matrix*, Phys. Rev. **159** (1967) 1251–1256.

[53] Y. Golfand and E. Likhtman, *Extension of the Algebra of Poincare Group Generators and Violation of p Invariance*, JETP Lett. **13** (1971) 323–326.

[54] P. Ramond, *Dual Theory for Free Fermions*, Phys.Rev. **D3** (1971) 2415–2418.

[55] A. Neveu and J. Schwarz, *Factorizable dual model of pions*, Nucl.Phys. **B31** (1971) 86–112.

[56] D. Volkov and V. Akulov, *Is the Neutrino a Goldstone Particle?*, Phys.Lett. **B46** (1973) 109–110.

[57] J. Wess and B. Zumino, *A Lagrangian Model Invariant Under Supergauge Transformations*, Phys.Lett. **B49** (1974) 52.

[58] J. Wess and B. Zumino, *Supergauge Invariant Extension of Quantum Electrodynamics*, Nucl.Phys. **B78** (1974) 1.

[59] J. Wess and B. Zumino, *Supergauge Transformations in Four-Dimensions*, Nucl.Phys. **B70** (1974) 39–50.

[60] J. Iliopoulos and B. Zumino, *Broken Supergauge Symmetry and Renormalization*, Nucl.Phys. **B76** (1974) 310.

[61] S. Ferrara, J. Iliopoulos, and B. Zumino, *Supergauge Invariance and the Gell-Mann - Low Eigenvalue*, Nucl.Phys. **B77** (1974) 413.

[62] M. Drees, R. Godbole, and P. Roy, *Theory and phenomenology of Sparticles: an account of four-dimensional N=1 supersymmetry in high-energy physics*. World Scientific, Singapore, 2004.

[63] P. Fayet and S. Ferrara, *Supersymmetry*, Phys.Rept. **32** (1977) 249–334.

[64] J. R. Ellis, *Beyond the standard model for hill walkers*, `arXiv:hep-ph/9812235 [hep-ph]`.

[65] I. J. Aitchison, *Supersymmetry and the MSSM: An Elementary introduction*, `arXiv:hep-ph/0505105 [hep-ph]`.

[66] J. R. Ellis et al., *Supersymmetric Relics from the Big Bang*, Nucl.Phys. **B238** (1984) 453–476.

[67] E. Dudas et al., *Relating the CMSSM and SUGRA Models with GUT Scale and Super-GUT Scale Supersymmetry Breaking*, Eur.Phys.J. **C72** (2012) 2138, `arXiv:1205.5988 [hep-ph]`.

[68] M. W. Cahill-Rowley et al., *The Higgs Sector and Fine-Tuning in the pMSSM*, Phys.Rev. **D86** (2012) 075015, `arXiv:1206.5800 [hep-ph]`.

[69] M. W. Cahill-Rowley et al., *The New Look pMSSM with Neutralino and Gravitino LSPs*, Eur.Phys.J. **C72** (2012) 2156, `arXiv:1206.4321 [hep-ph]`.

[70] MSSM Working Group Collaboration, A. Djouadi et al., *The Minimal supersymmetric standard model: Group summary report*, `arXiv:hep-ph/9901246 [hep-ph]`.

[71] LHC New Physics Working Group Collaboration, *Simplified Models for LHC New Physics Searches*, J.Phys. **G39** (2012) 105005, arXiv:1105.2838 [hep-ph].

[72] W. Beenakker et al., *PROSPINO: A Program for the production of supersymmetric particles in next-to-leading order QCD*, arXiv:hep-ph/9611232 [hep-ph].

[73] T. Plehn et al., *Prospino2 webpage*, Oct, 2013. http://www.thphys.uni-heidelberg.de/~plehn/index.php?show=prospino&visible=tools.

[74] B. Allanach, *SOFTSUSY: a program for calculating supersymmetric spectra*, Comput.Phys.Commun. **143** (2002) 305–331, arXiv:hep-ph/0104145 [hep-ph].

[75] M. Bahr et al., *Herwig++ Physics and Manual*, Eur.Phys.J. **C58** (2008) 639–707, arXiv:0803.0883 [hep-ph].

[76] A. Buckley, *PySLHA: a Pythonic interface to SUSY Les Houches Accord data*, arXiv:1305.4194 [hep-ph].

[77] J. Alwall et al., *MadGraph 5 : Going Beyond*, JHEP **1106** (2011) 128, arXiv:1106.0522 [hep-ph].

[78] T. Sjöstrand et al., *PYTHIA 6.4 physics and manual*, JHEP **05** (2006) 026.

[79] H. Baer, V. Barger, and A. Mustafayev, *Implications of a 125 GeV Higgs scalar for LHC SUSY and neutralino dark matter searches*, Phys.Rev. **D85** (2012) 075010, arXiv:1112.3017 [hep-ph].

[80] L. J. Hall et al., *A Natural SUSY Higgs Near 126 GeV*, JHEP **1204** (2012) 131, arXiv:1112.2703 [hep-ph].

[81] A. Arbey et al., *Implications of a 125 GeV Higgs for supersymmetric models*, Phys.Lett. **B708** (2012) 162–169, arXiv:1112.3028 [hep-ph].

[82] S. Akula et al., *Higgs Boson Mass Predictions in SUGRA Unification, Recent LHC-7 Results, and Dark Matter*, Phys.Rev. **D85** (2012) 075001, arXiv:1112.3645 [hep-ph].

[83] P. Draper et al., *Implications of a 125 GeV Higgs for the MSSM and Low-Scale SUSY Breaking*, Phys.Rev. **D85** (2012) 095007, arXiv:1112.3068 [hep-ph].

[84] A. Arvanitaki and G. Villadoro, *A Non Standard Model Higgs at the LHC as a Sign of Naturalness*, JHEP **1202** (2012) 144, arXiv:1112.4835 [hep-ph].

[85] Z. Kang et al., *On Naturalness of the MSSM and NMSSM*, JHEP **1211** (2012) 024, arXiv:1201.5305 [hep-ph].

[86] H. Baer et al., *Leaving no stone unturned in the hunt for SUSY naturalness: A Snowmass whitepaper*, arXiv:1306.3148 [hep-ph].

[87] CDF Collaboration, *Inclusive Search for Squark and Gluino Production in $p\overline{p}$ Collisions at $\sqrt{s}$ = 1.96 TeV*, Phys. Rev. Lett. **102** (2009) 121801.

[88] D0 Collaboration, *Search for squarks and gluinos in events with jets and missing transverse energy using 2.1 fb^{-1} of $p\bar{p}$ collision data at $\sqrt{s}$ = 1.96- TeV*, Phys.Lett. **B660** (2008) 449–457, arXiv:0712.3805 [hep-ex].

[89] ATLAS Collaboration, *Search for squarks and gluinos using final states with jets and missing transverse momentum with the ATLAS detector in $\sqrt{s}$ = 7 TeV proton-proton collisions*, Tech. Rep. ATLAS-CONF-2012-033, CERN, Geneva, Mar, 2012.

[90] ATLAS Collaboration, *Hunt for new phenomena using large jet multiplicities and missing transverse momentum with ATLAS in $L = 4.7$ fb^{-1} of $\sqrt{s} = 7$ TeV proton-proton collisions*, Tech. Rep. ATLAS-CONF-2012-037, CERN, Geneva, Mar, 2012.

[91] ATLAS Collaboration, *Further search for supersymmetry at $\sqrt{s} = 7$ TeV in final states with jets, missing transverse momentum and isolated leptons with the ATLAS detector*, Phys.Rev. **D86** (2012) 092002, arXiv:1208.4688 [hep-ex].

[92] ATLAS Collaboration, *Search for squarks and gluinos with the ATLAS detector in final states with jets and missing transverse momentum using 4.7 fb^{-1} of $\sqrt{s} = 7$ TeV proton-proton collision data*, Phys.Rev. **D87** (2013) 012008, arXiv:1208.0949 [hep-ex].

[93] ATLAS Collaboration, *Hunt for new phenomena using large jet multiplicities and missing transverse momentum with ATLAS in 4.7 fb^{-1} of $\sqrt{s} = 7$ TeV proton-proton collisions*, JHEP **1207** (2012) 167, arXiv:1206.1760 [hep-ex].

[94] LHCb Collaboration, *Measurement of the $B_s^0 \to \mu^+\mu^-$ branching fraction and search for $B^0 \to \mu^+\mu^-$ decays at the LHCb experiment*, Phys.Rev.Lett. **111** (2013) 101805, arXiv:1307.5024 [hep-ex].

[95] CMS Collaboration, *Measurement of the $B_s \to \mu^+\mu^-$ branching fraction and search for $B_0 \to \mu^+\mu^-$ with the CMS Experiment*, Phys.Rev.Lett. **111** (2013) 101804, arXiv:1307.5025 [hep-ex].

[96] A. Arbey et al., *Supersymmetry confronts $B_s \to \mu^+\mu^-$: Present and future status*, Phys.Rev. **D87** (2013) 035026, arXiv:1212.4887 [hep-ph].

[97] Belle Collaboration, *Measurement of Inclusive Radiative B-meson Decays with a Photon Energy Threshold of 1.7-GeV*, Phys.Rev.Lett. **103** (2009) 241801, arXiv:0907.1384 [hep-ex].

[98] T. Hurth, *Present status of inclusive rare B decays*, Rev.Mod.Phys. **75** (2003) 1159–1199, arXiv:hep-ph/0212304 [hep-ph].

[99] L. Baudis, *Direct dark matter detection: The next decade*, Physics of the Dark Universe **1** no. 1–2, (2012) 94 – 108. Next Decade in Dark Matter and Dark Energy.

[100] R. Bernabei, P. Belli, et al., *New results from DAMA/LIBRA*, The European Physical Journal C **67** no. 1-2, (2010) 39–49. http://dx.doi.org/10.1140/epjc/s10052-010-1303-9.

[101] CoGeNT Collaboration, *Results from a Search for Light-Mass Dark Matter with a p-Type Point Contact Germanium Detector*, Phys. Rev. Lett. **106** (2011) 131301.

[102] G. Angloher et al., *Results from 730 kg days of the CRESST-II Dark Matter search*, The European Physical Journal C **72** no. 4, (2012) 1–22.

[103] CDMS Collaboration, *Silicon Detector Dark Matter Results from the Final Exposure of CDMS II*, Phys.Rev.Lett. (2013), arXiv:1304.4279 [hep-ex].

[104] XENON100 Collaboration, *Dark Matter Results from 225 Live Days of XENON100 Data*, Phys.Rev.Lett. **109** (2012) 181301, arXiv:1207.5988 [astro-ph.CO].

[105] L. Evans and P. Bryant, *LHC Machine*, Journal of Instrumentation **3** no. 08, (2008) S08001.

[106] ATLAS Collaboration, *The ATLAS Experiment at the CERN Large Hadron Collider*, Journal of Instrumentation **3** no. 08, (2008) S08003.

[107] CMS Collaboration, *The CMS experiment at the CERN LHC*, Journal of Instrumentation **3** no. 08, (2008) S08004.

[108] M. Lamont, *LHC Operation: Past and Future.*, Academic Training Lecture Regular Programme (CERN) (2013). http://indico.cern.ch/conferenceDisplay.py?confId=266730.

[109] S. Redaelli, *The operation of the LHC accelerator complex*, LHCC student lectures (CERN) (2010). http://indico.cern.ch/conferenceDisplay.py?confId=87719.

[110] C. Lefèvre, "The CERN accelerator complex. complexe des accélérateurs du CERN." Dec, 2008.

[111] LHCb Collaboration, *The LHCb Detector at the LHC*, Journal of Instrumentation **3** no. 08, (2008) S08005.

[112] ALICE Collaboration, *The ALICE experiment at the CERN LHC*, Journal of Instrumentation **3** no. 08, (2008) S08002.

[113] LHCf Collaboration, *The LHCf detector at the CERN Large Hadron Collider*, Journal of Instrumentation **3** no. 08, (2008) S08006.

[114] TOTEM Collaboration, *The TOTEM Experiment at the CERN Large Hadron Collider*, Journal of Instrumentation **3** no. 08, (2008) S08007.

[115] MoEDAL Collaboration, *Technical Design Report of the MoEDAL Experiment*, Tech. Rep. CERN-LHCC-2009-006. MoEDAL-TDR-001, CERN, Geneva, Jun, 2009.

[116] ATLAS Collaboration, *Atlas Computing: technical design report.* CERN, Geneva, 2005.

[117] P. Calafiura et al., *The Athena Control Framework in Production, New Developments and Lessons Learned*, in *Computing in High Energy Physics and Nuclear Physics 2004*. 2005.

[118] G. Barrand et al., *GAUDI - A software architecture and framework for building HEP data processing applications*, Comput.Phys.Commun. **140** (2001) 45–55.

[119] R. Brun and F. Rademakers, *ROOT: An object oriented data analysis framework*, Nucl.Instrum.Meth. **A389** (1997) 81–86. See also http://root.cern.ch/.

[120] The author thanks Yuichi Sasaki (University of Tokyo) and Naoko Kanaya Omachi (University of Tokyo) for producing the analysis ready, smaller n-tuples which the author used for parts of this work.

[121] D. Adams et al., *The ATLAS Computing Model*, Tech. Rep. ATL-SOFT-2004-007. ATL-COM-SOFT-2004-009. CERN-ATL-COM-SOFT-2004-009. CERN-LHCC-2004-037-G-085, CERN, Geneva, Dec, 2004.

[122] R. Jones and D. Barberis, *The ATLAS computing model*, Journal of Physics: Conference Series **119** no. 7, (2008) 072020.

[123] R. Jones and D. Barberis, *The Evolution of the ATLAS Computing Model*, J. Phys.: Conf. Ser. **219** no. 7, (2010) 072037.

[124] S. Campana et al., *Evolving ATLAS Computing For Today's Networks*, Journal of Physics: Conference Series **396** no. 3, (2012) 032019.

[125] ATLAS Collaboration, *Improved luminosity determination in pp collisions at $\sqrt{s} = 7$ TeV using the ATLAS detector at the LHC*, Eur.Phys.J. **C73** (2013) 2518, arXiv:1302.4393 [hep-ex].

[126] S. van der Meer, *Calibration of the effective beam height in the ISR*, Tech. Rep. CERN-ISR-PO-68-31. ISR-PO-68-31, CERN, Geneva, 1968.

[127] ATLAS collaboration, *Public plot: Number of colliding bunches versus time*, November, 2013. https://atlas.web.cern.ch/Atlas/GROUPS/DATAPREPARATION/PublicPlots/ 2012/DataSummary/figs/bunchesvstime.eps.

[128] ATLAS collaboration, *Public plot: Peak pileup versus time*, November, 2013. https://atlas.web.cern.ch/Atlas/GROUPS/DATAPREPARATION/PublicPlots/2012/ DataSummary/figs/muvstime.eps.

[129] ATLAS collaboration, *Public plot: Peak Luminosity versus time*, November, 2013. https://atlas.web.cern.ch/Atlas/GROUPS/DATAPREPARATION/PublicPlots/2012/ DataSummary/figs/lumivstime.eps.

[130] ATLAS collaboration, *Public plot: Delivered Luminosity versus time for 2010,2011,2012 (pp data only)*, November, 2013. https://atlas.web.cern.ch/Atlas/GROUPS/DATAPREPARATION/PublicPlots/2012/ DataSummary/figs/intlumivsyear.eps.

[131] ATLAS Collaboration, *Further search for supersymmetry at $\sqrt{s}$=7 TeV in final states with jets, missing transverse momentum, and isolated leptons with the ATLAS detector*, Phys. Rev. D **86** (2012) 092002.

[132] ATLAS Collaboration, *Search for supersymmetry at $\sqrt{s} = 7$ TeV in final states with large jet multiplicity, missing transverse momentum and one isolated lepton with the ATLAS detector*, Tech. Rep. ATLAS-CONF-2012-140, CERN, Geneva, Oct, 2012.

[133] ATLAS Collaboration, *Search for supersymmetry in final states with jets, missing transverse momentum and one isolated lepton in $\sqrt{s}$=7 TeV pp collisions using 1 fb^{-1} of ATLAS data*, Phys. Rev. D **85** (2012) 012006.

[134] J. Allison et al., *Geant4 developments and applications*, Nuclear Science, IEEE Transactions on **53** no. 1, (2006) 270–278.

[135] M. Dobbs et al., *Les Houches guidebook to Monte Carlo generators for hadron collider physics*, `arXiv:hep-ph/0403045 [hep-ph]`.

[136] A. Buckley et al., *General-purpose event generators for LHC physics*, Phys.Rept. **504** (2011) 145–233, `arXiv:1101.2599 [hep-ph]`.

[137] M. H. Seymour and M. Marx, *Monte Carlo Event Generators*, Apr, 2013. Comments: Lectures given at 69th Scottish Universities Summer School in Physics (SUSSP 69), St. Andrews, 19th August - 1st September 2012.

[138] J. C. Collins et al., *Factorization for short distance hadron-hadron scattering*, Nuclear Physics B **261** no. 0, (1985) 104 – 142.

[139] M. Whalley et al., *The Les Houches accord PDFs (LHAPDF) and LHAGLUE*, `arXiv:hep-ph/0508110 [hep-ph]`.

[140] B. Andersson et al., *Parton fragmentation and string dynamics*, Physics Reports **97** no. 2–3, (1983) 31 – 145.

[141] B. Andersson, *The Lund Model.* Cambridge Books Online, 1998.

[142] G. C. Fox and S. Wolfram, *A model for parton showers in QCD*, Nuclear Physics B **168** no. 2, (1980) 285 – 295.

[143] D. Amati and G. Veneziano, *Preconfinement as a property of perturbative {QCD}*, Physics Letters B **83** no. 1, (1979) 87 – 92.

[144] G. Corcella et al., *HERWIG 6: An Event generator for hadron emission reactions with interfering gluons (including supersymmetric processes)*, JHEP **0101** (2001) 010, `arXiv:hep-ph/0011363 [hep-ph]`.

[145] J. Butterworth et al., *Multiparton interactions in photoproduction at HERA*, Z. Phys. **C72** (1996) 637–646, `arXiv:hep-ph/9601371 [hep-ph]`.

[146] B. P. Kersevan and E. Richter-Was, *The Monte Carlo event generator AcerMC version 2.0 with interfaces to PYTHIA 6.2 and HERWIG 6.5*, `arXiv:hep-ph/0405247 [hep-ph]`.

[147] M. L. Mangano et al., *ALPGEN, a generator for hard multiparton processes in hadronic collisions*, JHEP **0307** (2003) 001, `arXiv:hep-ph/0206293 [hep-ph]`.

[148] S. Frixione and B. R. Webber, *Matching NLO QCD computations and parton shower simulations*, JHEP **0206** (2002) 029, `arXiv:hep-ph/0204244 [hep-ph]`.

[149] ATLAS Collaboration, *Electron performance measurements with the ATLAS detector using the 2010 LHC proton-proton collision data*, The European Physical Journal C **72** no. 3, (2012) 1–46.

[150] C. Anastopoulos et al., *Supporting document on electron efficiency measurements using the 2012 LHC proton-proton collision data*, Tech. Rep. ATL-COM-PHYS-2013-1295, CERN, Geneva, Nov, 2013. Corresponding paper by the ATLAS Collaboration in preparation.

[151] W. Lampl et al., *Calorimeter Clustering Algorithms: Description and Performance*, Tech. Rep. ATL-LARG-PUB-2008-002. ATL-COM-LARG-2008-003, CERN, Geneva, Apr, 2008.

[152] T. Cornelissen et al., *Concepts, Design and Implementation of the ATLAS New Tracking (NEWT)*, Tech. Rep. ATL-SOFT-PUB-2007-007. ATL-COM-SOFT-2007-002, CERN, Geneva, Mar, 2007.

[153] R. Frühwirth, *Application of Kalman filtering to track and vertex fitting*, Nucl. Instrum. Methods Phys. Res., A **262** no. HEPHY-PUB-503, (1987) 444. 19 p.

[154] T. G. Cornelissen, M. Elsing, et al., *The global χ^2 track fitter in ATLAS*, Journal of Physics: Conference Series **119** no. 3, (2008) 032013.

[155] ATLAS Collaboration, *Improved electron reconstruction in ATLAS using the Gaussian Sum Filter-based model for bremsstrahlung*, Tech. Rep. ATLAS-CONF-2012-047, CERN, Geneva, May, 2012.

[156] ATLAS Collaboration, *Preliminary results on the muon reconstruction efficiency, momentum resolution, and momentum scale in ATLAS 2012 pp collision data*, Tech. Rep. ATLAS-CONF-2013-088, CERN, Geneva, Aug, 2013.

[157] R. Nicolaidou et al., *Muon identification procedure for the ATLAS detector at the LHC using Muonboy reconstruction package and tests of its performance using cosmic rays and single beam data*, Journal of Physics: Conference Series **219** no. 3, (2010) 032052.

[158] ATLAS Collaboration, *Identification of muon candidates in pp collisions at $\sqrt{s} = 900$ GeV with the ATLAS detector*, Tech. Rep. ATLAS-CONF-2010-015, CERN, Geneva, Jul, 2010.

[159] ATLAS Collaboration, *Muon reconstruction efficiency in reprocessed 2010 LHC proton-proton collision data recorded with the ATLAS detector*, ATLAS-CONF-2011-063. https://cdsweb.cern.ch/record/1345743.

[160] ATLAS Collaboration, *A measurement of the muon reconstruction efficiency in 2010 ATLAS data using jpsi decays*, ATLAS-CONF-2012-125. https://cds.cern.ch/record/1474642.

[161] ATLAS Collaboration, *Muon Momentum Resolution in First Pass Reconstruction of pp Collision Data Recorded by ATLAS in 2010*, ATLAS-CONF-2011-046. https://cdsweb.cern.ch/record/1338575.

[162] M. Cacciari et al., *The Anti-k(t) jet clustering algorithm*, JHEP **0804** (2008) 063, arXiv:0802.1189 [hep-ph].

[163] ATLAS Collaboration, *Jet energy measurement with the ATLAS detector in proton-proton collisions at $\sqrt{s} = 7$ TeV*, The European Physical Journal C **73** no. 3, (2013) 1–118.

[164] ATLAS Collaboration, *Jet energy scale and its systematic uncertainty in proton-proton collisions at sqrt(s)=7 TeV with ATLAS 2011 data*, Tech. Rep. ATLAS-CONF-2013-004, CERN, Geneva, Jan, 2013.

[165] S. Catani et al., *Longitudinally invariant K_t clustering algorithms for hadron hadron collisions*, Nucl.Phys. **B406** (1993) 187–224.

[166] S. D. Ellis and D. E. Soper, *Successive combination jet algorithm for hadron collisions*, Phys. Rev. D **48** (1993) 3160–3166.

[167] Y. Dokshitzer et al., *Better jet clustering algorithms*, Journal of High Energy Physics **1997** no. 08, (1997) 001.

[168] M. Wobisch and T. Wengler, *Hadronization Corrections to Jet Cross Sections in Deep-Inelastic Scattering*, hep-ph/9907280.

[169] S. Resconi, *Jet and Missing Transverse Momentum Reconstruction, Calibration and Performance with the ATLAS Detector at LHC*, Tech. Rep. ATL-PHYS-PROC-2013-203, CERN, Geneva, Jul, 2013.

[170] M. Cacciari et al., *The Catchment Area of Jets*, JHEP **0804** (2008) 005, arXiv:0802.1188 [hep-ph].

[171] ATLAS Collaboration, *Jet energy resolution in proton-proton collisions at $\sqrt{s} = 7$ TeV recorded in 2010 with the ATLAS detector*, The European Physical Journal C **73** no. 3, (2013) 1–27.

[172] ATLAS Collaboration, *Commissioning of the ATLAS high-performance b-tagging algorithms in the 7 TeV collision data*, Tech. Rep. ATLAS-CONF-2011-102, CERN, Geneva, Jul, 2011.

[173] ATLAS Collaboration, *Measurement of the b-tag Efficiency in a Sample of Jets Containing Muons with 5 fb^{-1} of Data from the ATLAS Detector*, Tech. Rep. ATLAS-CONF-2012-043, CERN, Geneva, Mar, 2012.

[174] ATLAS Collaboration, *Measuring the b-tag efficiency in a top-pair sample with 4.7 fb^{-1} of data from the ATLAS detector*, Tech. Rep. ATLAS-CONF-2012-097, CERN, Geneva, Jul, 2012.

[175] ATLAS Collaboration, *b-jet tagging calibration on c-jets containing D^{*+} mesons*, Tech. Rep. ATLAS-CONF-2012-039, CERN, Geneva, Mar, 2012.

[176] ATLAS Collaboration, *Measurement of the Mistag Rate with 5 fb^{-1} of Data Collected by the ATLAS Detector*, Tech. Rep. ATLAS-CONF-2012-040, CERN, Geneva, Mar, 2012.

[177] *Performance of Missing Transverse Momentum Reconstruction in ATLAS studied in Proton-Proton Collisions recorded in 2012 at 8 TeV*, Tech. Rep. ATLAS-CONF-2013-082, CERN, Geneva, Aug, 2013.

[178] ATLAS Collaboration, *Performance of Missing Transverse Momentum Reconstruction in ATLAS with 2011 Proton-Proton Collisions at $\sqrt{s}$ = 7 TeV*, Tech. Rep. ATLAS-CONF-2012-101, CERN, Geneva, Jul, 2012.

[179] ATLAS Collaboration, *Search for squarks and gluinos in events with isolated leptons, jets and missing transverse momentum at $\sqrt{s} = 8$ TeV with the ATLAS detector*, Tech. Rep. ATLAS-CONF-2013-062, CERN, Geneva, Jun, 2013.

[180] ATLAS Collaboration, *Search for strongly produced supersymmetric particles in decays with two leptons at $\sqrt{s}$ = 8 TeV*, Tech. Rep. ATLAS-CONF-2013-089, CERN, Geneva, Aug, 2013.

[181] ATLAS Collaboration, *Search for Supersymmetry in Events with Large Missing Transverse Momentum, Jets, and at Least One Tau Lepton in 21 fb^{-1} of $\sqrt{s}$ = 8 TeV Proton-Proton Collision Data with the ATLAS Detector*, Tech. Rep. ATLAS-CONF-2013-026, CERN, Geneva, Mar, 2013.

[182] UA1 Collaboration, *Experimental Observation of Isolated Large Transverse Energy Electrons with Associated Missing Energy at $\sqrt{s}$ = 540 GeV*, Phys.Lett. **B122** (1983) 103–116.

[183] UA2 Collaboration, *Observation of Single Isolated Electrons of High Transverse Momentum in Events with Missing Transverse Energy at the CERN anti-p p Collider*, Phys.Lett. **B122** (1983) 476–485.

[184] J. Lorenz et al., *Search for Supersymmetry with jets and missing transverse momentum and one lepton at $\sqrt{s}$ = 7 TeV (supporting INT note)*, Tech. Rep. ATL-PHYS-INT-2011-008, CERN, Geneva, Feb, 2011. Internal documentation to [3].

[185] ATLAS Collaboration, *Search for supersymmetry at $\sqrt{s}$ = 8 TeV in final states with jets, missing transverse momentum and one isolated lepton*, Tech. Rep. ATLAS-CONF-2012-104, CERN, Geneva, Aug, 2012.

[186] ATLAS SUSY group, 2013. Webpage at https://twiki.cern.ch/twiki/bin/viewauth/AtlasProtected/SusyFitter.

[187] J. Pumplin et al., *New generation of parton distributions with uncertainties from global QCD analysis*, JHEP **0207** (2002) 012, arXiv:hep-ph/0201195 [hep-ph].

[188] H.-L. Lai et al., *New parton distributions for collider physics*, Phys. Rev. **D82** (2010) 074024, arXiv:1007.2241 [hep-ph].

[189] ATLAS Collaboration, *New ATLAS event generator tunes to 2010 data*, Tech. Rep. ATL-PHYS-PUB-2011-008, CERN, Geneva, Apr, 2011.

[190] S. Catani et al., *Vector boson production at hadron colliders: a fully exclusive QCD calculation at NNLO*, Phys.Rev.Lett. **103** (2009) 082001, arXiv:0903.2120 [hep-ph].

[191] A. Martin et al., *Update of parton distributions at NNLO*, Phys. Lett. **B652** (2007) 292–299, `arXiv:0706.0459 [hep-ph]`.

[192] J. M. Campbell et al., *Next-to-leading order QCD predictions for W + 2 jet and Z + 2 jet production at the CERN LHC*, Phys. Rev. **D68** (2003) 094021, `arXiv:hep-ph/0308195 [hep-ph]`.

[193] M. Aliev et al., *HATHOR: HAdronic Top and Heavy quarks crOss section calculatoR*, Comput. Phys. Commun. **182** (2011) 1034–1046, `arXiv:1007.1327 [hep-ph]`.

[194] K. Melnikov and F. Petriello, *Electroweak gauge boson production at hadron colliders through $O(\alpha(s)^2)$*, Phys. Rev. **D74** (2006) 114017, `arXiv:hep-ph/0609070 [hep-ph]`.

[195] N. Kidonakis, *Next-to-next-to-leading-order collinear and soft gluon corrections for t-channel single top quark production*, Phys. Rev. **D83** (2011) 091503.

[196] N. Kidonakis, *NNLL resummation for s-channel single top quark production*, Phys. Rev. **D81** (2010) 054028.

[197] N. Kidonakis, *Two-loop soft anomalous dimensions for single top quark associated production with a W^- or H^-*, Phys. Rev. **D82** (2010) 054018.

[198] J. Lorenz et al., *Search for Supersymmetry with jets and missing transverse momentum and one or more leptons at $\sqrt{s} = 7$ TeV (supporting INT note)*, Tech. Rep. ATL-PHYS-INT-2012-082, CERN, Geneva, Oct, 2012. Internal documentation to [131].

[199] J. Lorenz et al., *Search for Supersymmetry with jets and missing transverse momentum and one lepton at $\sqrt{s} = 8$ TeV (supporting INT note)*, Tech. Rep. ATL-PHYS-INT-2012-066, CERN, Geneva, Sep, 2012. Internal documentation to [185].

[200] J. Lorenz et al., *Search for Supersymmetry with jets and missing transverse momentum and one or more leptons at $\sqrt{s} = 7$ TeV*, Tech. Rep. ATL-PHYS-INT-2012-025, CERN, Geneva, Apr, 2012. Internal documentation to [224].

[201] ATLAS Collaboration, "Trigger rates at the event filter in 2012.". http://twiki.cern.ch/twiki/pub/AtlasPublic/TriggerOperationPublicResults/StreamRates2012.pdf.

[202] K. Nagano, *Algorithms, performance, and development of the ATLAS High-level Trigger*, in *International Conference on Computing in High Energy and Nuclear Physics (CHEP)*, no. ATL-COM-DAQ-2013-109. Geneva, Oct, 2013.

[203] I. Hristova, *The evolution and performance of the ATLAS calorimeter-based triggers in 2011 and 2012*, Tech. Rep. ATL-DAQ-PROC-2012-051, CERN, Geneva, Oct, 2012.

[204] ATLAS Collaboration, G. Aad et al., *Performance of the ATLAS Trigger System in 2010*, The European Physical Journal C **72** no. 1, (2012) 1–61.

[205] ATLAS Collaboration, *Performance of the ATLAS Electron and Photon Trigger in p-p Collisions at $\sqrt{s} = 7$ TeV in 2011*, Tech. Rep. ATLAS-CONF-2012-048, CERN, Geneva, May, 2012.

[206] ATLAS Collaboration, *Performance of the ATLAS muon trigger in pp collisions at $\sqrt{s} = 8$ TeV*, tech. rep., CERN, Geneva, Sep, 2013. Paper in preparation. Internal documentation: ATL-COM-DAQ-2013-088.

[207] ATLAS Collaboration, *Performance of the ATLAS Electron and Photon Triggers in p-p Collisions at $\sqrt{s} = 8$ TeV in 2012*, Tech. Rep. ATL-COM-DAQ-2013-121, CERN, Geneva, Oct, 2013. Paper in preparation.

[208] ROOT Collaboration, K. Cranmer et al., *HistFactory: A tool for creating statistical models for use with RooFit and RooStats*, Tech. Rep. CERN-OPEN-2012-016, New York U., New York, Jan, 2012. See also http://twiki.cern.ch/twiki/bin/view/RooStats/HistFactoryXMLReference.

[209] L. Moneta, K. Belasco, et al., *The RooStats Project*, PoS **ACAT2010** (2010) 057, `arXiv:1009.1003 [physics.data-an]`.

[210] W. Verkerke and D. P. Kirkby, *The RooFit toolkit for data modeling*, eConf **C0303241** (2003) MOLT007, `arXiv:physics/0306116 [physics]`.

[211] G. Cowan, K. Cranmer, E. Gross, and O. Vitells, *Asymptotic formulae for likelihood-based tests of new physics*, European Physical Journal C **71** (2011) 1554, `arXiv:1007.1727 [physics.data-an]`.

[212] S. Wilks, *The Large-Sample Distribution of the Likelihood Ratio for Testing Composite Hypotheses*, Annals Math.Statist. **9** no. 1, (1938) 60–62.

[213] A. Wald, *Tests of Statistical Hypotheses Concerning Several Parameters When the Number of Observations is Large*, Transactions of the American Mathematical Society **54** no. 3, (1943) 426–482.

[214] G. Cowan, *Statistics for Searches at the LHC*, `arXiv:1307.2487 [hep-ex]`.

[215] ATLAS statistics forum, October, 2013. https://twiki.cern.ch/twiki/pub/AtlasProtected/StatisticsTools/CLsInfo.pdf.

[216] A. L. Read, *Presentation of search results: The CL(s) technique*, J. Phys. G **G28** (2002) 2693–2704.

[217] W. Beenakker, S. Brensing, et al., *Soft-gluon resummation for squark and gluino hadroproduction*, JHEP **0912** (2009) 041, `arXiv:0909.4418 [hep-ph]`.

[218] W. Beenakker, S. Brensing, et al., *Squark and Gluino Hadroproduction*, Int.J.Mod.Phys. **A26** (2011) 2637–2664, `arXiv:1105.1110 [hep-ph]`.

[219] W. Beenakker, R. Hopker, et al., *Squark and gluino production at hadron colliders*, Nucl.Phys. **B492** (1997) 51–103, `arXiv:hep-ph/9610490 [hep-ph]`.

[220] A. Kulesza and L. Motyka, *Threshold resummation for squark-antisquark and gluino-pair production at the LHC*, Phys.Rev.Lett. **102** (2009) 111802, `arXiv:0807.2405 [hep-ph]`.

[221] A. Kulesza and L. Motyka, *Soft gluon resummation for the production of gluino-gluino and squark-antisquark pairs at the LHC*, Phys.Rev. **D80** (2009) 095004, `arXiv:0905.4749 [hep-ph]`.

[222] M. Kramer, A. Kulesza, et al., *Supersymmetry production cross sections in pp collisions at $\sqrt{s} = 7$ TeV*, `arXiv:1206.2892 [hep-ph]`.

[223] LEP SUSY Working Group (ALEPH, DELPHI L3,OPAL), "Report No. LEPSUSYWG/01-03.1.". http://lepsusy.web.cern.ch/lepsusy/Welcome.html.

[224] ATLAS Collaboration, *Further search for supersymmetry at $\sqrt{s} = 7$ TeV in final states with jets, missing transverse momentum and one isolated lepton*, Tech. Rep. ATLAS-CONF-2012-041, CERN, Geneva, Mar, 2012.

[225] J. Lorenz et al., *Search for strongly produced supersymmetric particles in decays with leptons at $\sqrt{s} = 8$ TeV (supporting INT note)*, Tech. Rep. ATL-PHYS-INT-2013-017, CERN, Geneva, Oct, 2013. Internal documentation to [179].

[226] J. T. Linnemann, *Measures of significance in HEP and astrophysics*, eConf **C030908** (2003) MOBT001, `arXiv:physics/0312059 [physics]`.

[227] S. Frixione, P. Nason, and G. Ridolfi JHEP **0709** (2007) 126, `arXiv:hep-ph/0707.3088`.

[228] T. Gleisberg et al., *Event generation with Sherpa 1.1*, JHEP **02** (2009) 007, `0811.4622 [hep-ph]`.

[229] J. M. Campbell and R. K. Ellis JHEP **1207** (2012) 052, `arXiv:hep-ph/1204.5678 [hep-ph]`.

[230] A. Lazopoulos et al., *Next-to-leading order QCD corrections to $t\bar{t}Z$ production at the LHC*, Phys.Lett. **B666** (2008) 62–65, `arXiv:0804.2220 [hep-ph]`.

[231] M. Baak et al., *Search for Supersymmetry with compressed mass spectra in events involving soft-leptons, jets plus missing transverse momentum at $\sqrt{s} = 8$ TeV*, Tech. Rep. ATL-PHYS-INT-2013-019, CERN, Geneva, Okt, 2013. Internal documentation to [179].

[232] ATLAS Collaboration, *Search for squarks and gluinos with the ATLAS detector in final states with jets and missing transverse momentum and $20.3fb^{-1}$ of $\sqrt{s} = 8$ TeV proton-proton collision data*, Tech. Rep. ATLAS-CONF-2013-047, CERN, Geneva, May, 2013.

[233] ATLAS Collaboration, *MSUGRA summary plot*, September, 2013.
https://twiki.cern.ch/twiki/pub/AtlasPublic/CombinedSummaryPlots/
ATLAS_SUSY_MSUGRA_CMSSM_susy13-1.pdf.

[234] CMS Collaboration, *Search for new physics in events with same-sign dileptons and jets in pp collisions at $\sqrt{s}$=8 TeV*, Tech. Rep. arXiv:1311.6736. CMS-SUS-13-013. CERN-PH-EP-2013-213, CERN, Geneva, Nov, 2013. Comments: Submitted to JHEP.

[235] CMS Collaboration, *Search for New Physics in the Multijets and Missing Momentum Final State in Proton-Proton Collisions at 8 TeV*, Tech. Rep. CMS-PAS-SUS-13-012, CERN, Geneva, 2013.

[236] ATLAS Collaboration, *Limits on Supersymmetry*, August, 2013.
https://twiki.cern.ch/twiki/pub/AtlasPublic/CombinedSummaryPlots/
AtlasSearchesSUSY_SUSY2013.pdf.

[237] CMS Collaboration, *Limits on Supersymmetry*, August, 2013.
https://twiki.cern.ch/twiki/pub/CMSPublic/SUSYSMSSummaryPlots8TeV/barplot
_blue_orange_SUSY2013.pdf.

Acknowledgements